UNIVERSITY OF READING

Department of Meteorology

Dynamics of Sting Jets and their Relation to Larger-Scale Drivers

Ambrogio Volonté

A thesis submitted for the degree of Doctor of Philosophy

January 2018

Declaration

I confirm that this is my own work and the use of all material from other sources has been properly and fully acknowledged.

Ambrogio Volonté

Abstract

Sting jets (SJ) occur as an additional region of low-level strong, and possibly damaging, winds in some Shapiro-Keyser extratropical cyclones. While SJs are widely accepted as being distinct from the warm and cold conveyor belts, this contribution addresses the unresolved questions of the mechanisms responsible for their generation and descent, along with the dependence of their existence and characteristics on environmental conditions. These questions are tackled by using a case study and extending the findings to idealised simulations and related sensitivity experiments, focusing on the generation and release of mesoscale instabilities also from a Lagrangian perspective.

This study shows that synoptic-scale frontal dynamics and mesoscale instabilities (e.g. symmetric instability) can both co-exist and drive the SJ evolution. While frontal dynamics can in itself lead to SJs, the formation and eventual release of a succession of mesoscale instabilities can substantially enhance their strength. This analysis outlines, for the first time, the mechanism of generation of dry symmetric instabilities along the SJ. Diabatically-caused frontal motions can lead to the formation, via tilting of horizontal vorticity, of symmetrically unstable regions travelling with the SJ towards the cloud-head tip.

SJs form in the majority of idealised experiments, suggesting that they are a common feature of Shapiro-Keyser cyclones. In the control run and in half of the sensitivity experiments, the SJ is associated with a localised symmetrically unstable environment which evolves through the outlined mechanism and enhances the SJ strength, which also depends on jet-stream intensity. Coarser-resolution simulations of both case study and idealised configuration confirm that vertical and horizontal resolution constraints apply to ensure that the release and even generation of mesoscale instabilities is not suppressed.

These results represent a substantial step in understanding the mechanisms driving the formation and evolution of SJs, highlighting a likely underestimation of their intensity in coarser-resolution weather/climate models.

Acknowledgements

I would really like to thank my supervisors, Peter Clark and Sue Gray, for their amazing support and guidance throughout all my PhD. They've always been available and willing to listen, focused not only on the project but also on my personal scientific growth. I can certainly look at them as role models, treasuring many aspects of their attitude towards me. For example, Peter's enthusiasm in front of the phenomena to be discovered and clarified really made the PhD an exciting journey. And also, Sue (who's been more than a 'co-supervisor'!) showed me how to be patient and welcoming, always smiling when I was randomly knocking at her office door. She's been always supportive and helpful, particularly in the final writing stages, spending an incredible amount of time trying to improve my shaky English writing and the quality of my results. Thanks to my monitoring committee, Bob Plant and Miguel Teixeira, for their useful comments and feedback and for their availability. I would also like to thank Neil Hart, for all his help with the project (oh, the trajectory code!) and for the deep and surprising friendship. Thanks also to Laura Baker, Oscar Martinez-Alvarado and to the many people around the department (IT, Admin ...) that promptly gave their time to solve all the problems I could have. Thanks to all the people in the department (from academics to outreach officers) that got me involved in demonstrating to students and to members of the public. Speaking of the department, thanks to all the friends (special mention to Nick and Eunice, really!), in our 'office', on the football pitch and elsewhere; in many ways they made the last 3.5 years very special. Special thanks also to the academics and researchers I met outside Reading, in conferences and schools (Heini and Olivia, thanks for allowing me to visit your departments!) Last but not least (first, actually!), thanks to God that made possible for me to meet all these people and also gave me this passion, which arose by looking at familiar skies, clouds and panoramas between fields, lakes and mountains. (see below a saying from my town, written in the local dialect, which in a funny way shows the daily-life relevance of meteorology).

se'l tempural al vegn da Comm, ciapa la sapa e vá a sapáa i pomm

se'l tempural al vegn da Galaráa, ciapa la sapa e scapa a cá! [1]

[1] If the thunderstorm is coming from Como, get the hoe and go hoeing the potatoes. If instead the thunderstorm is coming from Gallarate, get the hoe and run home!

Contents

1 Introduction **1**

1.1 Introduction and motivation 1

1.2 Aims of this PhD thesis 3

1.3 Thesis outline 5

2 Background theory and literature review **9**

2.1 Overview on Extratropical Cyclones 9

2.1.1 Conceptual models: Norwegian vs Shapiro-Keyser cyclones 9

2.1.2 The main features of intense cyclones 14

2.1.3 Airstreams related to strong low-level winds in extratropical cyclones 16

2.2 Focus on idealised baroclinic lifecycles 18

2.2.1 Baroclinic instability and "PV thinking" 18

2.2.2 Idealised simulations of Shapiro-Keyser baroclinic lifecycles 21

2.3 Focus on the generation of CSI and mesoscale instabilities 25

2.3.1 CI (conditional instability) and other instabilities released through upright convection 26

2.3.2 CSI (conditional symmetric instability) and other instabilities released through slantwise convection 28

2.4 Sting jets in extratropical cyclones 32

2.4.1 Introduction 32

2.4.2 Case-study modelling analyses of sting-jet storms 36

2.4.3 Idealised modelling analyses of sting-jet storms 44

2.4.4 Observational analyses of sting-jet storms 47

2.4.5 Climatologies of sting-jet storms 51

2.4.6 Summary and discussion of the state-of-the art theoretical understanding of SJ dynamics 53

3 Methodology **57**

3.1 Introduction 57

3.2 Description of the MetUM version 8.2 57

3.2.1 Model dynamics 58

3.2.2 Parameterisations schemes in the model 59

3.2.3 Poles and grid orientation 61

3.3 Differences between MetUM versions 8.2 and 10.5 61

3.4 The use of Lagrangian trajectories 63

3.5 Diagnostics to identify regions of atmospheric instability 64

3.6 PV tracers 66

4 Case study of Windstorm Tini: identifying a Sting Jet **67**

4.1 Setup of the model simulation of windstorm Tini 67

4.2 Development of windstorm Tini: observations and model simulation . . . 69

4.2.1 Background and synoptic overview 70

4.2.2 Satellite imagery 72

4.2.3 Observations of surface gusts 73

4.2.4 Observations of Aberystwyth NERC MST Radar 77

4.2.5 Summary of the comparison between storm observations and model simulation 80

4.3 Analysis of strong winds in windstorm Tini 80

4.3.1 Earth-relative wind speed 80

4.3.2 System-relative wind speed 81

4.3.3 Vertical motion and cross sections 82

4.4 Lagrangian trajectories: identification and kinematics of the SJ and CCB airstreams 85

4.4.1 Sting jet 85

4.4.2 Cold conveyor belt 85

4.4.3 Kinematics of the airstreams 86

4.5 Characterisation of the SJ airstream 88

4.5.1 Evolution of physical quantities along trajectories 88

5 Case study of Windstorm Tini: linking the Sting Jet with mesoscale instabilities 95

5.1 Evolution of instabilities along trajectories 95

5.1.1 Conditional Symmetric Instability 95

5.1.2 Dry mesoscale instabilities 96

5.1.3 Brief description of evolution of instabilities in the CCB airstream . 97

5.2 Mechanisms generating instabilities and connection with the SJ evolution 99

5.2.1 Vorticity structure . . . 99
5.2.2 Analysis of the vorticity equation . . . 103
5.2.3 Frontogenesis/lysis diagnostic . . . 106
5.3 Comparison with a coarser-resolution model . . . 108
5.3.1 Motivation . . . 108
5.3.2 Results . . . 109
5.4 Analysis of PV — and θ — tracers . . . 114
5.4.1 Motivation . . . 114
5.4.2 Brief characterisation of the SJ in the run with PV tracers . . . 114
5.4.3 Analysis of PV tracers . . . 118
5.4.4 Analysis of θ tracers . . . 123
5.4.5 General discussion of the results of this section . . . 126
5.5 Summary and conclusion of the case study . . . 127

6 Idealised modelling of a Sting Jet cyclone **133**

6.1 Introduction and motivation . . . 133
6.2 Model configuration and chosen initial state . . . 134
6.2.1 Domain geometry and initial balance . . . 135
6.2.2 Initial jet specification, temperature profile and moisture set up . . . 136
6.2.3 Temperature perturbation . . . 138
6.2.4 Model resolution . . . 138
6.3 Identification and characterisation of a SJ in the control simulation . . . 139

6.3.1 Overview of the storm's evolution 140

6.3.2 Analysis of strong winds in the frontal-fracture region 141

6.3.3 Description of selected starting points for sting-jet trajectories . . . 143

6.3.4 Analysis of relevant physical quantities on the airstream 144

6.3.5 Evolution of mesoscale instabilities along the airstream 147

6.3.6 Evolution of potential vorticity in the cloud head 148

6.4 Sensitivity experiments 152

6.4.1 Motivation for and summary of sensitivity experiments 152

6.4.2 Identification of SJs (or SJ-like airstreams) in the different experiments 154

6.4.3 Common characteristics of the SJs identified in the different sensitivity experiments 156

6.4.4 Sensitivity to model resolution 160

6.4.5 Sensitivity to initial moisture content 161

6.4.6 Sensitivity to upper-level jet strength 164

6.4.7 Sensitivity to latent heat 167

6.4.8 General discussion of the results of the sensitivity experiments . . 171

6.5 Comparison of the results with previous idealised studies 177

6.6 Summary and conclusion of the idealised study 179

7 Conclusion **183**

7.1 Introduction 183

7.2 Overview of the current key issues in SJ research and of the related questions addressed in the thesis 184

7.3 Summary of the main results of the thesis 187

7.3.1 Case Study of a SJ cyclone: windstorm Tini 187

7.3.2 Idealised simulations of SJ cyclones 190

7.4 Key results of this thesis 192

7.4.1 Summary list of novel contributions from this work to the SJ research 195

7.5 Possible future work and open questions 196

References 198

Appendices 209

A Initial Profiles for an Idealised Cyclone by Prof. Peter Clark, 2017 211

A.1 New Dynamics/Endgame equations of motion 211

A.2 Thermal wind balance for uniform zonal flow 212

A.2.1 Balanced zonal flow 212

A.2.2 Ian Boutle's approximation 213

A.2.3 An accurate algorithm 216

A.3 Reference θ_v Profile 218

A.4 Jet Specification 219

A.5 Moisture 220

A.6 Initial Perturbation 224

Chapter 1

Introduction

1.1 Introduction and motivation

Figure 1.1: Huge waves battering the Cornish coast at Porthleven on 5 February 2014. Photo by Matt Clark (http://www.metoffice.gov.uk/climate/uk/interesting/2014-janwind).

Winter storms constitute one of the main extreme weather hazards in Western and Central Europe. Winter 2013-2014 was classified as the stormiest on records for UK and Ireland (Matthews et al., 2014), with the UK hit by a succession of severe storms from late January to mid-February resulting in widespread impacts and damage. In particular, 6 major storms passed over the UK in that period separated only by 2–3 days. The occurrence of this stormy period, in addition to an earlier one from December 2013 to

January 2014, made this winter the stormiest for at least 20 years (UK Met Office, 2015). Strong winds and huge waves (Figure 1.1) posed an extreme hazard to exposed coastlines in south and west of Great Britain causing also widespread disruption to transport. Major flooding occurred, especially in Somerset (Figure 1.2) and along the River Thames. The total value of weather-related claims in the UK for winter 2013-2014 reached £1.1 billion (Risk Management Solutions, 2014). Hence, this hazard is now as relevant as ever.

A major risk related to winter storms is caused by strong surface winds that can occur in different regions of the storm. Generally, these strong surface winds are related to low-level jets along warm and cold fronts (Baker, 2009) but, analysing the Great Storm that affected the UK in October 1987, Browning (2004) and Clark et al. (2005) highlighted that an additional region of strong surface winds can exist. These additional strong winds are related to an airstream that exits from the tip of the hook-shaped cloud head (see Figure 1.3) and descends rapidly to the surface: the "sting jet" (SJ hereafter). The name derives from the analogy with the poisonous sting at the end of a scorpion's tail, used to describe localised strong winds in this region of cyclones, "the poisonous tail of the bent-back occlusion", as in the reference by Grønås (1995).

SJs have been found to occur in about 1/3 of storms occurring over the North Atlantic (see Martínez-Alvarado et al. (2012) and Hart et al. (2017)) and have caused widespread damage several times during recent years (Hewson and Neu, 2015). They have consequently moved on from a being newly-discovered weather phenomenon (UK Met Office, 2012a) to become one of the current key research topics concerning extreme weather. The importance of SJ events (and Reading's contribution to advancement of knowledge in this area) was recognised by the successful submission by University of Reading of an impact case study in the 2014 UK Research Excellence Framework (Research Excellence Framework, 2014).

Despite this increasing popularity, the evolution of SJs (along with the underlying dynamics) has not yet been clarified in many aspects. Main research questions concern the mechanisms leading to the generation and descent of the SJ, with an ongoing debate on the role of overall cyclone dynamics and localised release of mesoscale instability and on the possible contribution of other processes such as evaporative/sublimational cooling. Other key areas of open research revolve around the robustness of the SJ and its dependence on different environmental conditions, along with the assessment of model resolution constraints. These research issues lead to the formulation of the questions addressed in this thesis, which are briefly outlined in the next section.

Figure 1.2: Aerial view of flooded Somerset Levels on 2 February 2014. Photo by Tim Pestridge (http://www.metoffice.gov.uk/climate/uk/interesting/2014-janwind).

1.2 Aims of this PhD thesis

The SJ occurs in some intense Shapiro-Keyser cyclones and it is described as a short-lived airstream that descends from the tip of the cloud head into the frontal-fracture region leading to a distinct region of low-level strong winds (see definition in Clark and Gray (2018)). It is now widely accepted that SJs are not part of the warm or cold conveyor belts, whose dynamics is now generally well-known. However, the dynamics of SJs and the mechanisms responsible for their occurrence are yet to be fully understood.

One of the key aspects of the current research concerns the dependence of SJ generation and strengthening upon the release of mesoscale instabilities and upon the balanced dynamics in the frontolytic region of the cyclone. Other main topics refer to the existence of model resolution constraints in simulating SJs and in the assessment of its robustness as a feature in intense Shapiro-Keyser cyclones , along with its dependency on different

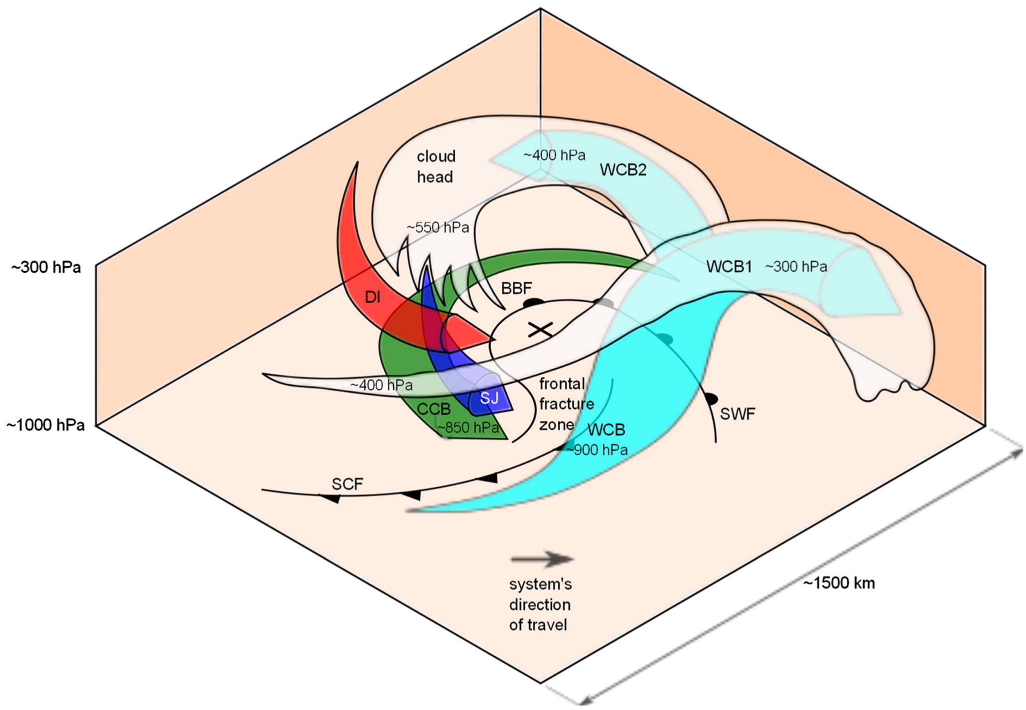

Figure 1.3: Figure 1 in Martínez-Alvarado et al. (2014a) showing the structure of an extratropical cyclone developing a frontal fracture in which the descent of a sting jet (SJ) occurs. Other features displayed are: surface cold front (SCF), surface warm front (SWF), bent-back front (BBF), warm conveyor belt (WCB) with anticyclonic (WCB1) and cyclonic (WCB2) branches, cold conveyor belt (CCB) and dry intrusion (DI). The pale shading represents cloud top while the large X indicates the surface cyclone centre.

environmental conditions. The questions arising from these issues (which are explained in more detail throughout Chapter 2 and reviewed in Section 7.2) are summarised in the following:

- Do 'frontolysis' and 'mesoscale instabilities' mechanisms both play a role in driving SJ evolution?

  - If yes, how do they co-exist and co-operate? What is the relative importance of each of these mechanisms?

  - Are other processes (e.g. evaporative/sublimational cooling) involved in SJ evolution?

- If mesoscale instability does take part in SJ evolution, how is it generated?

  - Is it possible to outline a mechanism of generation of instability along the SJ?

- What are the model constraints, in terms of horizontal and vertical resolution, to correctly simulate SJ evolution and allow the relevant processes to act?

- Which environmental and large-scale conditions favour the development and strengthening of a SJ?
- Is the SJ a robust feature of intense extratropical cyclones evolving according to the Shapiro-Keyser model?

The work to be presented in this thesis addresses these questions using a two-stage approach. At first, the case study analysis of windstorm Tini (see Chapters 4 and 5 and Volonté et al. (2018), to be published soon), chosen as a potential SJ case, has been performed to learn about the role of different mechanisms and to demonstrate the ability of the model in simulating SJs. The related investigation is carried out through simulations run with the MetUM and Lagrangian trajectories are used to gain further information on the dynamics of the SJ. Particular attention is devoted to the evolution of mesoscale atmospheric instabilities in the region where the descending airstream originates and in the analysis of frontogenesis field and of vorticity budgets, to highlight the processes driving the evolution of the SJ. Secondly, the findings are extended through the use of idealised simulations (see Chapter 6). In this way, using a framework in which external parameters can be systematically changed, the effect of different processes on the SJ evolution can be investigated, looking at the dependency of the SJ dynamics on different environmental and larger-scale conditions. The discussion of the results of this study, answering to the questions outlined, can be found in Chapter 7.

1.3 Thesis outline

This section provides an overview of the structure of this thesis.

In Chapter 2 the relevant background theory and literature are reviewed. The structure and evolution of extratropical cyclones are discussed in Section 2.1, with particular focus on the regions where strong winds at low levels occur. Idealised baroclinic lifecycles, related to the simulations presented in Chapter 6, are reviewed in Section 2.2. An overview of the mesoscale instabilities playing a main role in the sting-jet dynamics, as clarified in Chapter 5, is provided in Section 2.3. The chapter is concluded by Section 2.4, focused on extratropical cyclones containing sting jets. A review of the body of literature currently available is provided, with particular attention on observations, simulations (both real-case and idealised) and climatologies of sting-jet storms.

In Chapter 3 the modelling and post-processing tools used in this analysis and mentioned throughout the thesis are described. The Met Office Unified Model (Met UM) has been used for both real-case and idealised simulations. After an introduction in Section 3.1, the model settings used for case study and idealised analyses are described in Sections 3.2 and 3.3 respectively. For the latter section, an analysis of the initial basic state is presented along with a comparison with the relevant literature. The rest of the chapter focuses on the use of Lagrangian trajectories (in Section 3.4), on the methods to diagnose and identify regions of atmospheric instability (Section 3.5) and on the use of potential vorticity (PV) tracers (Section 3.6)

The first part of the analysis of windstorm Tini is contained in Chapter 4. After a summary of the model setup (Section 4.1), observations suggesting the possible occurrence of a sting jet in the storm are presented and compared with model simulations in Section 4.2. The rest of the chapter is focused on the identification of a sting jet in model simulations of windstorm Tini. The areas in which strong winds occur are described in Section 4.3 while Lagrangian trajectories representing the evolution of the sting-jet airstream are presented in Section 4.4 and 4.5.

The analysis of simulations of windstorm Tini continues in Chapter 5. This chapter is devoted to the dynamics of the identified sting jet, with particular focus on the evolution of mesoscale instabilities along the jet. The evolution of instabilities along SJ trajectories (and, briefly CCB trajectories) is described in Section 5.1 while the evolutions of vorticity on the jet and of the frontogenesis pattern in the storm are presented in Section 5.2. The results obtained with coarser-resolution simulations are shown in Section 5.3, highlighting the effects of model resolution in capturing sting-jet dynamics. An analysis of potential vorticity (PV) tracers is contained in Section 5.4, showing which processes lead to negative values of PV, i.e. to the onset of instability, on the jet. A summary of the main results of the case study is contained in Section 5.5, which concludes the chapter.

In Chapter 6 idealised simulations of sting-jet cyclones are presented. The chapter is opened by an introduction and motivation of the analysis (Section 6.1), followed by a discussion on the initial state chosen for the idealised moist baroclinic wave simulation (Section 6.2). The results obtained by the control simulation are presented in Section 6.3 while Section 6.4 is devoted to the description of sensitivity experiments. A comparison of these results with previous findings from other studies is in Section 6.5, while a final discussion concludes the chapter (Section 6.6).

A summary of the key results of this thesis is contained in Chapter 7. An evaluation of how these results meet the targets stated in Section 1.2 is included in the chapter. Suggestions for future work end the chapter and the thesis.

Chapter 2

Background theory and literature review

2.1 Overview on Extratropical Cyclones

Sting jets occur in some intense extratropical cyclones. An extensive review of the theory and classification of extratropical cyclones goes beyond the scope of this chapter and can be found in Catto (2016). However, some aspects of it need to be reviewed in order to put into context the discussion about sting jets (for a similar account of the topic see the PhD thesis of Baker (2011) and Section 2 of Clark and Gray (2018)).

2.1.1 Conceptual models: Norwegian vs Shapiro-Keyser cyclones

Extratropical cyclones are a common feature in mid-latitude weather. It is not surprising thus that the first conceptual model describing their evolution was formulated almost a century ago (see Bjerknes (1919) and Bjerknes and Solberg (1922)). A formal description of baroclinic instability (see Eady (1949) and Charney (1947)), that we know now leads to the intensification of cyclones, had yet to come at that time. Nevertheless, Vilhelm Bjerknes and his group made use of surface-based weather observations to develop a conceptual understanding of North Atlantic cyclones. Their methods and teachings are known as "the Bergen School of Meteorology" (Catto, 2016). They referred to cyclones as consisting of two different air masses, of warm and cold origin, with rather distinct boundary surfaces (i.e. fronts) running through the cyclone centre and separating them. They outlined the evolution and life cycle of extratropical cyclones in a conceptual model

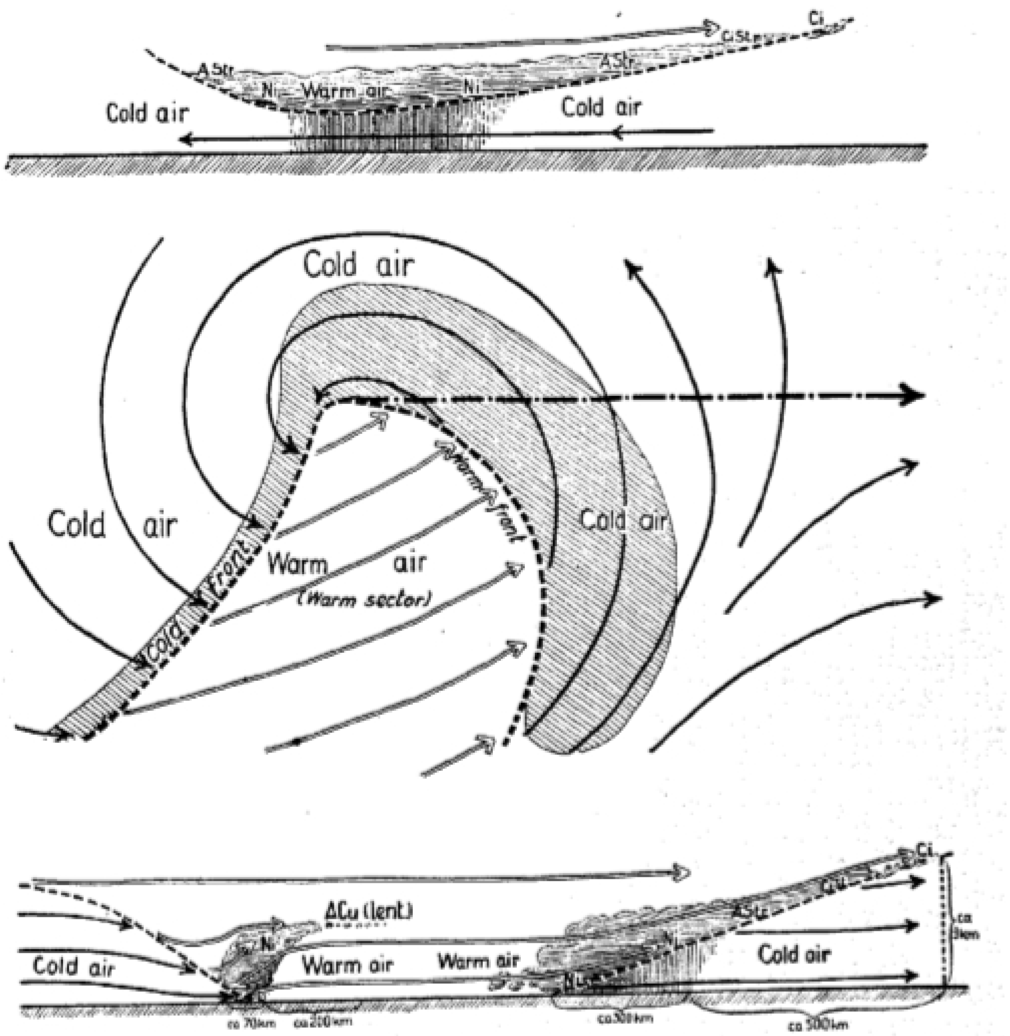

Figure 2.1: From Bjerknes and Solberg (1922) Fig. 1. Idealised schematics of the main features of a cyclone.

that is generally called "the Norwegian Model" in their honour (Figure 2.1). The Norwegian cyclone model is rightly regarded as a remarkable achievement in weather science and considered as the foundation of synoptic meteorology, or at least of its observational branch. We can summarise the cyclone evolution depicted in the model in essentially four stages (compare with Figure 2.2).

- Stage I: a stationary front marks the boundary between a colder airmass on its northern side and warmer air to the south (in the Northern Hemisphere).
- Stage II: a wave starts to form, with the "warm tongue" moving towards north and flowing over the denser cold air.

- Stage III: the wave grows in amplitude while the system travels eastward and the cold air curves around the northern end of the warm tongue and the cyclone centre.
- Stage IV: the cold air from the rear side of the cyclone reaches the warm air cutting off the warm sector (i.e. forming an "occlusion"). At this point the cyclone starts to weaken.

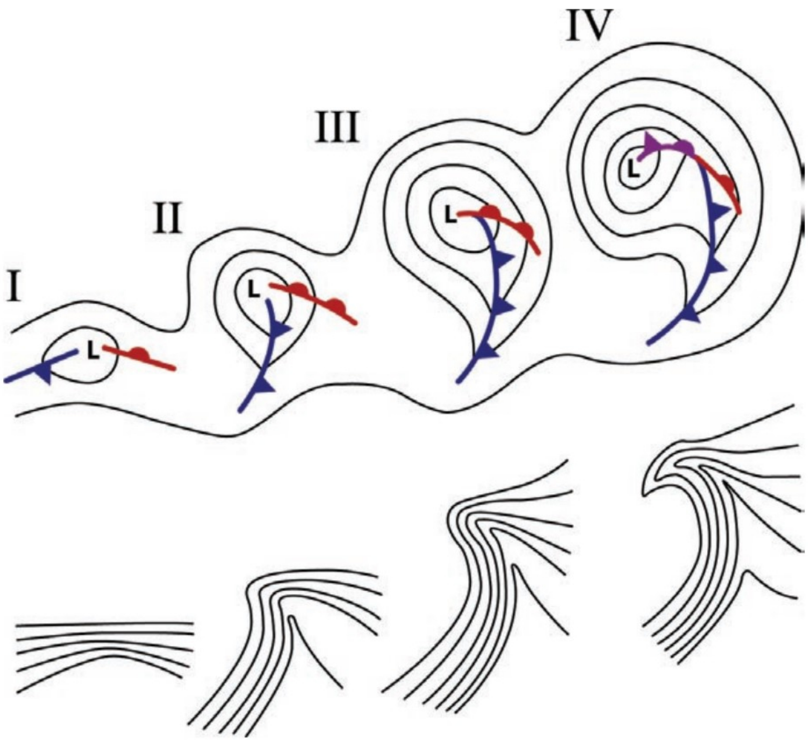

Figure 2.2: From Schultz and Vaughan (2011) Fig. 2. Conceptual model of a Norwegian cyclone showing geopotential height and fronts (top) and potential temperature (bottom) in the lower troposphere. The figure displays the cyclone evolution divided in the four stages described in the text.

As explained earlier, this model has been considered adequate to describe structure and evolution of cyclones for several decades. However, with the significant growth in available observations that occurred in the second half of the last century and the consequent improvements in theoretical understanding, it became evident that the Norwegian model was often not accurately describing the actual evolution of cyclones. A thorough review of the relevant literature can be found in Schultz and Vaughan (2011). Different conceptual models have been proposed depending on the location and environment in which the cyclone evolves, including the "Shapiro-Keyser" model (Shapiro and Keyser, 1990), on which we focus.

The Shapiro-Keyser conceptual model aims at describing the life-cycle of marine cyclones and is displayed in Figure 2.3 with its four stages of cyclone evolution.

- Stage I: incipient frontal cyclone (as in the Norwegian model).
- Stage II: a frontal fracture starts to develop with a separation between warm and cold fronts with the former becoming more intense and zonally elongated.
- Stage III: the cyclone undergoes further deepening while the bent-back front begins to hook around its centre. A frontal 'T-bone" structure is now present with the two fronts almost perpendicular to each other.
- Stage IV: final stage of evolution with formation of a warm seclusion in the cyclone centre, now completely encircled by the wrapped-up bent-back front.

The main differences between Norwegian and Shapiro-Keyser models can be summarised looking at the occlusion process. Using the terminology adopted in Schultz and Vaughan (2011), in the Norwegian model the occlusion occurs as a "catch-up" with the cold front reaching the warm front and cutting it off the surface. In the Shapiro-Keyser model the occlusion is described rather as a "wrap-up" process, with the formation of a warm seclusion around the cyclone centre. This different evolution is associated with the opening of a frontal fracture, a key feature for sting-jet dynamics, as it will be explained in the following sections.

Schultz et al. (1998), using analyses of observed mid-latitude oceanic cyclones and idealised simulations of vortices in a non-divergent barotropic model, showed that the resemblance of cyclones to the Norwegian or to the Shapiro-Keyser model is dependent on the background flow in which they are embedded. Diffluent background flow favours meridional elongation of fronts, with cyclones developing similarly to the Norwegian model and showing strong cold fronts. On the contrary, confluent flow is associated with more zonally elongated fronts and the development of a frontal fracture in cyclones developing accordingly to the Shapiro-Keyser model. Thus, the results in Schultz et al. (1998) show how the along-jet shear plays a role in cyclone evolution. A few other studies (see Davies et al. (1991), Thorncroft et al. (1993) and Shapiro et al. (1999)) took a complimentary approach looking at across-jet shear influence on cyclone development. They

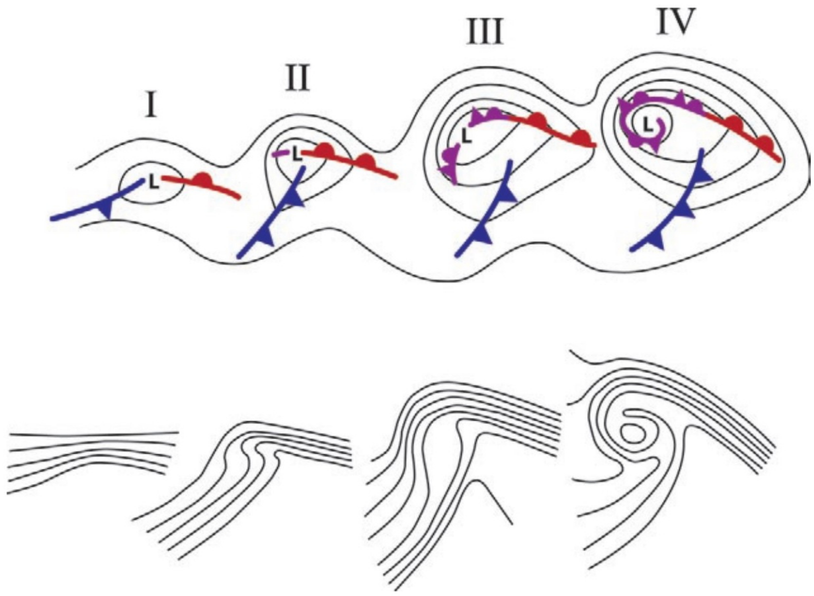

Figure 2.3: From Schultz and Vaughan (2011) Fig. 12. Conceptual model of a Shapiro-Keyser cyclone showing geopotential height and fronts (top) and potential temperature (bottom) in the lower troposphere. The figure displays the cyclone evolution divided in the four stages described in the text.

outlined that cyclones with a cyclonic barotropic shear superimposed on the initial symmetric jet configuration, which is in fact baroclinic, develop according to the Norwegian model (LC2 cyclones in Thorncroft et al. (1993), see Section 2.2 for more details). Cyclones without this additional cyclonic barotropic shear added to the initial symmetric jet configuration (LC1 cyclones) develop instead in good agreement with the Shapiro-Keyser model. Schultz and Zhang (2007) looked for a synthesis between the two different approaches. They confirmed that zonal variability (i.e. the along-jet paradigm) controls cyclone evolution, supporting their statement with observational and modelling evidence linking cyclogenesis with jet-entrance and jet-exit regions. Coronel et al. (2016) recently complemented the discussion using idealised simulations to show that cyclones follow the Shapiro-Keyser model when initialised on the warm side of the upper-level jet whereas cyclones initialised on the jet axis undergo to a Norwegian-like evolution. It is also worthwhile mentioning that cyclones starting to develop on the southern side of the upper-level jet are likely to undergo to an intense growth when crossing the jet axis (Gilet et al., 2009) and that many of the cyclones undergoing explosive development have been found to cross the jet (Pinto et al., 2009). These findings suggest that Norwegian cyclones are more likely to be found "at the end of storm track", as Schultz et al.

(1998) already realised; Shapiro-Keyser cyclones might instead be more common at its entrance. In this case, it would appear that the locations of research centres where the two models have been developed reflect the prevalent observed cyclone structure (Clark and Gray, 2018). Nevertheless, Shapiro-Keyser cyclones do occur sometimes also in the Eastern Atlantic. The next sections include case studies of SJ-containing Shapiro-Keyser cyclones that affected the British Isles and North-Western Europe.

2.1.2 The main features of intense cyclones

Sting jets can occur in intense Shapiro-Keyser extratropical cyclones. The previous section outlined the main features of the evolution of a cyclone following the Shapiro-Keyser conceptual model. It is thus necessary to understand when an extratropical cyclone can be regarded as "intense" and what are its main features.

A broadly accepted definition exists for "explosive cyclogenesis", stating that central pressure must fall by at least $24(\sin\phi/\sin 60^{\circ})$ hPa in 24 hours (Sanders and Gyakum, 1980). This value should not be taken as a hard threshold, but rather as a benchmark for a first evaluation of the severity of the intensification process of a storm before performing more detailed analyses. In fact, intense storms do not necessarily reach this intensification rate threshold and, while the target of this criterion is exactly to separate rapidly deepening, some of them might even go through their main evolution in less than 24 hours. Also, the same pressure drop can be associated with different values of eddy kinetic energy and of vorticity (other ways to measure the intensity of the cyclone), so it cannot be regarded as a comprehensive measure of the overall cyclone intensity, but rather as an indication of it. In this regard it is interesting to note that Browning and Roberts (1994) used a moderately intense cyclone, not fulfilling the definition of Sanders and Gyakum (1980) but showing many of the characteristics of severe cyclones, as a case study to outline the main features of rapidly deepening cyclones. Some of those features will be described in the rest of this section (and in the following section their links to strong winds will be outlined).

In his review of the processes contributing to the rapid development of extratropical cyclones, Uccellini (1990) stressed that baroclinic instability produces deepening rates smaller than observed. Dynamical processes alone are not sufficient for rapid cyclogenesis. In fact, looking at the evidence available, he argued that "the nonlinear interaction among the various dynamic and thermodynamic processes within relatively small space and temporal domains is crucial for the rapid evolution of these storms". More recently, Gray et al. (2011) pointed out the important role played by latent-heat release in the development of explosively deepening cyclones. They cite, among others, Grønås (1995) and Shutts (1990b). Grønås (1995), using a case study, showed that an important role for the formation of the warm seclusion at the cyclone centre is played by potential vorticity (PV) anomalies linked with latent-heat release along the bent-back front. [1] The intensification of this seclusion is in turn linked to the generation of strong winds. Shutts (1990b) analysed the "Great October Storm" that battered southeast England in 1987 (more details in Section 2.4.1) finding that about two thirds of the central pressure drop could be ascribed to the release of latent heat. Hence, the importance of moisture and latent heat for the explosive development of extratropical cyclones should not be underestimated, along with the complexity they add to the cyclone structure. Quoting Browning (2005), among extratropical cyclones in the UK "the richest diversity of mesoscale sub-structures does occur in association with the most intense cyclones".

A common feature in cases of intense cyclogenesis associated with a confluent upper trough (i.e. likely to develop as one of those Shapiro-Keyser cyclones we are interested in) is the cloud head (Figure 2.4). Described by Bader et al. (1995) as a signature of explosively developing cyclones, the cloud head is distinguishable as a bulk cloud structure clearly distinct from other clouds, developing a hooked tip linked to the bent-back front. As pointed out by Böttger et al. (1975), the cloud head is a characteristic feature of a large part of extreme-winds producing extratropical Atlantic storms. This hook-shaped region of cloud lies to the poleward side of the cyclone centre. The dry slot (see below), looking like a "prominent dry wedge", separates the cloud head from the main cloud band. As the cyclone develops and gets deeper, the cloud head broadens (up to a width around 300 km) and becomes well-defined with a convex edge on its poleward side. When the cyclone reaches a development stage similar to Stage III of the Shapiro-Keyser conceptual model, the cloud head develops a hooked tip linked with the bent-back front.

[1] Ertel (or Ertel-Rossby) potential vorticity, commonly known as potential vorticity or just PV, is defined as $PV = \rho^{-1}\zeta \cdot \nabla\theta$ where ρ, ζ and θ indicate respectively density, absolute vorticity and potential temperature. PV is conserved in adiabatic frictionless motion (Hoskins and James, 2014).

The dry slot is another feature that is common in these storms. It is described by Browning and Roberts (1994) as a, satellite- detected, almost cloud-free area between the cloud head and polar-front cloud band. It indicates that an intrusion of dry air from the upper troposphere and lower stratosphere is approaching the centre of a developing cyclone. The dry slot is usually located above or close to the frontal fracture, the already-mentioned gap area occurring behind the primary cold front in the development of Shapiro-Keyser extratropical cyclones.

2.1.3 Airstreams related to strong low-level winds in extratropical cyclones

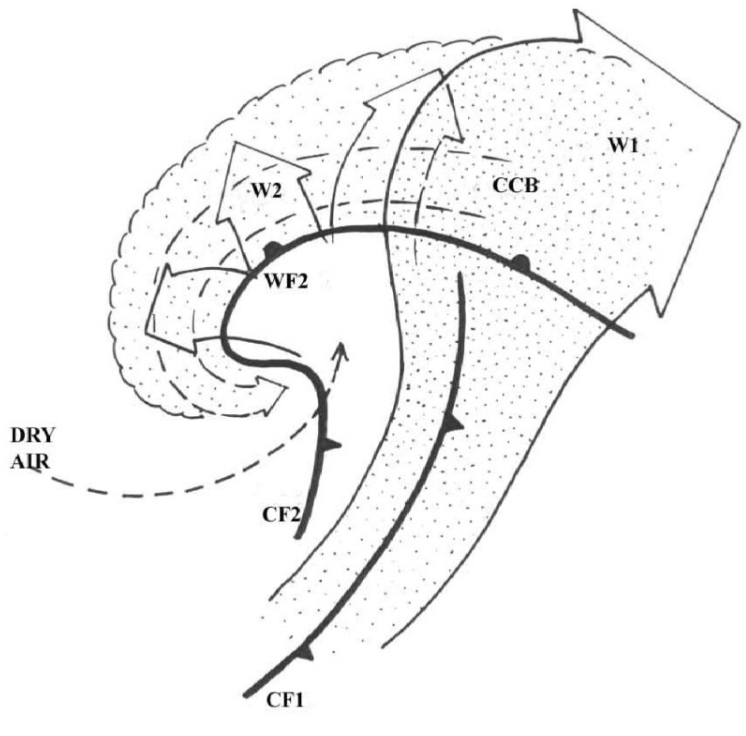

Figure 2.4: From Browning (2004) Fig. 2. Conceptual model of the principal airflows, fronts and cloud features in an extratropical cyclone undergoing transition between Stage III to Stage IV of the Shapiro-Keyser evolution model. The cloud head can be identified wrapping around the cyclone centre and containing the CCB. The anticyclonic and cyclonic branches of the WCB are indicated respectively as W1 and W2. Dry air intrusion (DI) occurs in the frontal fracture between the primary cold front (CF1) and the bent-back front (WF2-CF2).

The structure and evolution of extratropical cyclones can be represented in terms of the motion of discrete airstreams, providing a physical picture of the movement of air through the systems (e.g. see in Figure 2.5 the main low-level strong-winds-containing airstreams of Shapiro-Keyser cyclones). In these conceptual models, fronts are generated by the confluence of airstreams that can be widely different in origin and properties. A number of studies over the past few decades have attempted to explain the features of cloud and precipitation in extratropical cyclones in terms of cyclone-relative motion of airflows and with the use of isentropic flow maps (see Harrold (1973), Carlson (1980) and Browning (1990)). The three main airstreams in extratropical cyclones described in the mentioned studies are defined as warm conveyor belt (WCB), cold conveyor belt (CCB) and dry intrusion (DI).

The WCB has its origin at low levels within the warm sector of the storm. As it ascends on the warm side of the polar front, it carries along warm and moist air. Travelling polewards in the main cloud band of the cyclone, the WCB is the main airstream in terms of producing precipitation within extratropical cyclones. It is associated with long-lasting strong winds at the surface on the warm side of the primary cold front. At the top of its ascent the WCB turns anticyclonically. Going into more detail, Browning and Roberts (1994) and Bader et al. (1995) argued that two components of WCB can be defined. A first component, W1, rises anticyclonically above the warm front after having ascended along the polar-front cloud band. The other component, W2, is slightly less warm than W1. It ascends quickly above the bent-back front and then turns cyclonically and widens out to form the upper part of the cloud head.

The CCB is a shallow layer of moist and cool air that originates at low levels and flows rearward relative to the cyclone propagation. As the CCB flows on the poleward side of the warm front, it undercuts the WCB. As Schultz (2001) pointed out, the main path of the CCB is a cyclonic rotation around the cyclone centre. However, a part of the airstream that can be considered transitional between WCB and CCB turns eventually anticyclonically while ascending. The CCB is associated with strong winds on the cold side of the warm front. These winds can be as strong as the ones linked to the WCB or even stronger, as the CCB wraps around the centre of the cyclone and aligns with the system motion.

Analysing two case studies, Rivière et al. (2015) found that the evolution of the relative strength of the cold and warm conveyor belts during explosive cyclone development is dependent on the redistribution of lower-tropospheric eddy kinetic energy. In particular, the more intense low-level winds move from the WCB region to the CCB region as the cyclone crosses the upper-level jet going towards its cold-air side. This explosive development is associated with extremely strong winds in the region of cold advection at the tip of the CCB (i.e. behind the bent-back front) that they claimed can be attributed to rapid pressure rises occurring behind the upper-level short wave trough.

The DI is a flow of colder and drier air that originates in the upper troposphere or lower stratosphere and descends behind the cyclone, forming the dry slot region mentioned in Section 2.1.2 and tending to fan out at lower levels either anticyclonically or cyclonically (Thorncroft et al., 1993). After descending towards the cyclone centre, DI air ascends above the bent-back front and separates the two components of the WCB (Bader et al., 1995). The overrun of DI above CCB can create potential instability that can in turn give rise to convection in the dry slot (see Browning (1990), Bader et al. (1995) and Raveh-Rubin (2017))

In addition to these airstreams, another one can occur: the SJ. As the SJ is the focus of this thesis, it will be treated separately in Section 2.4 of this literature review.

2.2 Focus on idealised baroclinic lifecycles

Baroclinic instability is the primary mechanism of development of extratropical cyclones. As pointed out at the beginning of this chapter, an extensive account of the topic goes beyond the scope of this review. However, a brief summary of the concept of baroclinic instability is provided in the next section (in similar fashion to how it is covered in Catto (2016)), followed by a review of some studies constituting a basis for idealised simulations of Shapiro-Keyser cyclones, like the ones presented in Chapter 6 of this thesis. More technical discussions about different choices in the initial conditions and model settings for idealised simulations of baroclinic waves can be found in Chapter 3.

2.2.1 Baroclinic instability and "PV thinking"

The significant difference in the amount of solar heating between equator and poles (along with the associated responses in terms of long-wave radiative effects and air motions) is the ultimate cause of the strong meridional temperature gradients present at

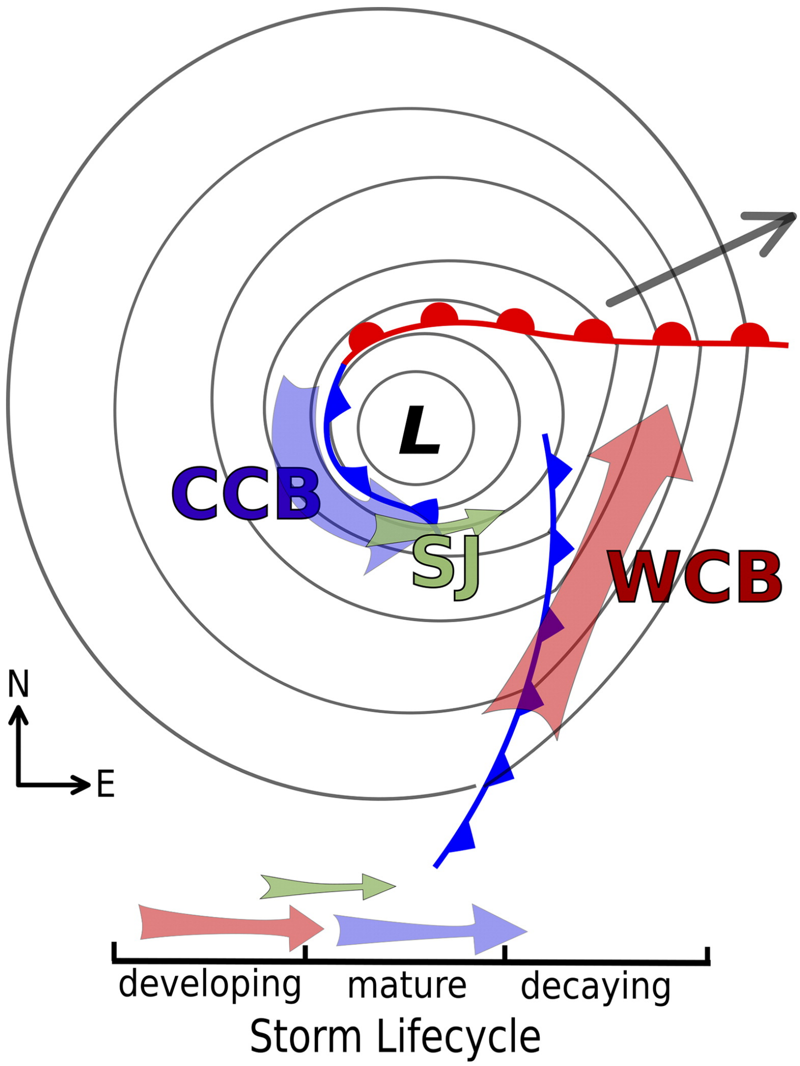

Figure 2.5: From Hart et al. (2017) Fig. 1. Schematic of low-level jets in explosively developing extratropical cyclones. Note that the jets occur at different times in the storm lifecycle, as shown by the diagram at the bottom of the figure. Approximate direction of storm propagation is shown by the grey arrow.

midlatitudes. Assuming thermal wind balance (which is correct practice when looking at synoptic and planetary scales) the temperature gradients will have to be associated with a vertical shear in zonal wind, resulting in a flow that is hydrodynamically unstable to small perturbations. The developing wave instability acts to convert the available potential energy into kinetic energy, generating cyclones and anticyclones. The resulting meridional heat transport reduces the baroclinicity, weakening the temperature gradients.

The mechanism of baroclinic growth can be visualised in terms of the interaction of two Rossby waves, one near the tropopause and one close to the surface, as explained in Hoskins et al. (1985). Figure 2.6 shows the concept, explained below, with the help of a diagram. Fig 2.6 is in fact a schematic picture of cyclogenesis associated with the arrival of an upper-air PV anomaly over a low-level baroclinic region. Consider a mean state with a positive poleward PV gradient at upper levels and a negative poleward temperature gradient at the surface. In (a) the upper-air cyclonic (i.e. positive in the northern hemisphere) PV anomaly, associated with an upper-level trough and the low tropopause shown and indicated by a solid plus sign, has just arrived over a region of significant low-level baroclinicity. The circulation induced by the anomaly is indicated by solid arrows, and potential temperature contours are shown on the ground. The low-level circulation is shown above the ground for clarity. The upper-level trough is thus inducing a cyclonic circulation at low levels. As a consequence, the advection by this circulation leads to a warm temperature anomaly somewhat ahead of the upper PV anomaly as indicated in (b), and marked with an open plus sign. This warm anomaly induces the cyclonic circulation indicated by the open arrows in (b). Hence, both the upper-level and surface anomalies act to intensify each other, through the "action at a distance" mechanism, and the initially small perturbation grows. This process in which upper- and lower-level waves work together to intensify each other is exactly what is called baroclinic instability. In most cases the upper-level wave propagates westward relative to the mean flow, while the low-level wave propagates eastward relative to the mean flow, leading to a reduction of the vertical tilt between the waves and eventually to a decay of the instability (unless phase locking, that may be provided by vertical shear, keeps the instability growing). Moreover, if the equatorward motion at upper levels advects high-PV polar lower-stratospheric air, and the poleward motion advects low-PV subtropical upper-tropospheric air, then the action of the upper-level circulation induced by the surface potential temperature anomaly will, as a result, strengthen the upper air PV anomaly and slow down its eastward progression.

Early conceptual models describing baroclinic instability include the Eady Model (Eady, 1949) and the Charney Model (Charney, 1947). As mentioned by Catto (2016) in their review, the maximum growth rate from the Eady Model has often been used to assess the baroclinicity in the atmosphere and hence to diagnose the possibility of extratropical cyclone development.

The mechanism of baroclinic growth just outlined assumes initially small perturbations. However, this is often not the case in the real atmosphere. The concept of "PV

thinking" has been developed in Hoskins et al. (1985) with the aim of understanding how atmospheric flows respond to the interactions of these finite anomalies. PV is a conserved quantity in adiabatic flows so its rate of change can be predicted by advection, with any other changes that are then associated with diabatic processes like friction, latent heating/cooling and radiative processes. Assuming that some balance condition (e.g. geostrophic balance) holds, PV can also be inverted allowing to infer the dynamic and thermodynamic state of the atmosphere (Hoskins and James, 2014). This property of invertibility is what leads to the concept of "action at a distance", with a disturbance at upper levels able to influence the near-surface circulation and vice versa.

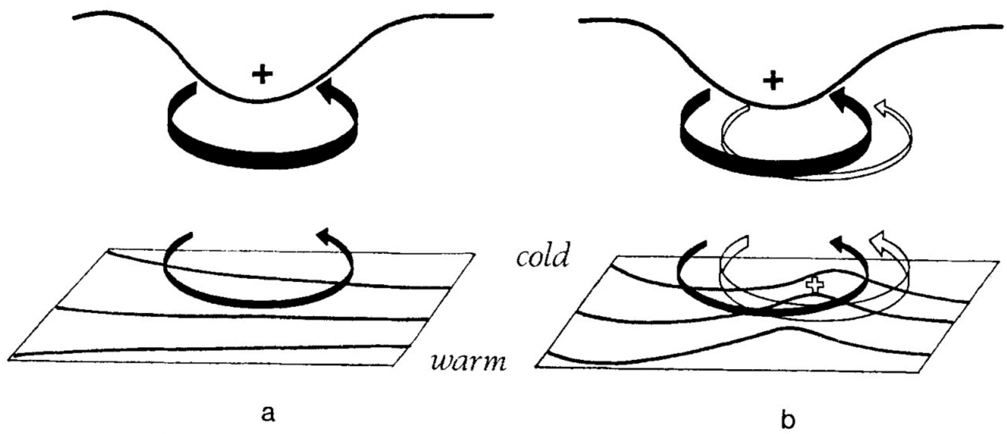

Figure 2.6: From Hoskins et al. (1985) Fig. 21. Schematic diagram of baroclinic instability in the Northern Hemisphere showing the "action at a distance" mechanism of intensification outlined in the text (see text for the meaning of the different features present in the figure).

2.2.2 Idealised simulations of Shapiro-Keyser baroclinic lifecycles

Basic state and barotropic shear

The analysis of idealised baroclinic waves has been a very useful tool to develop our current understanding on many different aspects of the evolution and dynamics of extratropical cyclones. Among them, for the research presented in this thesis, the influence that initial conditions (mainly in terms of upper-level jet structure and of moisture content) have in determining the shape of the developing cyclone is particularly relevant.

Following up earlier work from Simmons and Hoskins (1980), the investigation of the effects of adding barotropic shear to the basic state was performed by Thorncroft et al. (1993). As the former study had found quite large consequences associated with this change, in terms of time and magnitude of the maximum eddy kinetic energy (EKE) reached, Thorncroft et al. (1993) performed a more detailed examination. They used two different settings. LC1 (life cycle 1), without any barotropic shear component applied, and LC2 (life cycle 2), that has a cyclonic barotropic shear component applied to the initial jet (i.e. an additional westerly wind component on the southern side of the jet centre and an easterly component on its northern side). The two life cycles showed substantial differences in their evolution. LC1 showed cyclones developing similarly to the Shapiro-Keyser conceptual model with the occurrence of frontal fracture and, in later stages, warm seclusion. Anticyclonic wave breaking developed leading to an eventual cut-off of cyclonic PV. LC2 showed instead stronger cyclones and no anticyclones. The cyclones, characterised by weaker cold fronts and stronger warm fronts than in LC1, had a longer lifetime with a later peak of EKE and a less evident decay, a consequence of a circulation still cyclonic at upper levels even in the final stages of the simulations. In light of these results, confirmed by similar works of Wernli et al. (1998) and Shapiro et al. (1999), subsequent studies adopted LC1-like initial settings when looking for idealised cyclones resembling the Shapiro-Keyser model of evolution in their development.

Effects of moisture in idealised cyclones

All the studies mentioned in the section up to this point refer to dry idealised experiments. However, the evolution of cyclones in the real atmosphere is affected by the presence of moisture. Particularly in the case of intense deepening, as pointed out in Section 2.1, latent heating and other moisture related processes cannot be regarded as secondary factors in the development of explosive cyclones and associated strong winds. The results from previously described real-case studies that stressed the importance of moisture in the evolution of intense cyclones were confirmed by idealised simulations. Following Coronel et al. (2015) we can explain the intensification of a cyclone by latent-heat release by looking at these fields:

- Vertical velocity: condensational heating is responsible for an additional forcing term in the Omega equation. [2] Furthermore, the presence of saturation decreases

[2] The Omega equation is one of the main results of quasi-geostrophic theory. It can be obtained combining

static stability, tending to amplify the response to a given forcing in the same Omega equation. This enhanced upward motion in the warm sector in turn increases the vorticity, intensifying the cyclone.

- Energetics: condensational heating creates a source of eddy available potential energy and reinforces the energy transfer of from the mean-flow available potential energy to the eddy available potential energy and, in turn, to EKE.
- Potential vorticity: latent heating creates positive and negative PV anomalies in the lower and upper troposphere, respectively, in the region of maximum ascent, mainly on the warm side of the cyclone. The positive PV anomaly at low levels strengthens the surface cyclonic circulation, which is already increasing its intensity as a consequence of the baroclinic interaction.

Alternatively, as pointed out by Baker (2011), the effects of moisture can be visualised in terms of the maximum growth rate of the Eady model, whose values are expected to be larger and associated with a smaller wave number, due to the reduced static stability. Thus, cyclones developing with the presence of moisture are expected to show a more rapid development and a smaller length scale than their dry counterparts. The results from the idealised simulations in Coronel et al. (2015) confirm that moisture plays a primary role, through the intensification of the PV dipole in the troposphere. In particular, moist processes intensify the downstream ridge of the PV dipole and accelerate the cross-jet motion. This confirms the idea that moist processes are not of secondary importance in the cyclone development and they act by intensifying the dry dynamics, rather than through a new mechanism.

The study from Schemm and Wernli (2014) continues the investigation of baroclinic waves focusing in particular on the relationship between the evolution of PV and the dynamics of airstreams like the WCB and the CCB. Their main result consists in showing how the development of the PV dipole associated with ascent and latent heating on the warm side affects both these airstreams. A positive PV anomaly at low levels intensifies the cyclonic CCB while a negative PV anomaly near the tropopause drives the dynamics

the quasi-geostrophic vorticity and thermodynamic equations and it provides a method to diagnose the vertical motion from the known distribution of geopotential. It can be written as $N^2\nabla_h^2\omega + f_0^2\frac{\partial^2\omega}{\partial z^2} = S$ where the source term S is composed by terms involving differential vorticity advection, thermal advection, Coriolis effects, friction and heating (see Holton (2004) or equivalently Hoskins and James (2014)).

of the anticyclonic branch of the WCB outflow. The linkage shown between airstreams in different regions of the storm and diabatic effects of moist processes remarkably demonstrates the utility of PV as a tool for the analysis of cyclone evolution (Figure 2.7).

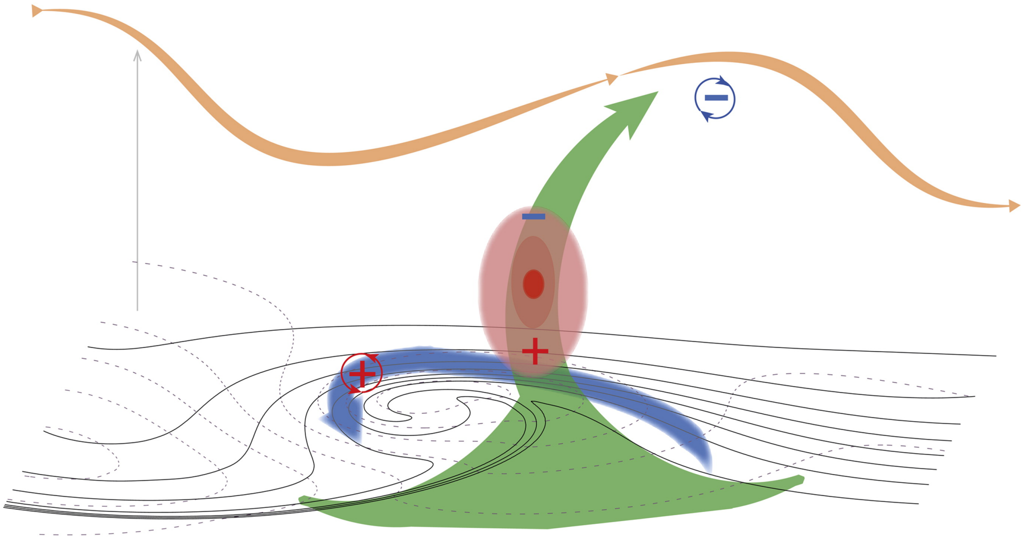

Figure 2.7: From Schemm and Wernli (2014) Fig. 9. Conceptual model of the interaction between the WCB (green arrow) and the CCB (blue arrow), the induced diabatic PV tendencies (plus and minus signs), and the resulting circulation anomalies at the end of the airstreams. A maximum region of diabatic heating (reddish colours) is formed at midtropospheric levels due to the ascending WCB. Also shown is the upper-level jet stream (orange line), where the WCB induces a stronger anticyclonic curvature of the flow and, because of the increase of the PV gradient, higher wind speeds. At lower levels, the CCB induces a stronger cyclonic curvature and enhances the wind speeds along the tail of the bent-back front.

Basic state for SJ-containing idealised cyclones

Having the aim to reproduce SJ dynamics in idealised baroclinic waves, in this research the study of Baker et al. (2014) is used as a starting point for model settings (see Chapter 3 for the methodology and Chapter 6 for the results of the simulations). The set up of that study has in turn taken advantage of the LC1 set up outlined in Polvani and Esler (2007), with the addition of moisture as in Boutle et al. (2011). A thorough examination of the initial state of our idealised simulation (along with a comparison with other methods and choices of initial balanced state) can be found in Chapter 3.

2.3 Focus on the generation of CSI and mesoscale instabilities

The release of conditional symmetric instability (CSI) has been indicated as a possible driving mechanism for SJ since the first conceptual model and then in the following literature. The actual contribution of the release of mesoscale instabilities to the descent and acceleration of the jet is one of the most vibrant areas of research in the field at the moment. It is thus necessary to explain what CSI and the other mesoscale instabilities mentioned are, introducing their definition, their properties and the related constraints and issues. The instabilities considered are summarised together with their conditions in Table 2.1 and organised in terms of temperature lapse rate in Table 2.2.

	Gravitational	Symmetric	Inertial
Dry	Absolute instability $\frac{d\theta}{dz} < 0$	Symmetric instability $\left.\frac{d\theta}{dz}\right\|_M < 0$ $PV < 0$	Inertial instability $\frac{dM}{dx} < 0$
Conditional	Conditional instability $\frac{d\theta_e^*}{dz} < 0$	Conditional symmetric instability $\left.\frac{d\theta_e^*}{dz}\right\|_M < 0$ $MPV^* < 0$	
Potential	Potential instability $\frac{d\theta_e}{dz} < 0$	Potential symmetric instability $\left.\frac{d\theta_e}{dz}\right\|_M < 0$ $MPV < 0$	

Table 2.1: Definitions of different types of instabilities. Adapted from Table 1 in Schultz and Schumacher (1999). Note that potential temperature (in its dry, equivalent and wet-bulb forms) should be regarded as hydrostatically balanced mean-state potential temperature. In the same way PV, MPV, $MPV*$ and M should be intended as geostrophically balanced quantities. However, many studies are conducted using environmental potential temperature and full winds (see Section 2.3.2).

Classification scheme for stability
A) Lapse rate exceeding dry adiabatic $\rightarrow$ dry absolute instability B) Lapse rate less than moist adiabatic $\rightarrow$ absolute stability C) Lapse rate between moist and dry adiabatic $\rightarrow$ conditional instability 1) Saturated: moist absolute instability 2) Unsaturated: stability unknown - No CAPE : stability to all vertical displacements - CAPE > 0 : instability to some finite displacements

Table 2.2: Classification scheme for instabilities based on environmental lapse rate. Adapted from Schultz et al. (2000).

The release of CSI has been previously mentioned in connection with the onset of slantwise convection. As convection in the troposphere occurs most commonly in an upright direction, this section starts with a brief review of those instabilities that are released via vertical motions. Later in the section, the focus moves to instabilities released in slantwise orientations, which are reviewed highlighting analogies to and differences with their upright counterparts. A similar elaboration of the topic can be found in the book of Markowski and Richardson (2010) and in the review paper from Clark and Gray (2018). Measures of energy available to be released by the instabilities, like CAPE and DSCAPE, are described thoroughly in Gray et al. (2011) and in Martínez-Alvarado et al. (2013), amongst others.

2.3.1 CI (conditional instability) and other instabilities released through upright convection

Static Instability

Static instability is a local gravitational instability released by infinitesimal vertical motion (ascent or descent). It can be diagnosed by looking at the vertical gradient of buoyancy $\partial b/\partial z$, with negative values indicating instability. In a moist and non-saturated atmosphere this condition can be re-written as $\partial\theta_v/\partial z < 0$ with θ_v virtual potential temperature ($\partial\theta/\partial z < 0$ if referring to dry air and dry absolute instability). Inside a cloud the buoyancy gradient can be replaced by the vertical gradient of equivalent or wet-bulb potential temperature (θ_e and θ_w, respectively) if neglecting the vertical gradient of total mixing ratio. In this case negative values indicate moist static instability. Static instability can also be assessed by looking for negative values of the square of the Brunt-Väisälä frequency N, dry or moist depending on the case ($N^2 = (g/\theta)(\partial\theta/\partial z)$ for dry air, see Durran and Klemp (1982) for its moist counterpart).

Conditional Instability

Conditional Instability (CI) is the finite-amplitude analogue of moist static instability as it is released by a finite vertical displacement of a parcel. If the parcel achieves saturation (which is in turn associated with the generation of additional buoyancy by the release of latent heat through condensation) in the process and that makes it statically unstable to further infinitesimal displacements, then it is considered conditionally unstable. In saturated air CI is equivalent to moist static instability and can be assessed by looking for negative values of $\partial\theta_e^*/\partial z$. If air is not saturated the parcel values of θ_e or θ_w (conserved for moist adiabatic flow) can be compared to the corresponding variable for the environment if it were saturated. It is important to remark that this does acquire meaning only if saturation is reached during the displacement. Measures related to finite parcel ascent like CAPE (see below) are more helpful in this latter case.

Potential Instability

Potential instability (PI), also referred to as "convective instability", is a finite amplitude instability as well, but instead of being associated with the lifting of an air parcel it concerns the displacement up to saturation of an atmospheric layer. The lower part of a layer typically contains more moisture than the upper one. Hence, PI occurs where on lifting a layer its lower part condenses sooner than the upper part such that the initially stable positive potential temperature gradient becomes negative. In this way θ_e and θ_w are conserved not only for the moving parcel, but also with their vertical gradients in the whole layer, with respect to hydrostatic pressure. A negative value of $\partial\theta_w/\partial z$ indicates that the layer is potentially unstable, i.e. moist statically unstable if lifted up to saturation.

Convective Available Potential Energy

Convective available potential energy (CAPE) is commonly used to measure the energy that can be obtained by the release of CI through parcel ascent. Following Emanuel (1994), CAPE can be defined as

$$CAPE = \int_{p_{LNB}}^{p_0} R_d(T_{v,parcel} - T_{v,env})d(ln\ p),$$

where p_{LNB} and p_0 are the pressures of the level of neutral buoyancy and origin level of a pseudo-adiabatic parcel ascent respectively, R_d is the gas constant for dry air and $T_{v,parcel}$ and $T_{v,env}$ are the virtual temperatures of the parcel and environment, respectively. (Updraught) CAPE represents thus the maximum kinetic energy that is available to an air parcel that ascends without mixing in a steady-state statically unstable environment, neglecting the gravitational effects of condensed water and assuming an instantaneous adjustment to the local environmental pressure. Latent heat release through condensation during the ascent of the parcel reduces its moist static stability, favouring the release of CAPE with the associated upward acceleration.

Downdraught CAPE (DCAPE) on the contrary refers to the maximum kinetic energy available to a descending air parcel. It is defined as

$$DCAPE = \int_{p_0}^{p_n} R_d(T_{v,env} - T_{v,parcel})d(ln\ p),$$

where p_n is the pressure of the level of neutral buoyancy (or of the surface if closer to the origin) and p_0 is the origin level of the pseudo-adiabatic descent of the parcel. In this case latent cooling from processes like evaporation or sublimation of precipitation in sub-saturated air or melting at the freezing level have an analogous role to the one of latent heating from condensation for updraught CAPE, providing a potential cooling that generates a downward acceleration.

2.3.2 CSI (conditional symmetric instability) and other instabilities released through slantwise convection

Measures of instability exist also for slantwise displacements and can be related to upright analogues. However, a fundamental difference in the nature of these instabilities resides in the properties of conservation of PV, that can be used to assess the onset of symmetric instability, as it is explained below.

Symmetric Instability

Symmetric instability (SI) occurs when a parcel is inertially and gravitationally stable, but it is unstable to slantwise displacements (Emanuel, 1994). SI is indicated by negative values of (geostrophic) PV. The concept of symmetric instability was first introduced during the study of frontal circulations and associated slantwise circulations. The condition for symmetric stability is identical to the condition of ellipticity of the Sawyer-Eliassen equation (see Sawyer (1956) and Eliassen (1962)).

SI can be visualised in terms of potential temperature and absolute geostrophic momentum (M_g) lines (see Markowski and Richardson (2010) for a thorough explanation of the concept and for an accurate definition of absolute momentum) with the condition for instability being: "θ-lines are steeper than M_g-lines" (Figure 2.8). This condition is usually met in highly baroclinic frontal zones, where the advection of different air masses can increase the slope of θ-lines (horizontal in barotropic atmosphere) and decrease the slope of M_g-lines (vertical in barotropic atmosphere).

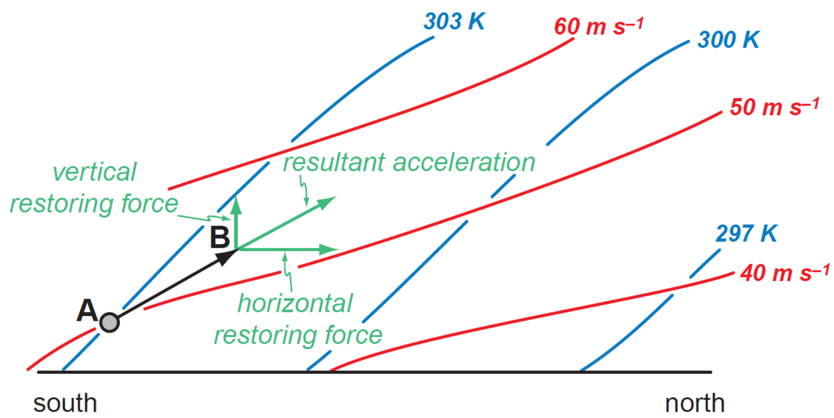

Figure 2.8: From Markowski and Richardson (2010) Fig. 3.9. Schematic meridional cross section of geostrophic momentum surfaces (red) and isentropic surfaces (blue) in a symmetrically unstable atmosphere. A tube of parcels is displaced from position A toward position B and experiences a resultant acceleration directed away from the initial equilibrium position.

SI can be regarded as a generalisation of inertial instability (II, an instability that leads to horizontal acceleration when geostrophic balance is perturbed) to baroclinic flow. While SI occurs when the Ertel potential vorticity (PV, defined in Section 2.1.2) is negative, II requires the vertical component of absolute vorticity ζ_z to be negative. For this reason, II can be regarded as a special case of SI in the limit of horizontal θ surfaces (Xui and Clark, 1985), with the instability associated with a folding of M_g-lines.

Given that the condition for SI is to have negative values of Ertel potential vorticity, and that PV is conserved in adiabatic flow, frictional effects and heat sources and sinks need to be involved in its generation (Hoskins, 1974). The generation of negative PV is often related to variations in static stability due to diabatic heating. However, negative

PV can be generated without being associated with negative static stability in case of a substantial contribution of negative vertical vorticity. In any case, as the field is likely to undertake further changes while adjusting to balanced flow, it is often helpful to take into account both the values of the vorticity component and of the static stability component alongside PV when inferring the stability of the flow.

An important property of SI (and of its moist counterparts that are presented below) resides in its link to PV. PV is conserved in a parcel in the absence of frictional and diabatic processes. Thus, an unstable point will retain its instability until these processes act to remove it. If this release is only provided by small-scale viscous dissipation, discrepancies will arise between reality and model simulations. In fact, numerical diffusion would remove the instability if it moves to scales that are too small to be represented by the model (Clark and Gray, 2018)

Conditional (and Potential) Symmetric Instability

Conditional instability is released by an upright lifting that makes the parcel saturated. Likewise, Conditional Symmetric Instability (CSI) requires slantwise lifting to saturation. In this case, the most appropriate local measure for the instability (occurring when values of these fields are negative) is saturated equivalent geostrophic PV ($EPV*_g = \rho^{-1}\zeta \cdot \nabla\theta_e^*$, also called saturated moist geostrophic PV, $MPV*_g$) (Bennetts and Hoskins, 1979).

θ_e^* is conserved in a parcel only when saturated. This makes the local measure of CSI via $MPV*_g$ relevant only in saturated air. θ_e is conserved for a parcel regardless of its saturation. Hence, EPV_g (or MPV_g), unsaturated analogues of $EPV*_g$ and $MPV*_g$, are measures of instability in a non-saturated environment. Schultz and Schumacher (1999) rightly point out that this latter case refers to PSI, potential symmetric instability (see definition of PI in previous section for comparison) rather than CSI. CSI and PSI are equivalent in saturated air. Saturation in a slantwise downdraught can be maintained through sublimation of ice, in addition to the evaporation of water, into the descending airstream (Clough and Franks, 1991).

A final remark concerns the fact that up to now we have mentioned geostrophic quantities, that should be used if sticking strictly to the definition of these instabilities. However, many authors prefer to use full winds instead of geostrophic ones for theoretical arguments (e.g. full winds are likely to be more representative than geostrophic winds in environments exhibiting curved flows) or considerations on numerical noise (see Gray et al. (2011)). Full winds are used in the research performed for this thesis too. In the same way, in this project and in many other studies environmental potential temperature is used instead of the hydrostatically balanced mean-state potential temperature that should be required if using the definitions of the instabilities just presented. Since the atmosphere is usually almost hydrostatic this approximation usually introduces only very small errors (Schultz and Schumacher, 1999).

Slantwise Convective Available Potential Energy

SCAPE (or DSCAPE if downdraught) measures the energy available from releasing CSI (Shutts, 1990b). SCAPE and DSCAPE can be computed in 2-dimensional (2D) or three-dimensional (3D) versions, depending on the flow considered. SCAPE is defined, for a 2-dimensional flow, as

$$SCAPE = \int_{p_0}^{p_{LNB}} \Gamma(s_p - s_e)\big|_M \, dz,$$

where Γ indicates the adiabatic lapse rate, LNB is the level of neutral buoyancy and s_p and s_e refer to the specific moist entropy of the parcel and of the environment, respectively (see Gray and Thorpe (2001) for the derivation of both 2D and 3D SCAPE). SCAPE has been used much less than its upright analogue CAPE, partly because of issues in interpreting the values obtained and in situations in which also CAPE is present or active slantwise convection is already occurring (Schultz and Schumacher, 1999). 2D SCAPE (DSCAPE) is calculated using a 2D thermally wind balanced and steady flow, measuring the maximum kinetic energy available to an ascending (descending) parcel in a CSI-unstable environment. The parcel moves along absolute momentum surfaces. 3D SCAPE (DSCAPE) applies to a fully 3D wind field and it is calculated on the surface of intersection of the two components of horizontal absolute momentum that passes through the initial location of the parcel (see Shutts (1990a) and Gray et al. (2011)). For the 3D version of SCAPE, the choice of path travelled by the parcel might be subject to discussion, a further issue for the calculation of SCAPE (DSCAPE). The calculation of CAPE and SCAPE (and downdraught counterparts) relies on the assumption that the time-scale of the parcel ascent is substantially shorter than the time-scale for the development of the system in which the diagnostics are computed. While this is a safe assumption for CI, it is less so for CSI. Thus the evolution of winds might have to be taken into account in the process of calculating SCAPE (see Gray et al. (2011) for more details).

2.4 Sting jets in extratropical cyclones

2.4.1 Introduction

The occurrence of an additional region of strong and damaging winds related to the development of a bent-back front has been observed since the 1960s. As Grønås (1995) pointed out, Norwegian forecasters used to refer to these winds as the "poisonous tail of the bent back occlusion". He adopted the same terminology to describe the occurrence of exceptionally strong surface winds at the tip of the bent-back front in a case study of a severe Shapiro-Keyser type cyclone. It is from this expression that Browning (2004) started to refer to the damaging winds in the frontal-fracture region as "the sting at the end of the tail", i.e. the **Sting Jet**.

However, the study of this additional region of low-level strong winds as a distinct phenomenon has only begun relatively recently. The first formal interpretation and conceptual model of the SJ was presented in two linked papers, Browning (2004) and Clark et al. (2005), that focus respectively on the observations and on a numerical weather prediction (NWP) model simulation of the Great Storm that battered UK in October 1987 (UK Met Office, 2012a). It is indeed with these two studies of the Great Storm that the SJ came to the attention of the scientific community. Massive damage and fatalities were caused by a storm, whose intensity had been underestimated by operational forecasts and whose dynamics was not clearly understood. This prompted research looking at the accuracy of the storm's forecasts (Morris and Gadd, 1988) and at its dynamical features, including the evolution of PV and the role of latent heat in its explosive intensification (see Hoskins and Berrisford (1988) and Shutts (1990b)). However, it was not until Browning (2004) that this short-lived and extremely damaging wind feature was identified as "a sting jet".

In his observational paper Browning (2004) showed that the most damaging winds occurred near the tip of the hooked cloud head. The cloud head displayed a banded structure consistent with the existence of multiple slantwise circulations with descending air moving significantly faster than the rate of travel of the cloud-head tip, implying rapid evaporation and diabatic cooling. The study thus indicated a well-established association between the evaporating tip of the cloud head and the most damaging winds. The question of the dynamical cause of the observed slantwise circulations is not addressed in the paper, but the likely connection with evaporation and sublimation is stressed. Browning (2004) remarked that, while latent-heat release via condensation is certainly of primary importance in the deepening of the storm (see also Shutts (1990b)) and so in the generation of strong winds, there might also be a role for evaporative heat sinks in the cloud-head tip evolution. He thus hypothesized that mesoscale circulations and associated evaporative cooling might have played an active role in a further strengthening of the damaging winds.

The same hypothesis is suggested also in Clark et al. (2005), whose purpose was to establish the existence and the 3D structure of the SJ through the use of an observationally validated forecast run from a high-resolution NWP model (the UK Met Office Unified Model, MetUM hereafter). Clark et al. (2005) stress the importance of resolution in the mesoscale model used. The horizontal spacing is around 12 km, as usual for MetUM mesoscale settings at the time. The vertical resolution had instead been enhanced with the use of 90 vertical levels. A comparison of the simulation ran with this setup with a 38-vertical-levels one showed a significantly deeper cyclone in the higher resolution simulation, closer to observations. That setup had also been chosen to be consistent with the recommendations of Persson and Warner (1993) to resolve slantwise circulations (i.e a ratio of 1:50 between horizontal and vertical spacing is needed). Another important annotation from Clark et al. (2005) concerns the use of Lagrangian trajectories as a method to isolate the SJ airstream and inspect its dynamics by looking at the evolution of physical quantities on the jet, in a Lagrangian framework. Many of the subsequent contributions to the field took advantage of the use of this technique.

The paper showed that the damaging surface winds in the Great Storm were associated with a well-defined mesoscale SJ. They identified the SJ as a distinct mesoscale entity, a coherent airstream originating at mid-levels in the cloud head and descending out of its tip while accelerating. In their simulations the SJ evolves in the frontal-fracture region behind the primary cold front (Figure 2.9). It is separated from the cold conveyor belt (CCB) which remains below and behind it, turning cyclonically within the cloud head, and from the warm conveyor belt (WCB) that stays on the warm side of the cold front. The SJ is also distinct from the main dry intrusion, associated with even drier air flowing above the cloud head in a descent related to the folding of the tropopause (Figure 2.10). Multiple slantwise circulations occur at the cloud-head tip, suspected to be a manifestation of the release of CSI. The SJ descent originates in the descending branch of one of these circulations and flows in a zone where sloped isentropes signal the occurrence of broad descent. The importance of evaporation is highlighted by the behaviour of dry and wet-bulb potential temperature along the SJ trajectories. The former decreases by around 5 K during the SJ descent while the latter remains constant, indicating evaporative cooling, consistent with the decrease in relative humidity and the slight increase in specific humidity. As a result, the air within the SJ accelerates up to an earth-relative wind speed of 50 m s^{-1} in a few hours while descending towards the low levels, reaching the top of the boundary layer.

To summarise, the conceptual model presented in these two papers includes the following components:

- A large part of the strength of low-level winds in the area between the cloud head and the primary cold front can be explained in terms of the synoptic-scale balanced dynamics.
- The actual descending jet, focused and narrow, (the SJ) is embedded in this favourable environment, but its strength could also be enhanced by evaporative effects and/or by the release of CSI (slantwise circulations might be evidence of this).

Following Baker et al. (2014), we can summarise the characteristics of the SJ as it has been depicted in this pioneering conceptual model with five points. A SJ in an extratropical cyclone is defined as a stream of air that has the following characteristics:

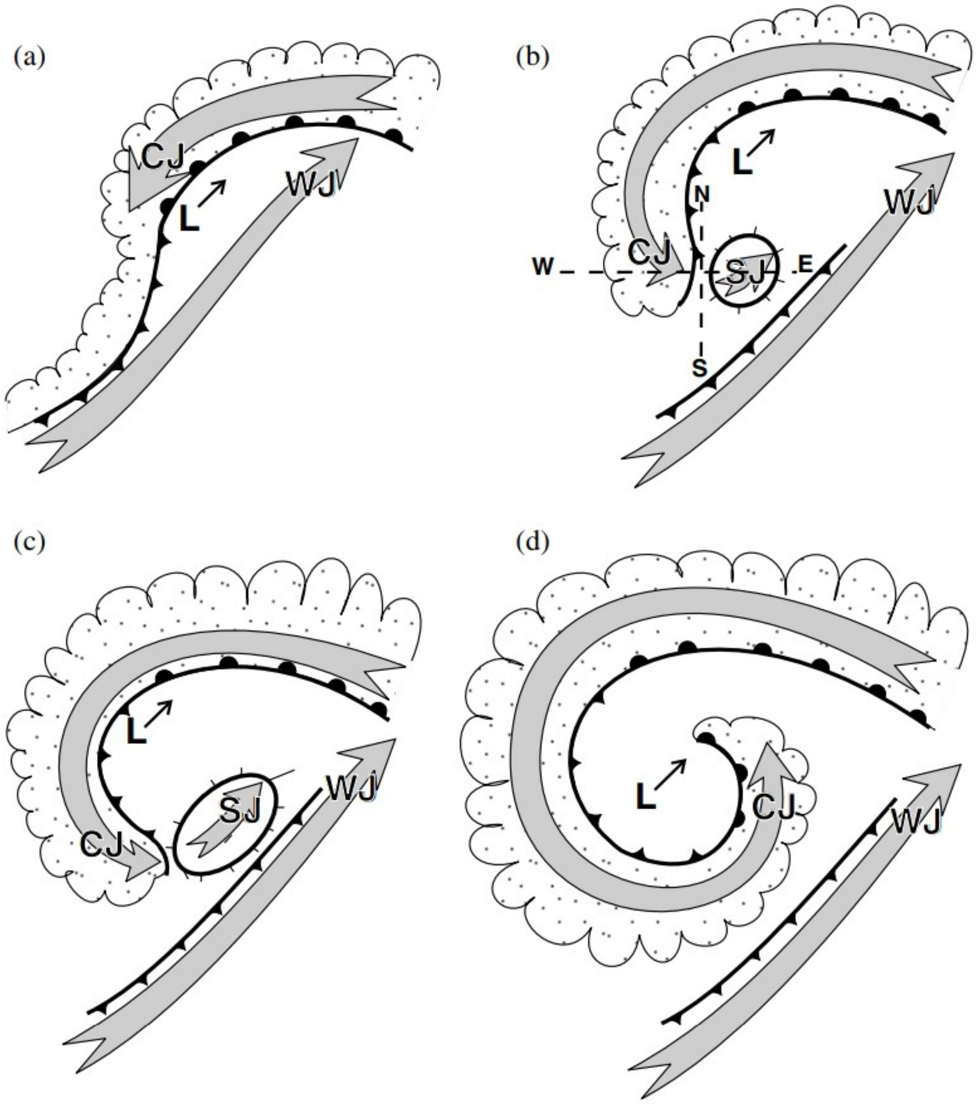

Figure 2.9: From Clark et al. (2005) Fig. 17. Conceptual model of low-level flows in an intense Shapiro-Keyser extratropical cyclone. The SJ descends towards low levels while exiting from the cloud head and accelerating into the widening frontal fracture, between stages II and III of the Shapiro-Keyser conceptual model. In the last stage of evolution the SJ disappears as the bent-back front fully wraps around the cyclone centre generating a warm seclusion in stage VI. Note that WJ and CJ refer respectively to WCB and CCB in the text.

- Originates at mid-levels (600-800 hPa) within the cloud head;
- Descends along a sloping surface of constant θ_w;
- Accelerates and reduces in relative humidity during the descent;
- Results in strong winds near the top of the boundary layer;
- Is distinct from the low-level jets associated with the warm and cold conveyor belts.

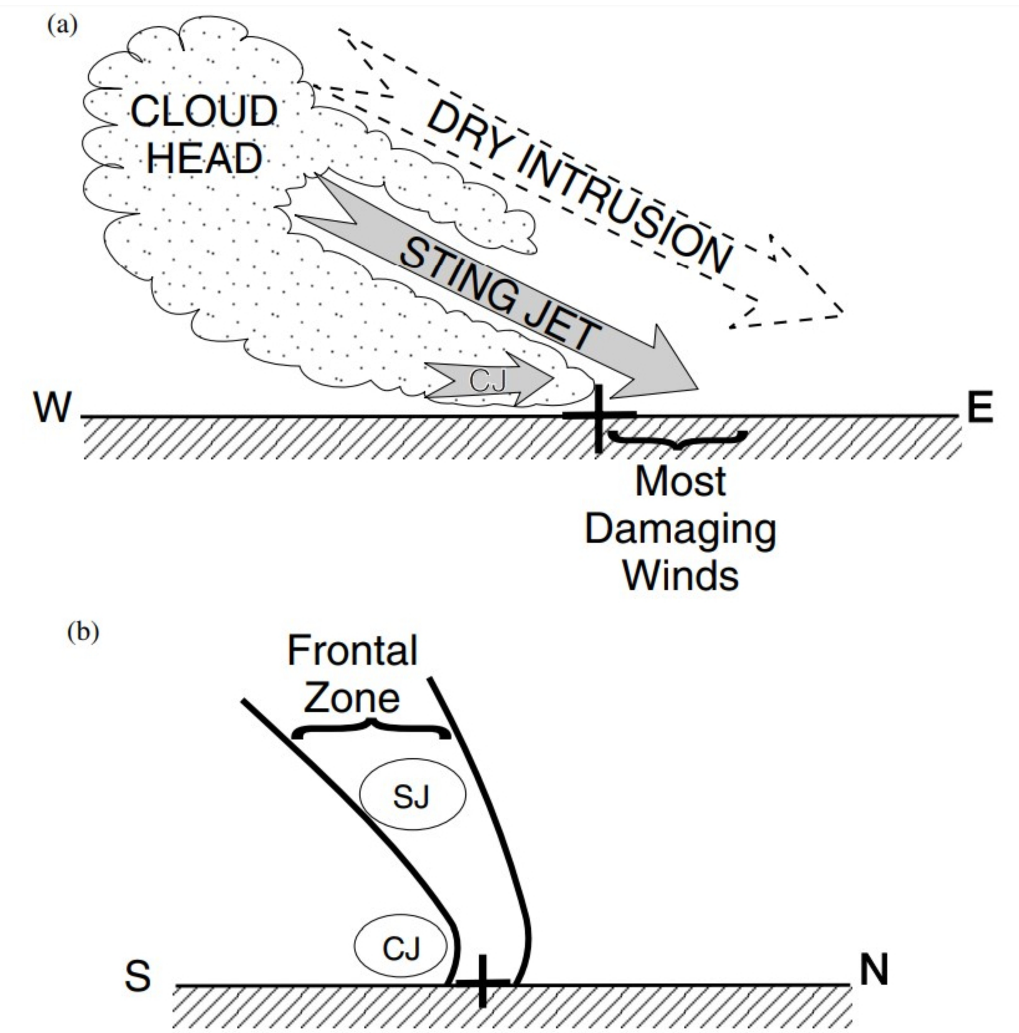

Figure 2.10: From Clark et al. (2005) Fig. 18. Conceptual model of cross sections through an intense Shapiro-Keyser extratropical cyclone (see transects in Figure 2.9). The east-west section (a) shows the SJ descending above the CCB and beneath the DI, a separate airstream lying in the frontal-fracture region, as shown by the south-north section (b).

The conceptual model presented in these two initial studies clearly needed to be confirmed and complemented. In recent years a considerable body of literature followed up on this, looking at all the various aspects of SJ-research. The main results are mentioned in the next paragraphs, to illustrate the state-of-the-art situation and help to identify the key open research questions.

2.4.2 Case-study modelling analyses of sting-jet storms

As explained in Section 2.4.1, the research on SJs started to develop from the analysis of a real case. Other case studies have been performed in the last decade highlighting further characteristics of the airstream and generating new questions. The main results from those studies are listed in the following:

Baker (2009) ran simulations of windstorm Gudrun (mentioned also in Baker et al. (2014) for comparison with idealised simulations of SJ storms), which had an explosive development and brought strong winds over the UK on 7-8 January 2005. Using a model with similar resolution to Clark et al. (2005), the study was able to identify the SJ as a separate airstream, and the use of Lagrangian trajectories confirmed that its descent out of the cloud head was accompanied by a decrease in relative humidity. The study pointed out that the SJ is not always responsible for the strongest winds in a storm, with the CCB being more intense in this particular case. Also, the storm evolved only initially as a classic Shapiro-Keyser type cyclone and then showed a double warm front (with associated double CCB). This indicated a certain robustness of the occurrence of SJ, which is not only restricted to cyclones that strictly follow the conceptual model of development.

Martínez-Alvarado et al. (2010) used two different limited-area mesoscale models, MetUM and COSMO, to simulate the explosive cyclone that produced strong winds over the UK on 26 February 2002. The main aim of the study was to investigate the influence of model differences on the representation of sting jets. An additional target of the study was to provide further investigation, through a case study, of the possible mechanisms leading to the development of a SJ, testing the conceptual model presented in Clark et al. (2005). As occurred in the studies just reviewed, the enhancement of vertical resolution to meet the requirements explained in Clark et al. (2005) produced stronger winds and an overall better representation of the storm. The work includes an analysis of SJ trajectories, selected as dry air parcels descending from a cloudy region and characterised by values of θ_w representative of the frontal-fracture region, sitting in between higher values typical of the WCB or lower values associated with the CCB. It is of primary importance to stress that this method of identification considers only airstreams that have thermodynamic characteristics incompatible with CCB and WCB, based on the assumption that the SJ is an additional distinct airstream. A SJ satisfying these criteria was found in both models. The three common characteristics listed here emerged as robust features of the SJ in the case study.

- The trajectories indicate a short-lived feature (whereas CCB and WCB are present throughout most of the storm's evolution) exiting from the cloud head and descending into the frontal fracture, whose shape is similar in both models;

- Evaporative cooling occurs during the descent of the airstream;
- Favourable conditions for the release of CSI are present in the area of initial descent of the SJ.

Although some differences between the two models are present, the study was able to support the conceptual model of SJ evolution, showing also that the SJ does not necessarily reach the surface or even the top of the boundary layer.

The work from Gray et al. (2011) represented an attempt to go deeper in the understanding of the mechanisms generating SJ. In the introduction of the paper they stressed that Browning (2004) had proposed two possible dynamical causes for the SJ:

- Evaporation associated with slantwise convection might be increasing the strength of low-level winds. This hypothesis relates to the observation of fast-moving cloud often emerging from the cloud-head tip and evaporating and to the evidence of the primary role played by latent-heat release in explosively developing storms.
- Slantwise circulations could be the consequence of CSI release, as suggested by the presence of multiple bands of cloud and precipitation in the cloud head. The SJ thus forms the descending branch of a slantwise circulation exiting the cloud head.

The target of the study was, starting from these two hypotheses, to look at the evolution of CSI in space and time with the use of a suitable diagnostic. An additional goal was to consider whether the occurrence of SJ could be inferred via diagnostics. Their method to diagnose a SJ consisted of the use of Lagrangian trajectories on which the values of relevant quantities to detect the presence of instability were interpolated (Figure 2.11). Also energetic quantities namely CAPE and (D)SCAPE were analysed. As explained in detail Section 2.3, convective available potential energy (CAPE) is a commonly used measure of the energy that can be obtained by the release of CI by upright convection. In the same way SCAPE and DSCAPE (updraught and downdraught slantwise CAPE, respectively) can be considered diagnostics measuring the energy available from the release of

CSI via slantwise convection. Another measure used to diagnose CSI is moist saturated potential vorticity ($MPV*$), whose negative values indicate the presence of the instability. For more details on these diagnostics see Section 2.3. Gray et al. (2011) tested their diagnostics on four storms. A SJ had been identified in three of them (including the 1987 Great Storm and windstorm Gudrun) whereas the fourth storm did not have a SJ despite showing many of the apparent SJ-storms features. The results of the study showed SJ storms having much greater and more extensive CSI (and CI) than the non-SJ storm. As a consequence, they claimed that CSI release plays a role in generating the SJ and that the release of instability to both ascending or descending parcels in slantwise circulations at the cloud-head tip might be driving the SJ. They also indicated that DSCAPE could be used as a discriminating diagnostic for SJ, based on the results of their four case studies. However, Gray et al. (2011) noted that their results do not exclude the possibility that evaporative cooling of the descending air could have a role in the evolution of SJ. An open question remained on whether the SJ is the descending branch of a slantwise circulation induced by the release of near-surface CSI through the ascent of air or whether it is the slantwise flow induced by the release of mid-tropospheric CSI through descending air.

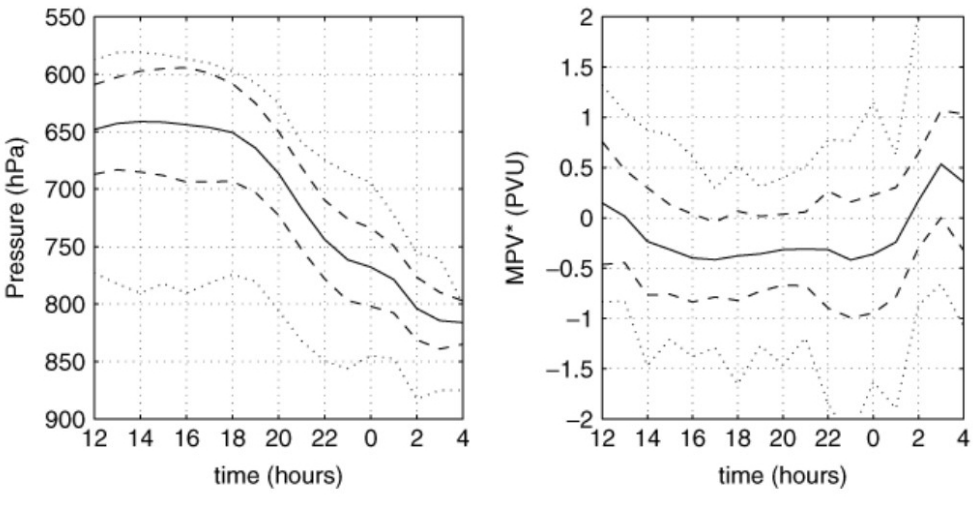

Figure 2.11: From Gray et al. (2011) Fig. 12. Timeseries of pressure and moist saturated potential vorticity along sting-jet trajectories in windstorm Gudrun during its descent. The solid line indicates the ensemble mean of trajectories while dashed and dotted values indicate respectively standard deviation and instantaneous extreme values. This figure represents a classic example of the analysis of the evolution of relevant quantities on the airstream.

Up to this point, all the studies described confirmed the model outlined by Browning

(2004) and Clark et al. (2005) and their hypotheses of evaporative cooling and CSI release playing a role in SJ generation and strengthening. Schultz and Sienkiewicz (2013) instead questioned the necessity of these two factors arguing that the dynamics driving the evolution of the frontal structure is sufficient to explain the occurrence of strong winds in the region. They simulated the intense storm that moved across the UK on 7-8 November 2005 using the WRF model with a grid spacing of 12 km (vertical resolution is not specified in the paper). The analysis is focused on the behaviour of frontogenesis, that is the Lagrangian time rate of change of the magnitude of the horizontal gradient of potential temperature (see Petterssen (1936) and Keyser et al. (2000)), in the cloud head and in the frontal-fracture region. Their results showed that the transition from frontogenesis to frontolysis (i.e. negative frontogenesis) in the frontal fracture is crucial to the formation of a possible SJ and to its descent out of the cloud head (Figure 2.12). In particular, in their simulations a couplet of frontogenesis and frontolysis is present along the bent-back front. Frontogenesis is associated with the ascent within the cyclonic branch of the WCB, contributing to the development of the cloud head. Frontolysis is instead related to the descent occurring within and on the warm side of the front that brought higher-momentum air towards the lower troposphere. They stressed that the frontolytic region was located at the end of the bent-back front, where the isentropes spread, i.e. in the frontal-fracture region. The main result contained in Schultz and Sienkiewicz (2013) concerned the claim that downward momentum transfer associated with frontolysis occurs in the frontal-fracture region producing, combined with the low static stability, the descent of the SJ. The transition between ascent and descent of the SJ observed in previous studies is consistent with the pattern of frontogenesis and also with the descent-caused evaporation at the tip of the cloud head. They argued that, although evaporation might act to make the air negatively buoyant, it is not necessary to the generation and strengthening of the SJ. Similarly, the presence of CSI might enhance the frontal circulation, producing stronger descent and greater acceleration, but it is not required for the occurrence of the SJ: that can happen even in a symmetrically-stable environment.

The following studies had to take into account the work from Schultz and Sienkiewicz (2013) that contrasted the initial view (and the successive articles) that CSI and evaporative cooling play a main role in the generation and strengthening of the SJ. Smart and Browning (2014) took this into account in their study, in which a WRF model with 5 km

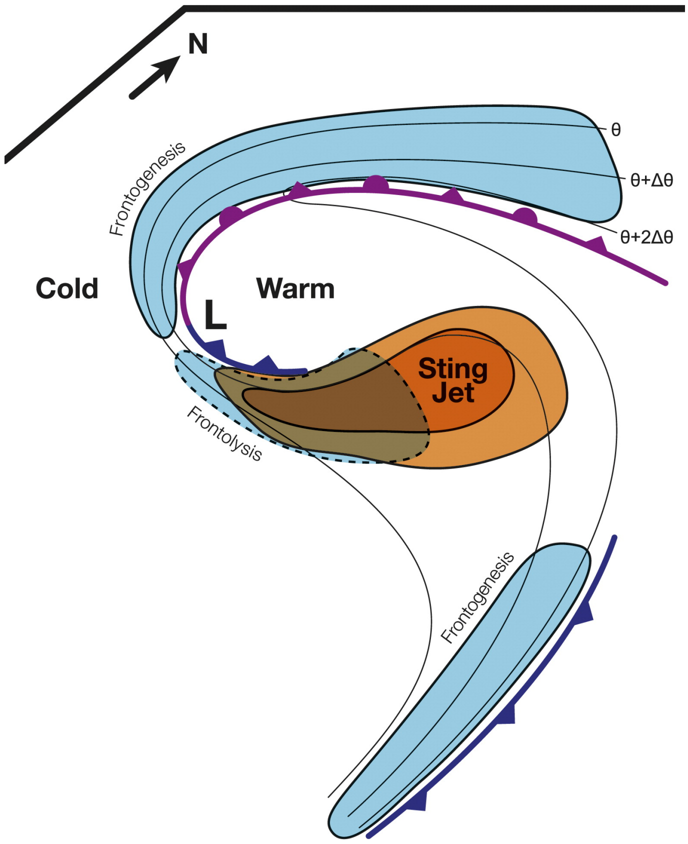

Figure 2.12: From Schultz and Sienkiewicz (2013) Fig. 6. Conceptual model for the location of a Sting Jet in a Shapiro-Keyser cyclone, highlighting lower-tropospheric fronts, isentropes and regions of frontogenesis and frontolysis.

horizontal grid spacing and vertical resolution similar to Clark et al. (2005) was used to simulate storm Ulli (affecting Northern Ireland and Scotland on 3 January 2012). They used Lagrangian trajectories to isolate SJ and CCB airstreams and to show their own evolutions, highlighting the expected differences in location, potential temperature and vertical motion between the two airstreams. Smart and Browning (2014) showed some interesting results that are summarised here:

- Although quite short-lived, the SJ is present and descends into the frontal-fracture region as expected, showing a remarkable acceleration;
- The SJ is not the strongest airstream in the storm, with the CCB reaching larger wind speeds;
- There are no signs of CSI or evaporative cooling affecting the SJ.

On one hand, the lack of instability and cooling might be connected to the reduced relative strength of the SJ in the case study. On the other hand, the hypothesis raised by Schultz and Sienkiewicz (2013) that the transfer of momentum from aloft in the frontolytic region in which the SJ descends is sufficient to explain its dynamics is consistent with these results. In fact, open questions on SJ dynamics remain, as Smart and Browning (2014) observe that *"the wind speed of the SJ air just before it commenced its descent was quite low. The outstanding issue that still has to be resolved is what causes the SJ air to accelerate so strongly as it descends"*.

At the same time, the study from Martínez-Alvarado et al. (2014a) showed a model simulation of a storm with a SJ spending relatively long time in regions characterised by the presence of CSI and a CCB moving through largely stable regions. The aim of the article was to present airborne observations and model simulations of the strong winds located on the equatorward side of storm Friedhelm, included in the DIAMET (DIAbatic influence on Mesoscale structures in ExTratropical storms) field campaign (Vaughan et al., 2015), and to relate them to the different airstreams. More details on the observational side of the study can be found in Section 2.4.4. The simulations had been performed with the standard MetUM settings at the time for the North Atlantic-European domain, i.e. 12 km of horizontal grid spacing and 70 vertical levels (lid at 80 km). The use of back-trajectories allowed them to identify three distinct airstreams composing the strong-wind region (Figure 2.13). Two of the airstreams were identified as part of the CCB as they turn around the cyclone centre, ahead of the warm front and on the cold side of the bent-back front. They show little ascent from the boundary layer. The third airstream instead shows westerly motion and rapid acceleration associated with descent from the cloud head. It was thus identified as the SJ. The main results in Martínez-Alvarado et al. (2014a) can be summarised as follows:

- The airstreams identified as part of the CCB were found to be in mainly stable regions during their evolution. On the contrary, the SJ airstream passes through (for more than half of the trajectories composing it) regions with negative $MPV*$, hence satisfying conditions for CSI;
- SJ and CCB are composed by different air masses and follow different trajectories. However, they can end up at the same horizontal location. The SJ is expected to remain above the CCB, but its influence on damaging wind at the surface (mainly

following the same path of the CCB) cannot be ruled out.

The Martínez-Alvarado et al. (2014a) study is thus another piece of research supporting the idea that CSI has a role in enhancing the wind strength in the SJ.

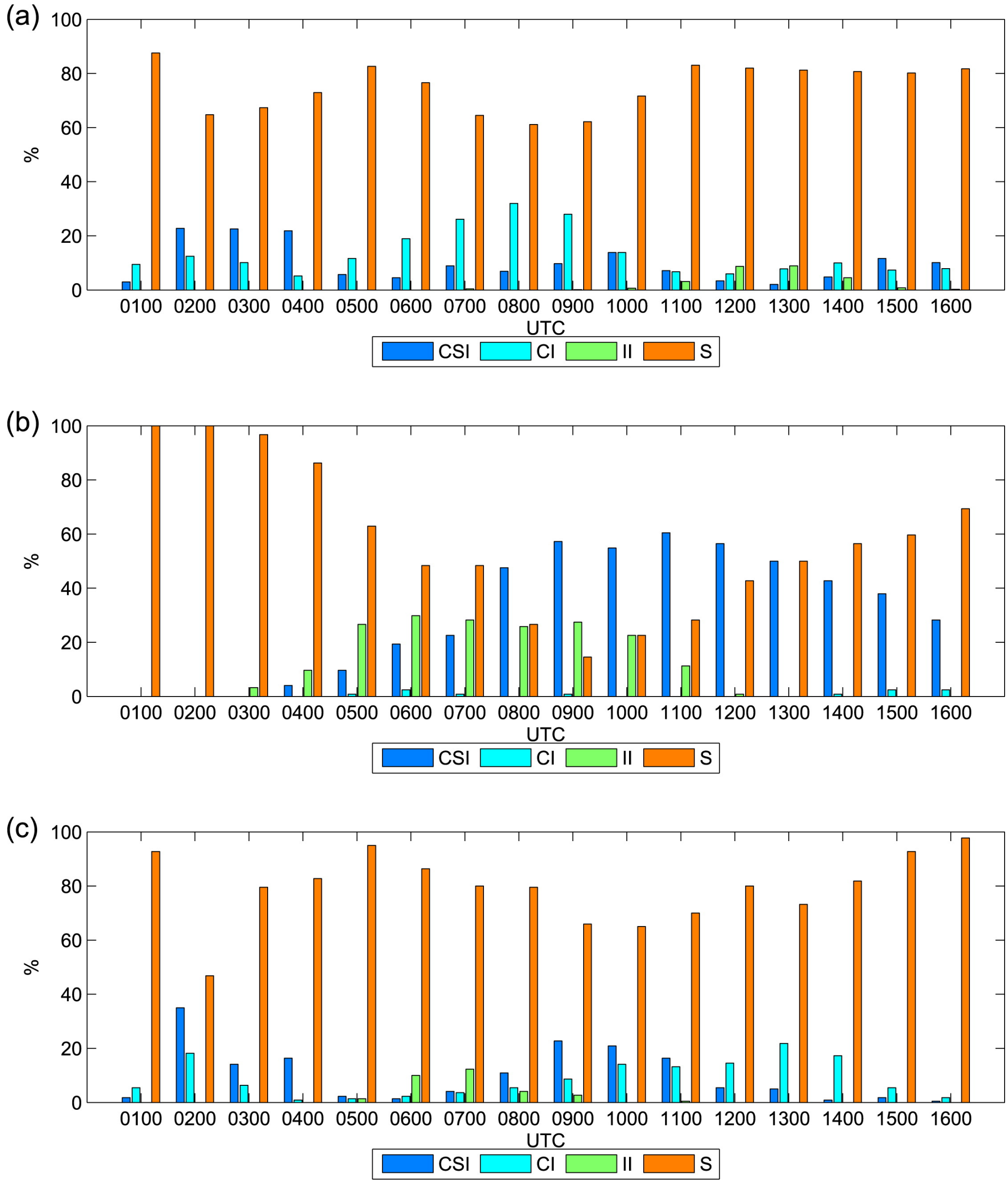

Figure 2.13: From Martínez-Alvarado et al. (2014a) Fig. 11. Diagnosis of the environmental conditions for instability along trajectories for the airstreams identified as belonging to the CCB ((a) and (c)) and to the SJ (b). The histograms show the percentage of trajectories in each airstream satisfying each instability criterion at hourly intervals. Trajectories that do not satisfy any of the instability criteria are classified as stable, S. Categories are mutually exclusive so that the bars sum to 100% in each hour.

The last paper presented in this section uses a model simulation of windstorm Tini, the same storm analysed as a case study in this project (see Chapters 4 and 5). Before presenting the results contained in Slater et al. (2017) it is necessary to notice that the model resolution used in this study does not comply with the recommendations from previous literature. In fact, Slater et al. (2017) performed simulations with the WRF model in a setting having horizontal grid spacing around 20 km and 39 vertical levels, 8 of which are below 850 hPa. This configuration is not in agreement with what had been prescribed by Clark et al. (2005) and followed by subsequent literature. Slater et al. (2017) claimed to have identified a SJ whose acceleration is the effect of the increasing along-flow pressure gradient force (they used selected back-trajectories and looked at the different terms of the equation of motion on them). In an attempt to separate the local processes from the large-scale dynamics they looked at quasi-geostrophic quantities finding that the descent of the jet is associated with a maximum in quasi-geostrophic ω, in turn linked to frontolysis at the tip of the bent-back front. They thus argued that the near-surface wind maximum associated with the SJ is created by the balanced dynamics of the cyclone, whereas smaller-scale moist processes are negligible. Although this claim is consistent with the results shown, the relatively-poor resolution of the model cast some doubt on their argument as the localised processes that they judged as negligible might not have been represented by their simulations (more details in Chapter 5).

2.4.3 Idealised modelling analyses of sting-jet storms

Alongside the case studies presented, a few idealised analyses have been performed recently. Idealised simulations of SJ cyclones are just a small subset of the research on idealised baroclinic waves, as can be expected. In this section the focus is only on those studies that explicitly look at the occurrence of SJs in idealised extratropical cyclones. A general introduction to idealised moist baroclinic waves and to some of the related research can be found in Section 2.2.

The work from Baker et al. (2014), already discussed in relation to windstorm Gudrun, represents the starting point of the idealised analyses performed in this project (see Chapter 6 for more details). Their simulations consist of moist baroclinic waves developing in a periodic channel configuration with spherical geometry and a set-up based on the LC1 simulations of Thorncroft et al. (1993) with the addition of moisture and a modified boundary layer, to obtain cyclones similar to the observed SJ-storms. The resolution of the model is similar to that used in the various case studies described in Section 2.4.2 (0.11° horizontal grid spacing and 76 vertical model levels). The results of the paper describe the control simulation and some sensitivity experiments in which the vertical potential temperature gradient or the upper-level jet strength given as initial conditions are changed. All the runs show some pieces of evidence that the release of CSI plays a role in the evolution of the SJ (Figure 2.14). In particular, a region of CSI is present in the cloud head, dissipating as the SJ leaves to descend into the frontal-fracture region. SJ trajectories show negative or near-zero $MPV*$ while being stable to CI and II (inertial stability), consistent with CSI release. Non-negligible evidence of the release of these other instabilities is indicated only in the run with weakest initial static stability. A simulation was run turning off the evaporative cooling from the beginning of the SJ descent. This had no significant effect on the strength or descent rate of the SJ, implying that evaporation does not play a primary role in SJ evolution in the case. However, a consequence of the missing evaporation is a decrease in the stability of the air through which the descent of the SJ takes place. Hence, Baker et al. (2014) argued that this effect on the environment counteracts any reduction in descent rate due to the lack of evaporative cooling. Another main result from the study is the robustness of the existence of a SJ in moist simulations. In all the runs with moisture a SJ does occur around Stage III of the Shapiro-Keyser conceptual model. A dry simulation instead produces a cyclone with a similar evolution, but without a SJ. To summarise their results, Baker et al. (2014) claimed that instability release is a dominant SJ-driving mechanism and that, whilst caution is needed in generalising idealised results to typical SJ storms, there is potential for the release of CI and II as additional mechanisms acting on SJ evolution.

The study from Slater et al. (2015) instead uses dry idealised simulations. The periodic baroclinic channel f-plane used for their idealised simulations neglects spherical geometry and moisture. A setting with 20 km of horizontal grid spacing and 40 vertical levels was chosen after tests with better resolution did not show significant differences. As in Slater et al. (2017), the decomposition of the equation of motion on the identified airstreams was used as a method to investigate the dynamics. A wind maximum at low-levels develops on the southwestern side of the low and Lagrangian analysis shows that the wind maximum was associated with three different airstreams. One is part of the CCB while a second airstream enters the wind maximum descending from above

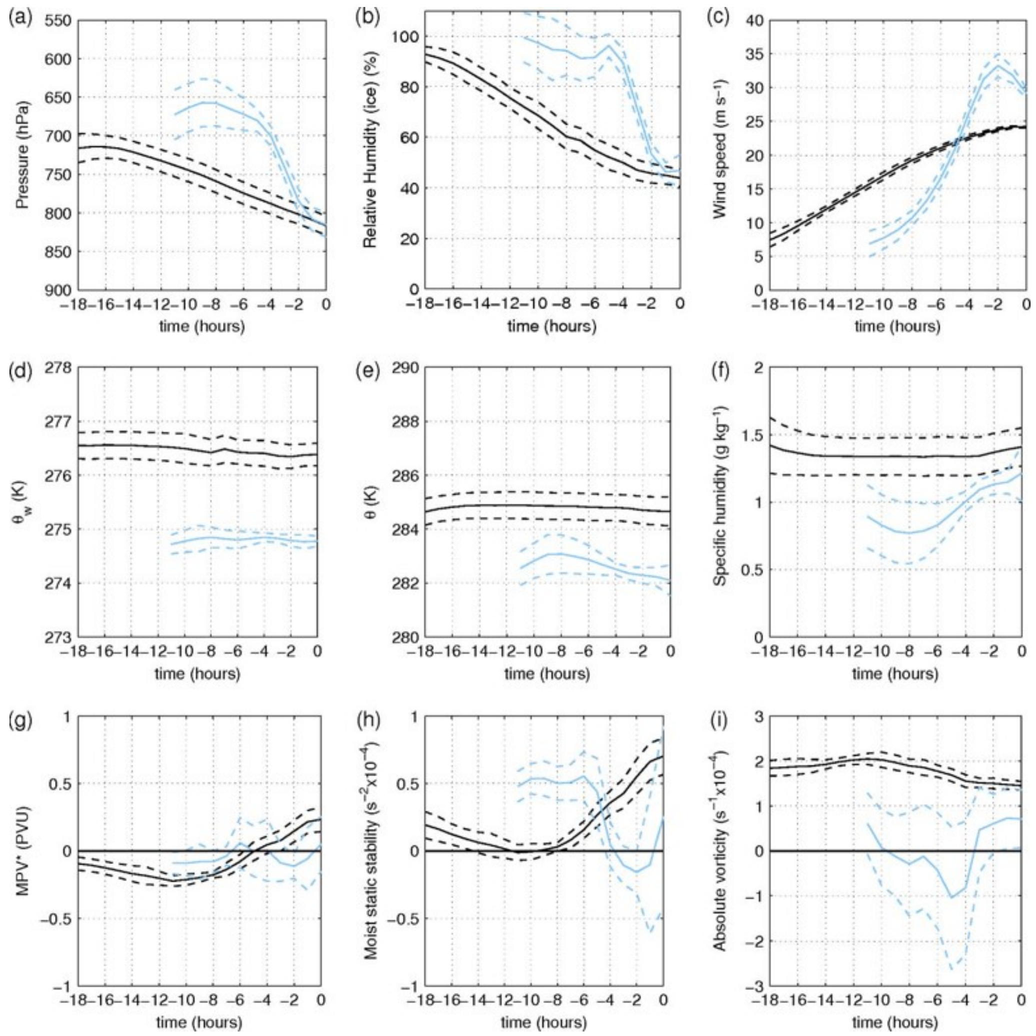

Figure 2.14: From Baker et al. (2014) Fig. 12. Time series of different variables along SJ trajectories in runs with larger (black) and smaller (light blue) initial static stability. The times shown are relative to the time of sting jet wind maximum. Lines show the mean (solid) and standard deviation (dashed) of the trajectory ensemble. Negative values in the bottom panels indicate respectively CSI (g), CI (h) and II (i). See reference for further details.

and bringing high-momentum mid-tropospheric air towards the surface (reminiscent of a DI). Between these two airstreams some transitional trajectories were identified as "SJ-resembling" as they accelerated whilst descending to the top of the boundary layer as a result of a positive pressure gradient force along the flow in absence of friction. Following on these results they controversially claimed that the presence of these transitional trajectories suggested that SJ-like airstreams can form without the release of CSI or evaporative cooling and even in dry simulations.

The work from Coronel et al. (2016) contains idealised SJ cyclones with different model resolutions. They found the best result in terms of correct representation of the storm (i.e. well-formed slantwise circulations near the cloud head and a distinction between the CCB and SJ) in simulations with grid spacing of 4 km in the horizontal and 200 m in the vertical. Decreasing the vertical spacing to 80 m (consistent with the 1:50 aspect ratio prescribed in Persson and Warner (1993)) led to similar results but with increased noise. As a first result, Coronel et al. (2016) stressed that a SJ cyclone forms when the initial disturbance is on the warm side of the jet. They used backward Lagrangian trajectories to analyse SJ dynamics finding that a minority group of trajectories entering the SJ region undergo diabatic cooling due to the sublimation of snow and graupel whereas the majority of the trajectories do not show this diabatic cooling, descending from the cloud-head in an environment close to neutral with respect to CSI. $MPV*$ is near zero in the main slantwise descent apart from localised regions with negative values (i.e. with possible CSI release). Simulations with lower horizontal resolution fail to show any negative $MPV*$ while producing similar slantwise circulations and comparable SJ strengths. The study looks also at quasi-geostrophic quantities finding a strongly divergent Q vector [3] in the region of SJ descent, particularly in the high resolution runs in which the vertical motion is more intense. They argued that this suggests a SJ descent that is not driven by instability but rather quasi-geostrophically forced. Furthermore, they claimed that the overall cyclone evolution forces the initiation of the descents, not slowed down by any restoring force since the conditions for CSI are near-neutral.

2.4.4 Observational analyses of sting-jet storms

As discussed in Section 2.4.1, the two pioneering papers in the study of SJ in extratropical cyclones are focused on the analysis of the Great Storm of 1987, looking respectively at observations (Browning, 2004) and model simulations (Clark et al., 2005). Browning (2004) highlighted that the most damaging winds in the storm occur at the end of the bent-back front, close to the banded tip of the cloud head. The study makes a case for evaporation and CSI-release being two possible factors in driving the evolution of the SJ, based on the evidence of the presence of descending air exiting fast from the cloud

[3] The Q-vector form of the Omega equation (quasi-geostrophic equation diagnosing vertical motion, see Section 2.2.2) is given by $N^2\nabla_h^2\omega + f_0^2\frac{\partial^2\omega}{\partial z^2} = 2\nabla_h \cdot \mathbf{Q}$. The source term in this version of the equation is proportional to the divergence of the Q-vector, $\mathbf{Q} = -|\nabla_h b|\mathbf{k} \times \frac{\partial \mathbf{v_g}}{\partial \mathbf{s}}$, where b is buoyancy and s indicates a b-contour. Hence, a convergent (divergent) Q is associated with quasi-geostrophic ascent (descent) (See Holton (2004) or Hoskins and James (2014)).

head and entering into the dry slot. The observation of banding at the tip of the cloud head was key in developing the first conceptual model of SJ dynamics, in which it was speculated that the bands are associated with a structure of multiple slantwise convective circulations that can be attributed to the release of conditional symmetric instability (CSI) and strengthened by diabatic effects.

In a related paper, Browning and Field (2004) put together all the evidence of SJ descent coming from satellite imagery available for the Great Storm. In addition to the banding at the tip of the cloud head they mentioned shallow cloud features present within the dry slot, regarded as a consequence of the interaction between the descending SJ and the boundary layer air. As the descending jet gets to the top of the boundary layer the formation of convergence lines is detected, with convection also associated with the downward transport of momentum from the SJ towards the surface (see Figure 2.15 and Figure 2.16).

Other observational studies followed using output from various instruments.

Parton et al. (2009) presented observations from radar wind profilers of strong winds in windstorm Jeanette (27 October 2002), which occurred in the mid- and low-troposphere after the passage of the cold front. The radars could observe for the first time mid-tropospheric winds up to 50 m s^{-1} at the tip of the cloud head associated with pronounced vertical and horizontal banding, with wind structures parallel to moist-isentropic surfaces and with horizontal and vertical scales of the observed structures compatible with the release of CSI within the cloud head. The SJ was detected to be merging with the CCB in the mature stage of the storm, thus showing a remarkably long life-span throughout the storm evolution. A MetUM simulation (similar configuration to analogous studies described in Section 2.4.2) managed to reproduce the banding structure and the strong winds. However, the model run shows poor results in depicting the convective downward momentum transfer from the SJ into the boundary and surface layer.

Airborne observations from dropsondes also became recently available thanks to two research flights through cyclone Friedhelm (8 December 2011) performed during the DIAMET field campaign (Vaughan et al., 2015). These observations are analysed

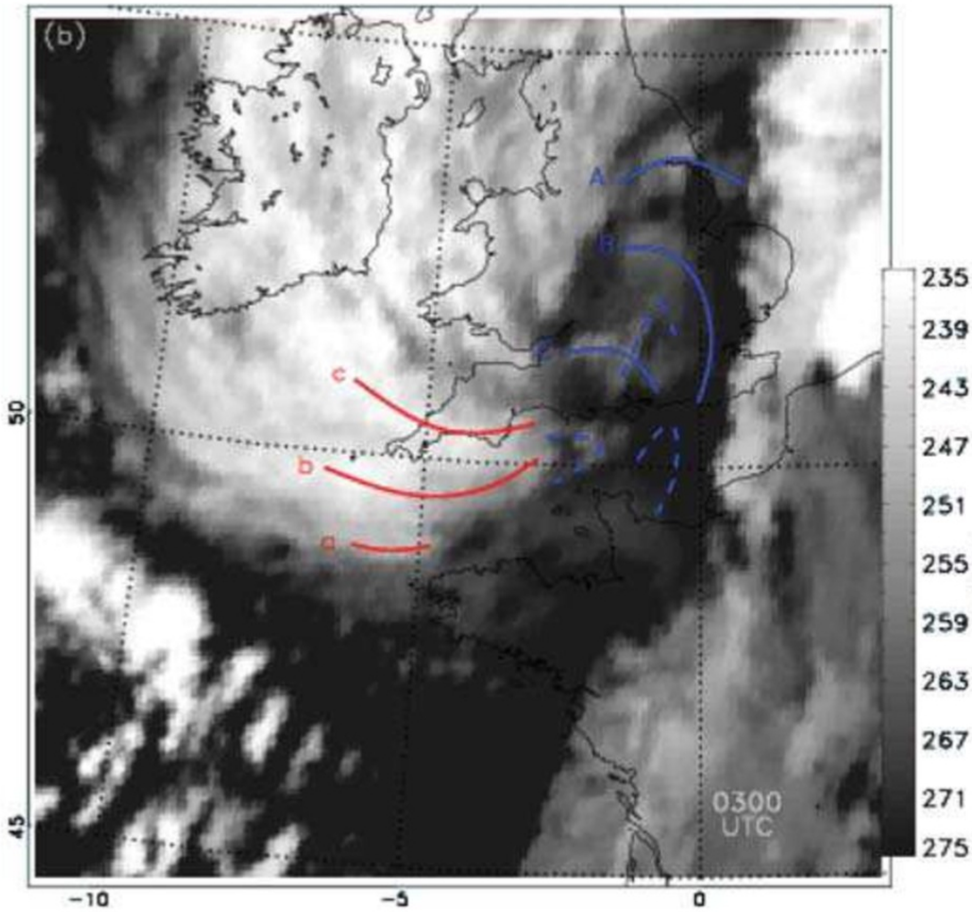

Figure 2.15: From Browning and Field (2004) Fig. 6b. Meteosat infra-red image of the Great Storm showing banding at the tip of the cloud head (red lines) and convergence lines in the dry slot (blue lines).

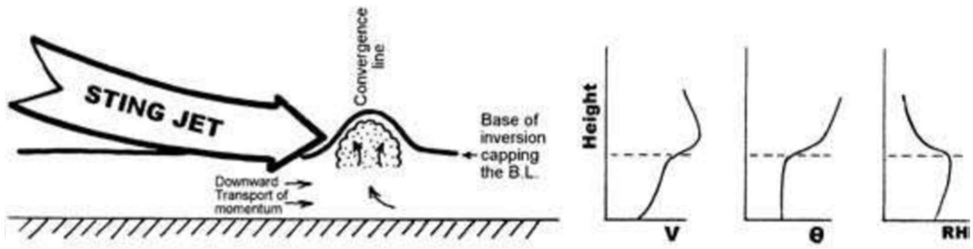

Figure 2.16: From Browning and Field (2004) Fig. 9. Conceptual model of the interaction between a dry, high-momentum SJ outflow and a colder and relatively moist boundary layer. The interaction results in strong wind gusts a the surface just behind a convergence line detectable as a line of boundary-layer cloud.

in Martínez-Alvarado et al. (2014a), reviewed in Section 2.4.2. The dropsondes were instrumental in detecting the high-speed wind regions just above the boundary layer and in showing the sloped structure of the cloud-head tip, consistent with the release of CSI. Observations showed (for the first time using chemical tracers) that SJ and CCB are airstreams composed by distinct air masses, even when the wind maxima associated with them are not spatially separated.

When the intense 'St Jude's Day' windstorm travelled across southern England on 28 October 2013, it passed just over the Doppler radar in Chilbolton. As a consequence, Browning et al. (2015) used the data from the radar to look at the evolution of the storm, with particular focus on the momentum transfer from the SJ through the boundary layer. An observationally-validated WRF model run was used to confirm that the low-level jet detected by the radar was actually the SJ that occurred in the storm. Momentum was brought down from the SJ to the foremost edge of the CCB and towards the surface by convective circulations. Shafts of evaporating precipitation within the SJ region helped to reduce the static stability allowing convection to extend downwards to the surface.

All these results represented step forwards in the observational description of the SJ evolution and in the understanding of the momentum transfer from the jet to surface winds. This aspect can be summarised looking at the study of Hewson and Neu (2015). This article used observational and reanalysis data from twenty-nine historic windstorms, trying to bridge the gap between observational papers (just presented) and the climatology papers mentioned in Section 2.4.5. The paper aims to link the evolution of a windstorm and its conceptual model to the footprints of strong winds at the surface. In the study, strong winds are divided in three distinct causal classes: WJ (warm jet, i.e. WCB), CJ (cold jet, CCB) and SJ. Whilst the SJ is the phenomenon with the lowest frequency of occurrence, it is the most damaging overall among the three (Figure 2.17). Two processes are found to be driving the SJ and helping the transfer of momentum towards the surface. First, imagery shows pulses propagating forwards relative to the cyclone, through a region of broadly cold advection and towards a warmer environment. Second, evaporation and sublimation occur on the jet and lower the potential temperature of the air composing it. The authors argued that both processes would increase DCAPE/DSCAPE hence favouring slantwise convection and that it is not necessary for both of them to occur at the same time. The analysis of different SJ storms allowed Hewson and Neu (2015) to observationally confirm the banded structure at the cloud-head tip and the short-lived, quick-onset characteristics of the jet. This is reflected in the SJ having a smaller footprint than the other jets, usually less than 100 km wide. The article also tackled the issue of the resolution needed to satisfactorily represent an extra-tropical cyclonic windstorm. Following up from the recommendations in Clark et al. (2005) they highlighted that the typical resolution of reanalysis, around a few tens of km for the horizontal grid spacing, is not ideal. They argued that the difference in intensity of a SJ between low-and high-resolution models is larger than for WCB and CCB.

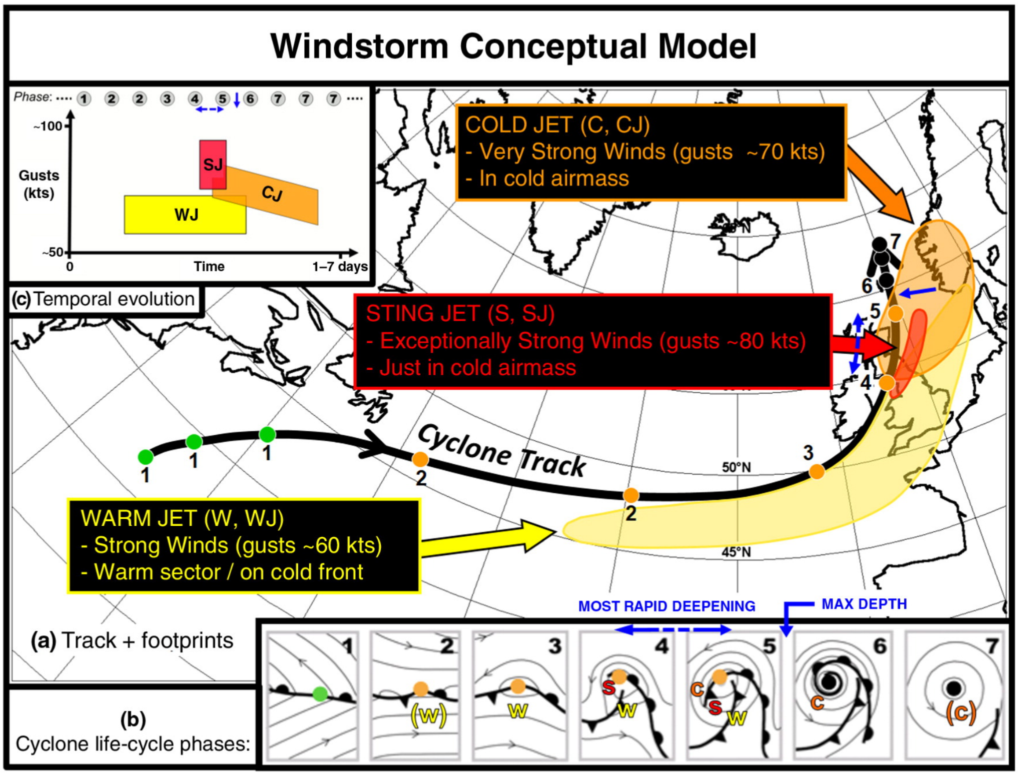

Figure 2.17: From Hewson and Neu (2015) Fig. 1. Conceptual model of an extra-tropical cyclonic windstorm. Panel (a) shows the cyclone track (black) and the footprints attributable to the different jets. Panel (b) shows the synoptic-scale evolution of fronts and isobars around the cyclone and panel (c) denotes the temporal evolution of gust strength for each jet zone.

2.4.5 Climatologies of sting-jet storms

The last category of studies on SJs presented in this section is climatological studies. As the SJ phenomenon is characterised by small scales both spatially and temporally it is difficult to produce extensive climatologies of it. In fact, published climatologies up to date refer only to North Atlantic cyclones, although there is no suggestion that the SJ cyclones can be found only in that basin.

The work in Parton et al. (2010) refers to 7 years of wind profiling radar data located in Aberystwyth, Wales. These data enabled the generation of wind -speed and direction-probability distributions and the selection of the most intense cases. Nine SJ events are identified, shown to belong to rapidly developing storms and to be associated with evidence of slantwise structure with a slope usually close to the 1:50 aspect ratio indicated in Section 2.4.1. The SJs are seen to be westerly and located close to a cloud head hooking around the storm centre, in Stage III or IV of the Shapiro-Keyser model of development.

Three intense cyclones were examined in the work of Martínez-Alvarado et al. (2013). The article argues that while SJ evolution and CSI release are not resolved in low-resolution models, the signature of CSI on low-resolution data can be used to infer the actual occurrence of a SJ in a cyclone. For this reason, a method to diagnose a SJ precursor is adopted in the analysis, consisting of the detection of downdraught CSI (indicated by the presence of DSCAPE) in the vicinity of a cold front (and hence near to a frontal-fracture region). Two different model resolutions are used in the study to compare the SJ evolution in the three case studies. A SJ is identified (through the use of trajectories in the high-resolution simulation) in two of the storms, associated with regions satisfying the precursor diagnostic at both resolutions. No regions satisfying the diagnostic are found in the other storm, in which the SJ is missing despite a similar storm structure. The study is also useful in setting the threshold for DSCAPE at 200 J kg^{-1}. However, the authors stressed that further evaluation was still needed given the very small sample of storms analysed.

Following upon the study just presented, Martínez-Alvarado et al. (2012) produced the first regional climatology of SJ. Reanalysis data from ERA-Interim (Dee et al., 2011) were used to select 100 cyclones (Martínez-Alvarado et al., 2014b) passing over the North Atlantic in winter seasons between 1989/90 and 2008/09. Given the insufficient resolution of reanalysis data for representing mesoscale processes, the same SJ precursor used in Martínez-Alvarado et al. (2013) is adopted. A subset of 15 randomly-selected cyclones is then simulated with the usual high-resolution MetUM settings. SJ occurrence is verified through the use of trajectories in high-resolution simulations of those 15 cyclones to make a comparison between SJ precursor in the reanalysis data and the occurrence of the actual airstream in higher resolution forecasts. This analysis showed the skill of the precursor diagnostic in identifying SJ with p-values around 0.05 (i.e. a 95% significance level). Almost one third of the 100 cyclones constituting the considered set satisfied the SJ-precursor diagnostic. However, the results of the precursor diagnostic depend on the thresholds chosen to define the moist frontal-fracture region, the minimum energy available to be released by a SJ-associated instability and the highest pressure level from which the SJ descent can start. There is a certain level of subjectivity in the choice of these thresholds as features consistent with SJ definition exist on a spectrum of various available energies and descent ranges. The article admitted that further work was needed on the topic. In any case, the authors were able to suggest a relatively common occurrence of SJ in intense North-Atlantic cyclones, with the authors arguing that the previously analysed SJ case-studies were more exceptional in their path over populated areas than in their strength compared to other SJ storms (however, the Great Storm was exceptional in both strength and path).

The most recent and complete climatology of SJ is contained in Hart et al. (2017). The methodology used in previous papers is adopted and ERA-Interim reanalyses are used to look at 33 extended winter seasons from 1979–2012. Of over 5000 cyclones tracked, 32% displayed the SJ precursor (42% if looking only at the subset of $\sim$1000 explosively developing cyclones). Storms with precursor show a more southerly and zonal storm track and a larger low-level relative vorticity (indicating a larger intensity of the storm) than the others. In fact, storms with the precursor have been found likely to have a strong CCB, probably as a consequence of the overall larger intensity of the storm and of a more developed cloud head associated with larger instability and with more intense latent heating processes (consequence of a more southerly track (Figure 2.18)). The study claims that storms with SJ precursors are the dominant cause of cyclone-related resolved strong wind events over the British Isles for wind speeds exceeding 30 m s^{-1} at 850 hPa. It is important to remember that the SJ is not resolved in their data and it is thus likely to further increase the wind strength in higher resolution datasets.

2.4.6 Summary and discussion of the state-of-the art theoretical understanding of SJ dynamics

The previous sections show that after the initial conceptual model for SJ in extratropical cyclones proposed in the pioneering works of Browning (2004) and Clark et al. (2005), a considerable body of literature tried to tackle all the aspects of SJ-related research

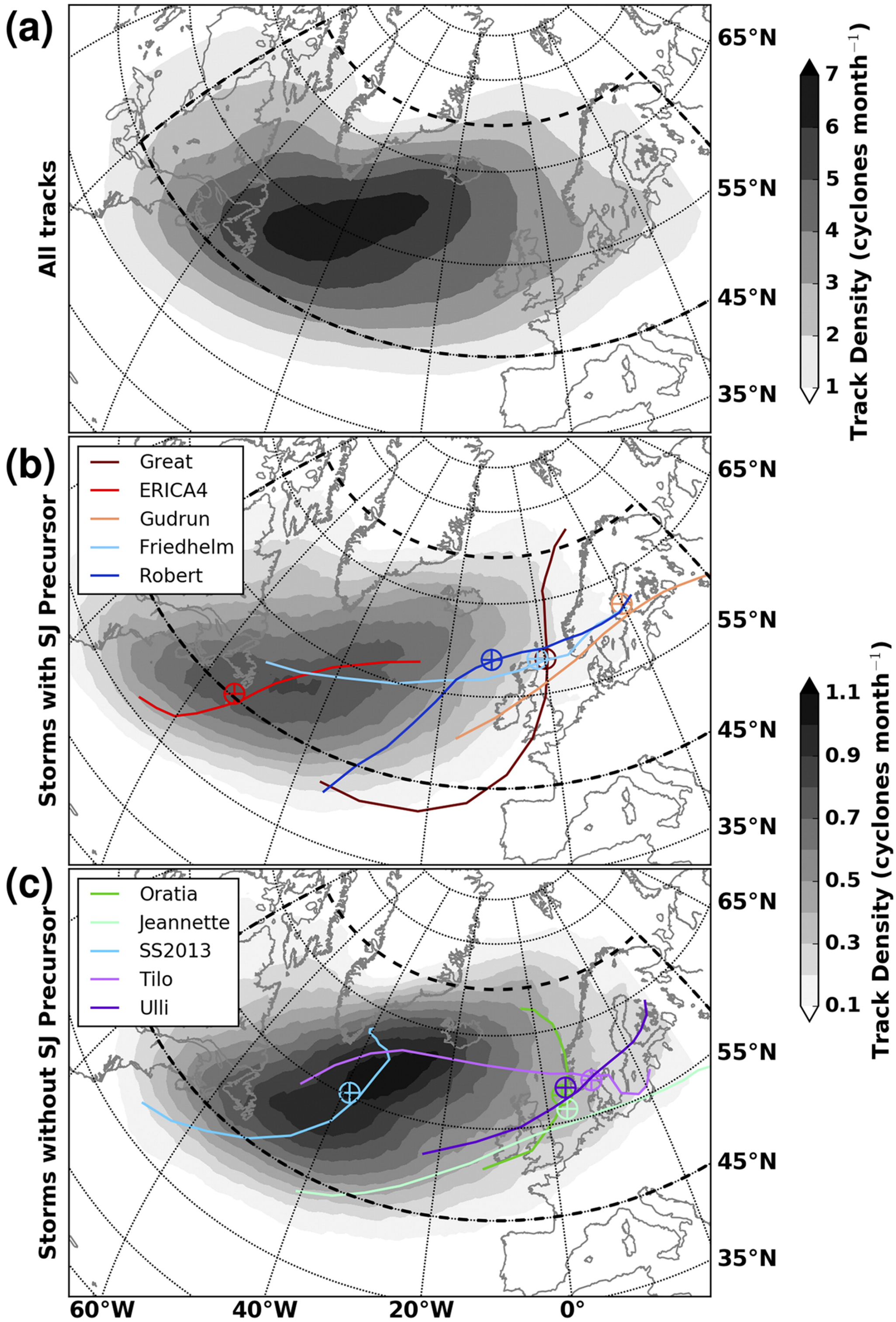

Figure 2.18: From Hart et al. (2017) Fig. 4. Extratropical cyclone density (number density per month in a unit area) for (a) all cyclone tracked, (b) explosively developing cyclones without SJ precursors, (c) explosively developing cyclones with SJ precursors. Selected tracks from cyclones with published case studies are shown by coloured lines with legend.

(see Clark and Gray (2018)).

This research has now made clear that the SJ is a distinct airstream, not part of the CCB or the WCB. The SJ exits from the banded tip of a hooked cloud head and descends into the frontal-fracture region while exhibiting a large acceleration. The SJ can be extremely damaging with wind speed sometimes reaching or even exceeding 50 $m\ s^{-1}$ just above the top of the boundary layer. The SJ does not always reach the surface and it is not uncommon to record the strongest gust in a SJ-containing storm in association with the CCB. Climatological studies referred to North-Atlantic storms have started to show that the SJ can be a rather common feature of intense extratropical cyclones, although more research is needed to assess a global-SJ climatology. Modelling analyses have stressed that the SJ is a mesoscale feature that requires high model resolution (i.e. a grid spacing not exceeding 10-15 km in the horizontal and 200-300 m in the vertical in the low- and mid-troposphere) to be resolved in its dynamics.

The identification of the mechanisms driving SJ generation and strengthening is indeed a key open question and the main focus of this PhD project. While there is plenty of evidence that moist processes are important in SJ evolution and there is no evidence of SJ forming in dry (idealised) cyclones, research is still needed to understand the exact role that those processes play in SJ dynamics. The mechanisms causing the descent and acceleration of the SJ have been subject of debate with some apparently contrasting results portrayed in different papers. Various papers confirmed the existence of SJ as a distinct airstream arguing that its dynamics is driven by the release of mesoscale instabilities and with possibly a role played by evaporative cooling (Gray et al. (2011), Baker et al. (2014), Martínez-Alvarado et al. (2014a) amongst others). On the other hand, Schultz and Sienkiewicz (2013) showed that an airstream descending out of the cloud head is associated with frontolysis connected with the frontal-fracture region and Coronel et al. (2016) claimed that dynamical geostrophic forcing is largely responsible for initiating the slantwise descent, in an environment nearly neutral to CSI. It is argued in this thesis that the two paradigms are not necessarily contradictory and that localised process can act “on top” of the larger-scale cyclone dynamics.

Taking into account all the pieces of evidence described up to this point, Clark and Gray (2018) conclude their review defining the sting jet as “a distinct region of stronger winds that descends from mid-levels inside the cloud head into the frontal-fracture region of a Shapiro-Keyser cyclone over a period of a few hours. This definition is consistent with the first hypothesis advanced in Clark et al. (2005) and it is not process-based, in the sense that the sting jet is not attributed to a specific mechanism in its definition. As Clark and Gray (2018) explain, a continuous spectrum of sting-jet descent and speed-up mechanism can occur, from balanced frontolytic descent to local evolution of conditional — or even dry — symmetric instability along the jet, enhancing its descent and wind speed. Starting from this definition and from the literature described here, the occurrence of these unstable mechanisms is analysed in detail in Chapters 4 and 5 in a case study. This continuous spectrum of sting jets occurring in different environmental conditions is investigated in Chapter 6 using an idealised model.

Chapter 3

Methodology

3.1 Introduction

In this chapter the tools and techniques used for the modelling and analysis in this thesis are described. A description of the model used for case-study and idealised simulations, along with the different specifications and settings, is provided. The chapter is then completed with a description of particular techniques and diagnostics used in the analyses, specifically Lagrangian trajectories, instability diagnostic tests and PV tracers.

3.2 Description of the MetUM version 8.2

This summary of the main features of the MetUM version 8.2, which uses the New Dynamics dynamical core (Davies et al., 2005), is based on the description in Baker (2011), adapted where necessary. Further details can be found in the user guide for this version of the model (UK Met Office, 2012b). The MetUM is a finite-difference model that solves the non-hydrostatic deep-atmosphere dynamical equations. The integration scheme is semi-implicit and semi-Lagrangian (Davies et al., 2005).

3.2.1 Model dynamics

The MetUM is a non-hydrostatic model that solves the fully compressible, deep-atmosphere Navier-Stokes equations (Staniforth et al., 2006):

$$\frac{D\mathbf{u}}{Dt} = -2\Omega \times \mathbf{u} - \frac{\nabla p}{\rho} - g\mathbf{k} + \mathbf{S}^u, \tag{3.1}$$

$$\frac{\partial \rho}{\partial t} + \nabla \cdot (\rho \mathbf{u}) = 0, \tag{3.2}$$

where $\mathbf{u} = (u, v, w)$ is the velocity vector, Ω is the rotation rate of the Earth, ρ is density, p is the atmospheric pressure, g is the magnitude of apparent gravity and $\mathbf{S}^u$ is the frictional force per unit mass. In addition to these, the thermodynamic equation and equation of state are used, which are given, respectively, by

$$\frac{D\theta}{Dt} = S^\theta, \tag{3.3}$$

$$p = \rho RT, \tag{3.4}$$

where θ is potential temperature, T is temperature, R is the gas constant for dry air and S^θ is a heat source term. Moisture is represented by the moist mixing ratios m_X, where X denotes a given quantity, for example liquid water. The moisture budget is given by

$$\frac{Dm_X}{Dt} = S^{m_X}, \tag{3.5}$$

where S^{m_X} is a source term of the water substance. The full equations and method of solution are given in Staniforth et al. (2006). The prognostic variables are the velocity vector $\mathbf{u}$, potential temperature θ, dry density ρ, and moist mixing ratios m_x. Exner pressure, given by $\Pi = \left(\frac{p}{p_0}\right)^{\frac{R}{C_p}}$, is used instead of the diagnosed variable p, where $p_0 = 1000$ hPa is a reference pressure and C_p is the specific heat at constant pressure for dry air. The potential temperature is then given by $\theta = \frac{T}{\Pi}$. If moisture is present, the virtual potential temperature is given by $\theta_v = \frac{T_v}{\Pi}$ where T_v is the virtual temperature.

The model uses finite-difference schemes on a spherical polar co-ordinate system. The equations are discretized using a horizontally staggered Arakawa C-grid (Arakawa and Lamb, 1977) and a terrain-following hybrid-height Charney-Phillips grid in the vertical (Charney and Phillips, 1953). The C-grid method was chosen because it gives improved geostrophic adjustment and prevents decoupling of solutions. The Charney-Phillips method gives better balanced structures than the more usual Lorenz grid and does not have a computational mode. The prognostic variables are stored on staggered parts of the grids. In the horizontal, the horizontal wind components u and v are stored half a level offset in the direction of each wind component from the Exner pressure Π, and other prognostic variables are stored with Π. In the vertical, w, θ and m_X are stored on θ-levels (or full-levels) while u, v, ρ and Π are stored on ρ-levels (or half-levels). The vertical grid uses terrain-following co-ordinates, with hybrid-height levels that become horizontal at higher levels. The spacing of the vertical levels is defined by a quadratic function, with higher resolution at lower levels to give better representation of the boundary layer, low-level fluxes and vertical gradients.

The model uses a semi-Lagrangian time integration with semi-implicit timestepping, which gives improved accuracy and stability (Davies et al., 2005). The semi-Lagrangian scheme integrates the equations along trajectories. The semi-implicit timestepping uses a predictor-corrector scheme. This calculates a first estimate of the solution in the predictor step, which is then used in the corrector step to find a better approximation to the solution at the next timestep using an iterative solver. The model is designed such that no explicit diffusion is required for stability.

3.2.2 Parameterisations schemes in the model

Longwave and shortwave radiation (Edwards and Slingo, 1996), boundary layer mixing (Lock et al., 2000), cloud microphysics, and large-scale precipitation (Wilson and Ballard, 1999), extended to include up to 4 prognostic hydrometeor classes (rain, ice, snow and graupel), and convection (Gregory and Rowntree, 1990) are the physical processes included in model parameterisations.

The large-scale cloud is parameterised using the scheme of Smith (1990). This scheme calculates the amount of condensate in a grid box and the fraction of the grid box that is covered by condensate. The variability of the specific humidity q is related to a symmetric triangular distribution function about the grid box mean of a variable which is the generalisation of q_{cl} (cloud liquid water content) - in fact, it is essentially q_{cl} when positive and represents subsaturation when negative. In this way temperature fluctuations are taken into account as well as moisture.

A threshold relative humidity parameter is defined so that cloud will form if the relative humidity in a grid box exceeds this threshold value. This value is set to 91% in the lowest model level, decreasing throughout the lowest model levels to 80% by 1 km of height, in every vertical resolution setting used, and remaining at 80% above this.

The scheme of Wilson and Ballard (1999) deals with microphysical processes and large-scale precipitation by determining the transfer of water between vapour, liquid and ice phases. In all the simulations of this study (apart from the run with PV tracers described in Chapter 5) rain is treated as a prognostic variable.

Convection is parameterised using the method of Gregory and Rowntree (1990). This uses a bulk cloud model to represent shallow, deep, mid-level and dry convection. The method is based on parcel theory with the inclusion of entrainment and detrainment. This scheme is used to represent an ensemble of different convective clouds within each gridbox. Convection is initiated if a parcel with excess buoyancy (given by a temperature excess of 0.2K) is identified that is still buoyant by more than a threshold value after ascending to the next layer. The parcel will continue to rise until it is no longer buoyant. Convection is identified as shallow convection if the buoyancy becomes zero or negative within the boundary layer. The shallow convection scheme is based on that of Grant (2001), which determines the cloud-base mass flux from the sub-cloud turbulent kinetic energy budget. If the buoyancy is still positive beyond the top of the boundary layer then the convection is identified as deep convection. If the convection is initiated above the boundary layer it is classified as mid-level convection. The classification of convection as shallow, deep or mid-level determines the choice of the mass flux parameter, initial buoyancy and entrainment and detrainment rates (Gregory et al., 2009). The values for entrainment and detrainment are the same for both deep convection and mid-level convection.

Radiation is parameterised using the radiation code of Edwards and Slingo (1996). This uses a two-stream method to model vertical upward and downward fluxes of long-wave and shortwave radiation through gridbox columns. The code represents the interaction of radiation with aerosols, ice crystals and liquid cloud droplets, as well as gaseous and continuum absorption. A parameterisation of the optical properties of cloud particles is also included.

The atmospheric boundary layer is parameterised so that turbulent processes, which occur at much smaller scales than the grid box size, can be represented. The scheme is actually active throughout the whole troposphere and includes the cloud scheme and a turbulent mixing scheme. Mixing within the boundary layer is driven by surface fluxes and cloud-top processes and is represented by the scheme of Lock et al. (2000). This identifies seven different boundary layer types, which require different entrainment and mixing parameterisations. Entrainment is parameterised using the method described by Lock (2001).

3.2.3 Poles and grid orientation

The MetUM is a grid point model with a latitude-longitude grid. The resolution is therefore specified by the grid box size, given in degrees. This means that as the grid approaches the poles, the gridbox size decreases as the lines of longitude converge. This problem is overcome by applying a horizontal diffusion filter near the poles to damp short wavelengths (Davies et al., 2005). In limited area model (LAM) configurations, a different method is used to avoid this problem. Instead of using the standard latitude-longitude grid, a new rotated lat-long grid is defined such that the equator passes through the centre of the LAM domain. This means that within the LAM domain, the gridbox size is approximately constant across the domain, and the rotated poles are far away from the edges of the domain.

3.3 Differences between MetUM versions 8.2 and 10.5

The MetUM version 10.5 uses the ENDGame (Even Newer Dynamics for General atmospheric modelling of the environment) dynamical core (Wood et al., 2014). ENDGame has many similarities with the previous (New Dynamics) dynamical core. Nevertheless, some significant differences are present. These differences are summarised here, see Walters et al. (2014) for more details. Both cores solve the same set of fully-compressible deep-atmosphere equations (see Section 3.2.1) and use a semi-implicit semi-Lagrangian time scheme. However, ENDGame is not limited to the use of spherical geometry and its semi-implicit semi-Lagrangian scheme is more stable and accurate than that in New Dynamics. Although still using an Arakawa C grid in the horizontal and a Charney-Phillips grid in the vertical, ENDGame uses a different placement of variables with respect to the pole than New Dynamics: this contributes to a better scaling on parallel-processing computers. ENDGame also has also a more accurate discretisation of the Coriolis terms, leading to improved numerical dispersion and energy properties and a reduced application of artificial damping (Staniforth et al., 2013).

The improvements to the physical parameterisations that are particularly relevant to the simulations presented in Chapter 6 are listed here. The large-scale cloud scheme used in these experiments is still the one described in Smith (1990), with rain, and now also total ice, treated as prognostic variables. This scheme now includes an improved method to represent cloud erosion and a better definition for mixed-phase cloud, along with improvements to the representation of ice cloud and a smoother phase change for cloud condensate detrained from convective plumes. An improved size distribution of water droplets is implemented, to better match the observations of drizzle. The improved microphysics substepping enables the performance of multiple calculations over each column in a single model time step.

An increase of the entrainment rate for deep convection with related modifications to the detrainment rate is included in the convection scheme, along with a smoothed adaptive detrainment of cloud liquid water, ice and tracers. An increase in the frequency of calls to the radiation scheme reduces the radiation time step to 1 hour improving its accuracy. The boundary layer scheme is revised and has now a better physical basis. Turbulent mixing is reduced for stably stratified boundary layers while revised stability functions for unstable boundary layers and diagnosis of shear-dominated boundary layers are present.

These changes might lead to small changes in forecast scores, and will make subtle changes to diabatic forcing that may affect the detail of simulations. However, they are very unlikely to have a substantial impact on the overall evolution of a system.

3.4 The use of Lagrangian trajectories

Lagrangian trajectories have been used extensively in sting-jet research (e.g. Clark et al. (2005); Baker et al. (2014); Martínez-Alvarado et al. (2014a); Smart and Browning (2014)). Indeed, Schultz and Browning (2017) emphasise that "definitive evidence of the existence of the sting jet requires trajectories and/or other diagnostics". It is possible in a Lagrangian framework to isolate airstreams and assess their properties and their evolution in time. In this study trajectories were computed using the LAGRANTO Lagrangian analysis tool (Wernli and Davies (1997), Sprenger and Wernli (2015)). LAGRANTO uses an iterative Euler scheme with an iteration step equal to 1/12 of the time spacing of input data. Ideally, data every model time step (2.5 minutes for the simulations with 0.11° horizontal spacing) would be used to compute the trajectories, but in practice some compromise is necessary, and acceptable, to reduce the amount of output required from the model. It was found that trajectories computed with input frequency of model data of 15 minutes (i.e 6 model time steps), showed a marked improvement in their quality compared with hourly input data judged in terms of conservation of relevant physical quantities such as wet-bulb potential temperature. The results of the high-resolution simulation in windstorm Tini use this input frequency. The coarser simulation of windstorm Tini (which has a model time step of 10 minutes), the PV-tracers simulation and the idealised simulations use instead hourly input for trajectories. In the PV-tracers simulation this choice has been taken to save time as the analysis of trajectories is not the main focus of that section. The idealised simulations show a substantially slower development, making 15 minutes an unnecessary high input frequency for trajectories. For the coarser simulation of windstorm Tini the lower input frequency reflects the longer model time step. The software NDdiag (Panagi, 2011) has been used to convert to pressure levels the model output and to compute further diagnostic fields, then interpolated onto trajectories.

3.5 Diagnostics to identify regions of atmospheric instability

An objective of this thesis is to evaluate the role of mesoscale instabilities in the generation of the SJ simulated in Tini. The method followed here to detect these atmospheric instabilities on the SJ airstream follows that presented in Martínez-Alvarado et al. (2014a). The criteria for labelling are shown in Table 3.1. Diagnostics for each instability are evaluated at each grid point and interpolated onto relevant trajectories. The additional constraint for the two conditional instabilities (CI and CSI) of $RH_{ice} > 80\%$ is used because these instabilities can only be released if the air is saturated (where RH_{ice} is relative humidity calculated with respect to ice, chosen instead of RH because of the interest in levels mainly above the freezing level for CSI release). In the model, partial cloud formation occurs when RH exceeds a certain threshold, 80% in the free troposphere. A slightly more accurate diagnostic could probably be designed, but in practice regions identified with these instabilities at this RH are contiguous with similar cloudy regions that are close to saturated. Grid points where the diagnostic tests for CSI or CI indicate instability, but the saturation constraint is not met, are not labelled as stable (S) and do not belong to any of the categories in Table 3.1. A grid point is labelled as stable only if none of the four diagnostic tests indicate instability.

Label	${N_m}^2$	RH_{ice}	ζ_z	PV	MPV^*
Conditional Instability (CI)	< 0	$> 80\%$			
Inertial Instability (II)			< 0		
Symmetric Instability (SI)				< 0	
Conditional Symmetric Instability (CSI)		$> 80\%$			< 0
Stable	≥ 0		≥ 0	≥ 0	≥ 0

Table 3.1: Criteria for trajectory instability and stability labels. ${N_m}^2$ is the moist Brunt-Väisälä frequency as defined by Durran and Klemp (1982). ζ_z is the vertical component of absolute vorticity (on pressure levels). PV is the potential vorticity and MPV^* the moist saturated potential vorticity (Bennetts and Hoskins, 1979). Note that we use MPV^* and not MPV_g^* for the reasons outlined in Gray et al. (2011). Multiple entries in a row require all criteria to be satisfied (i.e. 'and' rather than 'or').

Every point can be labelled with more than one instability at the same time if two or more conditions are met. It should be borne in mind that the underlying theory for each of these instabilities relies on assumptions regarding the background state upon which perturbations grow: uniform flow for CI, uniform potential vorticity (PV) for CSI, and barotropic atmosphere for II. These conditions are rarely met in practice and are certainly not met in an intense cyclone such as Tini where strong pressure gradients, wind shears and PV gradients occur. Our approach is to take these criteria as indicators of the underlying atmospheric state to highlight the processes leading to instabilities that might drive the dynamics of the SJ. For example, a formal definition of CSI states that a point is only defined having CSI if II and CI are absent (Schultz and Schumacher, 1999). However, we have labelled points with CSI if MPV*<0 even when II (and SI) and CI are present — as will be shown this provides useful insight into the whole period when MPV* is negative in a nearly-saturated environment, even though the contemporary presence of SI and/or II means that we would interpret any release of instability as due to the latter rather than slantwise convection induced by CSI release. Likewise, SI and II can be present at the same time. Arguably, in most circumstances, SI and II are the same thing, and would be labelled as SI (with II reserved for barotropic flow), but we have kept both to keep track, in particular, of the vorticity.

While PV can be related most simply to the absolute vorticity on potential temperature (θ) surfaces, it is evident that the θ surfaces are undergoing quite substantial deformation in the region of the SJ. Ertel's theorem tells us about conservation of PV, and the nature of sources and sinks. In many cases, PV is changed by diabatic processes through changes in static stability. These processes are expressed as a change in the flow through adjustment to a balanced flow. The adjustment process requires time that may be similar to, or even longer than, the process generating the change in PV. We therefore cannot assume a perfectly adjusted flow (only, in the case of negative PV, the lack of existence of one). On the other hand, direct changes to vorticity (which may well be occurring as part of the adjustment process) are more straightforward to analyse, at least kinematically. In particular, where diabatic processes generate negative PV due to negative static stability it is likely that vertical turbulent convection rapidly removes the resulting instability before there is any impact on the vorticity. Where negative PV is produced and persists on an air parcel, this could then be due to the indirect effect of diabatic processes tilting the horizontal component of vorticity.

3.6 PV tracers

This section introduces the concept of PV tracers, as for the analysis performed on a simulation of windstorm Tini (see Section 5.4), following the methodology outlined in Saffin et al. (2016). As explained in their study, numerical models of the atmosphere combine a dynamical core, producing approximate solutions to the adiabatic, frictionless governing equations for fluid dynamics, with tendencies coming from the parameterisation of other physical processes. Potential vorticity (PV) is a conserved quantity for fluid flow in adiabatic, frictionless circumstances. Hence, it is possible to isolate the effects of non-conservative processes by accumulating PV changes in an air-mass-relative framework. The 'PV tracer technique' is used to accumulate the separate effects on PV of each of the different non-conservative processes represented in a numerical model of the atmosphere. The details of the online computation of the tracers by the model can be found in Saffin et al. (2016).

The most relevant tracers for this analysis are the microphysics tracer (containing the slow moist processes, such as nucleation of ice, evaporation and freezing of rain, deposition on ice, melting, freezing of cloud, Bergeron-Findeisen process) the boundary layer scheme (which, as specified earlier, is actually active throughout the whole troposphere and includes the cloud scheme and a turbulent mixing scheme), the convection tracer and the long-wave radiation tracer. All other physical processes can be safely neglected when looking at PV contribution, as verified also in the evolution of windstorm Tini. θ tracers are also used to clarify the results coming from PV tracers.

The analysis of PV and θ tracers highlights which processes are involved in changing PV and potential temperature in the regions where the SJ travels, contributing to clarify its evolution (see Section 5.4 for the results).

Chapter 4

Case study of Windstorm Tini: identifying a Sting Jet

The SJ is a phenomenon which has only been studied in detail in a relatively small number of, often relatively sparsely-observed, extra-tropical cyclones. As a result, the dynamics producing a SJ are still a matter of debate (see Section 2.4). Indeed, the SJ has been defined based on its kinematic properties and it is not yet clear if a single mechanism is responsible for all SJs. Amongst those papers that broadly agree with the definition of a SJ used here, the primary question is the relative importance of larger-scale cyclone dynamics and mesoscale instabilities. In this chapter and the next this question is addressed in a case study: windstorm Tini. Model simulations, validated by the comparison with observations, are presented. Although the results of this analysis are drawn from a single case study, their consistency with those from other studies enables to make broad conclusions regarding the contribution of mesoscale instability release to SJ generation and descent in extra-tropical cyclones as well as the potential limitation of simulating these storms with insufficient model resolution.

4.1 Setup of the model simulation of windstorm Tini

The simulation (technically a hindcast) of windstorm Tini was performed with the MetUm version 8.2 (see Chapter 3 for details) using two different sets of resolution and domain. The primary hindcast used a global domain, comprising 1024×769 horizontal grid points, with horizontal grid spacing around 26 km at mid-latitudes. 70 vertical levels were used (as per the operational global model) with the top level around 80 km and spacing smoothly stretching from the surface, ranging from 170 m to 300 m at heights between 1 km and 3 km. Initial conditions to the global simulation were given by the Met Office operational analysis valid at 1200 UTC 11 February 2014. The global domain provided initial and lateral boundary conditions (every 3 hours) for a limited area model. This corresponds to the Met Office's recently operational North Atlantic-Europe (NAE) domain, comprising 600×360 horizontal grid points. The horizontal grid spacing was 0.11° (∼12 km) in both longitude and latitude on a rotated grid centred around 52.5°N, 2.5°W. The NAE domain extends approximately from 30° to 70°N in latitude and from 60°W to 40°E in longitude. A different set of 70 vertical levels was used, with top level around 40 km, the same vertical levels used in the 1.5 km horizontal grid spacing operational UK Variable resolution (UKV) model. Vertical spacing gradually stretches from around 120 m to 200 m at heights between 1 km and 3 km.

The primary purpose of the global simulation was to drive the limited area model. However, it has been used also to test the sensitivity of the results to horizontal and vertical resolution. Model resolution is a key aspect when investigating the dynamics of mesoscale phenomena (e.g. sting jets) being part of evolving synoptic-scale weather systems, like extratropical cyclones. The results described in the following sections highlight how a change in horizontal and vertical resolution affects the ability of the model to correctly represent sting-jet related features and the underlying dynamics. Baroclinic systems are generally dominated by shallow slantwise motions of order 1:100 (roughly $f : N$, where f is the Coriolis parameter and N the Brunt-Väisälä frequency). Systems with strong frontal dynamics and/or the release of conditional symmetric instability (CSI) are often somewhat steeper (e.g. 1:50). Previous research has demonstrated that it is important to resolve the vertical spacing and aspect ratio of CSI-related circulations (Persson and Warner, 1993; Lean and Clark, 2003), requiring a grid spacing of 200-250 m in the lower mid-troposphere or better. With 1:50 slope this implies a horizontal spacing of around 10-12 km. In practice, the solution developed by the model tends to be dominated by the poorer of the horizontal resolution and the vertical divided by the aspect ratio of the flow (so a 20 km horizontal grid simulating a flow with 1:50 aspect ratio tends to produce a solution similar to a model with 400 m vertical grid spacing even if the actual spacing is higher). Incidentally, if ice sublimation is important in the frontal dynamics of a system (as it often is), a similar resolution is required to capture the depth-scale of sublimation (Forbes and Clark, 2003).

Previous simulations of sting jets have shown that they descend out of the cloud head with roughly this (1:50) aspect ratio, and have shallow vertical depth requiring a grid spacing of 200-250 m (Clark et al., 2005; Gray et al., 2011). Both the global simulation and the limited-area simulation conform (approximately) to this aspect ratio, but the global model resolution does not meet the required vertical resolution criterion. Hence, there are two simulations. One that, as shown through Chapters 4 and 5, adequately resolves sting-jets while the other does not (see Section 5.3). Initial runs were also performed using the limited area domain but with the global model level set. This resulted in a simulation, as expected, closer to the global simulation. Results are not reported here as they merely confirm that intermediate behaviours occur.

Model data were interpolated onto pressure levels with 15 hPa spacing for both model configurations before calculating the diagnostics and performing the Lagrangian analysis described later on in this paper. The spacing is similar to the one between limited-area model levels in the mid-low troposphere and comparisons between the interpolated data and the original model-level data confirm that no significant degradation occurred through this process.

All figures in this chapter and in the next regarding the output of model simulations are referred to the high-resolution limited-area run unless explicitly mentioned (i.e. apart from in Section 5.3 where the coarse-resolution global run is analysed).

4.2 Development of windstorm Tini: observations and model simulation

In this section observations and related products from model simulation of windstorm Tini are compared. This analysis gives an indication of the features occurring in the evolution of the storm that are reminiscent of sting-jet occurrence and allows us to assess the discrepancy between observations and model simulation.

4.2.1 Background and synoptic overview

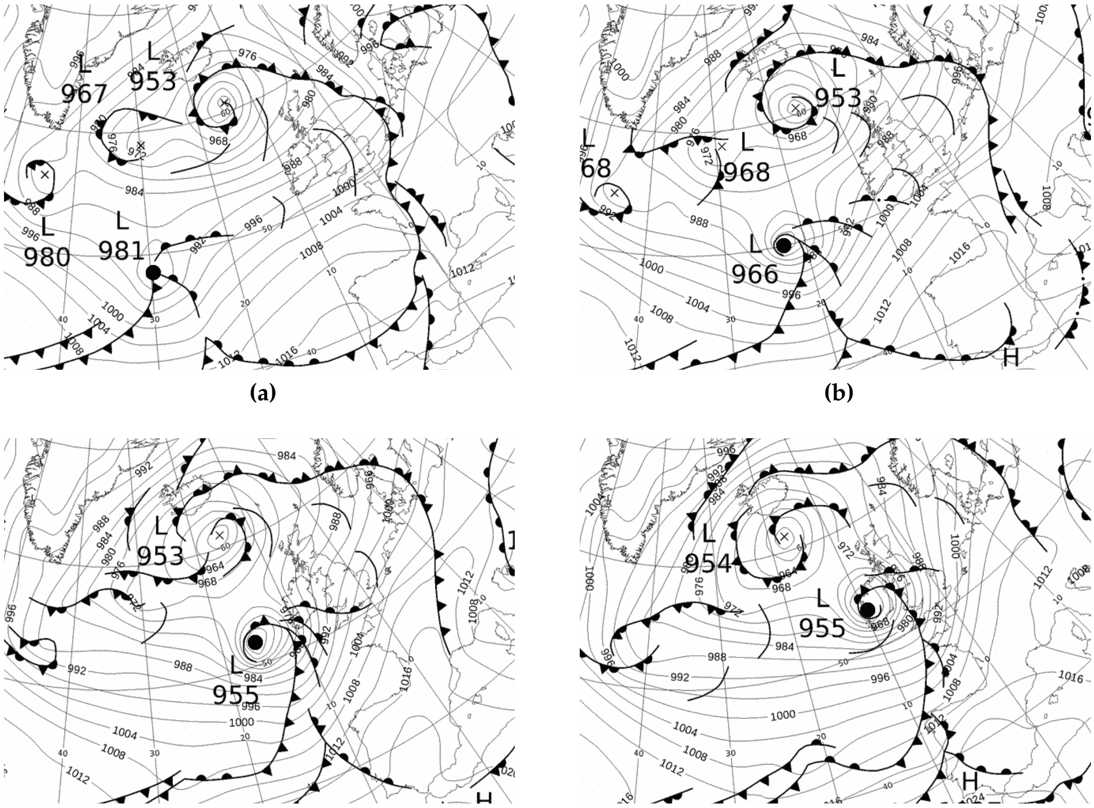

(a) (b) (c) (d)

Figure 4.1: Adapted from Met Office analysis charts valid at (a) 18 UTC 11 February, (b) 00 UTC 12 February, (c) 06 UTC 12 February and (d) 12 UTC 12 February 2014 showing Windstorm Tini (whose cyclone centre is indicated with a black dot) deepening and moving eastward across the North-Atlantic Ocean towards the British Isles. Figures courtesy of the Crown, archived by www.wetter3.de .

Windstorm Tini was one of the many intense extra-tropical cyclones that passed over the British Isles during winter 2013–2014 (Figure 4.1), the stormiest winter on record in the UK according to Matthews et al. (2014). Tini was arguably the most severe of all those intense cyclones, with the analysed surface pressure minimum dropping 40 hPa in 18 hours, from 995 hPa at 12 UTC on 11 February (not shown) to 955 hPa at 06 UTC on 12 February (Figure 4.1c), with an associated deepening rate (see various panels in Figure 4.1) around twice the 24 hPa/24 hours threshold (at 60°N) used by Sanders and Gyakum (1980) to define explosive cyclogenesis (see Section 2.1.2). According to the Met Office, Tini was defined as one of the most intense storms to affect Wales and north-west England in recent decades (UK Met Office, 2015).

The comparison between Figure 4.2 and the various panels of Figure 4.1 show that

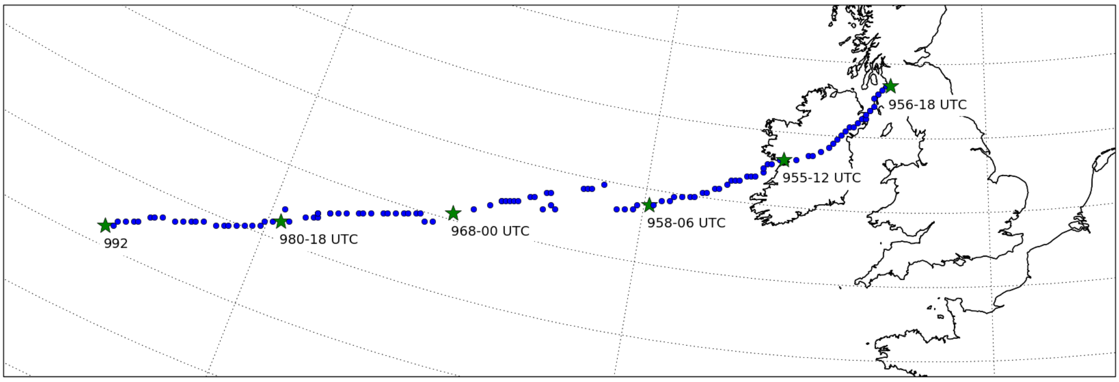

Figure 4.2: Simulated track of minimum sea level pressure values associated with windstorm Tini from 12:15 UTC on 11 February 2014 to 18:00 UTC on 12 February. Blue dots refer to the instantaneous position of the pressure minimum every 15 minutes. Minimum sea level pressure values (indicating the cyclone centre) in hPa are showed, together with a green star, every 6 hours and after the first output of the simulation at 12:15 UTC on 11 February 2014.

the cyclone-centre track in the model simulation follows the one in the analysis throughout all its evolution, with discrepancies usually in the range of $\sim$ 100 km. The same two figures show that there is a good agreement between observations and simulation also in terms of cyclone deepening. Minimum sea level pressure values evaluated every 6 hours are always within 3 hPa from the related observed values. The total pressure drop in the simulated storm is slightly smaller than in observation, with a decrease of 34 hPa from the first output of the simulation (12:15 UTC on 11 February) to 06 UTC on 12 February (compared to 40 hPa in the analysis). However, as the 6-hourly deepening rates are very similar throughout the course of Tini's intensification and the minimum sea level pressure value at 12 UTC is equal to 955 hPa in both cases, the simulation looks accurate in terms of storm intensity. The discrepancies could be related to inaccuracies in measurement of cyclone-centre's pressure value in the Atlantic and/or to the spin-up phase of the model simulation.

Figure 4.2 shows the cyclone path, with the surface cyclone centre quickly moving across the Atlantic Ocean. Tracking the location of the sea-level pressure minimum, the speed of the cyclone can be estimated. In particular, a centred 6-hourly running mean of cyclone speed has been computed, removing temporary oscillations of the pressure minimum due to changes in the developing-cyclone-centre shape and hence smoothing the computed cyclone path. The cyclone speed computed is used in the rest of the analysis to produce system-relative fields. During its deepening stages, the cyclone travels over the Atlantic at an average speed of around 25 $\mathrm{m\,s^{-1}}$. The motion is close to zonal (with the magnitude of meridional wind well below 5 $\mathrm{m\,s^{-1}}$) until 0700 UTC. During the latter stages of cyclone evolution, not relevant for SJ generation and descent, the cyclone speed decreases and the direction turns towards the NW.

4.2.2 Satellite imagery

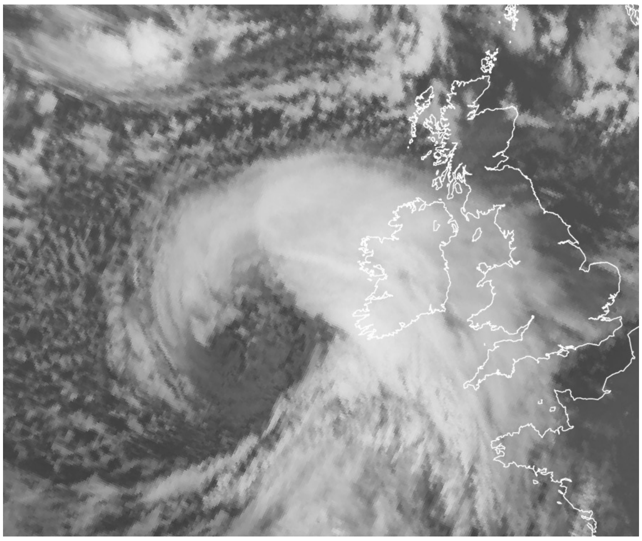

(a)

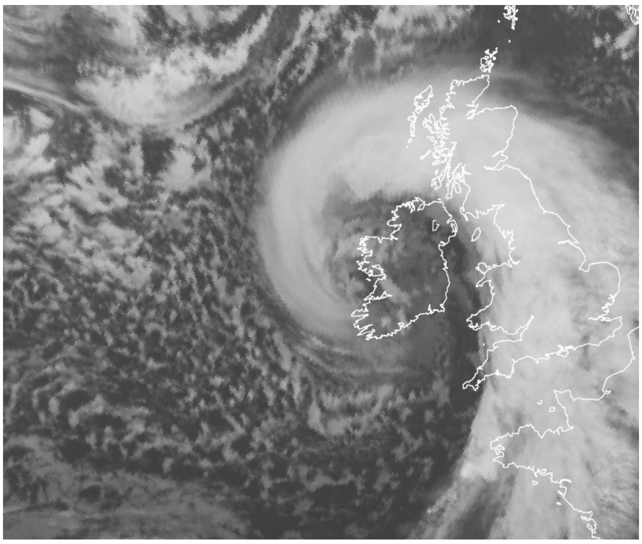

(b)

Figure 4.3: Extracts from infrared satellite imagery of Windstorm Tini at (a) 06 UTC and (b) 12 UTC on 12 February 2014 (Meteosat Second Generation).

Satellite imagery shows an evolution compatible with the Shapiro-Keyser conceptual cyclone model described in Chapter 2. A prominent cloud head formed during the cyclone-deepening stage, leading to the formation of a well-defined bent-back front. Some 'finger-shaped' cloud bands at the southern end of the cloud head occurred for a short period (approximately between 0400–0800 UTC on 12 February 2014) corresponding to the transition between stage II and stage III of the Shapiro-Keyser cyclone evolution. Figure 4.3a shows the cyclone structure at 0600 UTC, in the middle of this period. Similar banded structures at the cloud-head tip have been observed in SJ storms and linked to the multiple slantwise circulations associated with the release of CSI or similar mesoscale instabilities in the region (see also the observations of similar structures in different case studies contained in Browning and Field (2004) and Parton et al. (2009)). Figure 4.3b is referred to 1200 UTC, when the storm is in its mature stage IV when the bent-back front has wrapped around the cyclone centre and a warm seclusion has formed.

The limited-area model simulation follows a very similar pattern to the satellite imagery, with remarkably similar timing given the rapid development of the system. Figures 4.4a and 4.4b show simulated satellite images respectively at 0600 UTC and 1200 UTC on 12 February 2014 using broadband outgoing longwave radiation from the model radiation scheme. The similarities to the observed images in Figs. 4.3a and 4.3b are evident. The simulation is not only well-capturing the broad structure of the weather system and its overall location, but also some smaller-scale features. In particular, Figure 4.3a shows some cloud bands at the tip of the cloud head, resembling the banding observed in the actual satellite imagery. The ability of our model simulation to resolve this feature is dependent on vertical resolution: bands are only visible in the simulation with increased vertical resolution, i.e. using the UKV and not the NAE vertical levels (see Section 4.1).

4.2.3 Observations of surface gusts

The storm particularly affected coastal areas of north-west England and Wales: a Met Office red alert warning for wind was issued for these regions. Wind gusts were recorded to be close to record values reaching 94 kt (108 mph) at Aberdaron (Gwynedd), 83 kt (96 mph) at Lake Vyrnwy (Powys) and 81 kt (93 mph) at Capel Curig (Gwynedd), all in Wales (Figure 4.5). Most of the highest values of surface gusts are located to the south

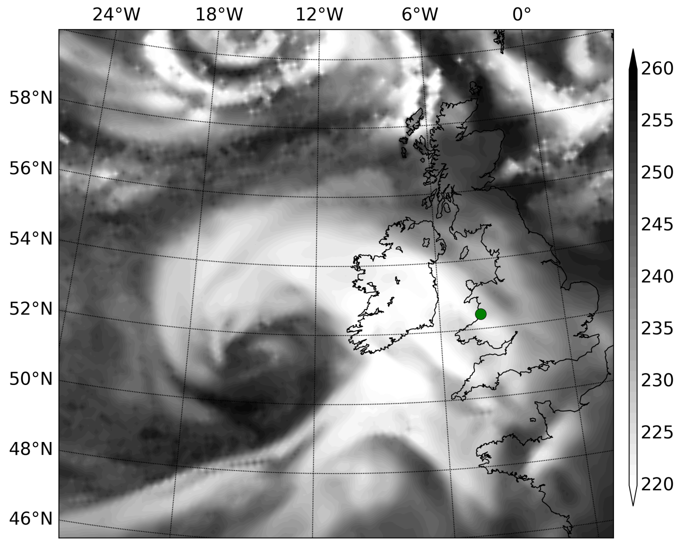

(a)

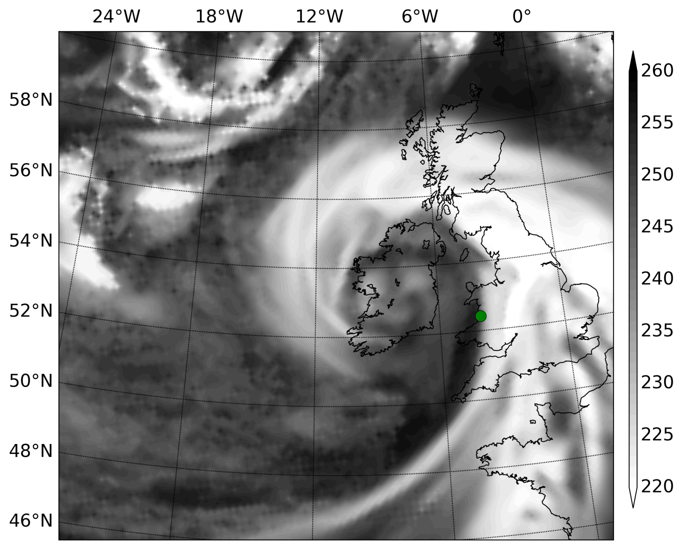

(b)

Figure 4.4: Simulated satellite infrared imagery using model outgoing longwave brightness temperature (K) at (a) 06 UTC and (b) 12 UTC on 12 February 2014. The green dot present in both panels indicates the location of the Aberystwyth MST Radar.

of the path of the cyclone centre (compare with Figure 4.2), consistent with literature on strong-wind regions in extratropical cyclones (see Section 2.1.3 and Figure 2.5 in particular). Windstorm Tini travelled mainly on sea, with its southern side reaching England and Wales only during its final stage of development. Hence, even stronger surface wind-

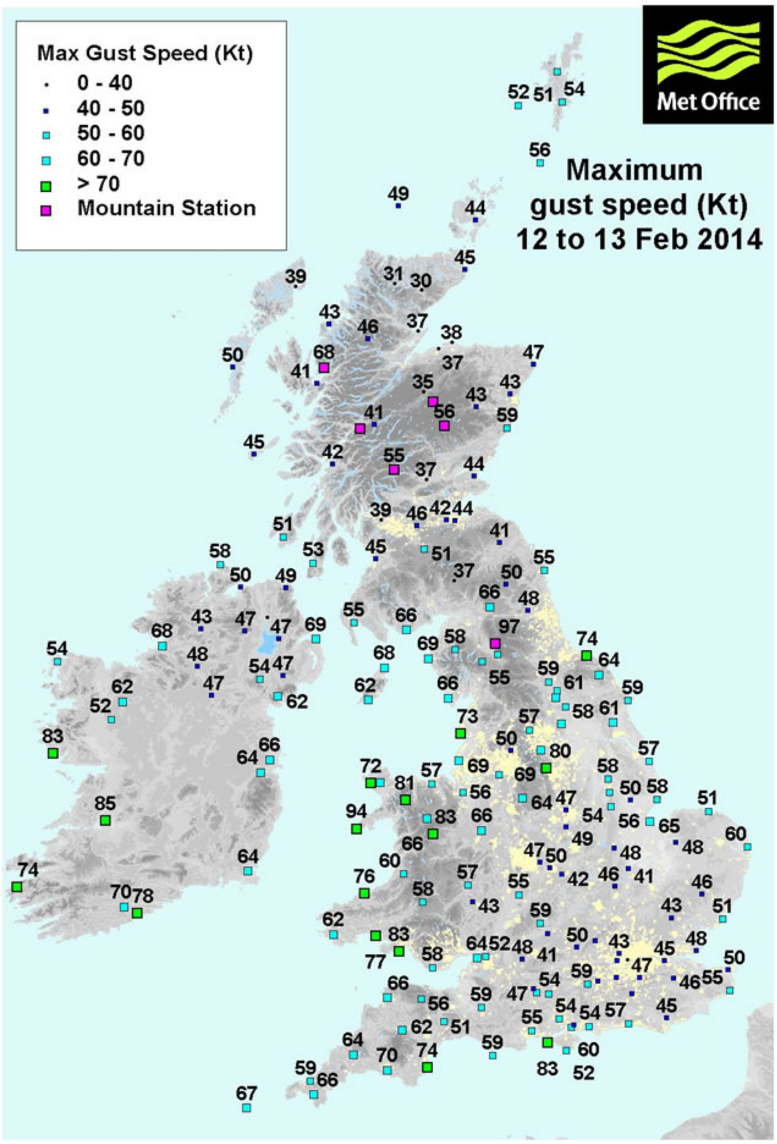

Figure 4.5: Maximum gust speed recorded in UK and Ireland on 12 and 13 February 2014. Figure courtesy of the Crown, available in UK Met Office (2015).

gusts can be expected to have happened on sea, without being measured.

Maximum gust wind speed at 10 m computed by the model has been used for a comparison with the observed values of maximum wind-gusts. Figure 4.6 shows simulated maximum wind gusts at different stages of the storm evolution. Only panels (c) and (d) can be compared with the observed values in Figure 4.5, while panels (a) and (b) show strong surface winds still above the Atlantic Ocean, well west of the British Isles. The good agreement for inland wind gusts during the mature stage of the storm gives further confidence in the overall accuracy of the simulation, though does not prove accuracy in

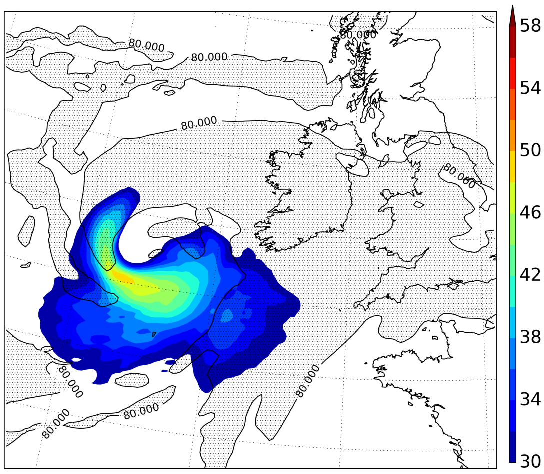

(a)

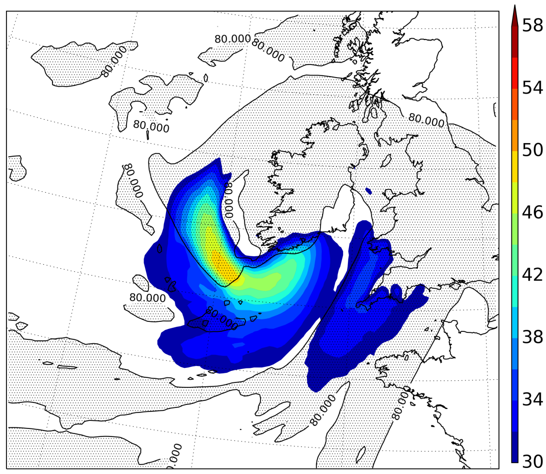

(b)

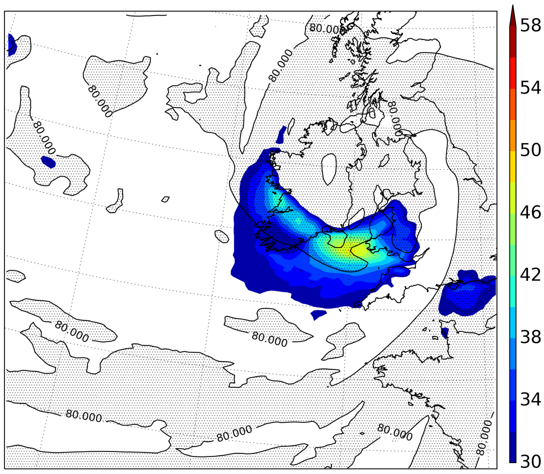

(c)

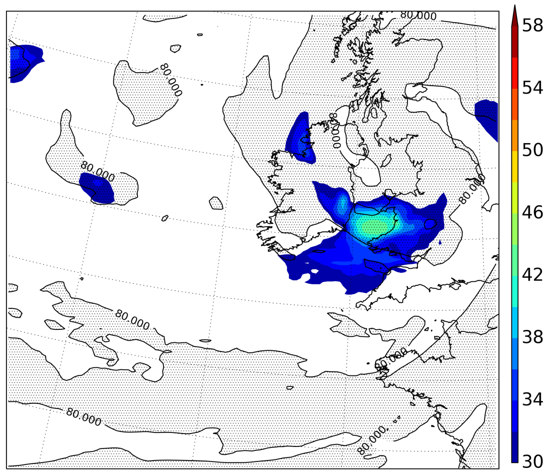

(d)

Figure 4.6: Model map of maximum gust windspeed at 10 m (contours, m s^{-1}) and cloudy regions at 700 hPa (RH>80%, black lines and dotted regions) at (a) 06 UTC, (b) 10 UTC, (c) 14 UTC, (d) 16 UTC on 12 February 2014.

the earlier stages over the sea. Figure 4.6a shows maximum gusts up to 50 m s^{-1} (97 kt) just outside the tip of the cloud head at 06 UTC on 12 February. With the cyclone in a development phase between Stage II and Stage III of the Shapiro-Keyser evolution model (see Chapter 2), this surface gust footprint suggests a connection with the descent of a sting jet (SJ), given its location and timing. Of course the analysis of wind gusts can only give hints on the occurrence of a strong-wind airstream, whose occurrence needs to be verified with a more accurate investigation of the storm dynamics (see the rest of this chapter).

Figure 4.6b, related to 10 UTC, shows similar values of wind gusts, this time underneath the cloud head, close to its tip. At this time the storm is developing towards a more mature stage with the bent-back front wrapping around the cyclone centre. For these reasons, the wind gusts are in this case more likely to be associated with the cold conveyor belt (CCB). Figure 4.6c shows strong wind gusts approaching Wales from the West at 14 UTC with maximum values slightly weaker than in previous panels but still above 46 m s^{-1} (89 kt). With the cyclone now in Stage IV of the Shapiro-Keyser model, these surface gusts are related to the CCB, almost completely encircling the cyclone centre. The last panel (Figure 4.6d) refers to 16 UTC and highlights the weakening of wind gusts occurring at this stage, with maximum values around 40 m s^{-1} (78 kt) in western Wales. The magnitude of maximum wind gusts shown in panels (c) and (d) of Figure 4.6 is consistent with the station recordings of Figure 4.5 (note that 1 m s^{-1} =1.94 kt, so maximum observed values around 80-85 kt have less than 10% discrepancy with maximum modelled values around 40 m s^{-1} (78 kt)).

4.2.4 Observations of Aberystwyth NERC MST Radar

The Mesosphere-Stratosphere-Troposphere radar wind profiler (Natural Environment Research Council, Aberystwyth Radar Facility [Hooper, D.], 2017) is located at Capel Dewi (52.42°N, 4.01°W) near Aberystwyth, Wales (see Figures 4.4a and 4.4b). This vertical profile of wind speed is located just south of the path followed by the cyclone centre. The recorded time series of wind speed vertical profile is shown in Fig. 4.7. This time series can be thought of as similar to a west to east cross section through the storm, with time displayed from right to left to facilitate interpretation, with the caveat that the storm was developing during this period. Nevertheless, many of the key features of the storm can be identified.

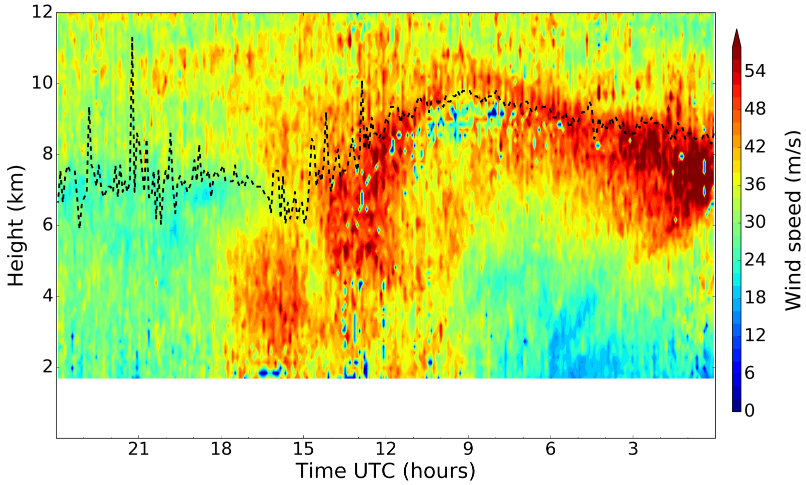

Figure 4.7: Time-height plot of Aberystwyth NERC MST Radar on 12 February 2014 showing Doppler wind speed. Black dashed line shows radar-derived tropopause altitude.

Figure 4.7 shows strong winds in the upper troposphere (the upper-level jet) in the first half of the day signalling the arrival of the weather system. From around 0900 UTC, a feature that is probably the warm conveyor belt (WCB) becomes evident. During the passage of the cold front, after around 1200 UTC, strong winds become widespread in the whole troposphere. There is also an indication of tropopause folding between 1400 and 1500 UTC, in the form of a weak-speed descending tongue. The maximum in wind speed at around 3–5 km height visible just after the frontal passage is suspected to be related to be a SJ (Graham Parton, personal communication). Its position compares well with the tip of the cloud head passing over the MST radar site and with the observed cloud striations and rain bands consistent with slantwise convection.

Figure 4.8 shows an equivalent time-height profile of wind speed from the limited-area simulation. Also shown are the θ_w isolines in the troposphere and the dynamical tropopause (defined as the height of the 2-PVU surface, where PVU stands for potential vorticity units [1]). Though the timing is perhaps an hour different, with the simulation ahead of the observations, the figure shows considerable correspondence with the observations, particularly in the passage of the cold front, indicated by a sharp decrease in θ_w

[1] 1 PVU $=10^{-6}$ m^2 s^{-1}K kg^{-1} . The 2-PVU surface is commonly considered as indicating the location of the dynamic tropopause (i.e. the tropopause defined using potential vorticity). This is because the tropopause separates the stratified stratosphere from the well-mixed troposphere, displaying a marked increase in static stability. This is reflected in a sharp increase in potential vorticity, resulting in the 2-PVU surface being located at the interface between the two atmospheric layers.

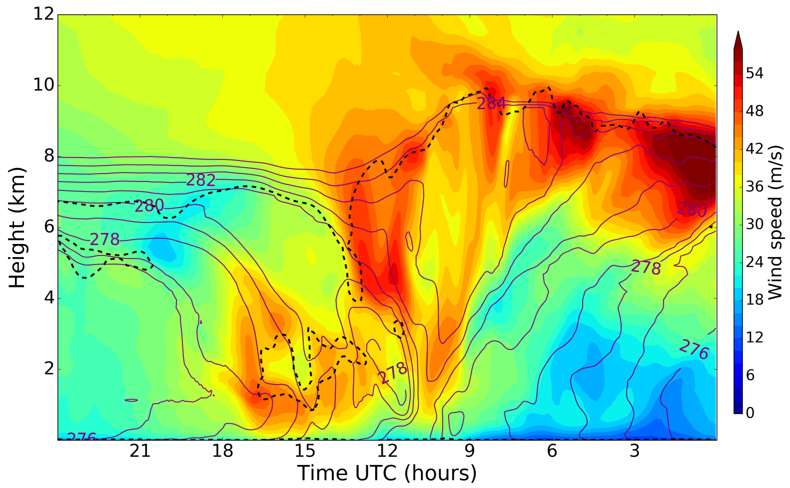

Figure 4.8: Simulated time-height plot of Aberystwyth Radar on 12 February showing wind speed (contours), wet-bulb potential temperature (purple solid lines, up to 285 K), and the height of 2PVU surface (black dashed line).

below 4 km height around 1200 UTC (in the model simulation), followed by tropopause folding associated with the fall of the 2-PVU tropopause down to 4 km height and with a weak-speed descending tongue. Comparing with horizontal plots from the model, it is possible to distinguish three different regions of low-level strong winds passing over the radar location. In time order, the first region visible in the plot, around 1000 UTC at around 2-4 km height associated with an extension down to the lower troposphere of the upper-level jet, is part of the WCB. It is located ahead of the cold front, with warm values of θ_w and with weak static stability above it. The last region, visible after 1500 UTC and characterised by values of θ_w cooler than 278 K, can be attributed to the cold conveyor belt (CCB). Between 1200–1500 UTC is a wind maximum below 3 km height characterised by θ_w ranging from 278 K to 280 K. The cold front passed at 1200 UTC and the bent-back front did not reach the Welsh coast before 1500 UTC, so this wind maximum was located in the frontal-fracture region and is attributable to the remnant of the already-descended SJ (given the appearance of bands in the cloud head around 8–10 hours earlier). Note that the modelled peak wind speed in this region seems to be in reasonably close agreement with the observations, peaking roughly in the range 45–50 m s^{-1}, even though, as shall be shown below, the peak modelled wind speed earlier (and slightly further south) approached 60 m s^{-1}.

A further region of strong winds is located above the CCB and characterised by SJ-like values of θ_w, visible around 3–4 km height between 1500-1700 UTC. The possibility of multiple SJ pulses in the storm cannot be ruled out (see similar arguments in terms of absolute vorticity analysis in Section 5.2.1). However, as a wind maximum reaching 45-50 $\mathrm{m\,s^{-1}}$ associated with this feature cannot be identified in the storm, a further investigation has not been performed, giving priority to other analyses.

4.2.5 Summary of the comparison between storm observations and model simulation

To summarise, the synoptic evolution and mesoscale structure of the limited-area simulation shows a strong, though not perfect, correspondence with the limited observations available. Even though the analysis of wind gusts suggests that maximum values inland are related to the CCB, both observations and simulations suggest the presence of a SJ in windstorm Tini. A more detailed analysis is necessary to assess if a SJ is actually present in the model simulation. This has been done in an Eulerian framework, investigating strong wind regions and θ_w patterns (Section 4.3), and in a Lagrangian sense, identifying a suspected SJ airstream (Section 4.4) and looking at its properties and evolution along trajectories (Section 4.5 and, with a specific focus on mechanisms driving SJ dynamics, Chapter 5).

4.3 Analysis of strong winds in windstorm Tini

The cyclone structure in the limited-area simulation at 0700 UTC, the time when the strongest winds occurred at 850 hPa and in which bands are visible at the cloud-head tip (cf. Fig 4.3), is presented in this section. Horizontal maps and a vertical cross section highlight the shape of the frontal-fracture region and the strong-winds pattern, which are shown as consistent with the occurrence of a SJ.

4.3.1 Earth-relative wind speed

The position of the fronts in the system is shown by moist isentropes (i.e. θ_w isolines) in Figure 4.9. The primary cold front is located south of it, orientated in a SW-NE direc-

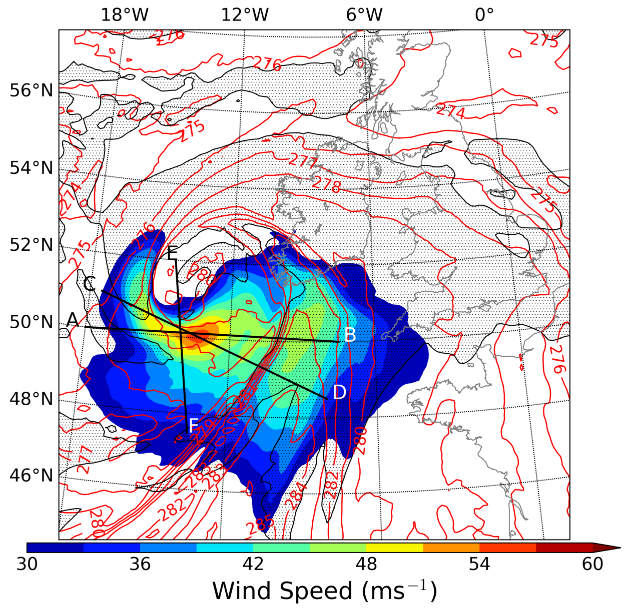

Figure 4.9: Model map of wind speed at 850 hPa (contours, m s^{-1}), wet-bulb potential temperature at 850 hPa (K, red lines) and cloudy regions at 700 hPa (RH>80%, black lines and dotted regions) at 0700 UTC on 12 February 2014.

tion and marking the western boundary of the warm-sector cloud. There are two warm fronts: a tight one is crossing the southern part of Ireland and there is also a clear gradient over Northern Ireland. The latter has the θ_w values of the bent-back front (compare with Figure 4.1). The bent-back front is evident to the west of the system, along with a warm seclusion represented by the 280-K contour; this seclusion is more clearly present at lower levels. The frontal-fracture region is indicated by an area of weak θ_w gradient, with the moist isentropes spreading out between the tip of the cloud head and the cold front. Comparing the location of these features with the pattern of strong winds, it is possible to identify the WCB on the eastern side of the cold front, centred around (9.5°W, 50° N), with winds reaching 48 m s^{-1} at 850 hPa. There is a much stronger wind maximum in the frontal-fracture region (13.5°W, 50° N), very focused and approaching 60 m s^{-1} that we identify as the SJ (see below in the rest of this section and chapter).

4.3.2 System-relative wind speed

As discussed in Section 4.2.1, Tini travels approximately eastward at an average speed of around 25 m s^{-1} during its deepening stages. Due to this rapid cyclone motion, wind

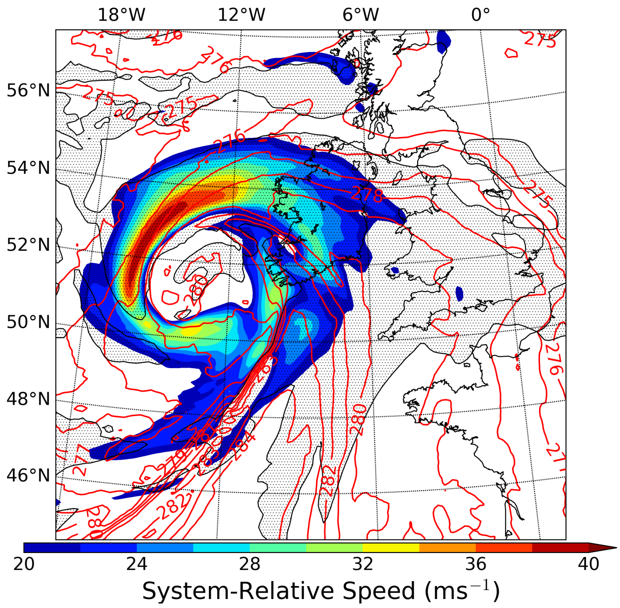

Figure 4.10: Same as 4.9 but with system-relative wind speed.

features like the CCB, mostly located on the northeastern side of the cyclone, are not evident in an Earth-relative frame of reference. System-relative wind speed is obtained subtracting this motion from the Earth-relative wind (Figure 4.10). The CCB is very clearly visible in this reference frame wrapping around the cyclone centre to its north and west and located inside the cloud-head region. The previously-identified wind maximum to the south of the system centre is clearly weaker in this reference frame, but also clearly distinct from the CCB. Given this distinction and its location, the wind maximum to the south of the system centre is tentatively identified as a SJ.

4.3.3 Vertical motion and cross sections

Figure 4.11 shows three cross section that pass through the possible SJ wind maximum and the frontal-fracture region in along-flow (Figures 4.11a and 4.11b) and across-flow (Figure 4.11c) directions. The transects of the sections are shown in Figure 4.9. There is a broad resemblance between the along-flow sections and Figure 4.8. Though the latter is not a strict cross section, as it is a fixed-space instead of a fixed-time section, the same general features can be identified.

All the three cross sections show the upper-level jet located between 300 hPa and

500 hPa, with its core exceeding 60 $\mathrm{m\,s^{-1}}$ at the edge of the warm-sector cloud. In the along-flow sections the WCB is visible underneath it on the warm side of the cold front, centred around 700 hPa and with winds exceeding 45 $\mathrm{m\,s^{-1}}$. The mid-level wind maximum close to 60 $\mathrm{m\,s^{-1}}$, located around 600 hPa in the along-flow sections, is possibly related to the dry-air intrusion. The leading edge of the CCB is visible below 800 hPa on the left side of Figure 4.11b, with θ_w-lines showing the separation between its 45 $\mathrm{m\,s^{-1}}$ peak winds and the warmer air in the frontal-fracture region. The intense wind maximum centred around 800 hPa in the frontal-fracture region in all cross-sections, identified as the SJ, reaches 60 $\mathrm{m\,s^{-1}}$, stronger than the maximum at mid levels and comparable with the upper-level jet.

A weaker wind maximum centred at 700 hPa, but contiguous with the lower maxima, may be a secondary SJ. However, there is no obvious connection from the SJ to the high-momentum air above. The jet is located just beneath some slanted isentropes (indicating weakly-descending flow on a broader scale in the region), in an area with very weak θ_w gradients, where isentropes have undergone folding or buckling, as Figures 4.11b and 4.11c show with particular clarity. It is also close to and 'downstream of' maxima of negative vertical velocity (based on the isentropic slope), particularly visible in Figure 4.11a. Note also two regions of slantwise descent (either side of the main cloud head) at the western end of Figure 4.11b, one above the CCB, the other to the west of it. The second band of cloud discussed above that wraps around the cyclone centre outside the CCB is evident in Figure 4.11a to the west of the SJ in a location outside the more western region of strong slantwise descent.

These cross sections are interpreted as indication that the wind maximum results from the acceleration of a jet (i.e. the SJ) descending out of the cloud head. In the next section, this is confirmed through the use of back trajectories.

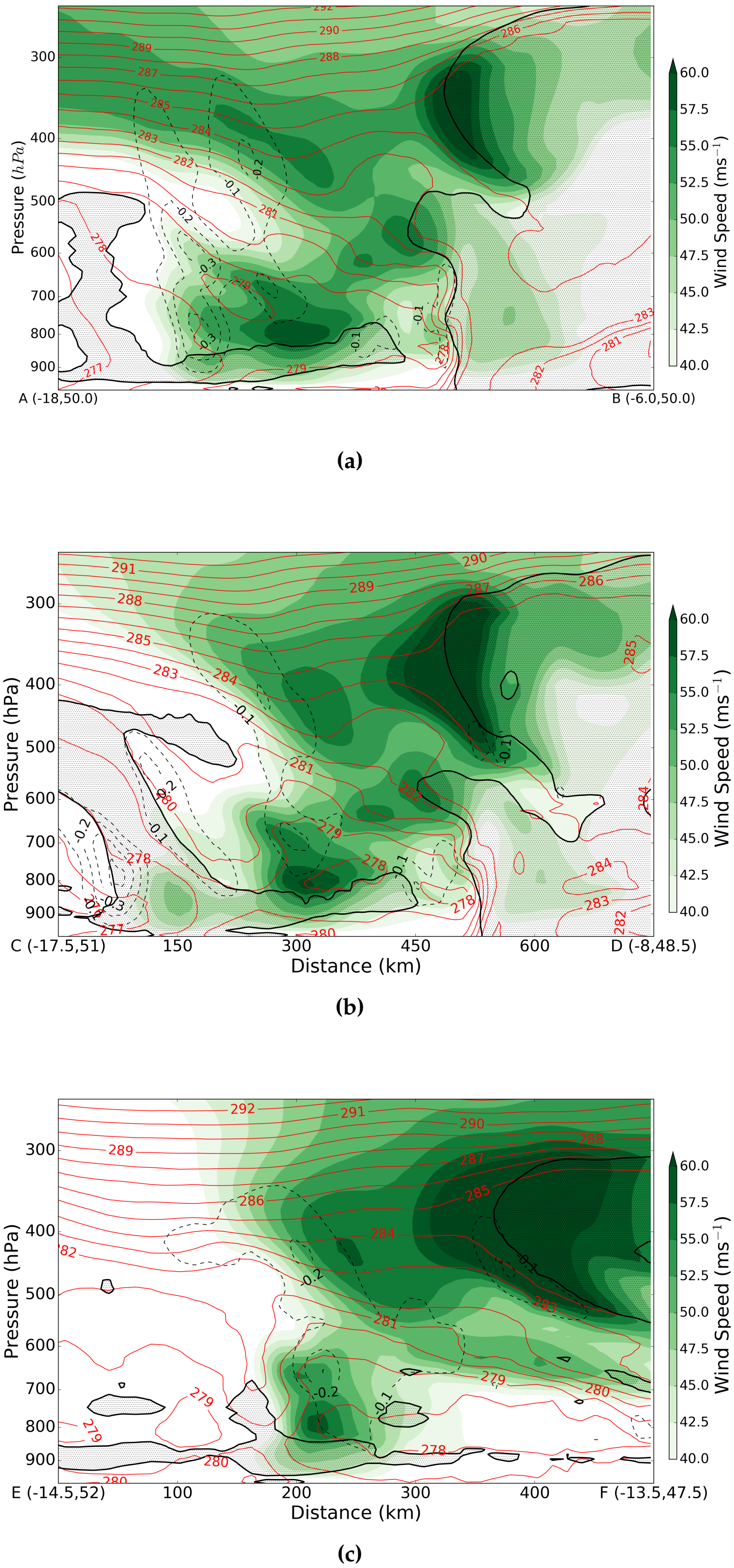

Figure 4.11: Model cross section (transects (a) AB, (b) CD and (c) EF in Figure 4.9 of wind speed (green filled contours,m s^{-1}), negative vertical velocity (dashed black lines, ms^{-1}), wet-bulb potential temperature (red lines, K) and cloudy regions (RH>80%, thick black lines) at 0700 UTC on 12 February 2014.

4.4 Lagrangian trajectories: identification and kinematics of the SJ and CCB airstreams

It is important to distinguish the SJ from the CCB and so Lagrangian trajectories have been used to follow the evolution of both. In this section the identification and kinematics of the airstreams are reviewed.

4.4.1 Sting jet

The grid points with wind speed exceeding 57 $\mathrm{m\,s^{-1}}$ at 0700 UTC located at 820 hPa or in contiguous levels (i.e. aligned vertically with the grid points selected at 820 hPa to form uninterrupted columns of points with speed exceeding the threshold) are selected as starting points for SJ trajectories. This methodology has been used to select a volume of trajectories belonging to the low-level wind maximum highlighted previously and to exclude any higher-level separate maxima. Trajectories from these selected points show strong descent, but with a variety of starting altitudes. At the core, however, is a substantial set of trajectories descending from above 650 hPa. To focus on this maximally descending core, the properties of the set of trajectories located at a pressure smaller than 650 hPa at 0200 UTC and descending by more than 100 hPa between 0400 and 0600 UTC are shown below. This selection does not qualitatively change the conclusions of this analysis, but it does make them clearer. The excluded trajectories appear to form the boundaries of the SJ and did not go through the whole process of descent. Figure 4.12 shows the path of the trajectories in earth-relative (a) and system-relative (b) reference frames. This path is described, along with the CCB one, in Section 4.4.3.

4.4.2 Cold conveyor belt

Starting points for CCB trajectories have been selected with the same methodology considering a threshold of 51 $\mathrm{m\,s^{-1}}$ centred at 820 hPa and evaluated at 1000 UTC, when the leading edge of CCB airstream is oriented in the same direction as the storm motion. In this later stage of the storm evolution, the strongest low-levels winds belong to the CCB and there is no longer an indication of a SJ. Figure 4.13 shows the path of the trajectories

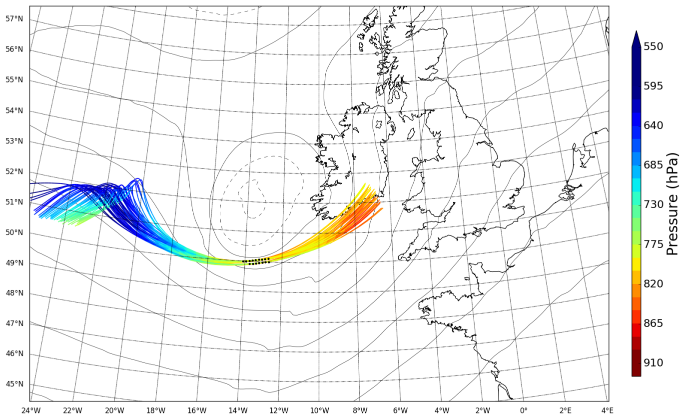

(a)

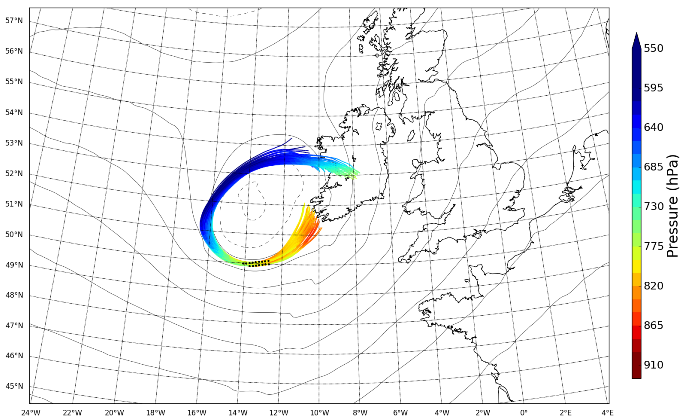

(b)

Figure 4.12: Model map of SJ trajectories in earth-relative (a) and system-relative (b) reference frames. Starting points are identified at 07 UTC on 12 February 2014 as indicated in the text and represented with black dots. Trajectories are computed backward to 19 UTC on 11 February and forward to 10 UTC on 12 February. Colours indicate the instantaneous pressure values for each trajectory. Black lines indicate geopotential height (contours every 50 m, dashed if negative) at 970 hPa at 07 UTC.

in earth-relative (a) and system-relative (b) reference frames.

4.4.3 Kinematics of the airstreams

Figure 4.14 shows a 3D visualisation of trajectories related to the SJ and CCB for 9 hours during the most intense phase of evolution of the storm. It shows that the SJ and CCB airstreams represent different air masses, each one undergoing its own evolution. The

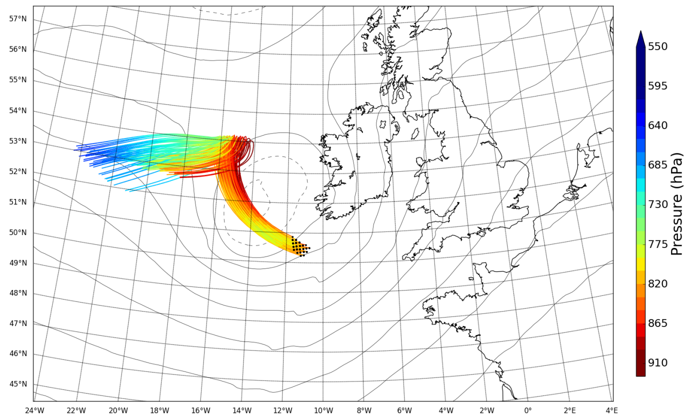

(a)

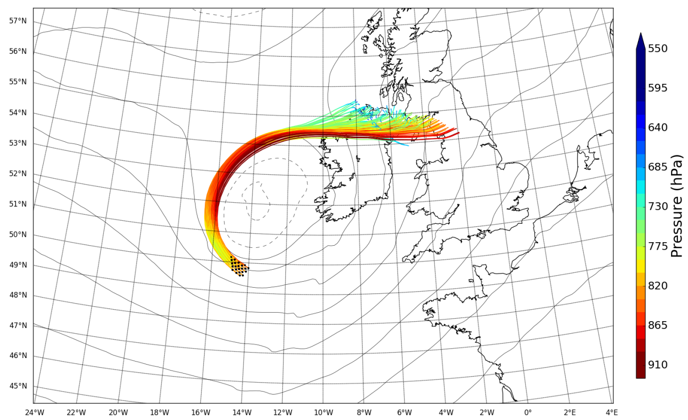

(b)

Figure 4.13: Same as Figure 4.12 but for the CCB. Starting points are identified at 10 UTC on 12 February and trajectories are computed backward to 19 UTC on 11 February. Black lines indicate geopotential height (contours every 50 m, dashed if negative) at 970 hPa at 07 UTC.

CCB stays at low levels and increases its RH_{ice} gradually, eventually becoming saturated while wrapping around the cyclone centre beneath the cloud head. The SJ trajectories instead start at about 700–800 hPa in the northern sector of the storm, enter into the cloud head rising up to 600 hPa, and later exit from its tip descending into the frontal-fracture region and drying out. Thus, the SJ is not an appendix of the CCB or its foremost part: the two airstreams are distinct and originate and evolve in two clearly different ways, as first described by Clark et al. (2005). In the rest of this Chapter the focus is on the SJ airstream, characterised by analysing time series of relevant physical quantities along its trajectories.

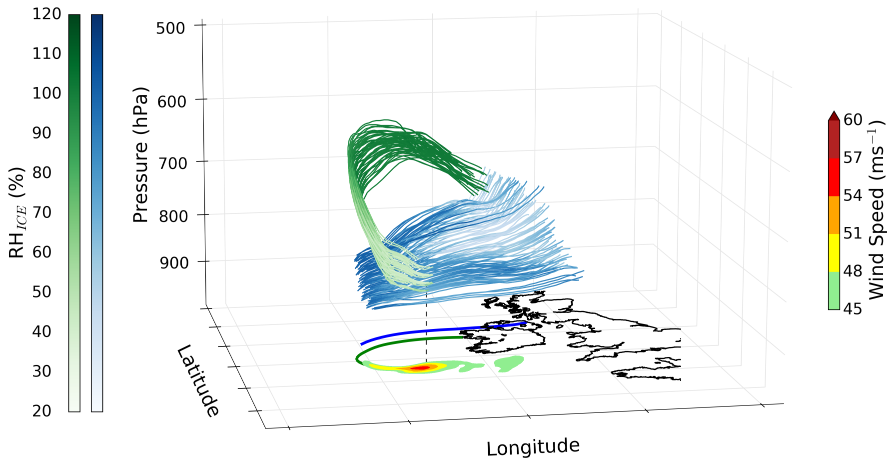

Figure 4.14: Model 3D (lon-lat-pressure) view of SJ (green) and CCB (blue) airstreams from model simulations of Windstorm Tini in a system-relative reference frame (trajectories from to 2200 UTC on 11 February to 0700 UTC on 12 February 2014). Solid lines indicate the surface projection of the median trajectory for each of the airstreams. Earth-relative wind speed at 850 hPa (shading, m s^{-1}) at 0700 UTC (same as Figure 4.9 but only for wind speed above 45 m s^{-1}) is included in the figure.

4.5 Characterisation of the SJ airstream

In this section the SJ airstream is characterised by looking at the evolution of various physical quantities along its trajectories. The accuracy of trajectories is also evaluated. This investigation gives information on the evolution of the airstream and starts to clarify its dynamics, although a more focused analysis of the evolution of mesoscale instabilities along trajectories (the main focus of Chapter 5) is necessary to get a comprehensive picture of the SJ evolution.

4.5.1 Evolution of physical quantities along trajectories

Figures 4.15 and 4.16 show the evolution of various physical quantities along the SJ-core trajectories identified as described above. Figure 4.15a shows the SJ undergoing a steady increase in Earth-relative speed, from $\lesssim$10 m s^{-1} at 0100 UTC to reaching up to 60 m s^{-1} at 0700 UTC. Part of this increase in speed is consistent with the fact that the airstream is rotating around the cyclone centre, moving eventually in the same direction of the overall motion of the storm (as previously said, Tini is moving at about 25 m s^{-1}). However, even in a system-relative reference frame, there is an increase in wind speed of about 15 $\mathrm{m\,s^{-1}}$ between 0500 and 0700 UTC (Figure 4.15b).

The descent of the SJ starts from about 650–600 hPa at around 0100–0300 UTC, but the bulk of the descent is between 0300 UTC and 0700 UTC (Figure 4.15c) with a descent of around 150 hPa in 3 hours. The descent is accompanied by a decrease in θ of about 1.5 K in total (Figure 4.16b) — mainly because the air becomes sub-saturated during the early part of the descent (0300–0500 UTC). Hence, the increase in pressure results in a temperature increase of more than 15 K (not shown) and a consequent dramatic drop in RH_{ice} to around 40%. Nevertheless, the temperature stays well below zero during all the stages prior SJ descent (not shown). For this reason all relative humidities quoted are with respect to ice.

The decrease in θ during the first part of the descent shown in Figure 4.16b (from 0300–0500 UTC) is accompanied by an increase in specific humidity (Figure 4.16a) and can be attributed to evaporative cooling, primarily of condensate in the initial cloud as confirmed by the decrease in cloud ice (particularly) and liquid water observed just above the jet. Panels in Figure 4.17 show the values of cloud ice at the pressure level that is immediately above the mean pressure of trajectories in the airstream. At 04 UTC (Figure 4.17a) the SJ is traveling just underneath the edge of a region with high values of cloud ice, moving towards the tip of the cloud head. At 05 UTC (Figure 4.17b) the SJ is about to exit from the cloud head and at at the same time is still located at the edge of the high cloud-ice values, now extending towards the cloud-head tip with a narrow tongue. The transport of cloud ice in an area of prevailing weakly-negative vertical motions (see Section 4.3.3, whose arguments are valid also at 04–05 UTC for the cloud-head-tip region) and the sharp decrease of cloud-ice values just above the location of the SJ are consistent with the hypothesis of sublimation into the jet. Cloud liquid water (not shown) shows a similar evolution, although in a less evident way and with smaller absolute values.

The second part of the descent (after 0500—0530 UTC up to 0700 UTC), i.e. the most rapid part with the strongest system-relative wind speed increase, is instead characterised by almost constant θ and specific humidity. Hence, evaporative cooling did contribute to the initiation of descent by decreasing the buoyancy of the SJ air, but it did not contribute to the large final acceleration of the airstream.

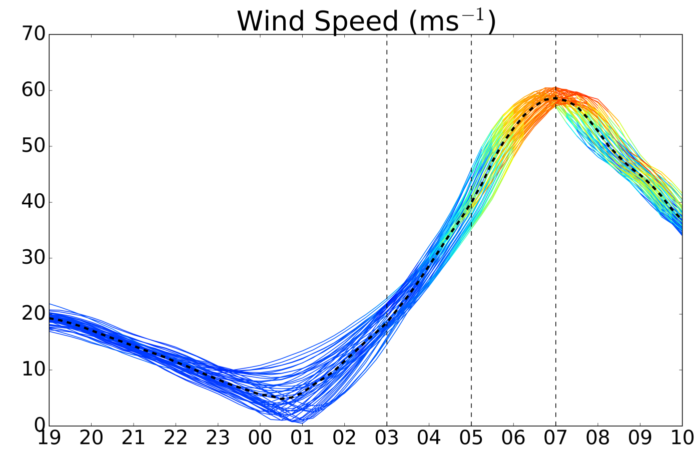

(a)

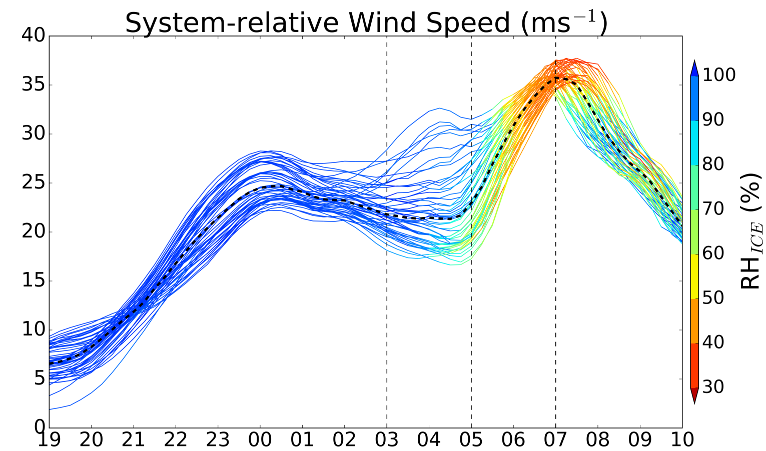

(b)

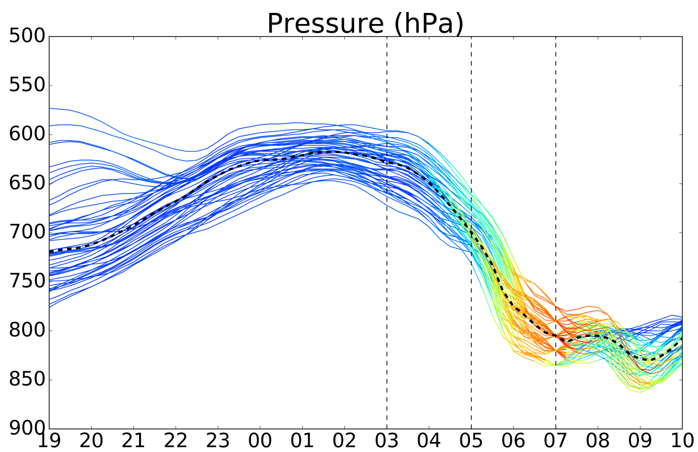

(c)

Figure 4.15: Model timeseries (UTC) of (a) wind speed, (b) system-relative wind speed and (c) pressure along SJ trajectories. Colours indicate relative humidity with respect to ice along trajectories and the dashed line indicates the median of trajectories.

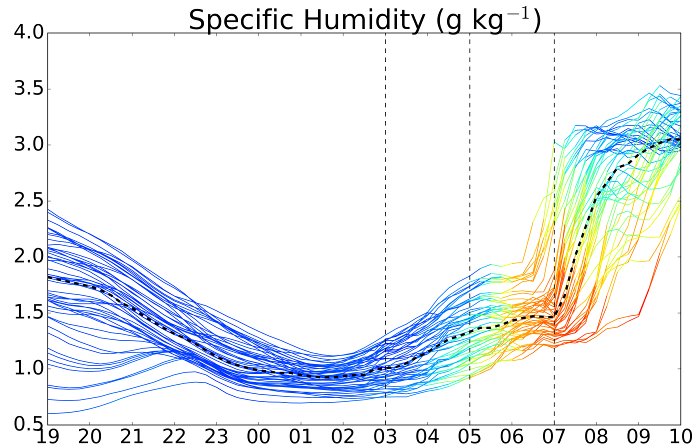

(a)

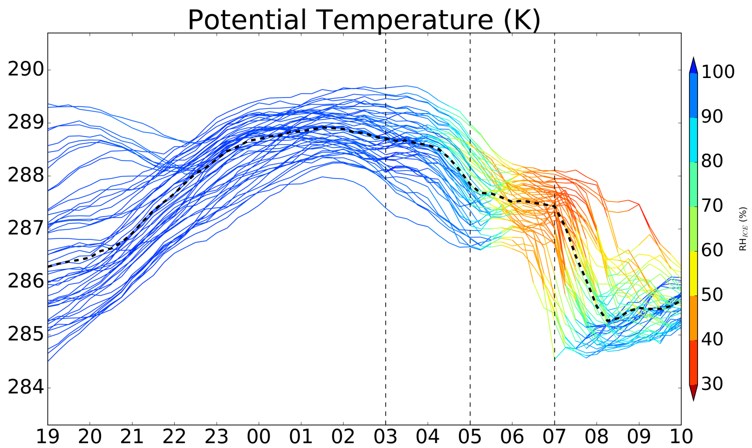

(b)

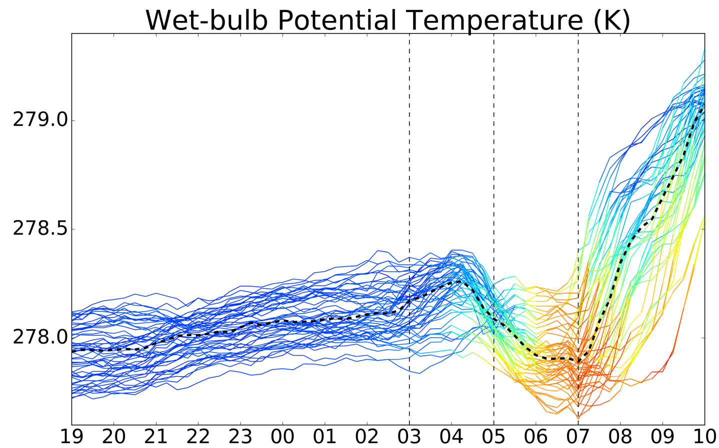

(c)

Figure 4.16: Model timeseries (UTC) of (a) specific humidity, (b) potential temperature and (c) wet-bulb potential temperature along SJ trajectories. Colours indicate relative humidity with respect to ice along trajectories and the dashed line indicates the median of trajectories.

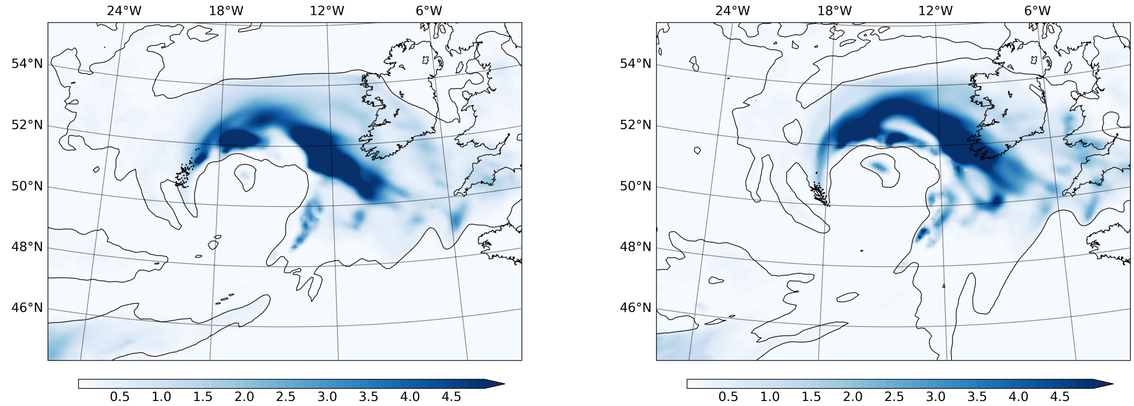

(a) (b)

Figure 4.17: Maps of model cloud ice (blue shading, 10^{-4} Kg/Kg, ice water content of the air expressed as the non-dimensional ratio of the mass of ice per unit volume to the mass of moist air, plus any condensate, per unit volume) and of cloudy regions (RH>80%, black lines). Black dots indicate the instantaneous location of SJ trajectories. Panel (a) refers to 04 UTC on 12 February 2014, cloud ice is evaluated on model level 30 (first model level above the mean pressure value of trajectory points at the time) and cloudy regions are evaluated at 655 hPa, the closest pressure level to the mean pressure value of trajectory points. Panel (b) refers to 05 UTC on 12 February 2014, cloud ice is evaluated on model level 27 and cloudy regions are evaluated at 700 hPa.

Wet-bulb potential temperature is conserved in both dry and moist adiabatic flows. However, ice processes (i.e. freezing, melting, deposition and sublimation) contribute an additional latent heat and so can change θ_w (since θ_w is referred to liquid water). The time variations in θ_w are small, much smaller than those in θ, and hence difficult to evaluate reliably given possible errors in the trajectories (compare Figure 4.16b and Figure 4.16c). The gradual increase in θ_w prior to about 0400 UTC), resulting in a total increase of less than 0.2 K, could well be the result of trajectory error, since the trajectories exist in a region of steep θ_w gradient. However, the rapid decline in θ_w during descent from 0400–0600 UTC (still amounting to only about 0.3 K) is consistent with a contribution from sublimation or melting of ice.

Furthermore, the behaviour of precipitation-caused temperature increments computed by the model is in good agreement with θ_w variations, showing the same pattern of increase before 0400 UTC and decrease after. In particular, Figure 4.18a shows that at 03 UTC the SJ is located at the edge of a region with positive values of large-scale-precipitation temperature increments. At 05 UTC (Figure 4.18b) the jet is instead in a narrow region of negative values of temperature increments. This region, as wide as the trajectory bundle and slightly extended behind it, can be seen starting to develop behind the jet at 03 UTC, consistent with an influence on the SJ around 04–06 UTC. This suggests a cooling due to evaporation in the SJ area of precipitation falling from above. Contributions from radiation and other diabatic processes are instead negligible (not shown), confirming that the change in θ_w can be mainly associated with sublimation and melting processes.

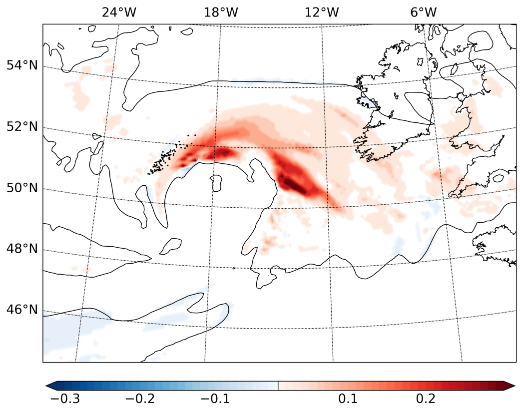

(a)

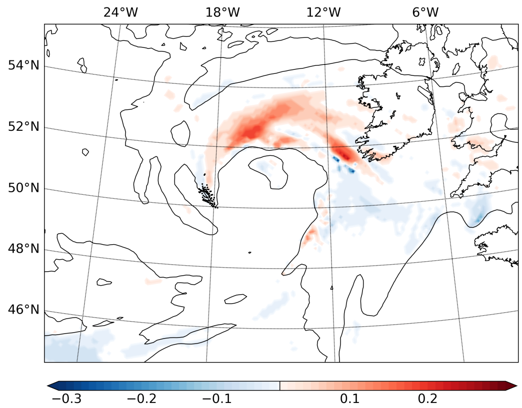

(b)

Figure 4.18: Maps of model large-scale precipitation temperature increment (shading, K, gridbox mean change in temperature solely as a result of the large-scale precipitation scheme) and of cloudy regions (RH>80%, black lines). Black dots indicate the instantaneous location of SJ trajectories. Panel (a) refers to 03 UTC on 12 February 2014, the temperature increment is evaluated on model level 30 (closest pressure level to the mean pressure value of trajectory points at the time) and cloudy regions are evaluated at 640 hPa, the closest pressure level to the mean pressure value of trajectory points. Panel (b) refers to 05 UTC on 12 February 2014, the temperature increment is evaluated on model level 26 and cloudy regions are evaluated at 700 hPa.

The size and nature of the variations in θ_w give us confidence that the trajectories are accurate enough for this study. The conservation properties were notably worse along trajectories derived using hourly model output, with variations of θ_w up to 2–3 K occurring during the SJ descent; this motivated the use of 15-minute model output (see Section 3.4).

At the end of the descent (i.e. after 0700 UTC) the SJ reaches the top of the boundary layer and interacts with it. The speed on trajectories rapidly decreases, while θ_w increases abruptly by a few K. Shallow convection is visible in the simulated satellite imagery at this time, in the form of an arc-chevron cloud which may be related to the cloud patterns discussed by Browning and Field (2004). Of course, it is difficult to rely on the properties of trajectories undergoing such marked turbulent mixing, as they no longer represent a coherent airstream. This difficulty does not affect our study as we are primarily interested in the dynamics of generation and strengthening of the SJ and not in its interaction with the boundary layer after the descent, but it is worth noting that interaction with the boundary layer is clearly occurring after 0700 UTC.

To summarise, the set of trajectories traced back from the 850-hPa wind maximum satisfies the criteria required to identify this airflow as a SJ. The trajectories originated at mid levels (650–600 hPa) inside the cloud head and descended rapidly (150 hPa in 3 h). They started out saturated, but adiabatic warming led to drying; a θ decrease during the first part of the descent is attributed to evaporative (and sublimation) cooling. During the final 2 h of descent, the trajectories experienced an increase in system-relative wind speed of about 15 $\mathrm{m\,s^{-1}}$.

Chapter 5

Case study of Windstorm Tini: linking the Sting Jet with mesoscale instabilities

In this chapter the analysis of windstorm Tini continues, with particular focus on the evolution of instabilities along the jet. A summary of the results of this case study is present at the end of the chapter.

5.1 Evolution of instabilities along trajectories

The evolution of mesoscale instabilities on the airstream identified as a SJ is performed to help test the hypothesis that the release of those instabilities has a role in driving descent and acceleration of that SJ. For this purpose, the method outlined in Martínez-Alvarado et al. (2014a) is followed (see Section 3.5 for details).

5.1.1 Conditional Symmetric Instability

Figure 5.1 shows the time-pressure profile of the airstream overlaid on bars representing the percentage of trajectories unstable to different instabilities at each time. In the hours prior the SJ descent, while the air is saturated within the cloud head, there is a steady build-up of CSI in the airstream. This process continues until nearly 0400 UTC when >80% of the trajectories are labelled as unstable to CSI. This result is consistent with the

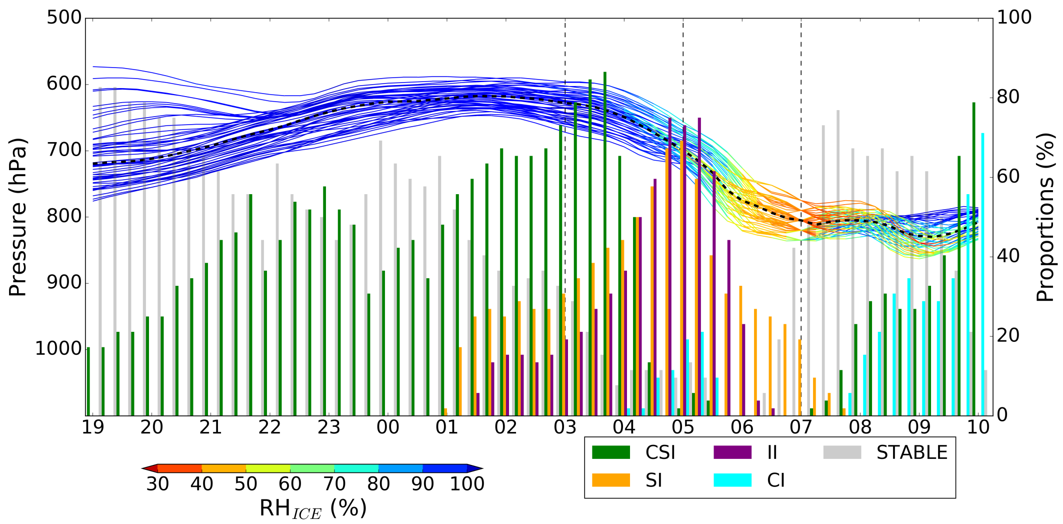

Figure 5.1: Model Timeseries (UTC) of pressure (colours indicate RH$_{ice}$) and diagnosis of instability conditions along SJ trajectories. The vertical bars indicate the fraction (proportion) of trajectories that are unstable to the different instabilities mentioned in the key table at the bottom of the figure and evaluated every 15 minutes (see Table 3.1 for the instability criteria).

findings of previous studies (Gray et al., 2011; Martínez-Alvarado et al., 2014a; Baker et al., 2014). As the descent begins, the number of CSI-unstable trajectories suddenly drops, primarily because the associated RH decreases to less than the threshold needed to label them as 'CSI'. In other words, while still perhaps conditionally unstable, the air is no longer actually unstable because it does not meet the saturation condition. Thus, while CSI release may be associated with the initial descent, it cannot explain the subsequent continued descent and acceleration when the airstream is outside the cloud head in a unsaturated environment.

5.1.2 Dry mesoscale instabilities

However, Fig. 5.1 also shows a rapid build-up of mainly dry mesoscale instabilities (i.e. SI and II, but with an additional relatively small contribution from CI) that lags the build-up of CSI by a few hours and reaches its maximum level at 0500 UTC, i.e. when the SJ descends more rapidly and strong acceleration starts to occur (after the initiation of descent related to the slight decrease in θ_w). A sudden drop in the number of unstable trajectories occurs during the descent, most of them changing to stable conditions by 0700 UTC, i.e. by the end of the SJ descent. II and SI are dry instabilities that do not need a saturated environment to be released and so can be released even when the airstream is out of the cloud head. Deformation of the saturated θ_w surfaces by the descending jet can create CI. Thus, the evolution of mesoscale instabilities appears to be closely related to the SJ descent and acceleration.

Tracing of individual trajectories shows that the trajectories that initially become unstable to CSI are the same as those that become unstable to SI and II (not shown), suggesting the occurrence of a single process of destabilisation and subsequent release of mesoscale instability within the airstream. This behaviour implies rapid changes of PV (as SI is associated with PV< 0), with PV becoming increasingly negative and then positive again in many of the trajectories between 0300 and 0700 UTC. Though mixing could possibly contribute to the decrease in PV, strong diabatic processes are clearly occurring in the cloud head. Mixing (parametrized or numerical) probably contributes to the increase to positive PV values (stable conditions) once the airstream reaches low levels.

5.1.3 Brief description of evolution of instabilities in the CCB airstream

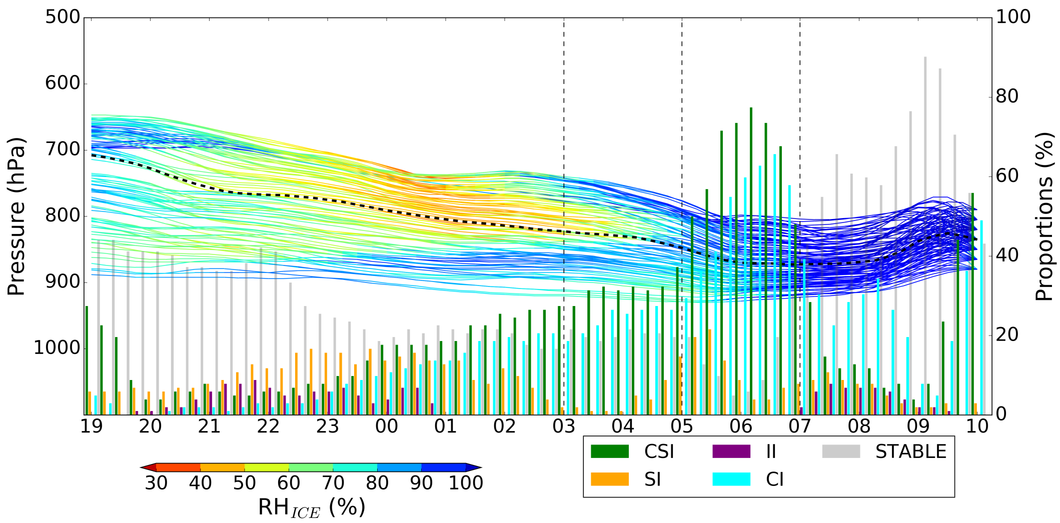

Figure 5.2: Same as Figure 5.1 but for the CCB airstream.

The same diagnostic is used in Figure 5.2 to assess the evolution of mesoscale instabilities, if present, on the CCB (identified as explained in Section 4.4). As mentioned in Section 4.3.2 the CCB trajectories stay between 700 hPa and 900 hPa for most of their lifetime, with the airstream gradually increasing its relative humidity while travelling underneath the cloud head and wrapping around the cyclone centre, descending very slowly and becoming eventually saturated.

Figure 5.2 shows that during the first stages of its evolution only a small portion of the trajectories composing the CCB airstream are unstable. Between 00 UTC and 05 UTC there is a slow increase of the number of unstable trajectories that becomes much larger at 05 UTC, with most of the instability then released or removed by 07 UTC. The plot indicates the instability can be labelled mainly as CSI and CI. It should be noted that in this analysis instabilities are not considered mutually exclusive. However, an analysis of timescales of slantwise and upright convection suggests that CI should have priority over CSI when both instabilities are indicated (see Schultz and Schumacher (1999)). Hence, Figure 5.2 is indicating the possible occurrence of upright convection around 06–07 UTC on the CCB. A steady decrease of potential temperature takes place on the airstream between 03 UTC and 07 UTC (not shown). Being associated with the increase in relative - and specific - humidity, this decrease in θ indicates the occurrence of evaporative cooling, now that the CCB is travelling underneath the foremost part of the cloud-head, getting closer to the frontal fracture where descending motions prevail. At the same time the SJ descends from the tip of the cloud head towards the frontal fracture and this is likely favouring additional mixing and thus to influence the stability of the boundary layer underneath and behind it, where the CCB is (see previous studies in Section 2.4). Wet-bulb potential temperature shows an increase that cannot be neglected from 06 UTC onwards, indicating the presence of mixing between the CCB air with other air masses and reinforcing the hypothesis of the occurrence of shallow convection.

To summarise, the evolution of the CCB is remarkably different from the SJ's one. The CCB evolves as a mainly stable airstream for large part of its lifetime, showing little vertical motions. However, some shallow convection looks likely to have occurred around 06 UTC, probably favoured by evaporative cooling and by additional mixing in the area. It is beyond the scope of this analysis to assess the effects of the convection on the CCB strength. In any case, a relationship between the SJ (through the additional mixing in the boundary layer caused by its descent and acceleration) and the evolution of the CCB has to be considered possible.

5.2 Mechanisms generating instabilities and connection with the SJ evolution

The focus of this analysis is on the instabilities that occur on the SJ airstream during its evolution. In this section, mechanisms generating these instabilities are assessed.

5.2.1 Vorticity structure

The condition used to label a trajectory as 'II-unstable' is a negative vertical component of absolute vorticity ζ_z on pressure surfaces, while the condition to label it as 'SI-unstable' is negative PV. Since static instability would rapidly lead to vertical mixing by the turbulence scheme, the behaviours of ζ_z and PV in the airstream are very similar. Figures 5.3 and 5.4 show the horizontal and vertical patterns of ζ_z at two different times during the evolution of the SJ.

Figure 5.3a shows ζ_z at 640 hPa and 0300 UTC. This is the pressure level where the SJ airstream was mainly located at this time and the time of the start of the SJ descent. The SJ cluster of trajectories (shown by black dots) is very small, around 40 km wide, reinforcing previous research showing that high resolution is needed to represent the flow. Also, the trajectories are mainly confined to a small area of negative ζ_z just outside the main cyclonic branch of the system. Figure 5.3b shows that this negative ζ_z region is located between 278–279-K θ_w contours, which have a gentle slope in the along-flow direction. A cross section in the across-flow direction (Figure 5.3c) similarly shows the SJ located on one side of the negative ζ_z region. Two hours later (Figure 5.4a) the SJ has descended to 700 hPa. The SJ remains located in the small region of negative ζ_z, which is now more focused and intense (and still located between 278–279-K θ_w contours, which are now much more sloped along the flow (Figure 5.4b).

The along-flow cross sections shown in Figures 5.3b and 5.4b show that the band of negative ζ_z is very narrow, forming part of a banded structure with strong positive ζ_z above and a second positive ζ_z band below that develops as the whole structure intensifies and becomes more slanted with time. Hence, the region with negative ζ_z travels with the SJ towards the tip of the cloud head, intensifying while retaining its shape and extension while at the same time descending and becoming more slanted. Moist isentropes simultaneously acquire a substantial slope along the flow (which is still within the 80%RH_{ice} contour). The across-flow cross sections (5.3c and 5.4c) show that θ-lines are also slanted in a radial direction. The band of negative ζ_z is located on the cold side of a frontal zone (bent-back front) and the buckling of θ_w-lines is developing at 0500 UTC just below this region (and hence just below the SJ).

These figures suggest that the growth of instability already highlighted in Figure 5.1 is a process taking place along the jet, in a Lagrangian sense.

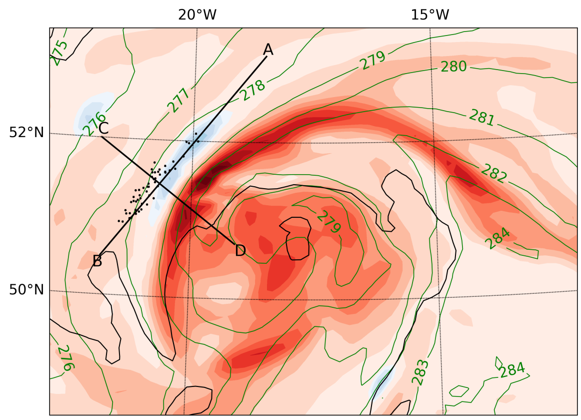

(a)

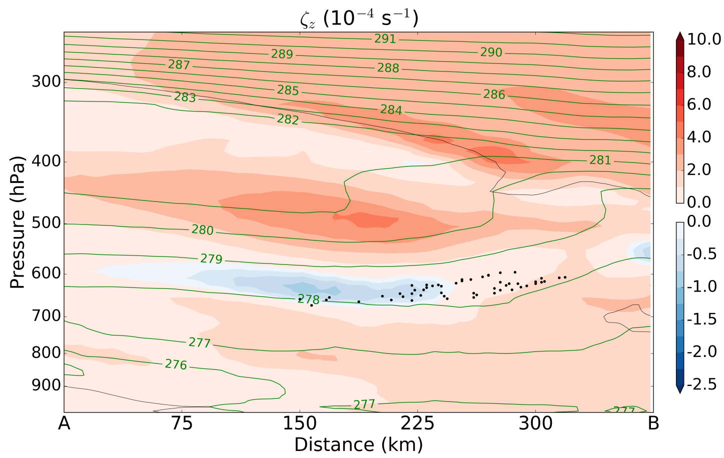

(b)

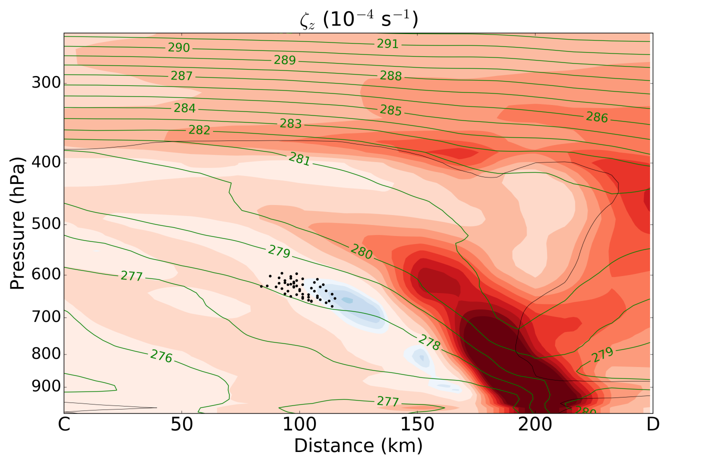

(c)

Figure 5.3: Model maps of (a): ζ_z (shading, $\times 10^{-4}\text{s}^{-1}$), θ_w (green contours, K) and cloudy regions at 640 hPa (RH$_{ice}$ =80%, black contours). (b,c): Same fields as in (a), but shown on cross sections (transect AB and CD respectively in panel (a)). All panels refer to 0300 UTC on 12 February 2014. The dots in (a) show the locations of the SJ trajectories; in (b) and (c) dots show the perpendicular projection of SJ trajectories onto the transects.

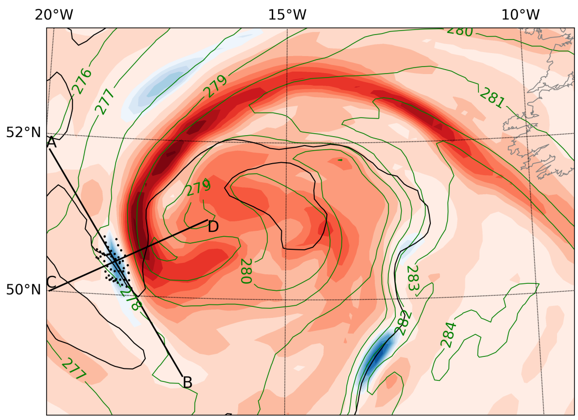

(a)

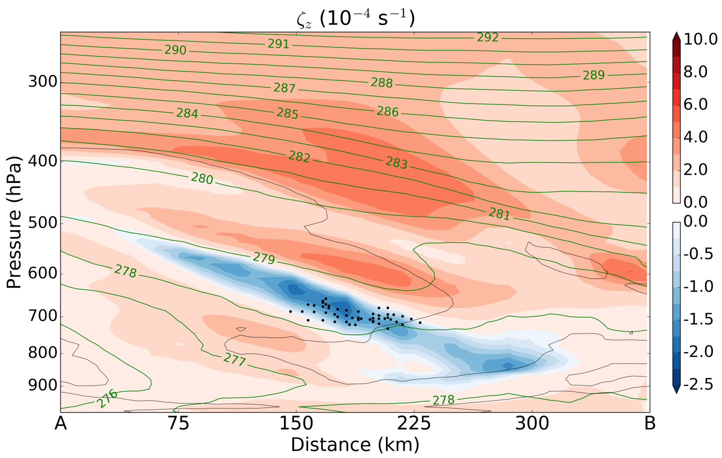

(b)

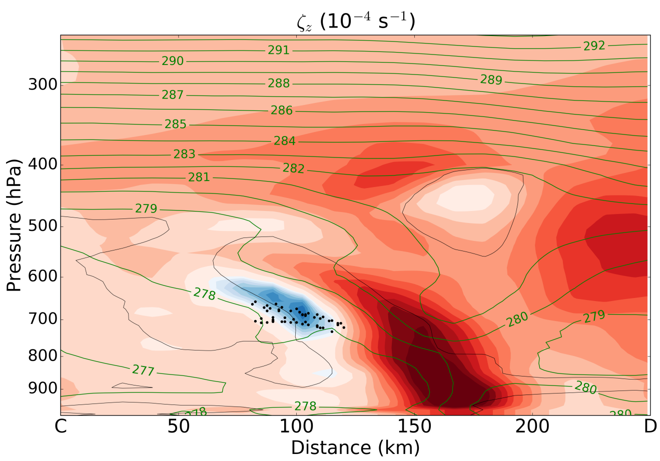

(c)

Figure 5.4: Model maps of (a): ζ_z (shading, $\times 10^{-4}$s^{-1}), θ_w (green contours, K) and cloudy regions at 700 hPa (RH$_{ice}$ =80%, black contours). (b,c): Same fields as in (a), but shown on cross sections (transect AB and CD respectively in panel (a)). All panels refer to 0500 UTC on 12 February 2014. The dots in (a) show the locations of the simulated SJ trajectories; in (b) and (c) dots show the perpendicular projection of SJ trajectories onto the transects.

5.2.2 Analysis of the vorticity equation

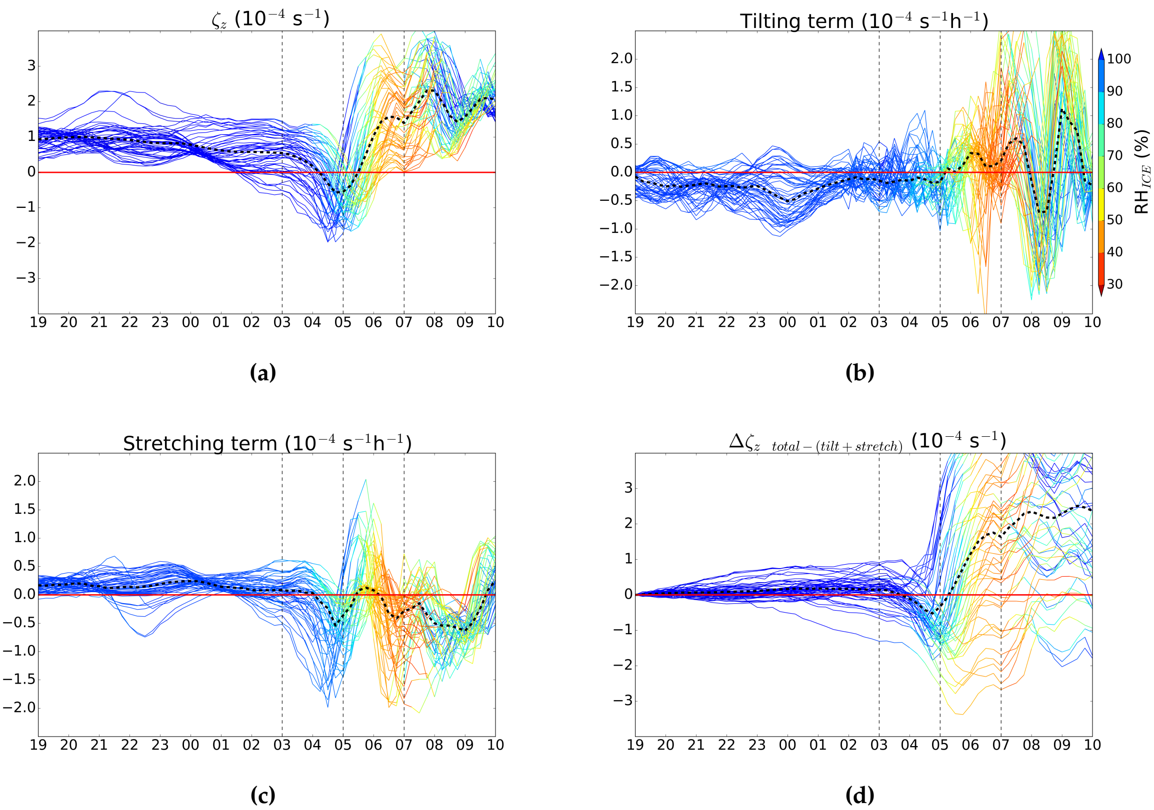

Figure 5.5: Model timeseries (UTC on 12 February 2014) along SJ trajectories of (a) vertical component of absolute vorticity ζ_z, (b) tilting term in vorticity equation, (c) stretching term in vorticity equation, (d) difference integrated over time between variations in ζ_z and the sum of tilting and stretching terms in vorticity equation: $\Delta\zeta_{z\ total-(tilt+stretch)}(\mathrm{t}_1) = \zeta_z(\mathrm{t}_1) - \zeta_z(\mathrm{t}_0) - \int_{t_0}^{t_1}(\mathrm{tilting}(\mathrm{t}) + \mathrm{stretching}(\mathrm{t}))\,\mathrm{dt}$.
Colours indicate RH$_{ice}$ along trajectories.

An analysis of the vorticity evolution equation has been performed along the trajectories and contributions of single terms to the overall changes in vorticity have been isolated to understand how the negative ζ_z values occurred. The vorticity equation on pressure levels is (Holton, 2004)

$$\frac{\partial\xi_z}{\partial t} + \mathbf{V}\cdot\nabla\zeta_z + \omega\frac{\partial\xi_z}{\partial p} = \mathbf{k}\cdot(\frac{\partial\mathbf{V}}{\partial p}\times\nabla\omega) - \zeta_z(\nabla\cdot\mathbf{V}) + \mathrm{friction}, \tag{5.1}$$

where ξ_z is the vertical component of relative vorticity. The first two terms on the right-hand-side are, respectively, the tilting and stretching terms. In our analysis we consider the z-components to investigate the evolution of ζ_z. As we are evaluating all the terms on the trajectories, and so in a Lagrangian reference frame, the advection term should not be

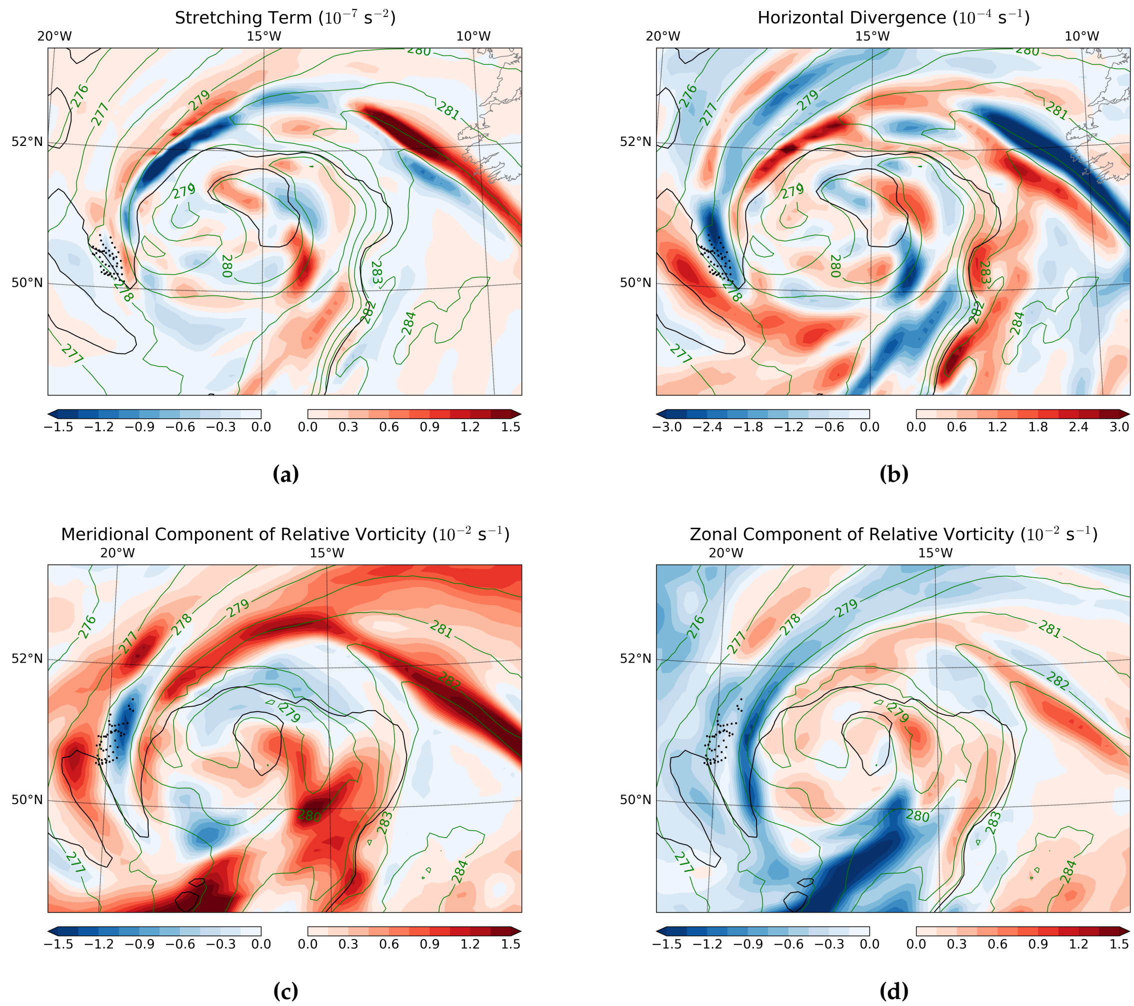

Figure 5.6: (a): Model map of stretching term in the vorticity equation (shaded), θ (green contours, K) and cloudy regions at 700 hPa (RH_{ice} =80%, black contour) at 0500 UTC. (b): same as (a) but for horizontal divergence. (c),(d): same as (a) but for meridional (c) and zonal (d) components of relative vorticity and at 655 hPa at 0400 UTC. Black dots show the locations of the SJ trajectories.

considered. So, the only terms that can contribute to changes in ζ_z are tilting, stretching and friction.

Figure 5.5a shows a time series of ζ_z on the SJ trajectories. In the first hours the value of ζ_z is very close to 10^{-4} s^{-1}, i.e. the value of planetary vorticity in mid-latitudes, indicating a very small ξ_z. A rather steady decrease in ζ_z occurs after 2300 UTC, with the majority of trajectories developing negative values around 0400–0500 UTC, implying II at the beginning of the SJ descent. After 0500 UTC, i.e. during the second part of the descent, a strong and sudden increase of ζ_z brings values well above zero, back to inertial stability.

Figure 5.5b shows that values of the tilting term are mainly negative around 0000 UTC, contributing to the initial decrease of ζ_z towards zero. During the following hours and up to 0500 UTC the values of the tilting term remain negative, although closer to zero, for many of the SJ trajectories. Figure 5.5c shows the stretching term is mostly negative between 0300–0500 UTC, the time when ζ_z becomes negative in the strongly descending SJ airstream. Figure 5.5d shows the difference between ζ_z and the increments due to the time integration of only the tilting and stretching terms. This time series demonstrates that tilting and stretching are causing much of the variations in ζ_z until the start of the descent, with values of $\Delta\zeta_{z\ total-(tilt+stretch)}$ close to zero. This result implies that the contribution of the frictional term is negligible prior to this time. After 0400 UTC, part of the decrease in ζ_z on some trajectories is not accounted for by the tilting and stretching terms. After 0500 UTC, most significantly, all the trajectories show a strong increase in ζ_z that is not accounted for by the tilting and stretching terms.

Figure 5.1 shows the steady increase in the number of trajectories with negative ζ_z between 0300–0500 UTC, with Figs. 5.3a and 5.4a highlighting that this is associated with an intensification of a localised region of negative ζ_z along the SJ airstream. During this stage the stretching term is negative for the trajectories that already have a negative ζ_z (not shown). This implies negative values of horizontal divergence on these trajectories (see Equation 5.1). Horizontal convergence indeed occurs on a growing number of trajectories at this time. Figures 5.6a and 5.6b show that stretching term and horizontal divergence are negative for almost the whole jet at 0500 UTC. As a result, the negative stretching term amplifies the magnitude of ζ_z on the trajectories whose values of ζ_z had already been brought below zero by the tilting term (i.e. the majority of the jet by 0400–0500 UTC). Figures 5.6c and 5.6c show that horizontal vorticity is negative, both in its zonal and meridional components, on almost the entire jet at 0400 UTC. This is associated with a direct circulation occurring on the slantwise frontal zone along which the SJ travels. The negative values of tilting term at this stage indicate that part of this horizontal vorticity is converted into negative vertical vorticity while the SJ starts to be oriented downward.

The downward tilting of negative horizontal vorticity allows the generation of negative ζ_z along the jet, which is then amplified by a negative stretching term. This combined effect of tilting and stretching terms is sufficient to explain a large part of the decrease of

ζ_z to negative values and thus the onset of II along the trajectories (cf. Fig. 5.5d). Conversely, neither of these two terms is capable of explaining the sudden increase in ζ_z happening after 0500 UTC. This overall behaviour suggests that the steady evolution of the SJ airstream from stable to unstable is mainly explained by the tilting and stretching terms, while the process that brings it back to stable conditions is definitely not explained by those two terms. As stretching, tilting and friction are the only contributing terms in the equation, we can infer that 'frictional' processes contribute to the rapid changes in vorticity after 0500 UTC. However, as will be discussed below, this corresponds to a period of folding and overturning of the flow and it seems likely that a significant contribution to this arises from numerical mixing between adjacent trajectories (i.e. small trajectory and interpolation errors in a rapidly changing environment). This can lead to mixing of vorticity — some trajectories apparently acquiring more negative vorticity from their neighbours and *vice-versa* — but overall the genuine frictional forcing has a primary role in the removal of instability.

5.2.3 Frontogenesis/lysis diagnostic

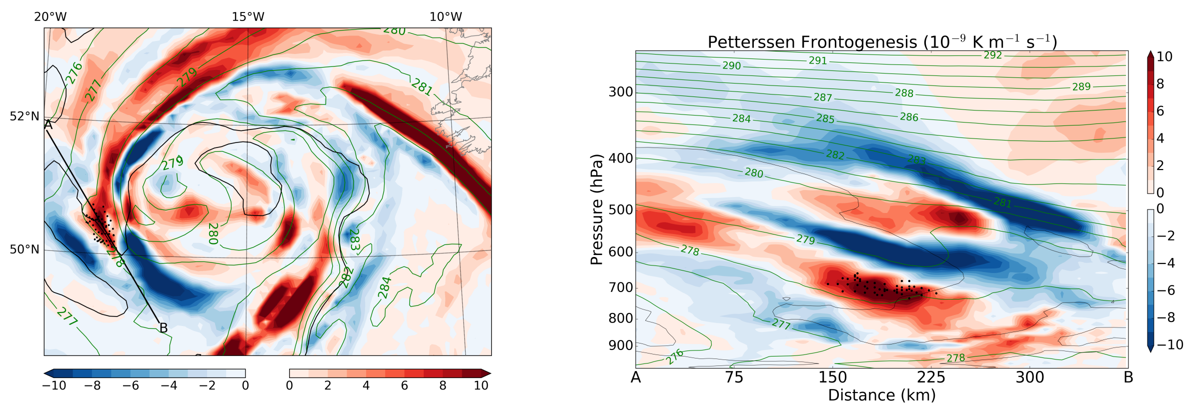

(a) **(b)**

Figure 5.7: (a): Model map of Petterssen frontogenesis (shading), θ_w (green contours, K) and cloudy regions at 700 hPa (RH_{ice} =80%, black contours). (b): Same fields as in (a), but shown on a cross section (transect AB in panel (a)). Both (a) and (b) are for 0500 UTC on 12 February 2014. The dots in (a) show the locations of the simulated SJ trajectories; in (b) the dots show the projection of SJ trajectories onto the transect.

In the analysis of the SJ airstream identified in the limited-area simulation the evolution of frontogenesis is also considered. Petterssen's decomposition of frontogenesis is used (Petterssen, 1936), as utilised by Schultz and Sienkiewicz (2013):

$$F = \frac{d}{dt}|\nabla_H \theta| = \frac{1}{2}|\nabla_H \theta|(E\cos 2\beta - \nabla_H \cdot \mathbf{V}_H), \tag{5.2}$$

where E is deformation and β the local angle between an isentrope and the axis of dilation (see Keyser et al. (2000) for more details). As mentioned in Section 2.4, positive frontogenesis is expected in correspondence with the main fronts (cold, warm and bent-back) and negative frontogenesis, i.e. "frontolysis", is expected in the frontal-fracture region.

Figure 5.7a shows Petterssen frontogenesis on the 700-hPa pressure level at 0500 UTC (matching the time and level of Figure 5.4a). It broadly confirms the expected frontogenesis structure. However, a smaller-scale pattern is present at the tip of the cloud head, with small-scale horizontal banding taking place in a radial direction (i.e. passing through the location of the trajectories in the orthogonal direction to the marked cross section). SJ trajectory points are located in a small region of positive frontogenesis (with a similar-sized region of frontolysis further out from the cyclone centre). The pattern of frontogenesis is well-correlated with the one of horizontal divergence described in the previous section (Sec. 5.2.2). The frontal fracture is an area of frontolysis and divergence while the SJ is enclosed in a localised (and time-intensifying) region of frontogenesis and convergence.

Figure 5.7b shows a cross section through the SJ (matching the time and section of Figure 5.4b). This shows that bands of frontolysis and frontogenesis are slanted and piled vertically, very much like the ζ_z structure. There is clearly a process operating on a smaller scale than, and different from, the larger-scale frontogenesis/frontolysis pattern expected in the cloud head. This banding can be viewed as arising from the slantwise motions previously discussed bending and distorting the θ field (although θ is not shown, note the distorted θ_w field in Figures 5.7b and 4.11). Frontogenesis is a kinematic quantity measuring Lagrangian tendency in the horizontal θ gradient, and it is difficult to interpret dynamically. However, it can certainly be said that while the broad structure of frontogenesis resembles that found in previous lower-resolution studies such as Schultz and Sienkiewicz (2013) and Slater et al. (2017), with widespread frontolysis in the frontal-fracture region, smaller-scale patterns related to the SJ motion are present at the tip of the cloud head and the SJ descent is certainly *not* associated (at least locally) with fontolysis.

5.3 Comparison with a coarser-resolution model

5.3.1 Motivation

In this section the impact of reducing the horizontal and vertical grid spacing is assessed. As discussed in Section 2.4, previous studies have claimed that a horizontal grid spacing of around 10–15 km and a vertical grid spacing not larger than 200–300 m at SJ heights are required to correctly resolve the feature, both in case studies (Clark et al. (2005); Martínez-Alvarado et al. (2010); Gray et al. (2011); Smart and Browning (2014)) and idealised simulations (Baker et al. (2014); Coronel et al. (2016)). The results of the previous sections in this chapter and in Chapter 4 confirm that the SJ is a mesoscale feature, a narrow airstream whose dimensions are on the order of a few tens of km across and a few 100 m deep.

Here the consequence of reducing resolution is investigated by analysing the results from the global simulation that was used to initialise and drive the limited-area simulation. While it cannot be expected that the coarser-resolution model would be able to correctly resolve the SJ airstream, it is not obvious what the model solution will look like. For example, a 4-km grid spacing model cannot resolve deep convection as well as a 1-km grid spacing model, but in practice both will generate their own form of convection (e.g. Lean et al. (2008)). The question is, therefore, would similar conclusions regarding mesoscale instabilities be drawn from a lower resolution ($\sim$26-km horizontal and 400-m vertical grid spacing) model?

Slater et al. (2017) also simulated windstorm Tini (see also Section 2.). Their simulation used a different model (the Advanced Research Weather and Forecasting Model Version 3.4) and a different initial analysis and boundary conditions (the Global Forecast System six-hourly, 0.5° analysis). It used a horizontal grid spacing of 20 km and 39 vertical levels, 8 of which were below 850 hPa, and so was coarser in both dimensions than the one described in previous sections here and most similar to the global model simulation used in this analysis. Thus, while their simulation cannot be directly compared to the results of this section, the similarity in resolution to this global model simulation means that it is worthwhile to note, *inter alia*, similarities to and differences from their simulations in the following.

5.3.2 Results

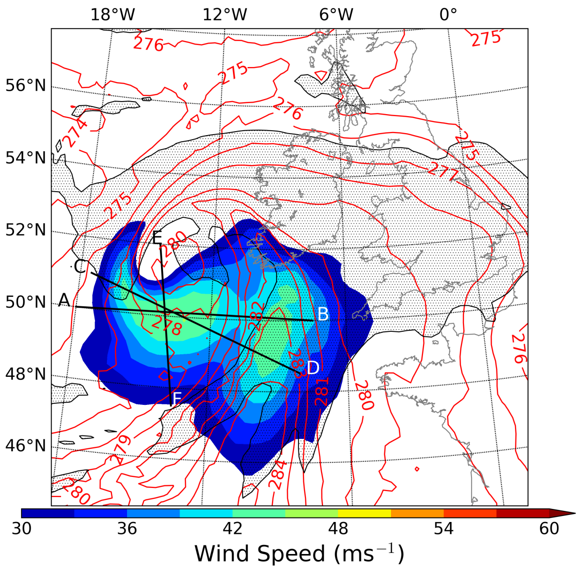

Figure 5.8: Global-model map of wind speed at 850 hPa (contours, m s^{-1}), wet-bulb potential temperature at 850 hPa (K, red lines) and cloudy regions at 700 hPa (RH>80%, black lines and dotted regions) at 0700 UTC on 12 February 2014.

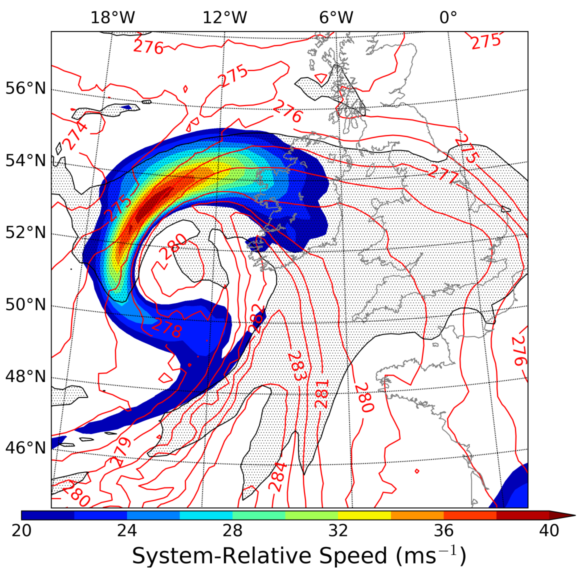

Figure 5.9: Same as 5.8 but with system-relative wind speed.

Figures 5.8, 5.9 and 5.10 for the global model simulation are analogous to Figures 4.9, 4.10 and 4.11 for the limited-area model simulation. The broad cyclone structure with clouds, fronts and strong-wind regions is very similar in the two simulations (compare Figure 5.8 and Figure 4.9); however, some differences are evident. The wind maximum in the frontal-fracture region is broader in the coarser-resolution simulation, less focused and definitely weaker, with speed reaching only 48 $\mathrm{m\,s^{-1}}$ compared to 60 $\mathrm{m\,s^{-1}}$ in the higher-resolution simulation. In contrast, the WCB maximum speed is only slightly weaker at 45 $\mathrm{m\,s^{-1}}$ compared to 48 $\mathrm{m\,s^{-1}}$. The system-relative winds in Figure 5.9 show a CCB that is similar in location and strength to the one in Figure 4.10. This extends into the frontal-fracture region, but there is no suggestion of a local maximum where the SJ was identified in the higher-resolution model. Note also that the second band of cloud in the 12 km simulation that wraps around the cyclone centre outside the CCB is entirely absent from the lower resolution simulation (Figures 5.8 and 5.9).

The cross sections shown in Figure 5.10 show many features in common with Figure 4.11, but, again, the weakening of the low-level wind maximum in the frontal-fracture region is particularly evident. This low-level wind maximum is now weaker than the one in mid-levels. Moist isentropes are downward sloped and divergent in the frontal-fracture region, with no suggestion of folding, corresponding to a region of broad and weak descent. Note also that the two regions of slantwise descent (either side of the cloud) at the western end of Figure 4.11d are considerably weaker in Figure 5.10b. Figure 5.10a again highlights the absence of the second band of cloud that wraps around the cyclone centre outside the CCB.

The results for the global model simulation (that cannot resolve mesoscale instability release) show none of the key mesoscale features such as a separate wind maximum (and possibly multiple maxima), multiple slantwise descents, cloud bands and isentrope folding that are evident in the 12 km simulation. Rather they are thus consistent with a hypothesis that the relatively strong winds are caused by the synoptic-scale and frontal dynamics in the region super-imposed on the storm motion with possible enhancement by mixing with high-momentum air from above.

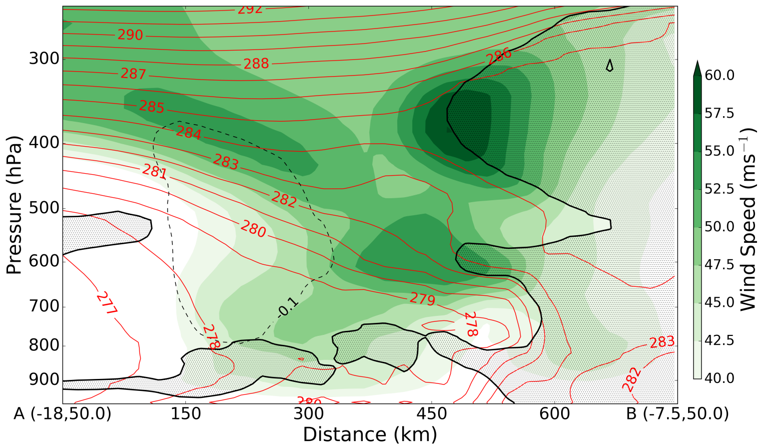

(a)

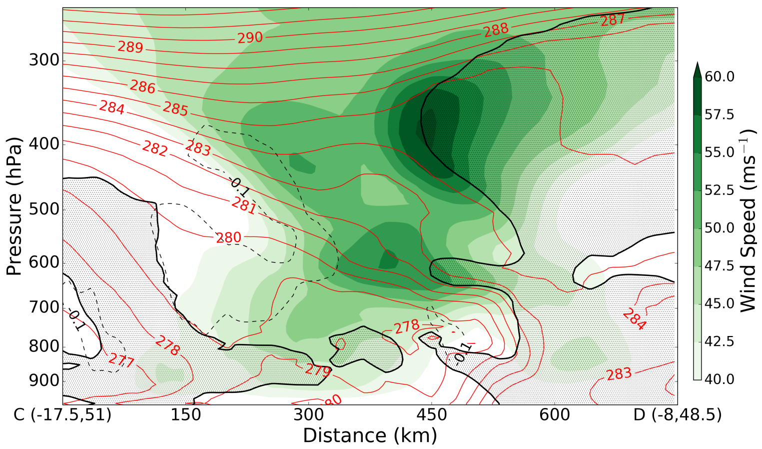

(b)

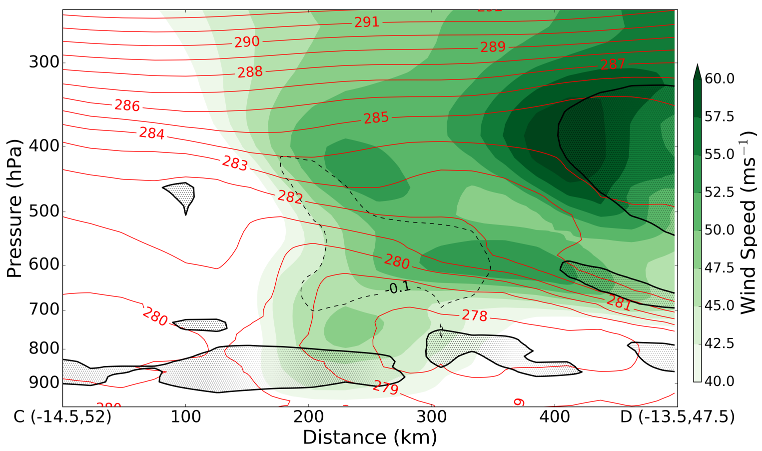

(c)

Figure 5.10: Global-model cross section (transects (a) AB, (b) CD and (c) EF in Figure 5.8 of wind speed (green filled contours,m s^{-1}), negative vertical velocity (dashed black lines, ms^{-1}), wet-bulb potential temperature (red lines, K) and cloudy regions (RH>80%, thick black lines) at 0700 UTC on 12 February 2014.

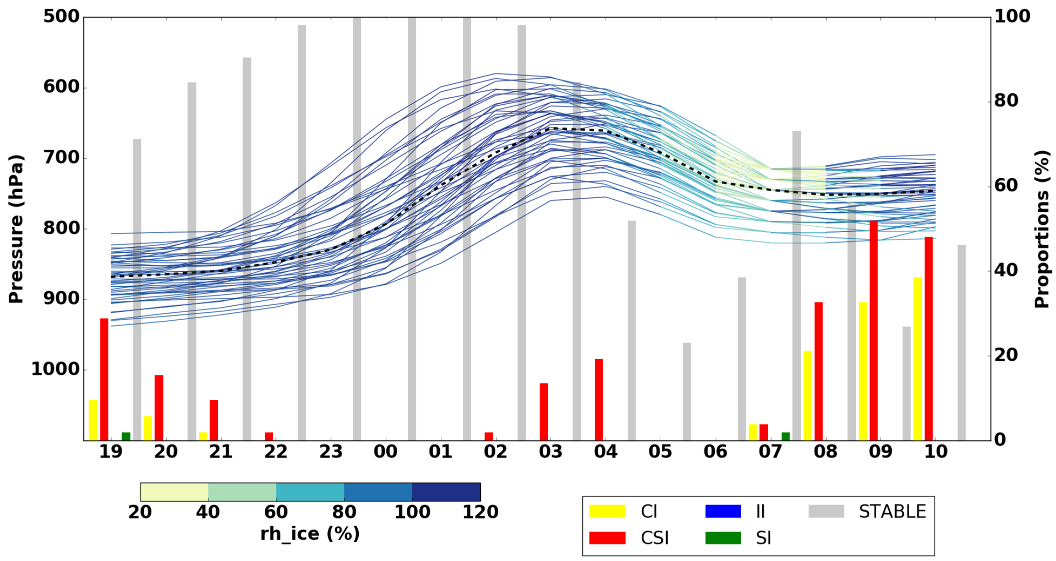

Figure 5.11: Global-model timeseries (UTC) of pressure (colours indicate RH_{ice}) and diagnosis of instability conditions along SJ trajectories. The vertical bars indicate the fraction (proportion) of trajectories that are unstable to the different instabilities mentioned in the key table at the bottom of the figure and evaluated every 15 minutes (see Table 3.1 for the instability criteria).

The trajectory analysis was repeated for the strong winds in the frontal-fracture region. Although there is not a clear and focused wind maximum, grid points were selected with wind speed exceeding 47 $\mathrm{m\,s^{-1}}$ at 0700 UTC located at 760 hPa, or in contiguous levels above or below, as the best compromise to characterise the low-level strong winds. To refine the airstream, we kept only trajectories located at a pressure greater than 800 hPa at 1900 UTC and descending more than 50 hPa between 0400 and 0600 UTC. Figure 5.11 shows the time-pressure profile of these trajectories and the related instability bars. The overall motion of the airstream is quite different to Figure 5.1. There is a considerable reduction in instability along the trajectories compared to the higher-resolution simulation, with most trajectories stable, though there is a weak signal of CSI at the time that the SJ starts descending. During the descent, the few trajectories with CSI lose this instability due to the reduction in RH associated with the descent. However, only about 20% are diagnosed as stable as the remaining trajectories still have negative MPV* or N_m^2. The descent of these trajectories, although still steady and coherent, and occurring at the same stage of cyclone evolution as in the higher-resolution simulation, is much weaker.

Figure 5.7 shows the horizontal and vertical frontogenesis pattern (to be compared with Figure 5.12). It shows frontogenesis in the inside flank of the cloud head and a broad

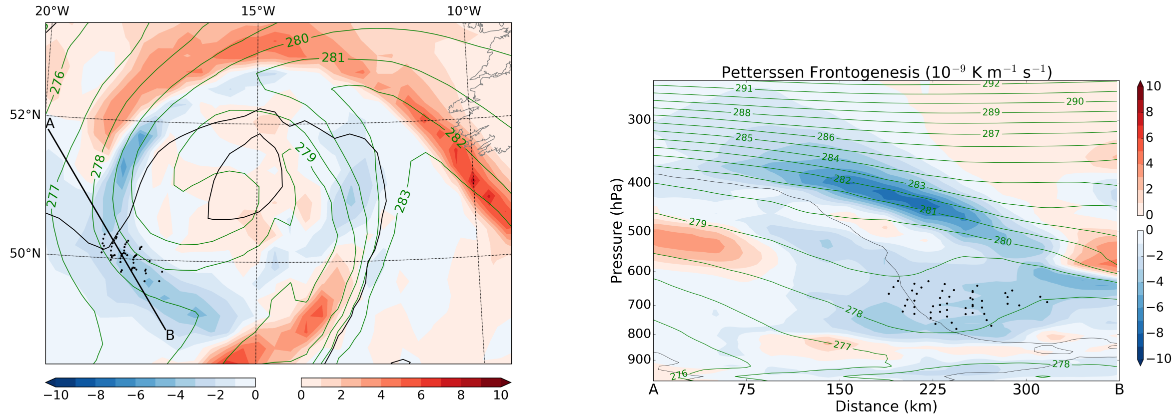

(a) (b)

Figure 5.12: (a): Global-model map of Petterssen frontogenesis (shading), θ_w (green contours, K) and cloudy regions at 700 hPa (RH$_{ice}$ =80%, black contours). (b): Same fields as in (a), but shown on a cross section (transect AB in panel (a)). Both (a) and (b) are for 0500 UTC on 12 February 2014. The dots in (a) show the locations of the SJ trajectories; in (b) the dots show the projection of SJ trajectories onto the transect.

area of frontolysis towards and into the frontal-fracture region, without any banding in the cloud head. There is much less fine-scale structure in this figure and the broad picture is very much in agreement with that shown in Schultz and Sienkiewicz (2013).

To summarise, the airstream represented by these trajectories in the lower-resolution simulation has quite different characteristics to the SJ airstream observed in the higher-resolution simulation. This is not only a difference in wind speed: rather, these are two different airstreams with very different characteristics. Furthermore, as far as it is possible to compare, these lower-resolution results are similar to those found by Slater et al. (2017). These results demonstrate that the lower-resolution model is capable of producing a weakly descending (and accelerating) airstream that has strong wind speed at lower levels and, by most criteria, might be classified as a SJ. However, this airstream has none of the characteristics exhibited by the much more focused and much stronger SJ diagnosed in the higher-resolution simulation; this SJ is associated with mesoscale instabilities, which require the higher resolution to develop and be released.

5.4 Analysis of PV — and θ — tracers

5.4.1 Motivation

Potential vorticity (PV) is conserved following an adiabatic and frictionless flow, as already discussed in Chapter 2. As a consequence, it is possible to separate the effects of different non-conservative processes by computing the variations in PV in a Lagrangian framework. This "PV tracer technique" (Saffin et al., 2016) can be used to isolate the effects of the various processes represented in a numerical model that are responsible for non-conservation of PV on an air parcel. Negative values of PV are associated with the occurrence of symmetric instability (SI, see Section 2.3.2 for a brief summary of SI and PV properties) and are also closely associated with inertial instability (II), as PV is defined by the dot product between vorticity and spatial derivatives in potential temperature. While the role of tilting and stretching of vorticity in the generation of negative values of its vertical component and hence in the occurrence of mesoscale instability has been highlighted in Section 5.2, the physical processes responsible for the mechanisms identified (through changes in PV and related motions) are yet to be identified. The importance of PV tracers resides thus in trying to isolate the different diabatic processes acting on the SJ airstream during the onset of instabilities.

The technique adopted follows Saffin et al. (2016) and is described in Section 3.6. The next sections instead contain an assessment that the simulation containing the tracers is representative of the SJ dynamics described in the high-resolution simulation. Results of the analysis of PV tracers are then outlined, along with a further analysis of θ tracers (analogous to PV tracers but for potential temperature).

5.4.2 Brief characterisation of the SJ in the run with PV tracers

In this section the characteristic of the SJ occurring in the simulation with tracers are briefly described. This simulation is run with MetUm version 7.3, as opposed to the MetUM version 8.2 used for the simulations of windstorm Tini described up to this point, because of compatibility issues between the model and the PV-tracers scripts. These two

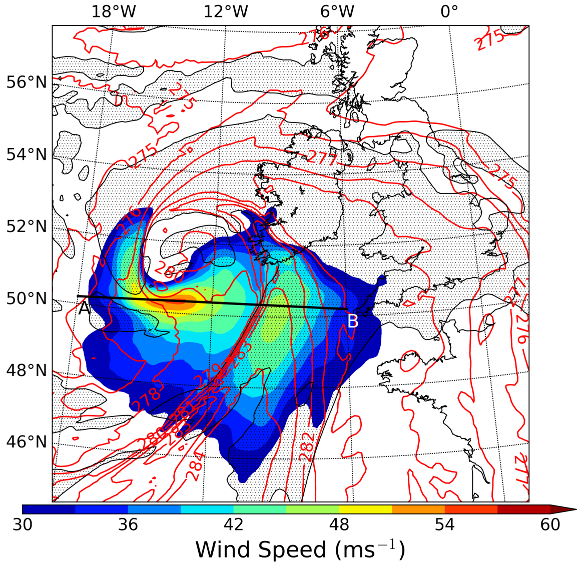

(a)

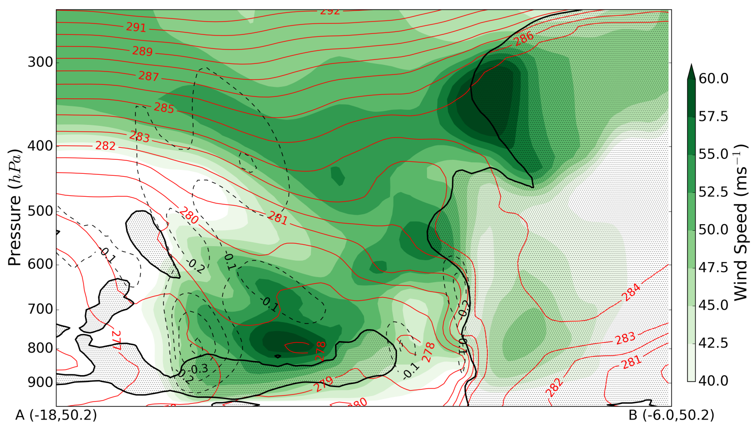

(b)

Figure 5.13: Same as Figures 4.9 (a) and 4.11 (b) but for the simulation with tracers

model versions share the same dynamical core and the physical processes in version 7.3 have been set to be as similar as possible to the ones in version 8.2. A difference remains in the handling of rain, which is treated as a prognostic variable in version 8.2 and, due to issues with the computation of tracers, as a diagnostic variable in version 7.3.

Figure 5.13a, to be compared with Figure 4.9, shows that all the main features of the cyclone (i.e. fronts and clouds) show a good resemblance and have only small discrepancies with respect to their counterparts in the main simulation. Looking more closely, a strong and focused low-level wind maximum is present in the frontal fracture in this simulation, just out of the cloud-head tip, consistent with the definition of a SJ. Location and shape of this SJ wind maximum are similar to the one present in the main high-resolution simulation, the only differences being a northward displacement around 20-40 km and a slightly more elongated shape.

Figure 5.13b, analogous to Figure 4.11, is a vertical cross section of the transect AB indicated in Figure 5.13a. This section, in a very similar way to the one in Figure 4.11, shows that the low-level wind maximum in the frontal fracture (i.e. the SJ) is located at the bottom of a region of slanted moist isentropes and generally weak descent. Localised area of stronger descent and buckling of θ_w isolines are present just above and behind the wind maximum, as in the main simulation. The SJ wind maximum is considerably more intense than the warm conveyor belt, on the right side of the warm front, almost reaching 60 m s^{-1}.

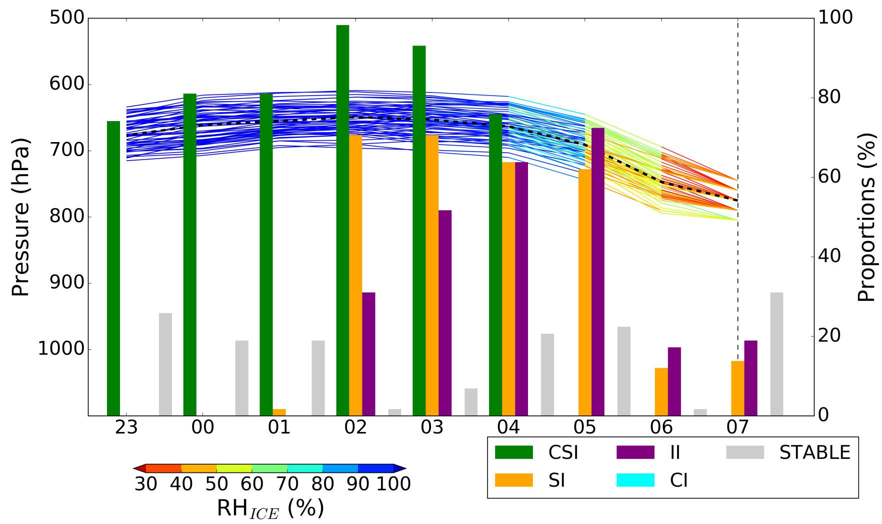

Figure 5.14: Same as Figure (b) 5.1 but for the simulation with tracers

Lagrangian backtrajectories have been computed also for this run, to assess the dynamics of the SJ. All the grid points with horizontal wind speed larger than 57 m s^{-1} at 820 hPa (or contiguous levels, in the sense explained in Section 4.4) at 07 UTC have been selected as starting points. It has to be noticed that time, pressure level and wind speed threshold are the same as the ones used in the main high-resolution simulation, confirming the similarity between the jets in the two runs. The airstream has then been refined keeping only the trajectories undergoing all the SJ descent, hence located at a pressure smaller than 700 hPa at 0200 UTC (compare with 650 hPa in the main simulation) and descending by more than 75 hPa between 0400 UTC and 0600 UTC (100 hPa in the main simulation). The values chosen highlight that the SJ in this simulation, although having the same strength and location at the end of its descent, undergoes to a slightly smaller descent than the one in the main simulation.

Figure 5.14 shows the evolution of mesoscale instabilities on the SJ identified as explained. In this case the trajectories have been computed with hourly frequency input data (rather than 15 minutes as in the main simulation) as the analysis of trajectories is not the main focus of this section. Nevertheless, Figure 5.14 can be compared with Figure 5.1, the analogous plot for the main simulation. Both figures share the same pattern of mesoscale instabilities even if with differences in the proportion of unstable trajectories at each time. Before the start of the descent the majority of trajectories become unstable to CSI (with the proportion close to 100 % at 02 UTC). II shows a later increase, reaching its maximum (above 70 % of the trajectories) at 05 UTC, while the SJ is descending. SI instead has an abrupt rise between 01 UTC and 02 UTC, going from < 5 % to around 70 %, and then staying almost constant before dropping below 20 % after 05 UTC, like II.

The general evolution of these instabilities is in agreement with the main simulation: most of the trajectories become unstable to CSI while the SJ is in the cloud head and then, when the SJ exits from the cloud head and starts to descend, the proportion of CSI-unstable trajectories drops with a simultaneous rise (and subsequent drop) in dry mesoscale instabilities. Secondary but still noticeable differences are present between the two simulations, particularly in the behaviour of SI and in general with more abrupt variations in the run with tracers, at least partly caused by the difference in time resolution of the input data for trajectories. Differences in the evolution of SI between the two runs are associated with a different evolution of PV (as the condition for SI is PV$<$ 0). Hence, this is reflected in the results shown by the PV tracers. The trajectories of the simulation with tracers are also characterised by a decrease in θ_w happening around 04–05 UTC that is roughly one third of the one observed in the main simulation (the same argument applies for the evolution of θ). It can then be inferred that the importance of cooling by evaporation and sublimation in the first stage of SJ descent is substantially smaller than in the main simulation.

Despite the differences just mentioned between the two simulations, the agreement in the general pattern, with in-cloud conditional slantwise instability followed by dry slantwise instability during the SJ descent, and the similarity in the airstream kinematics are remarkable. It is thus possible to link the results of the tracers with the SJ dynamics of the main run analysed in detail in the previous sections of this chapter, keeping in mind the differences between the two runs .

5.4.3 Analysis of PV tracers

Comparison between advection-only PV and full PV values

Before looking at the values of individual PV tracers it is useful to focus on the evolution of PV and to compare it with the evolution of the advection-only PV tracer, i.e. the tracer in which PV is only advected with the flow. Figure 5.15 shows this comparison throughout the time in which symmetric instability, indicated by negative values of PV, develops on the SJ.

Top panels show that at 00 UTC there are already substantial differences between full and advection-only PV, indicating that diabatic (i.e. non-conservative for PV) processes have taken place up to that time, reshaping the pattern of PV. The advection-only tracer only shows a band of values close to zero encircling the cyclone centre on its northwestern side and a streamer of high PV values coming from the southwest along the cold front. The full PV is different, as high values are present also on the northwestern side of the cyclone centre, indicating a diabatic generation of PV in the cloud-head area. However, the region of SJ trajectories has similar values in both panels, around 0.25 PVU, showing that the net effect of diabatic processes on the airstream is negligible up to that point. It is worth to note that in the frontal fracture there is a small area with negative values in the full PV field. This is another hint at the occurrence of multiple SJ-pulses, not always associated with the development of a SJ, during the storm lifetime (as already discussed when looking at radar observation in Section 4.2).

The middle panels show that the full PV decreases to negative values along the airstream while the values of advection-only PV remain stable in the SJ area. Hence, diabatic processes act to decrease PV below zero between 00 UTC and 03 UTC in a narrow region corresponding with the location of SJ trajectories. A similar situation is present in the bottom panels with negative values of full PV on the SJ and values of advection-only PV confined between 0.25 and 0.5 PVU. A later impulse is also starting to form behind the SJ (same considerations apply as for the earlier one detected at 00 UTC). In the next paragraph an analysis of the separate tracers is presented, in order to investigate which processes are responsible for the decrease in PV just described.

Evolution of PV tracers

Figure 5.16 shows maps of different tracers at relevant times. The panels show the cumulative effect of the various physical processes on PV from the start of the simulation to the instants chosen. Thus, differences in the values of tracers at different times are more relevant than absolute values, as we are not interested in the total effect of a certain physical process but rather in its contribution during the onset of SI on the SJ.

Panels a, b and c illustrate the evolution of the microphysics tracer from 00 UTC to 03 UTC and then 05 UTC. This tracer contains all the slow moist processes, such as nucleation of ice, evaporation and freezing of rain, deposition on ice, melting, freezing of cloud, and Bergeron-Findeisen process. The values of the tracer on the SJ airstream decrease steadily going through the three chosen times. In detail, values of the microphysics tracer range between 0.5 and 1 PVU at 00 UTC, are around 0.25 PVU at 03 UTC and mostly just below 0 PVU at 05 UTC. These panels indicate that there is a steady contribution in the microphysics tracer responsible for a decrease of almost 1 PVU (on average) along the SJ between 00 and 05 UTC, i.e. when SI develops.

Panel d shows the convection tracer at 05 UTC. Its values along the airstream stay generally constant from 00 UTC (not shown) to 05 UTC, in between 0 and -0.5 PVU. Convection is not having a noticeable effect on the values of PV on the SJ, whereas it gives a substantial contribution to changes in PV in frontal areas. The last two panels show, respectively, the long-wave radiation tracer and the boundary layer tracer (which includes the subgrid cloud scheme in addition to the turbulent mixing scheme and is active in the first 50 levels from the ground, i.e. in the whole troposphere), both at 05 UTC. Also in these cases, changes in PV between 00 UTC (not shown) and 05 UTC do not

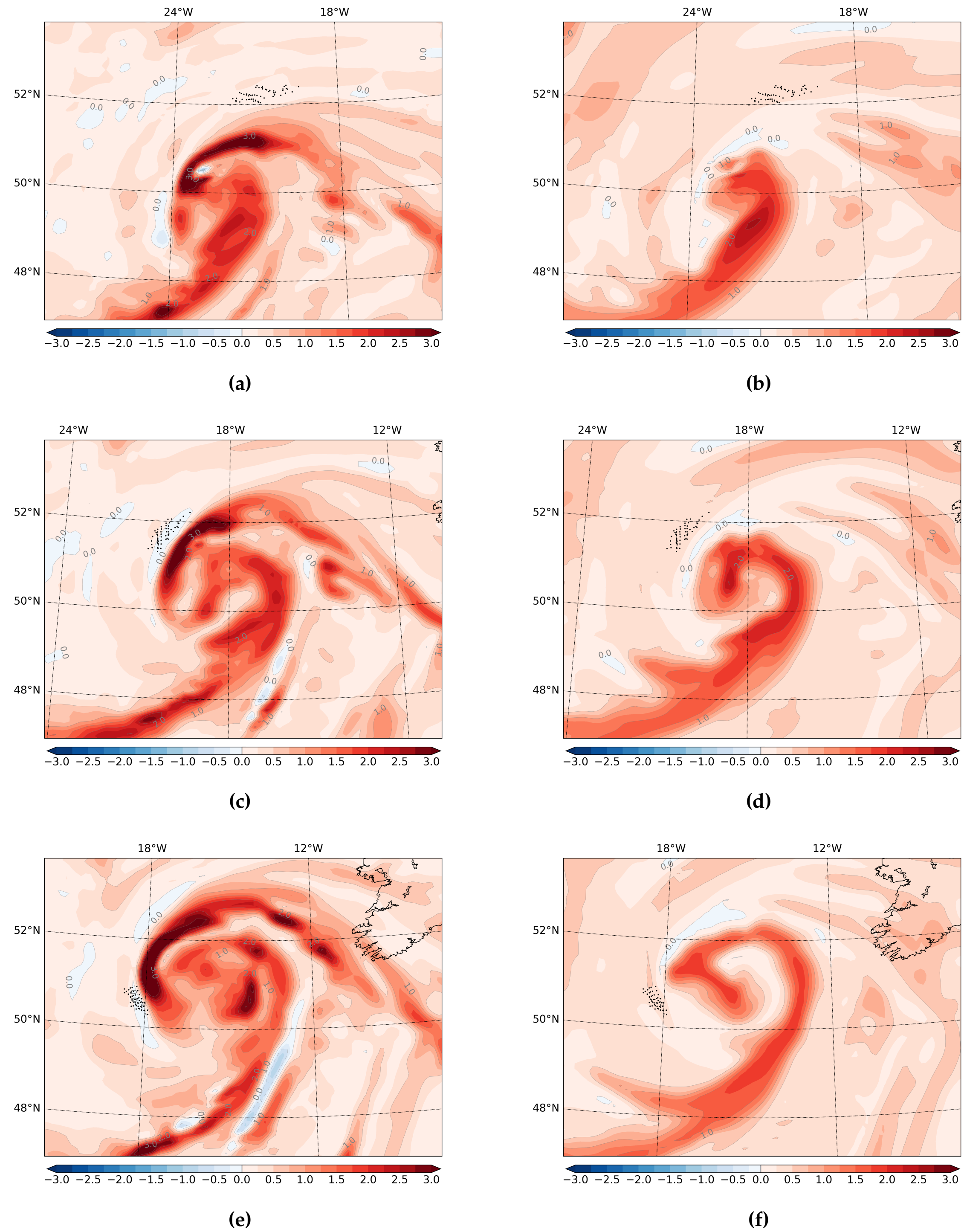

Figure 5.15: Model maps of PV (PVU, panels a, c and e) and of the advection-only PV tracer (PVU, panels b,d and f) evaluated on the closest model level to the mean height of trajectory points at the time (contour lines every 0.5 PVU). Black dots indicate the instantaneous location of SJ trajectories. Panels a and b refer to 00 UTC on 12 February 2014 and model level 27. Panels c and d refer to 03 UTC and model level 28. Panels e and f refer to 05 UTC and model level 26.

exceed ∼0.2 PVU along almost all the airstream for both tracers, indicating the absence of a primary impact on the onset of instability by these processes. Important variations in PV affect only the foremost edge of the airstream, which enters the western side of a strong dipole aligned with the bent-back front. However, it has to be noted that an almost complete cancellation of this dipole occurs, with the two tracers showing similar magnitude but opposite sign.

Some considerations from Chagnon et al. (2013) and Chagnon and Gray (2009) can be helpful in understanding that dipole-tripole structures and cancellation between tracers are frequently observed. First, these studies showed how horizontal and slanted dipole and tripole structures are the consequence of frontal circulations and narrow rain bands, generating characteristic heating-cooling patterns. Secondly, cancellation between different tracers is not uncommon as schemes can generate quite frequently opposite forcings (e.g. if the cloud scheme evaporates rain generated by the microphysics scheme there is cooling associated with the cloud scheme and heating associated with the microphysics scheme, and thus PV sources of opposite sign) However, we are more interested in linking the decrease in PV along the SJ with the net contributions from the processes included in the tracers rather than trying to disentangle all the eventual cancellations.

In summary, the results suggest that the primary cause of decrease in PV on the SJ resides in the microphysics tracer and hence in the slow moist physical processes. This behaviour can be possibly explained by the occurrence of evaporative/sublimational cooling above the jet exiting from the cloud head (already indicated as likely in previous sections), whereas the main microphysics processes produced maximum heating above the jet before 00 UTC. The decrease in PV between 00 UTC and 03 UTC has a similar magnitude to the variation observed in the microphysics tracer. However, while the PV undergoes most of its decrease in this time frame, the values in the microphysics tracer continue a steady decrease up to 05 UTC. Minor contributions in PV variations are contained in tracers related to convection, boundary layer and long-wave radiation (whereas all other physical processes are negligible) with the microphysics tracer having the main but not the only contribution. Further analyses are required for a more complete understanding of these results. For example, the boundary layer tracer contains both turbulent mixing and fast-physics moist processes. The analysis of θ tracers (described in the next section) can be helpful in disentangling contributions.

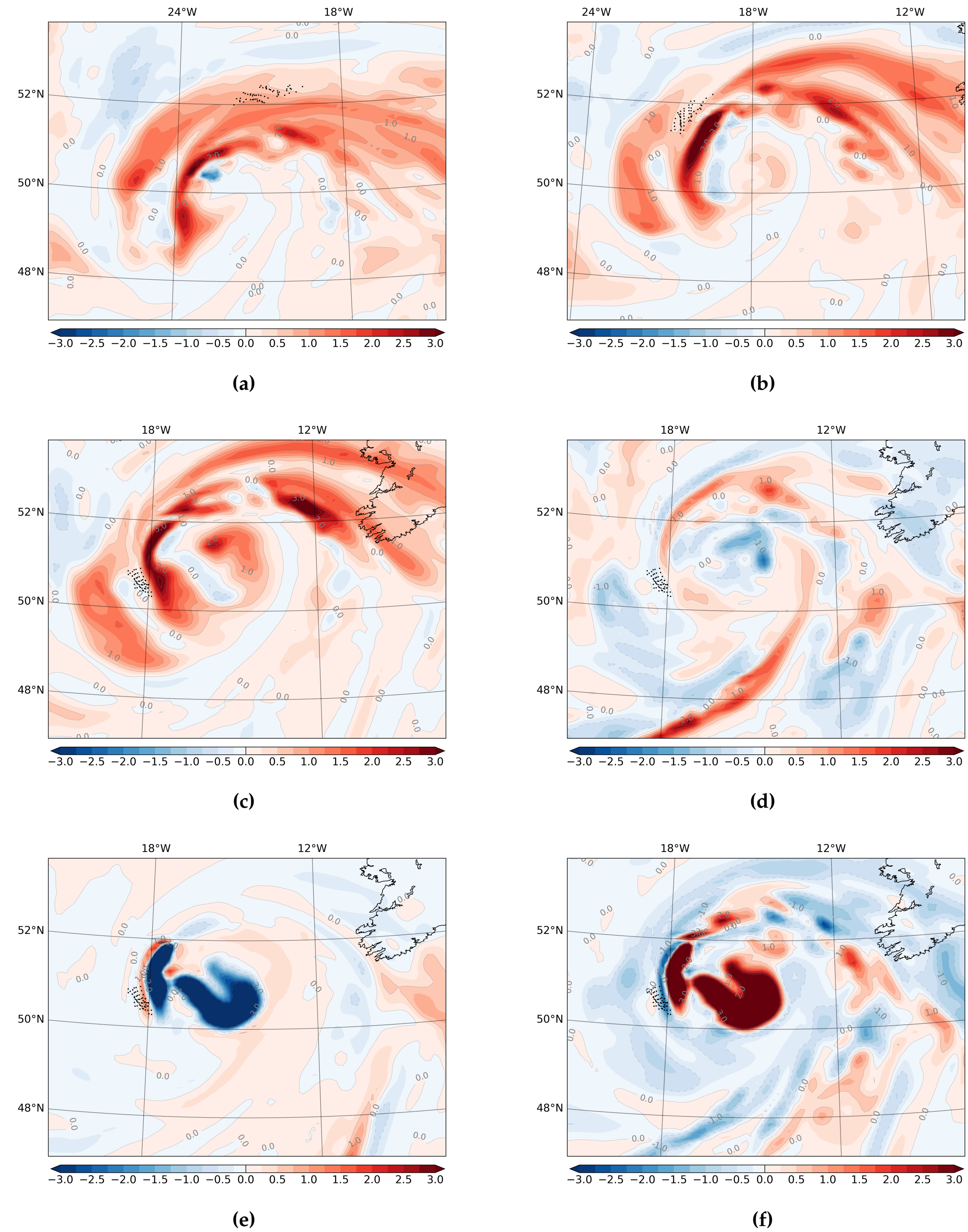

Figure 5.16: Model maps of various PV tracers (PVU, contour lines every 0.5 PVU) and SJ trajectory points (black dots). Panels a, b and c show the microphysics tracer, respectively, at 00 UTC on level 27, 03 UTC on level 28 and 05 UTC on level 26. Panels d, e and f show, respectively, the convection tracer, the long-wave radiation tracer and the boundary layer tracer all evaluated at 05 UTC on level 26.

5.4.4 Analysis of θ tracers

Comparison between advection-only θ and full θ values

Figure 5.17 is analogous to Figure 5.15 but for θ instead of PV. It shows that potential temperature is around 4-5 K lower in the advection-only tracer than in the full θ field along the SJ trajectories. In general, full θ is higher than its advection-only tracer along the warm and bent-back fronts and in the cloud-head area. This indicates that the cyclone is redistributing heat not only with advection but also with important diabatic processes. Values of θ on the SJ increase slightly between 00 UTC and 03 UTC ($\sim$1 K, from 286-287 K to 287-288 K) and then stay below 288 K between 03 UTC and 05 UTC. The shape of the 288 K contour, which encircles the airstream, suggests that in a context of general increase of θ (albeit with a magnitude not larger than 1 K) there is a process preventing the airstream from this warming. This is consistent with the hypothesis of evaporative/sublimational cooling inferred in the analysis of trajectories and of PV tracers. However, the analysis of single θ tracers is necessary to isolate the processes contributing to the changes in potential temperature in this whole time frame, between 00 and 05 UTC.

Evolution of θ tracers

Figure 5.18 includes the maps of the most relevant θ tracers. The top panels refer to the microphysics tracer, evaluated, respectively, at 03 UTC and 05 UTC. The two maps show a horizontal dipole extending along all the warm front and the bent-back front. Negative values of the tracer along the fronts indicate a substantial cooling that is very likely related to the falling of precipitation from above and the consequent evaporation/sublimation in unsaturated air. Positive values of the tracer, with smaller magnitude, constitute the northwestern side of this dipole and suggest the occurrence of warming, likely related to large-scale precipitation, in particular due to the Bergeron-Findeisen process. SJ trajectories travel mainly on this latter side of the dipole, with values in between 0 K and 2.5 K at 00 UTC (not shown) and 03 UTC. Between 03 UTC and 05 UTC many of the trajectories cross the zero-line separating the two sides of the dipole and experience a net decrease in the values of the tracer, reaching -2.5 K on average.

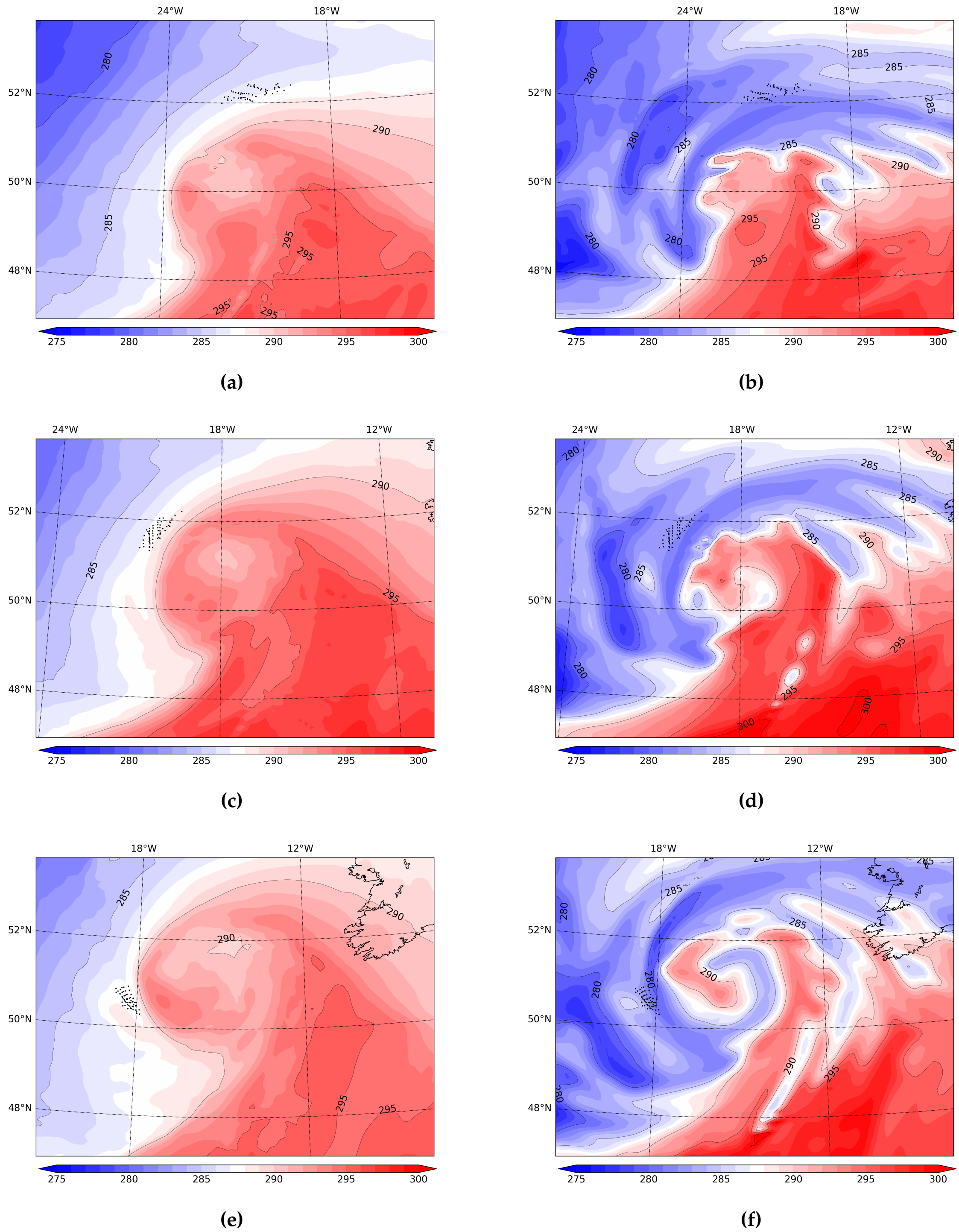

Figure 5.17: Model maps of θ (K, panels a, sc and e) and of the advection-only θ tracer (K, panels b,d and f) evaluated the closest model level to the mean height of trajectory points at the time (contour lines every 2.5 K). Black dots indicate the instantaneous location of SJ trajectories. Panels a and b refer to 00 UTC on 12 February 2014 and model level 27. Panels c and d refer to 03 UTC and model level 28. Panels e and f refer to 05 UTC and model level 26.

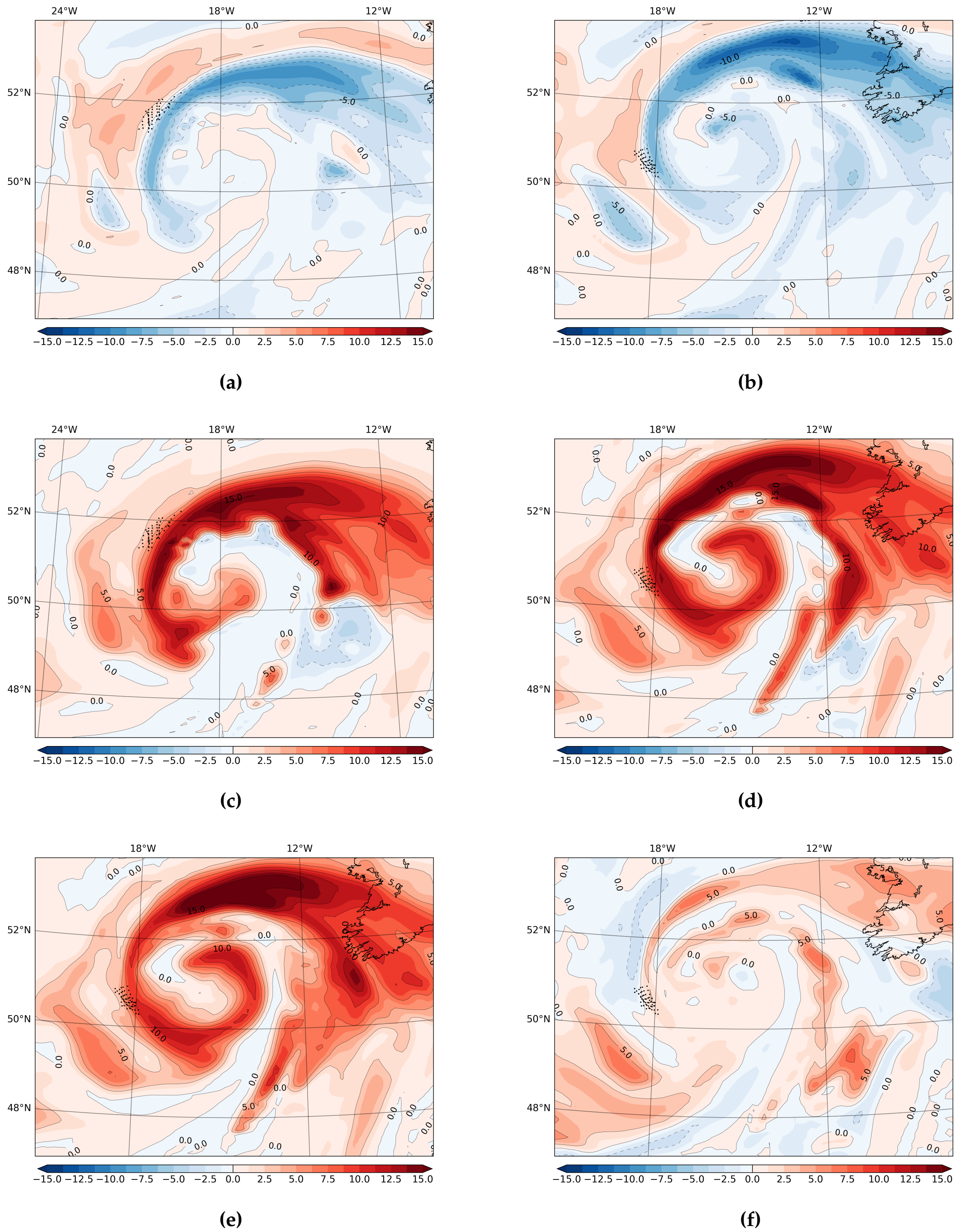

(a) (b) (c) (d) (e) (f)

Figure 5.18: Model maps of various θ tracers (K, contour lines every 2.5 K) and SJ trajectory points (black dots). Panels a and b show the microphysics tracer, respectively, at 03 UTC on level 28 and 05 UTC on level 26. Panels c and d show the boundary layer tracer at 03 UTC on level 28 and 05 UTC on level 26. Panel e shows the latent heat contribution to the boundary layer tracer at 05 UTC on level 26 and panel f shows the convection tracer at 05 UTC on level 26.

This behaviour is consistent with the idea of trajectories travelling in a region in which evaporative/sublimational cooling is occurring and, in case of maximum cooling above the jet, can be associated with a decrease in PV (observed when analysing the microphysics PV tracer). However, the pattern shown by the θ tracers is on a larger scale than previous findings would suggest, as opposed to localised decrease of PV along the airstream. There is also a discrepancy in time between the main decrease in θ included in the microphysics tracer, that occurs between 03 UTC and 05 UTC and the decrease in PV contained in the analogous tracer, which is steady throughout the period from 00 UTC to 05 UTC.

The mid panels refer to the boundary layer tracer, evaluated, respectively, at 03 UTC and 05 UTC. Strongly positive values are present in the cloud-head area and along the cold front, cancelling the negative contribution from the microphysics tracer and producing net positive values. Values along the SJ increase by around 2.5 K between 03 UTC and 05 UTC (although it is difficult to give a single value as strong gradients are present in the area), almost balancing the cooling observed in the microphysics tracer. The cancelling between the two tracers is particularly evident in the warm sector and along the bent-back front and indicates that two opposite forcings are acting: condensational heating in the cloud scheme (boundary layer tracer) and evaporative/sublimational cooling in the microphysics scheme.

Panel e shows the contribution of latent heat to the boundary layer tracer at 05 UTC. The strong similarity with panel d indicates that latent heat (that comes from the cloud scheme and indicates condensation during the ascent of moist air) constitutes almost all the contribution in the boundary layer θ tracer. All the other tracers have minor variations with the convection tracer being the only non-negligible one. Its small increase by 05 UTC shown in panel f goes in the same way as the boundary layer tracer, opposing the decrease in the microphysics tracer.

5.4.5 General discussion of the results of this section

The analysis of PV and θ tracers highlights the roles of moist processes (mainly in microphysics scheme and cloud formation in the boundary layer scheme) in changing PV and potential temperature on the SJ, with other diabatic processes having minor or negligible effects. However, the analysis of tracers does not make entirely clear how negative PV (with the onset of SI as a consequence) is generated. Further analysis would also be required to determine how much of the cooling caused by moist processes is related to the generation of negative PV. Cancellations and overlaps between different tracers make it difficult to put forward clear hypothesis based on the results just outlined.

It is also important to note that the simulation used for the analysis of the tracers shows remarkable similarities with the main high-resolution simulation in terms of kinematics of the SJ and general evolution of instabilities along the airstream but with some differences in the behaviour of SI (that is associated with negative PV as a condition for instability) and on the magnitude of evaporative/sublimational cooling. A few differences with the PV evolution of the SJ in the main simulation cannot be ruled out. Nevertheless, the analysis of tracers has proved useful in stressing the importance of a combination of moist processes on the dynamics of the SJ in the stage in which the airstream is starting to be unstable. An alternative investigation, that has not been performed in this project for time reasons, could use the approach outlined in Joos and Wernli (2012), in which diabatic heating rates caused by individual microphysical processes in an extratropical cyclone are considered.

5.5 Summary and conclusion of the case study

Windstorm Tini was a particularly intense and rapidly developing cyclone. The main tool used in this study was a limited-area simulation using the MetUM numerical weather prediction model. However, by chance the frontal-fracture region of the storm passed over the MST radar wind profiler at Aberystwyth and comparison with these data and other more routine observations suggests that the simulation reflects the key structures in the storm very well. A SJ has been identified in the simulation as a coherent airstream exiting from the cloud head, descending strongly (150 hPa in 3 h) while accelerating into the frontal-fracture region and producing a strong and focused wind maximum close to 60 m s^{-1}. This airstream descends in an environment that is already broadly descending, with slanted θ_w lines that show evidence of folding. The θ_w range characteristic of the SJ is intermediate between those of the WCB and the CCB. Through most of its lifetime, the SJ has a horizontal extent around 50 km and a vertical extent of no more than 1 km.

The SJ has its own evolution that is clearly different to the one that the CCB undergoes. The SJ descent can be divided in two stages:

1. Strong descent accompanied by decrease in θ_w (cooling via sublimation) without system-relative acceleration;
2. Even stronger descent conserving θ_w and with large system-relative acceleration.

Mesoscale instabilities have been evaluated along the back trajectories associated with the SJ. These show that the SJ becomes at first largely unstable to CSI and then to SI/II. The number of unstable trajectories associated with the SJ reaches a maximum as the SJ starts to descend; hence the descent of the SJ corresponds with the reduction of these instabilities, and by the time it reaches the top of the boundary layer most of the instability has been released. At the same time, during descent, the horizontal system-relative wind speed increases by around 15 $\mathrm{m\,s^{-1}}$.

The early stages of descent are most likely associated with the release of diagnosed CSI, but, as the descending airstream loses access to condensed water to evaporate or sublime, the airstream is no longer diagnosed as unstable to this process. However, by this time, the airstream is also unstable to SI. While it is very difficult to prove that the release of an instability causes the flow, this process of destabilisation and subsequent release (or removal) of mesoscale instability in the airstream can be strongly hypothesised to be affecting SJ dynamics.

The production of negative MPV* and, ultimately, PV arises through diabatic heating and cooling in the cloud head. However, this manifests itself through the tilting of horizontal vorticity to produce negative ζ_z, which is then amplified before the final stage of descent by stretching. Chagnon and Gray (2009) similarly describe how stretching and tilting of background vertical (planetary) and horizontal vorticity (associated with vertical wind shear), respectively, can lead to relative vorticity (and so PV) dipoles. Figure 5.19 is a schematic showing the typical SJ trajectory, lying (as indicated by its later descent in the frontal-fracture region) in the intermediate θ_w region of the frontal zone, between

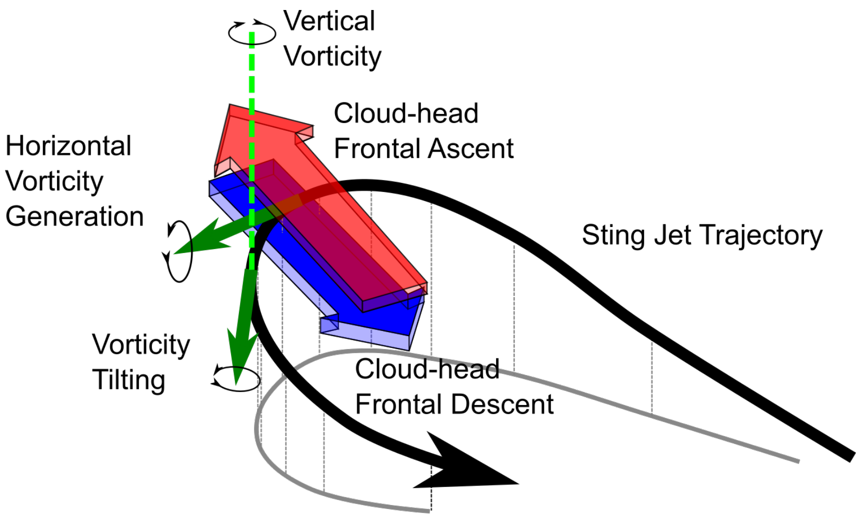

Figure 5.19: Schematic showing the generation of horizontal vorticity in the frontal zone and subsequent tilting along the SJ trajectory.

strong ascent and descent. This is strongly forced by diabatic processes (primarily condensation and evaporation). The horizontal buoyancy gradient here generates horizontal vorticity (associated with the ascent and descent) along the SJ flow (i.e. helicity) that is subsequently tilted downwards when the SJ starts to descend (initially probably due to frontolysis). This therefore generates negative vertical vorticity. In this case we have identified that buoyancy gradient as associated with the bent-back front, but, of course, should there be multiple slantwise ascending/descending regions (e.g. associated with CSI) the same mechanism would apply.

A slantwise-banded structure is present in ζ_z and the SJ travels towards the tip of the cloud head with a band of negative ζ_z that grows in amplitude while retaining its shape and extension while, at the same time, descending and acquiring a substantial slope. This banded structure is also shown in the frontogenesis field. Whereas the broad structure of frontogenesis resembles that already found in previous studies, with widespread frontolysis corresponding to the frontal-fracture region, smaller-scale patterns are present at the tip of the cloud head related to the SJ motion, and the small SJ region is actually associated with a local region of frontogenesis. On reaching the top of the boundary layer, ζ_z rapidly becomes positive. We assume that this largely reflects boundary-layer mixing, which is occurring in a cloudy boundary layer neutral or unstable to moist upright convection.

PV - and θ - tracers show the importance of moist processes, mainly represented in the microphysics and cloud schemes in decreasing PV values below zero and thus generating mesoscale instabilities (SI in this case) along the SJ. However, the tracers do not explain entirely the generation of instability. Further analysis would be required to clarify which moist processes contribute to the onset of instability.

A lower-resolution simulation (with resolution coarser than that required to release mesoscale instabilities) also shows a region of relatively strong winds descending out of the cloud head. On its own, this would satisfy the definition of a SJ: the peak wind speed achieved in the jet is notably strong, around 48 $\mathrm{m\,s^{-1}}$. However, the life history of the SJ in this lower-resolution simulation is in marked contrast to the flow observed in the higher-resolution simulation. The amount of descent is significantly less, so the peak wind speed does not reach 850 hPa (and barely reaches 800 hPa), and there is no clear wind maximum at 850 hPa. The SJ peak wind speed, while strong, is substantially weaker than the 60 $\mathrm{m\,s^{-1}}$ achieved in the SJ in the higher-resolution simulation, although the other main conveyor belts in the system are well represented and only marginally weakened by the lower resolution. The descent occurs in a region associated with frontolysis in the frontal-fracture region, and there is almost no indication of the generation and release of mesoscale instabilities. The SJ in the lower-resolution simulation is entirely consistent with the hypothesis of strong winds caused by the frontal dynamics in the region: descent due to frontolysis into a region with high pressure gradient with flow aligned with the system motion. There is much less fine-scale structure in the frontogenesis field and the broad picture is in close agreement with what is shown in Schultz and Sienkiewicz (2013). The results from the lower-resolution simulation are similar to those found by Slater et al. (2017) and it is reasonable to suppose that this frontolysis-associated SJ, resulting from essentially balanced dynamics, is a relatively robust feature. Given that the authors ran a different model with different initial conditions, it is unknown whether a SJ of the nature found in our higher-resolution simulation would have formed if they had run the model with adequate resolution to enable it to do so.

Windstorm Tini has been demonstrated to be a valuable exemplar of intense SJ-containing extra-tropical cyclones. While wind-profiler observations provided valuable verification of the model-simulations studied, the period of most interest occurred while the storm was still over the sea, thus removing complications due to surface orography. The formation and eventual release of a succession of mesoscale instabilities, from CSI through to SI and II, has been identified; this succession has been suggested, but not highlighted, in other studies. Furthermore, the suppression of the release, and even formation, of these instabilities in coarser-resolution models has been clearly demonstrated. These results have enabled us to draw the conclusion that these instabilities form in a background of (and probably enhanced by) synoptic and frontal dynamics that, in themselves, can lead to SJ-like structures, but that the release of these mesoscale instabilities can substantially enhance the final windspeed. Many of these features have been identified in other storms, but none has yet provided such a complete picture and, indeed, some features may not occur in all SJ cyclones.

To conclude, these results provide a valuable insight into the role of the various mechanisms that have been proposed for SJ formation. Concerning what can be loosely denoted as the 'frontolysis' and 'mesoscale instabilities' mechanisms, the results presented clearly demonstrate, for the first time to the author's knowledge, that not 'either/or' but 'both' mechanisms can occur. Had diabatic processes not been strong enough to generate CSI/SI in windstorm Tini, a very strong wind would still have occurred in the frontal-fracture region and been identified as a SJ. However, the CSI/SI that was generated led to a very substantial enhancement of this, both in strength (by 12 $\mathrm{m\,s^{-1}}$) and in depth of descent. This increase in windspeed (in a region of already strong windspeeds) can lead to a large increase in associated damage. It is very difficult to separate the direct effect of the instability from modifications to the frontogenetic/frontolytic flow as stability decreases and, as concluded by Clark and Gray (2018), there is probably a continuum of behaviour from one extreme to the other. Nevertheless, in this case, the release of instability clearly had a qualitative effect on the flow.

A further lesson to be reinforced from this case (as has been stated in numerous past papers) is that it is essential that models are run with sufficiently high resolution to allow mesoscale instabilities to be released (and, it would seem in this case, to form) even if a SJ associated with frontolysis is evident in lower resolution simulations. Weather forecasts of extra-tropical cyclone events containing sting jets that are generated with insufficient model resolution will likely underestimate the associated wind risk. This finding has implications for medium-range (several day lead time) weather warnings, which are generated using global-domain models.

Chapter 6

Idealised modelling of a Sting Jet cyclone

6.1 Introduction and motivation

In this chapter idealised simulations of moist baroclinic lifecycles with the occurrence of SJs are presented. Section 2.4 shows that only two studies investigating the occurrence of SJs in moist idealised cyclones have been published to date in the literature (Baker et al., 2014; Coronel et al., 2016). These two studies constitute an important initial contribution to the field and show that:

- a SJ can occur in an idealised cyclone that follows the Shapiro-Keyser conceptual model of evolution;
- moisture is a key ingredient in the evolution of the SJ-containing Shapiro-Keyser cyclone;
- the SJ can be associated with an environment neutral or even unstable with respect to mesoscale instabilities such as CSI and (only in Baker et al. (2014)) II;
- domain resolution — horizontal and vertical — affects the occurrence of these instabilities and the dynamics of the associated SJ;
- the occurrence of SJ is robust to changes in environmental static stability whereas its connection to mesoscale instabilities is dependent on these changes.

The simulations presented in this chapter build on these initial findings, confirming that it is possible to produce a SJ in an idealised cyclone and exploring a wider range of parameters and environmental conditions, on which the strength and dynamics of this airstream are dependent, than done in previous works. The range of sensitivity experiments performed and described in this chapter assess also the relationship between the release of mesoscale instabilities and the evolution of the SJ, analysing the robustness of the results and mechanisms presented in Chapters 4 and 5 for windstorm Tini in a wider set of environmental conditions. Idealised simulations of a SJ-containing cyclone following a realistic Shapiro-Keyser evolution are thus a powerful tool to assess the occurrence of a SJ, its strength (both in terms of descent and maximum wind speed) and its underlying dynamics in relation to the environmental conditions, providing a more general description of the robustness of the SJ and of the factors influencing it. Idealised simulations allow us to investigate how SJs and the associated cyclones might change in a wider variety (than the 'current-climate' and North-Atlantic case studies we currently have) of, still plausible, environments.

6.2 Model configuration and chosen initial state

The idealised cyclone in the various experiments described in this chapter develops in a spherical E-W periodic channel version of the Unified Model with ENDGAME dynamics (vn10.5) (see Chapter 3 for more details on the model version). The simulations have been performed using the UK National Supercomputing Service, ARCHER. The initial setup is developed from that of Baker et al. (2014) (described in greater detail in the PhD Thesis associated with the paper, see Baker (2011). This latter reference will be used in the rest of the section as it contains a more extensive description of the initial state. That setup was in turn based on previous works of Boutle et al. (2011), and Polvani and Esler (2007), designed to resemble the cyclones generated in previous dry studies from Thorncroft et al. (1993), with the addition of moisture in Boutle et al. (2011). This section contains an outline of the main features of the initial state chosen for the simulations presented in this chapter. A more thorough description of this setup including the full derivation of the initial balance and pictures of the base state can be found in the Appendix written by Peter Clark, who developed it.

6.2.1 Domain geometry and initial balance

The simulations described in this chapter are performed in a spherical geometry, with the periodic domain extending from 12 °N to 78.5 °N in latitude and from 20 °W to 25 °E in longitude. Baker (2011) contains a thorough description of the literature showing that spherical geometry has to be preferred when the target is to generate LC1-type cyclones of Thorncroft et al. (1993), whereas Cartesian geometry tends to produce cyclones more similar to the LC2 framework. Thorncroft et al. (1993) highlighted that LC1 cyclones develop similarly to the Shapiro-Keyser conceptual model with the occurrence of frontal fracture and, in later stages, warm seclusion (see Section 2.2.2); hence the choice of spherical geometry in this study.

The setup of thermal wind balance (Hoskins and James, 2014) in the initial state has been improved by Peter Clark with respect to what was used in Baker et al. (2014), based on Boutle et al. (2011). In more detail, Baker (2011) use a shallow atmosphere approximation and when they have to iteratively correct the temperature values after having first computed pressure integrating hydrostatic balance, they adjust the θ_v profile by using a constant value to make that at the surface at the jet centre equal to a reference θ_v profile. In this study instead all the terms of the deep atmosphere equations of motion are retained and the entire vertical θ_v profile is adjusted to make that at the jet centre equal to the reference. As a result of this improvement, the instability issues described in Baker (2011) are no longer present and so it has been possible to use a realistic temperature profile with a central value of potential temperature of 295 K at the surface, as opposed to the rather cold temperatures occurring in the former study. The SJ occurring in the control simulation shows values of θ_w around 285 K, 10 K warmer than the one in Baker (2011). The SJ generating when simulating the Great Storm (Clark et al., 2005) shows θ_w around 286 K while simulations of Gudrun (Baker, 2011), Ulli (Smart and Browning, 2014) and Tini (see Chapter 4) show SJs with θ_w around 279 K, 281 K and 278 K, respectively. This confirms that the thermal properties of the SJs generated in the simulations presented in this chapter are consistent with case studies, warm ones like the Great Storm in particular.

6.2.2 Initial jet specification, temperature profile and moisture set up

Following Baker (2011), the Polvani and Esler (2007) setup has been extended and amended in the way specified below. Assuming that the jet, which is zonally symmetric with no barotropic shear, is confined between latitudes ϕ_s and ϕ_e, ϕ^* is defined as:

$$\begin{aligned} \phi^* &= 0 & \phi &< \phi_s, \\ &= (\pi/2)(\phi - \phi_s)/(\phi_e - \phi_s) & \phi_s \leq \phi &\leq \phi_e, \\ &= 0 & \phi &> \phi_e. \end{aligned} \tag{6.1}$$

Then

$$u(r, \phi) = u_0 F_\phi(\phi) F_r(r) \tag{6.2}$$

where

$$F_\phi(\phi) = sin^3(\pi sin^2 \phi^*) \tag{6.3}$$

$$F_r(r) = \left(\frac{z}{z_T}\right)^\gamma exp\left\{\delta\left[1 - \left(\frac{z}{z_T}\right)^{\frac{\gamma}{\delta}}\right]\right\} \tag{6.4}$$

z is $r - r_0$ with r_0 being at the surface, z_T is the height of the tropopause above the surface and the values used in this study are $\phi_s = 15°$N, $\phi_e = 85°$N, $z_T = 10^4$ m, $u_0 = 45$ m s^{-1} (for the control run), $\delta = 0.2$ and $\gamma = 1$. This setup produces a jet centred at 50°N, with wind speed increasing from zero at the surface to a maximum u_0 at the tropopause and then decreasing upwards in the stratosphere. The values specified above for different parameters follow from Baker (2011), where the original values from Polvani and Esler (2007) were modified in order to generate cyclones more similar to real cases. In particular, the jet was moved further north and the baroclinic zone was made narrower changing ϕ_s from 0°N to 15°N, ϕ_e from 90°N to 85°N and thus moving the jet centre ϕ_c from 45°N to 50°N. Moreover, Baker (2011) looked for a stronger wind shear in the upper troposphere and a more realistic height of the tropopause reducing δ from 0.5 to 0.2 and z_T from 13 to 10 km.

As explained in the previous section, the temperature profile is calculated using thermal wind balance and from this the pressure field is derived using hydrostatic balance.

The vertical potential temperature profile used is the same as in Baker (2011):

$$
\begin{aligned}
\theta(z) &= \theta_0 + \Gamma_T z && z \leq z_T \\
&= \theta_0 + \Gamma_T z_T + \Gamma_s (z - z_T) && z > z_T
\end{aligned}
\tag{6.5}
$$

with $\Gamma_T = 0.004\,\mathrm{K\,m^{-1}}$, $\Gamma_S = 0.025\,\mathrm{K\,m^{-1}}$, $\theta_0 = 295\,\mathrm{K}$ and $z_T = 10^4\,\mathrm{m}$ (in fact Baker (2011) used $\Gamma_S = 0.016\,\mathrm{K\,m^{-1}}$ but that value would result in an unstable profile in the thermal-wind balanced setup of this study, as explained in better detail in the next paragraph when describing the moisture profile).

The moisture profile is defined in terms of relative humidity (RH), as

$$
\begin{aligned}
RH(r,\phi) &= RH_0 \Big[1 - 0.9 R(\phi) \Big(\frac{r - r_0}{z_T} \Big)^{\alpha} \Big] && r - r_0 \leq z_T \\
&= 0.0625 RH_0 && r - r_0 > z_T
\end{aligned}
\tag{6.6}
$$

with

$$
\begin{aligned}
R(\phi) &= 1.0 && \phi < \phi_s \\
&= 1 - 0.5 \frac{\phi - \phi_s}{\phi_e - \phi_s} && \phi_s \leq \phi \leq \phi_e \\
&= 0.5 && \phi > \phi_e
\end{aligned}
\tag{6.7}
$$

with $RH_0 = 0.8$, in the control simulation, and $\alpha = 1.25$. This follows from Baker (2011), as the setup for Polvani and Esler (2007) was designed for a dry simulation. As the thermal wind balance is computed in terms of θ_v without knowing the mixing ratio, m_v, the latter has to be computed iteratively. This produces a statically unstable solution in the stratosphere if the parameters chosen by Baker (2011) are used, with very large values of mixing ratio in the stratosphere leading to low θ_v and ultimately resulting in the model run failing after about a day of simulation (this issue did not occur in their work as a consequence of a different computation of m_v, with an initial state that was stable but effectively not balanced). The value of static stability in the stratosphere is not one of the main concerns of this study. Hence, to prevent the model to fail, Γ_S has been increased to $0.025\,\mathrm{K\,m^{-1}}$ and m_v decreased to $10^{(-6)}$ above the tropopause. The initial configuration is now slightly statically unstable in the high troposphere in a small region in the tropics but it does not fail.

6.2.3 Temperature perturbation

A small temperature perturbation is applied to the initial state to generate baroclinic growth, following Polvani and Esler (2007). The perturbation is independent of height and defined as

$$T'(\lambda, \phi) = T_p cos(m\lambda)[sech(m(\phi - \phi_c))]^2 \tag{6.8}$$

where λ and ϕ are, respectively, longitude and latitude, m is the wavenumber of the perturbation, $\phi_c = 50°$N is the latitude of the jet centre and $T_p = 1$K. A wavenumber of $m = 8$ (consistent with the 45° zonal extent of the model domain) is used in this study as in Baker (2011), chosen to generate cyclones with a smaller length scale, consistent with observed case studies, than those in Thorncroft et al. (1993) and Polvani and Esler (2007) (who used $m = 6$).

6.2.4 Model resolution

Different studies described throughout Chapter 2 highlighted the importance of model resolution in simulating SJ, a mesoscale feature that might not be resolved even by models capable to simulate the synoptic development of a Shapiro-Keyser extratropical cyclone. In particular Clark et al. (2005) highlighted that a correct representation of the SJ horizontal scale and of its slope of descent are essential when simulating SJ evolution. Hence, as the SJ has a horizontal scale of about 50–100 km, models with horizontal spacing larger than 10–12 km are not ideal for simulating SJs. They then recalled the study of Persson and Warner (1993), who pointed out that a necessary condition to resolve CSI release via slantwise circulation is an aspect ratio of 1:50 in model resolution. This means that for a model with horizontal spacing around 12 km, the vertical spacing between levels should be around 200–250 m at heights that are relevant for SJ dynamics. The analysis of windstorm Tini confirmed these constraints showing that, while the higher-resolution simulation displayed a SJ driven by the release of mesoscale instabilities with wind speed almost reaching 60 m s^{-1}, a coarser-resolution simulation failed to develop any instability associated with the frontolysis-related SJ which only reached 45 m s^{-1} (see Section 5.3). For this reason the idealised control run uses the same resolution as in the high-resolution simulation of Windstorm Tini, i.e. a horizontal spacing of 0.11° and 70 vertical levels. Table 6.1 shows the height of vertical model levels (ρ levels) between 1000 m and 3000 m, i.e. where the SJ evolves and descends, showing that for the 70-levels setting the vertical spacing stays between 120 m and 200 m in this region. Two simulations with coarser resolution are run to test the sensitivity of the idealised SJ with respect to model resolution. The horizontal spacing of these coarser resolution simulations is of 0.25° and 0.4° with respectively 63 and 38 vertical levels (see vertical spacing in Table 6.1).

70 levels setup	63 levels setup	38 levels setup
1013	1037	1130
1133	1210	1450
1260	1397	1810
1393	1597	2210
1533	1810	2650
1680	2037	
1833	2277	
1993	2530	
2160	2797	
2333		
2513		
2700		
2893		

Table 6.1: Table showing the height (m) of vertical model levels (ρ levels) between 1000 m and 3000 m in the different configurations used for the idealised experiments.

6.3 Identification and characterisation of a SJ in the control simulation

The results from the control simulation are presented in this section. An initial overview of the cyclone's structure is followed by the identification of a sting jet in the simulation, according to the definition in Clark and Gray (2018) (see the last paragraph of Chapter 2). This means that a distinct wind maximum at low levels is looked for and identified in the frontal-fracture region at the time of its widening. Backward (and forward) trajectories are computed from the grid points selected as belonging to the SJ, in order to verify that the airstream descends from the tip of the cloud head and to describe its characteristics, in terms of its kinematics and of the behaviour of relevant physical quantities. An analysis of the evolution of mesoscale instabilities on the SJ, with particular focus on PV, concludes the section clarifying the dynamics of the airstream.

6.3.1 Overview of the storm's evolution

As discussed in Chapter 2, SJs can occur in intense extratropical cyclones following the Shapiro-Keyser conceptual model of evolution. Before assessing the occurrence of a SJ in the idealised simulation, it is thus necessary to check that the moist baroclinic wave does evolve according to this model. Figure 6.1 shows the time evolution of surface pressure and potential temperature at 850 hPa throughout the main stages of evolution of the idealised moist baroclinic wave. Figure 6.1a displays a cyclone in its initial stage of development, 72 hours from the start of the run, with northward advection of warm air associated with the disturbance. Figure 6.1b refers to 84 hours after the run start and shows that the foremost part of the warm advection is pointing westward, going towards a frontal 'T-bone' structure with the opening of a frontal fracture to the south of the cyclone centre and the development of a bent-back front. At 96 hours from the start (Figure 6.1c) those features are fully developed, as the zoomed image shows, with the cyclone that is now deeper (minimum surface pressure below 970 hPa) and resembling a typical Shapiro-Keyser cyclone in Stage III of its development (see Section 2.1.1). Figures 6.1d and 6.1e show the warm seclusion on the cyclone centre almost completely encircled by the wrapped-up bent-back front, in what resembles a mature stage of evolution of a Shapiro-Keyser cyclone. The evolution just described follows the four stages of the Shapiro-Keyser model, correctly displaying its main features in time and space. In particular, it is between 84 and 96 hours (in particular) from the start that the cyclone displays a widening frontal fracture. Hence, it is in that time range that the full development of a SJ can be expected to take place.

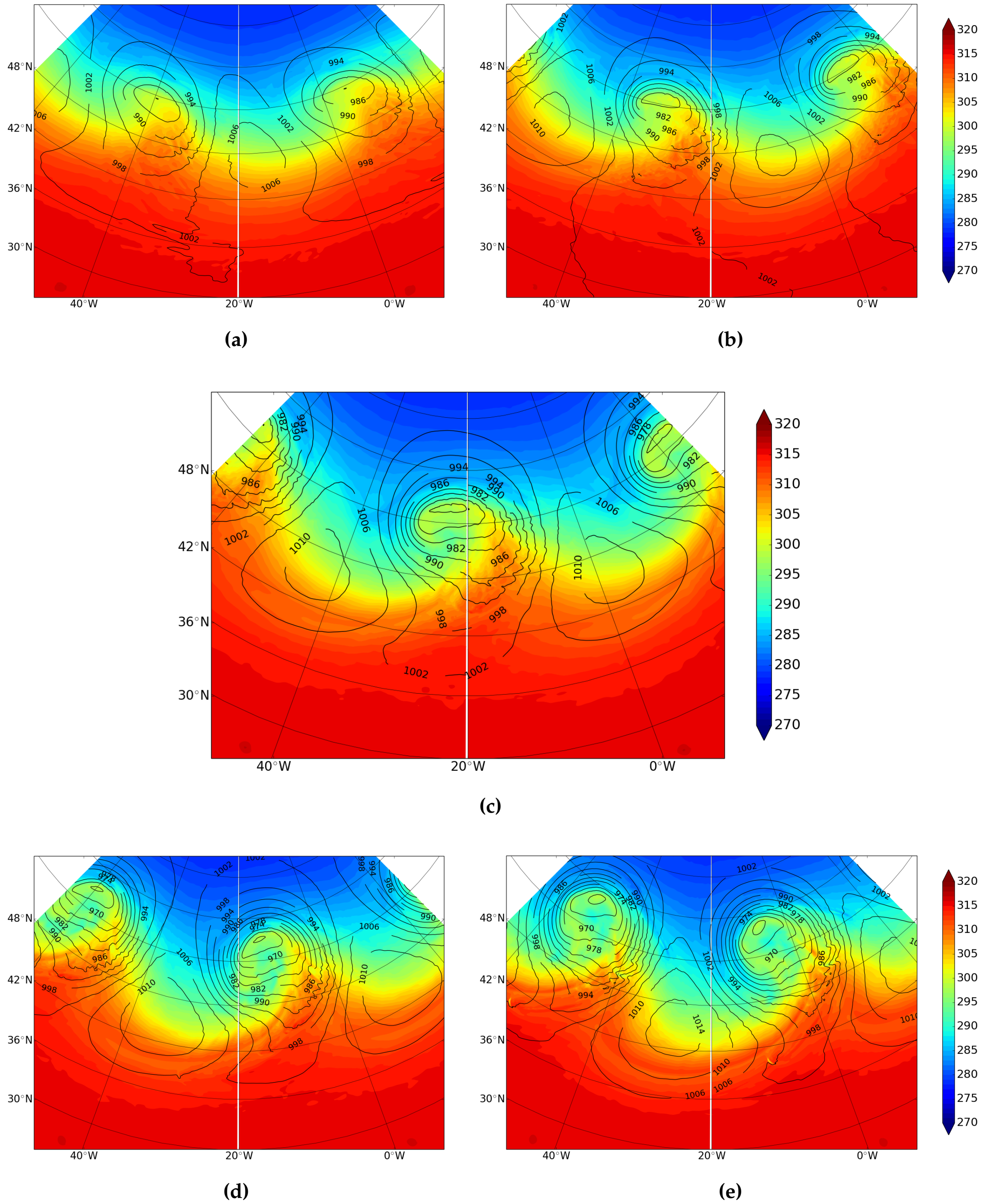

Figure 6.1: Surface pressure (black contours, hPa) and potential temperature at 850 hPa (colours, K) after (a) 72, (b) 84, (c) 96, (d) 108, and (e) 120 hours from the start of the control simulation. Note that the model domain (whose original zonal extension goes from 20°W to 25°E with periodic E-W boundary conditions) is repeated zonally to facilitate visualisation.

6.3.2 Analysis of strong winds in the frontal-fracture region

Figure 6.2a shows the baroclinic wave after 94 hours of simulation, when a low-level wind maximum can be clearly identified in the frontal-fracture region, with values ex-

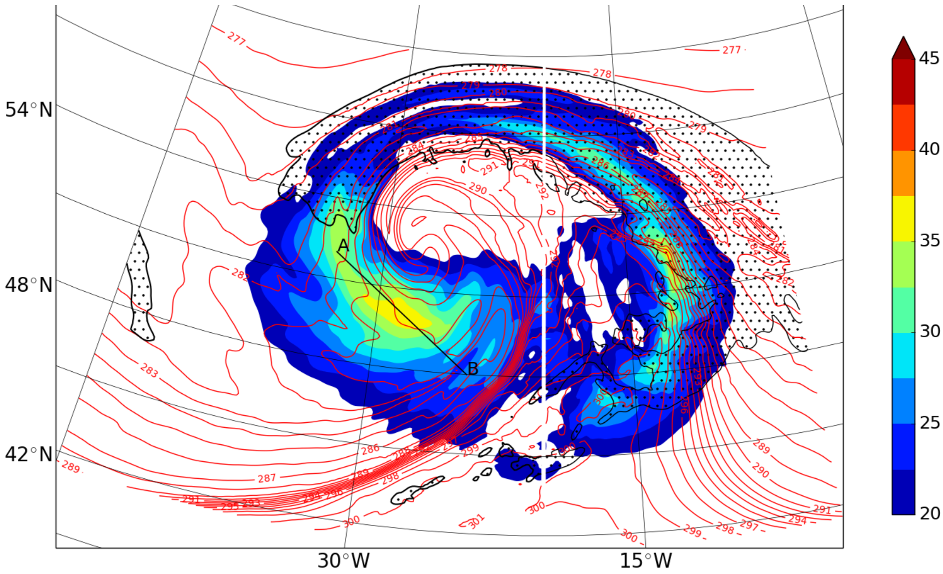

(a)

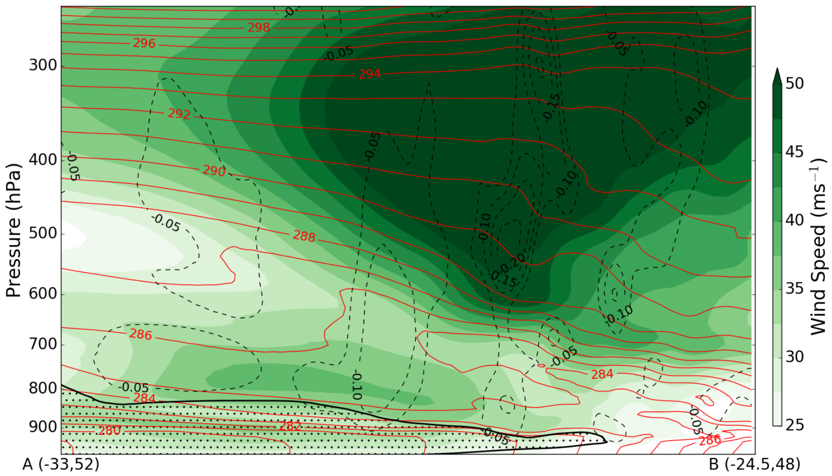

(b)

Figure 6.2: (a) Wind speed at 850 hPa (contours, m s^{-1}), wet-bulb potential temperature at 850 hPa (K, red lines) and cloudy regions at 700 hPa (RH$_{ice}$ >80%, black lines and dotted regions) after 94 hours from the start of the control simulation. Note that the model domain (whose original zonal extension goes from 20°W to 25°E with periodic E-W boundary conditions) is repeated zonally to facilitate visualisation but only data between 45°W and 5°W are shown here. (b) Cross section (transect AB in panel (a) of wind speed (green filled contours), negative vertical velocity (dashed black lines, ms^{-1}), wet-bulb potential temperature (red lines, K) and cloudy regions (RH$_{ice}$ >80%, thick black lines).

ceeding 35 m s^{-1} at 850 hPa. Other low-level strong-wind regions of similar or even larger magnitude can be found in other areas of the cyclone or at different times, e.g. in a more mature stage of the storm's evolution. The largest values of wind speed at 850 hPa in the whole lifetime of the storm, close to 40 m s^{-1}, occur around 120 hours from the start and are associated with the CCB (not shown). As discussed in Section 2.4, where the relevant literature is reviewed, and extensively assessed in Chapters 4 and 5 with the analysis of windstorm Tini, the SJ descends into a widening area of weak gradients and frontolysis, located behind the primary cold front, that we call the frontal-fracture region. For this reason, the wind maximum displayed in Figure 6.2a is the only one that can be associated with the occurrence of a SJ. This figure shows an intense cold front, separating airmasses with around 10 K of difference in wet-bulb potential temperature. The frontal-fracture region is located in between this cold front and the bent-back front, partially wrapped around the cyclone centre. An elongated region of wind speed above 30 m s^{-1} goes from the tip of the cloud head to the frontal-fracture region, where its maximum values exceed 35 m s^{-1}. It has to be noticed that the cloud-head tip at 700 hPa displays some waviness, consistent with the occurrence of cloud-banding.

Another elongated strong-wind region runs along the warm front, only locally up to 35 m s^{-1}, associated with the WCB. A cross section taken along the frontal-fracture region (Figure 6.2b) shows an evident fold in wet-bulb potential temperature inserted in an area of weak θ_w-gradients, underneath a more stable layer of downward-sloped isentropes in the middle troposphere. The wind maximum detected previously in 6.2a at 850 hPa can be clearly identified in this cross section, located at the bottom of the θ_w-fold, surrounded by regions of negative vertical velocity and with its core close to 40 m s^{-1} around 800 hPa. This wind maximum sits on top of the saturated boundary layer, which is neutral to slightly conditionally unstable but capped by a strongly stable layer, and contains a weaker low-level jet around 900 hPa possibly associated with the CCB's front edge. The situation depicted by these two panels agrees with the description of SJ-associated wind maxima in the literature (Section 2.4) and displays similarities in its main features with the SJ in windstorm Tini (Section 4.2), although with weaker wind speed and differences in the geometry of the frontal-fracture region and of the θ_w-fold. As for the analysis of windstorm Tini, Lagrangian trajectories are used in the next sections to assess the characteristics of the identified SJ.

6.3.3 Description of selected starting points for sting-jet trajectories

The grid points with wind speed exceeding 38.51 m s^{-1} at 94 hours from the start located at 805 hPa (the pressure level identified as the core of the wind maximum) or in contigu-

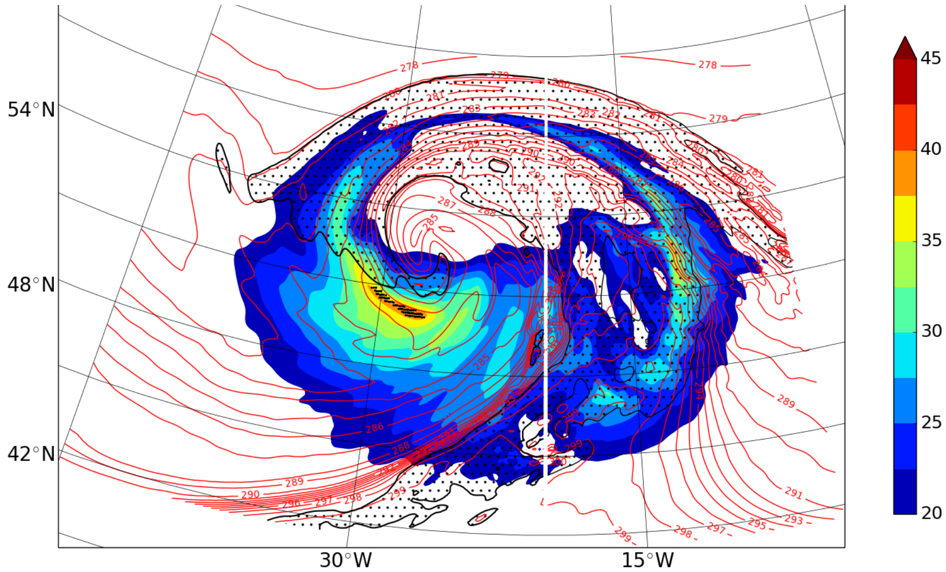

Figure 6.3: Wind speed (contours, m s^{-1}), wet-bulb potential temperature (K, red lines) and cloudy regions at 805 hPa (RH_{ice} >80%, black lines and dotted regions) after 94 hours from the start of the control simulation. AB is the same transect as in Figure 6.2. Black dots show the horizontal locations of SJ trajectories. Note that the model domain (whose original zonal extension goes from 20°W to 25°E with periodic E-W boundary conditions) is repeated zonally to facilitate visualisation but only data between 45°W and 5°W are shown here.

ous levels (i.e. aligned vertically with the grid points selected at 805 hPa to form uninterrupted columns of points with speed exceeding the threshold) are selected as starting points for SJ trajectories. The rather unusual value of 38.51 m s^{-1} has been chosen as threshold to produce an airstream composed of exactly 100 trajectories that represent the core of the descended jet. Figure 6.3, analogous to Figure 6.2a but with all the fields evaluated at 805 hPa, shows how the starting points selected for the trajectories are all located in the core of the wind maximum area in the frontal-fracture region.

6.3.4 Analysis of relevant physical quantities on the airstream

Figure 6.4 shows the evolution of various physical quantities along the trajectories identified above as the core of the SJ. Figure 6.4a shows a steady increase in wind speed between 81 and 94 hours front the start, with maximum values close to 40 m s^{-1}. This increase is displayed by all the trajectories after 85 hours, indicating that from that time the different populations of trajectories, showing different values of wind speed in early hours, behave as a single coherent airstream. The heterogeneous behaviour of different trajectories in the first part of the time period in analysis is evident also in Figure 6.4b,

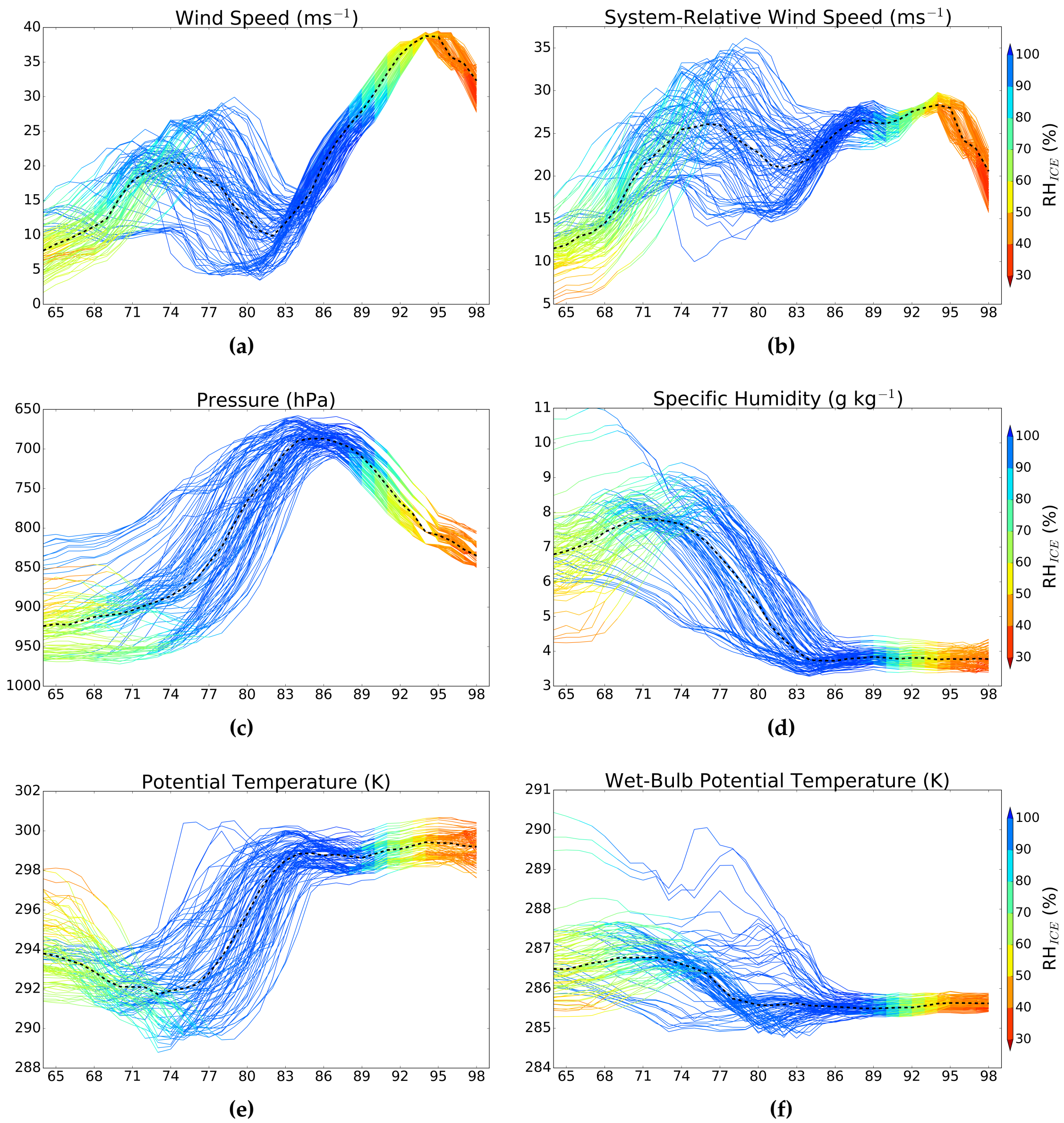

Figure 6.4: Timeseries (hours since start of the run) of (a) wind speed, (b) system-relative wind speed, (c) pressure, (d) specific humidity, (e) potential temperature and (f) wet-bulb potential temperature along SJ trajectories. Colours indicate relative humidity with respect to ice along trajectories and the dashed line indicates the median of trajectories.

which shows wind speed in a system-relative reference frame, i.e. having subtracted the motion of the storm (mainly zonal) from the earth-relative wind speed. An increase in system-relative wind speed is thus not associated with the airstream rotating around the cyclone centre and moving eventually in the same direction of the overall motion of the storm. Nevertheless, this figure shows that system-relative wind speed increases coherently for most trajectories by around 5 m s^{-1} between 84 and 88 hours. For approximately 1/3 of the trajectories the increase in system relative wind speed between 82 and 88 hours reaches 10 m s^{-1}. These values are consistently smaller than the average 15 m s^{-1} detected in windstorm Tini but they still indicate a non-negligible local acceleration of the airstream that is not related to the overall motion of the storm. The increase in (earth-relative) wind speed is associated with a decrease in relative humidity, consistent with the descent of the airstream after 84 hours shown in Figure 6.4c. The SJ increases its median pressure by 95 hPa in 5 hours, moving from 710 to 805 hPa between 89 and 94 hours, during the most intense descent. After 94 hours the descent gets weaker, as the SJ starts decelerating. This descent comes after an earlier ascent in which different populations of trajectories, mainly starting below the pressure level of 850 hPa, merge into a single airstream located around 700 hPa.

Throughout the ascent all the trajectories stay close to saturation. At the same time, after an initial increase, the specific humidity drops to less than 4 g kg^{-1}, approximately half the value at the beginning of the ascent, suggesting the occurrence of a substantial amount of condensation and precipitation while the airstream ascends within the cloud head (Figure 6.4d). In the first part of the descent, between 84 and 89 hours, the airstream stays close to saturation displaying a small increase in specific humidity, around 0.1 g kg^{-1}. This increase is one order of magnitude smaller than in windstorm Tini (see Section 4.4) indicating that the effects of evaporation and sublimation on the dynamics of the airstreams are substantially smaller. Figures 6.4e and 6.4f confirm this indication as it is difficult to find any non-negligible cooling signal in the period indicated. The presence of condensational heating during the ascent and the absence of evaporation cooling during the subsequent descent suggest the occurrence of precipitation removing the condensate during the ascending stages. Figure 6.4e confirms this hypothesis showing an associated median warming around 7 K during the ascent. Figure 6.4e shows that θ_w stays almost constant on the airstream during its descent, with variations not exceeding 0.1 K, indicating the accuracy of trajectories and confirming their 'single coherent airstream' behaviour. This is opposed to the large variations, up to a few K, happening particularly by the beginning of the ascent where different populations of trajectories merge before starting to travel along a narrow frontal zone. Hence, these trajectories can be safely considered representative of the motion of the SJ intended as a physical airstream only from halfway through the ascent, when the variations in θ_w to the end of the descent reduce below 1 K. This does not affect the value of this tool for the analysis as (see the next section) it is during the second part of the ascent and throughout the descent of the SJ that the dry mesoscale instabilities occur along the jet.

To summarise, the SJ identified shows an ascent-descent pattern that has been described in various previous studies (although the ascent is absent in windstorm Tini). The rate of the descent reaches values around 20 hPa/hour for 5 consecutive hours, substantially smaller than in windstorm Tini where a pressure increase rate around 50 hPa/hour is maintained for 3 hours. However, the slower development of the cyclone in this idealised setup has to be taken into account. This descent is associated with a substantial increase in wind speed that, again, is weaker than that shown by the simulation of windstorm Tini but still reaches values up to 40 m s^{-1} and exceeds by at least 5 m s^{-1} the acceleration expected by the location of the airstream in relation to the overall motion of the storm. The occurrence of condensation during the ascent of the airstream is evident while evaporative/sublimational cooling at the start of the descent looks small. In the next section the evolution of instabilities on the airstream is assessed, to complete the analysis of the dynamics of this idealised SJ.

6.3.5 Evolution of mesoscale instabilities along the airstream

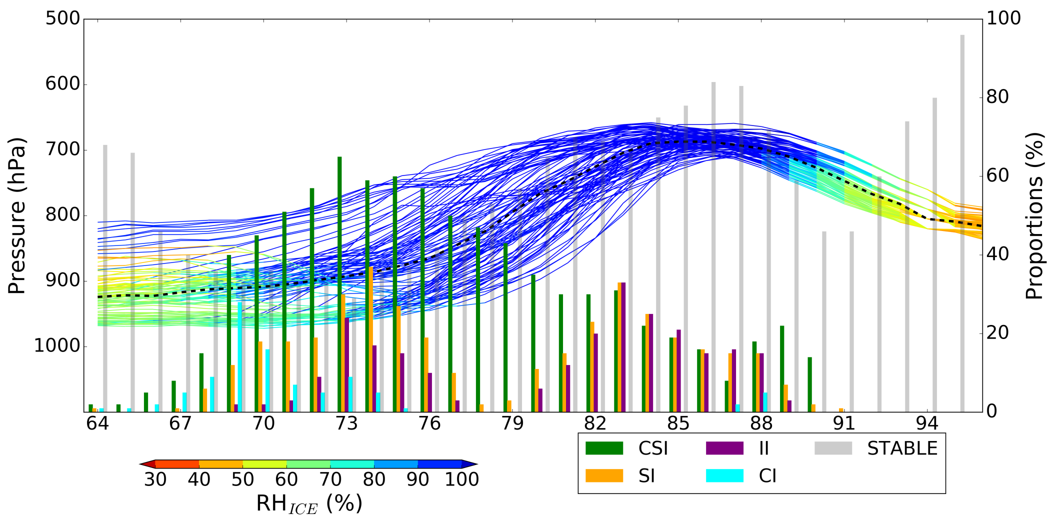

Figure 6.5: Timeseries (UTC) of pressure (colours indicate relative humidity wrt ice) and diagnosis of instability conditions along the trajectories (see Table 3.1).

Figure 6.5 shows the time-pressure profile of the airstream overlaid on bars representing the percentage of trajectories unstable to different instabilities at each time. In the hours preceding the ascent-descent dynamics of the airstream the number of trajectories unstable to CSI increases up to a temporary maximum over 60%. At the same time the number of trajectories unstable to SI gets close to 40%. As documented in the previous section, the non-conservation of quantities like θ_w does not allow to consider the bundle of trajectories as an accurate representation of a coherent airstream. Nevertheless, the large numbers of points where instability to CSI and SI is detected indicates the occurrence of widespread areas with negative PV and MPV*. Another interesting indication of the environment in which the airstream travels in these early hours is related to the smaller number of trajectories unstable to II than to SI, see for example at 74 hours from the start. Moist static instability is almost negligible at that time, as indicated by CI, and so it has to be dry static instability too. Hence, this means that a negative sign of PV in locations where ζ_z is not negative does not come from a negative value of static stability but from negative values of the horizontal components of the dot product between vorticity and potential temperature, indicating a very tilted environment in terms of momentum — and theta — lines.

During the ascent of the airstream there is a second build-up of SI and II, both exceeding 30% of trajectories at 83 hours, just above the value for CSI. As the airstream reaches the top of its ascent and then starts the subsequent descent, the values steadily decrease for all these instabilities. The number of trajectories unstable to dry mesoscale instabilities at this stage is substantially smaller than in windstorm Tini, where halfway through the descent around 75% of the trajectories were labelled as unstable to SI and II (Section 5.1). However, the evolution depicted does suggest that dry mesoscale instabilities such as SI and II do take part in the dynamics of SJ acceleration and descent. In the next section the location and extension of unstable regions, along with their relation to the SJ, is further assessed via maps of PV on pressure levels.

6.3.6 Evolution of potential vorticity in the cloud head

Figure 6.6 displays the evolution of PV at the tip of the cloud head and the associated location of trajectories between 83 and 91 hours from the run start. In each one of the panels

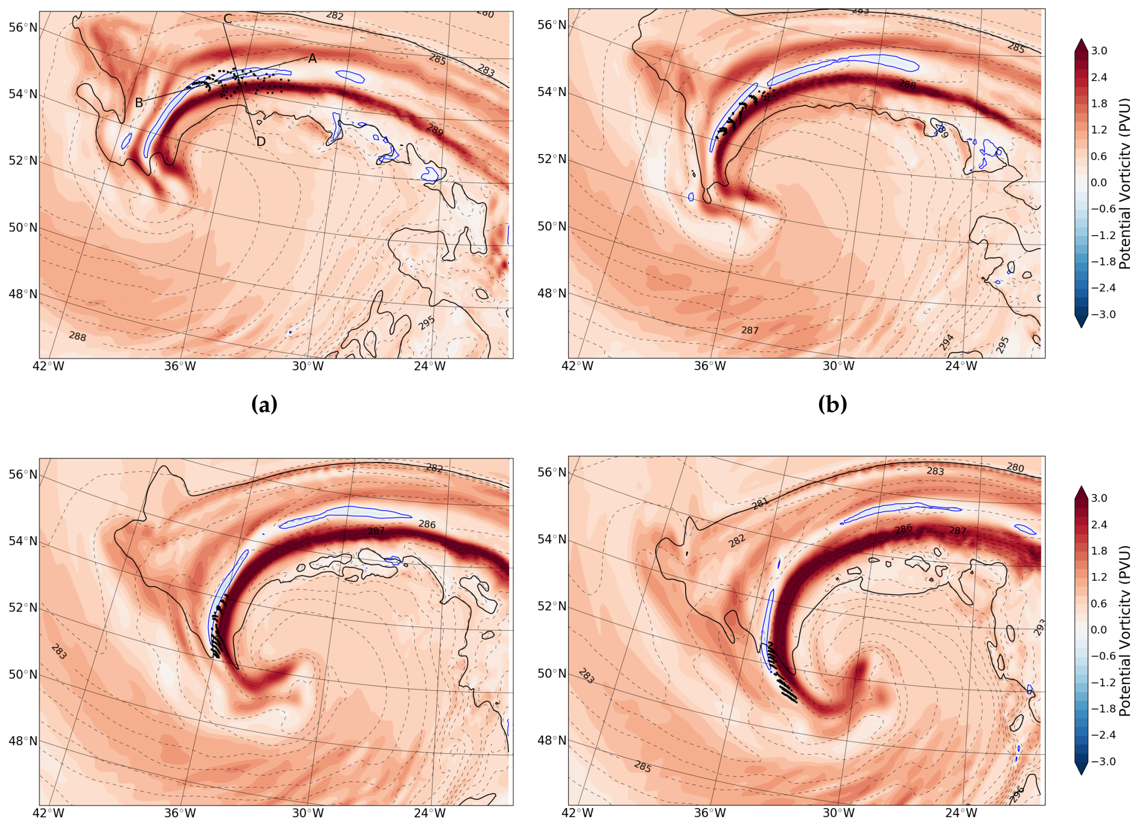

(a) (b) (c) (d)

Figure 6.6: Potential vorticity (shading, PVU), wet-bulb potential temperature (thin dashed contours every 1 K) cloudy regions (RH_{ice}=80%, black solid contours) at (a) 700 hPa at 83 hours from run start, (b) 685 hPa at 86 hours, (c) 715 hPa at 89 hours, (d) 745 hPa at 91 hours. Black dots show the locations of the trajectories.

the pressure level chosen is the closest to the median pressure of the SJ trajectories at that time. Figure 6.5 shows that 30% of the SJ trajectories become unstable to symmetric instability just before starting to descend, around 83 hours from the start. These panels give an insight into the evolution of SI along the trajectories from that instant onwards. All the panels highlight the presence of different 'pulses' of negative PV moving along a line in the cloud head, located just on the outer side of the warm, and then bent-back, front. The front is indicated by high values in PV that are consequence of large positive values in the vertical component of absolute vorticity, due to the horizontal wind shear associated with the front, and a tighter horizontal gradient in potential temperature across the front. The SJ trajectories travel around the front within the cloud head, along the same line on which the localised regions of negative PV move. When the airstream then reaches the banded tip of the cloud head and exits from it starting to descend, the negative values of

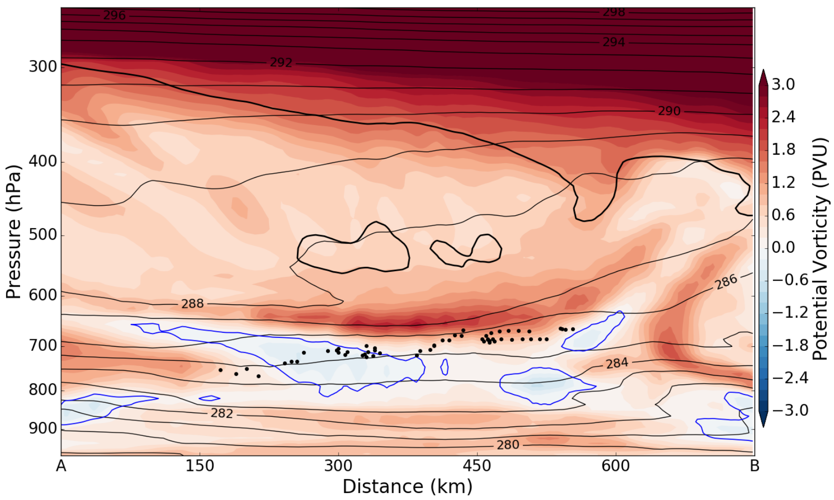

(a)

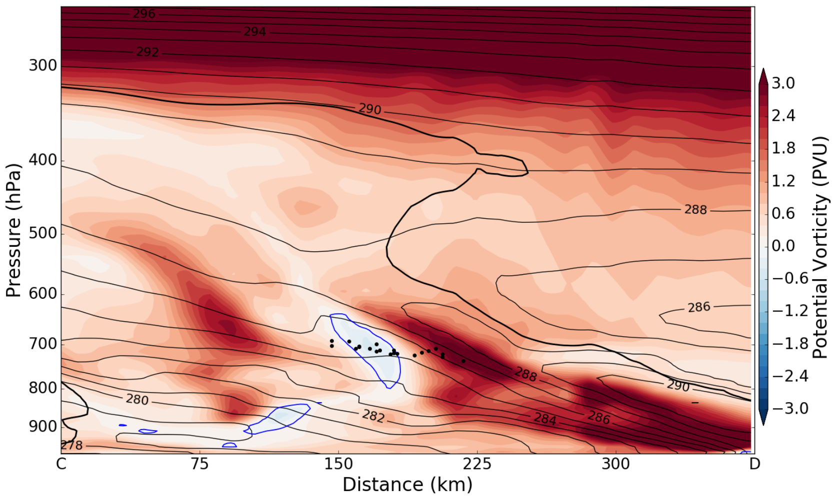

(b)

Figure 6.7: Cross sections on transect (a) AB and (b) CD of potential vorticity (shading), wet-bulb potential temperature (thin black contours, K) and cloudy regions (RH_{ice}=80%, black bold contours). Black dots show the perpendicular projection on the transect of the trajectories which are less than 25 km distant from the relevant transect.

PV gradually disappear, suggesting a release of symmetric instability via the slantwise descent experienced by the SJ trajectories.

Figure 6.7 shows two cross sections, one along-flow and one across-flow, taken at 83 hours from the start, i.e. at the instant when the number of SI-unstable trajectories is maximum. The transects of the sections are visible in Figure 6.6a. The along-flow section (Figure 6.7a) shows a band of negative PV centred around 300 km from point A, located at 700 hPa and slightly downward tilted. Some of the trajectories travel within this band, forming the 30% SI-unstable subset of the airstream already mentioned. It is important to note that some other trajectories are located ahead of this band, somewhat closer to the tail of another band of negative PV which is already in the tip of the cloud head, as the map shows. In general, the presence of several localised regions with small or negative values of PV suggests that the area close to the bent-back front in the cloud head represents a favourable environment for the onset of SI (or at least reduced symmetric stability). The across-flow section (Figure 6.7b) instead highlights the slantwise dipole of PV located along the narrow frontal zone, at around 700 hPa and between 150 and 225 km from point C, where the SJ moves. This pattern, along with the presence of positive static stability (not shown), suggests the occurrence of an ascent-descent pattern orientated with the slope of the frontal zone. This is consistent with the mechanism of generation of negative horizontal vorticity, that can be eventually tilted into negative vertical vorticity, outlined in the analysis of windstorm Tini.

To summarise, this evolution, despite the differences in magnitude and timing, recalls the behaviour of instabilities on the SJ airstream depicted in the analysis of windstorm Tini (see Section 5.2, albeit referred to ζ_z instead of PV) and indicates the presence of localised regions of negative PV created in the cloud head along a narrow frontal zone. These regions move towards the cloud-head tip and can be associated with a jet that descends and accelerates while the negative PV ceases to be present.

6.4 Sensitivity experiments

6.4.1 Motivation for and summary of sensitivity experiments

In the previous section it is shown that mesoscale instabilities (conditional and dry) play an active role in the evolution of the SJ in the control simulation. Taking advantage of the versatility of an idealised model, it is possible to explore different environmental conditions and to assess the robustness of the SJ occurrence and evolution. As discussed in the introduction to this chapter, initial sensitivity experiments (respectively, on static stability and on model resolution) have been performed in Baker et al. (2014) and in Coronel et al. (2016). The aim of this study, having produced a control run in which a SJ occurs and is associated with the release of symmetric instability, is to assess the evolution of the SJ exploring a wider range of parameters and environmental conditions and to assess the robustness of the SJ's occurrence and strength and the link with mesoscale instabilities. Variations in model resolution, jet strength, moisture content and magnitude of moist processes are thus investigated. Table 6.2 provides a summary of the parameters chosen for the different experiments.

In the first set of experiments the effect of horizontal and vertical model resolution on the evolution of the SJ is assessed. As discussed in Section 6.2.4, previous literature and the analysis of Windstorm Tini provide pieces of evidence of the dependence on model resolution of the SJ dynamics. This set of experiments consists of two simulations with horizontal spacing increasing from the 0.11° of the control run to 0.25° and 0.4° (and vertical resolution getting accordingly coarser as shown in Table 6.1).

The second set of experiments is focused on the effect of moisture on the SJ evolution. The value of the maximum initial relative humidity $RH_0 = 80\%$ (see Equation 6.6) was chosen by Baker et al. (2014) to produce a profile similar to real soundings. Increasing it to 90% and decreasing it to 70% in two different simulations provides an assessment of the influence of moisture content to the evolution of the cyclone and of the associated SJ.

The third set of experiments is composed of four simulations with different values of u_0, the initial central value of the jet-stream speed. u_0 takes the values of 35 m s^{-1},

Experiment	horiz. res. (°)	vert. res. (levels)	u_0 (m s^{-1})	RH_0 (%)	LH/LH_0
control	0.11	70	45	80	1
025deg	0.25	63	45	80	1
04deg	0.4	38	45	80	1
rh90	0.11	70	45	90	1
rh70	0.11	70	45	70	1
jet35	0.11	70	35	80	1
jet40	0.11	70	40	80	1
jet50	0.11	70	50	80	1
jet55	0.11	70	55	80	1
lh75	0.11	70	45	80	0.75
lh87	0.11	70	45	80	0.875
lh112	0.11	70	45	80	1.125
lh125	0.11	70	45	80	1.25

Table 6.2: Table showing the parameter values chosen for the different experiments. u_0 and RH_0 indicate, respectively, the maximum initial values of wind speed and relative humidity, as defined in Section 6.2.2. LH/LH_0 indicates the coefficient multiplying the latent heat constants, for both condensation and freezing. See Table 6.1 for the vertical spacing in the different level configurations.

40 m s^{-1}, 50 m s^{-1} and 55 m s^{-1} (compared with u_0 =45 m s^{-1} in the control run, see Equation 6.2), so that it is possible to assess the effect of different jet strength and, as a consequence, of different vertical wind shear and meridional temperature gradient on the evolution of the cyclone and of the associated SJ, if present.

The last set of experiments consists of four simulations in which the physical latent heat constants of condensation and freezing are scaled by 0.75, 0.875, 1.125 and 1.25, following Büeler and Pfahl (2017). This additional set of experiments is treated separately for essentially two reasons. The first reason is that changing the values of thermodynamical constants such as the latent heat ones produces an unphysical situation with latent heat processes that are more or less intense than in the real world. Furthermore, there is an inconsistency in the model as not all the variables can be updated according to the changes in these constants. In particular, the values of the specific humidity of saturation are taken from a look-up table, so they will not change if the value of the latent heat constants are changed, whereas all the thermodynamic quantities related directly or indirectly to those constants via an equation will. This generates a small inconsistency in the amount of cloud water, whose effects are difficult to quantify. Therefore, all the results from this set of experiments do not describe the behaviour of a real storm. However, these experiments can help in assessing the effect of a variation in the intensity of diabatic processes and, as a consequence, the effect of a changed static stability and resultant PV distribution without changing the initial wind and temperature profile.

6.4.2 Identification of SJs (or SJ-like airstreams) in the different experiments

The identification of SJ (or SJ-like) airstreams in the different experiments has been performed manually (i.e. without using an automated procedure and the use of common thresholds). One reason behind this choice is that the SJ is not always associated with the strongest low-level winds in the cyclone, but it is rather defined as a region of strong winds with precise characteristics. Furthermore, the differences in environmental conditions between the various runs are reflected in the generation of cyclones with different intensity and features (one of the main targets of the sensitivity study). This situation prevented the use of thresholds — in terms of wind speed or of descent — in the identification of SJs.

The manual process of identification has been performed using maps and cross sections analogous to Figure 6.2 to detect a low-level wind maximum located in a non-saturated area in the widening frontal-fracture region, outside the tip of the cloud head and associated with downward sloping and (at least partially) locally buckling or folding θ_w surfaces. This features are consistent with the definition of SJ by Clark and Gray (2018), stated at the end of Chapter 2 and recalled in Section 6.3 when identifying the SJ in the control run. In this way the airstreams are identified at the end of their strongest descent, when the wind speed is around its maximum. Of course the identification at that time does not assure that the airstream would have evolved according to the definition of a SJ in previous stages, i.e. originating in the cloud head and descending from its tip towards the frontal-fracture region (where it is then identified), hence the "SJ-like" addition in the title of this section. Lagrangian backward and forward trajectories of the identified airstreams have been computed for all the experiments and their analysis is necessary to assess if the identified airstreams fulfil the SJ definition with their evolution.

The analysis of physical quantities on those trajectories provides also a concise description of the airstreams' evolution and a comparison of their features in the different runs. For every airstream identified as a SJ with the procedure explained, the 100 contiguous grid points with highest wind speed have been selected as starting points for the trajectories. Hence, all the airstreams have the same size and they tentatively represent the core of the SJ in each simulation. Localised wind maxima located within low-level clouds in a statically stable environment associated with negligible vertical motions have not been considered in the SJ identification process as these features are more likely to be associated with the CCB jet.

Experiment	control	025deg	04deg	rh70	rh90
Speed threshold (m s^{-1})	38.51	35.52	33.25	37.35	38.46
identification time (hours)	94	93	93	96	95

Table 6.3: Table showing the speed threshold and identification time (time at which the trajectories are selected) of the 100-trajectories SJ airstreams for the control, 025deg, 04deg, rh70 and rh90 experiments.

Experiment	control	jet35	jet40	jet50	jet55
Speed threshold (m s^{-1})	38.51	27.25	32.63	41.18	40.30
identification time (hours)	94	115	104	85	76

Table 6.4: Same as Table 6.3 but for the control, jet35, jet40, jet50 and jet55 experiments.

Experiment	control	lh75	lh87	lh112	lh125
Speed threshold (m s^{-1})	38.51	38.77	38.76	37.79	33.47
identification time (hours)	94	94	94	95	95

Table 6.5: Same as Table 6.3 but for the control, lh75, lh87, lh112 and lh125 experiments.

Tables 6.3, 6.4 and 6.5 show identification times and wind speed thresholds used for the different experiments. These tables highlight that for most of the experiments the SJ is detected around 93-96 hours from the start of the run. The runs in which the upper-level jet speed is changed instead show earlier identification times (associated with a faster development of the storm) for stronger upper-level jets. The threshold speed is a good indication of the strength of the SJ, being less than 1 m s^{-1} smaller than the maximum wind speed of the median trajectory in all the experiments. However, detailed comments on the wind speed in the different experiments can be found later in the section.

Figure 6.8 shows the relevant map and cross section for the rh90 experiment, to give an example of the SJ features in sensitivity runs. The analogies with the control run (Figure 6.2) are evident. The wind maxima in the frontal-fracture region is the identified SJ, located in an area of weak thermal gradients and with a fold in θ_w. The wind maximum located to the left side of the SJ in the section, in a saturated region and at a lower height, is instead associated with the cold conveyor belt and will get stronger a few hours later in the storm evolution.

6.4.3 Common characteristics of the SJs identified in the different sensitivity experiments

The airstreams initially identified as SJ show some common characteristics displayed in Figure 6.9 and briefly reviewed in this section before looking at the different sets of experiments in detail. Latent-heat experiments are not considered here, for the reasons explained in the previous section. As previously discussed, in all the experiments the airstreams have been identified manually by looking for an earth-relative wind-speed maximum located close to an area of θ_w-folding in the frontal-fracture region and above the almost-saturated boundary layer. For all the airstreams but one the median trajectory is located close to 800 hPa at the time of identification, at the end of its descent. This does not occur in the jet35 run, where the median trajectory is around 700 hPa at the time of its identification, indicating a lack of downward propagation in the region of slanted moist isentropes. This is a first hint that the airstream in jet35 cannot be classified as a SJ, as will be documented later on in this chapter.

Figure 6.9a shows the evolution of pressure on the identified SJs. In 7 runs out of 9 an ascent-descent pattern can be identified with median trajectories rising from below 900 hPa to around 700–750 hPa before descending back to around 850 hPa. The coarsest resolution run (04deg) shows a much weaker ascent before the SJ descent, although it has large variations in its behaviour, as shown by its quartile trajectories. However, it is

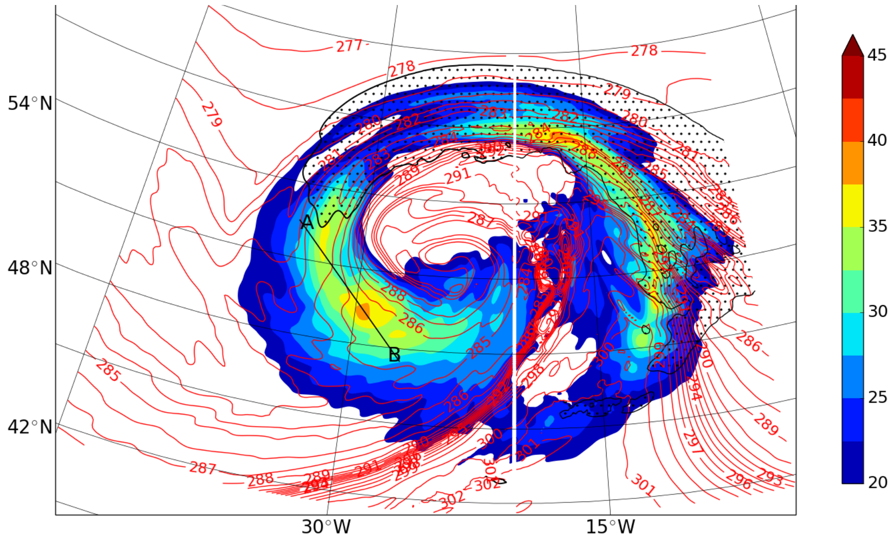

(a)

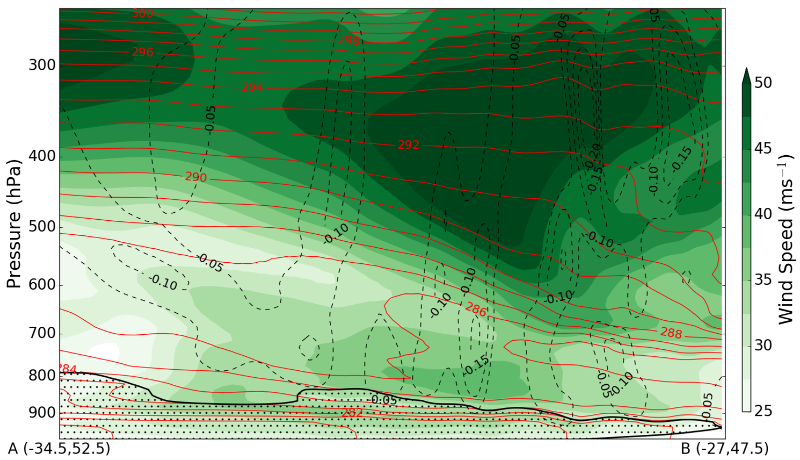

(b)

Figure 6.8: (a) Wind speed at 850 hPa (contours, m s^{-1}), wet-bulb potential temperature at 850 hPa (K, red lines) and cloudy regions at 700 hPa (RH$_{ice}$ >80%, black lines and dotted regions) after 95 hours from the start of the rh90 simulation. Note that the model domain (whose original zonal extension goes from 20°W to 25°E with periodic E-W boundary conditions) is repeated zonally to facilitate visualisation but only data between 45°W and 5°W are shown here. (b) Cross section (transect AB in panel (a) of wind speed (green filled contours,m s^{-1}), negative vertical velocity (dashed black lines, ms^{-1}), wet-bulb potential temperature (red lines, K) and cloudy regions (RH$_{ice}$ >80%, thick black lines).

necessary to note that all the airstreams generally show a poor conservation of θ_w until the first part of the ascent (not shown) and cannot yet be considered coherent airstreams, as already observed for the control run. The other airstream not displaying an initial ascent is the one in the jet35 run (although it has to be noted that the initial ascent is not part of the SJ requirement). This latter airstream also does not show a descent whose extent is comparable with the other runs, confirming that it cannot fit in the SJ definition.

Figure 6.9b focuses on the evolution of wind speed along the airstreams. In 6 airstreams out of 9 there is an oscillation in wind speed that is associated with the SJ turning around the cyclone centre while travelling in the bent-back cloud head. This oscillation does not occur in the two runs with coarser resolution and in the jet35 run, indicating a different origin of these airstreams that undergo a more zonal path during their evolution (not shown). This oscillation is followed by an evident acceleration that starts around 10–12 hours before the trajectories' identification time and ends around the identification time, to reach wind speeds around 35–40 m s^{-1}. Although differences in the magnitude of the maximum wind speed are present, the SJs show a remarkable similarity in this feature that can thus be considered as one of the main descriptors of SJ evolution, along the descent just described and with which this acceleration is associated.

Figure 6.9c shows the evolution of relative humidity (with respect to ice) and can be interpreted by relating it to the pressure evolution. The airstreams that start from the low-levels in early hours display an increase in relative humidity up to saturation, while the other airstreams are already close to saturation. A remarkably well-defined behaviour is visible later on in the evolution, with all the airstreams showing values between 97% and 100% at 10 hours before the identification time (apart from in the jet35 run, although that airstream is close to saturation too). This behaviour indicates that a saturated ascent into the cloud head is another robust feature of SJ evolution. In the 10 hours before the identification time of trajectories (i.e. during airstreams' descent) all the SJs go through a substantial decrease in relative humidity, a consequence of the descent out of the cloud head and into the frontal-fracture region. However, there is large variability in the final values of relative humidity, with median trajectories ranging between 30% and 60%.

The last common character of the identified SJs in these idealised simulations concerns moist static stability, shown in Figure 6.9d, which displays positive values for median trajectories, around $1 \cdot 10^{-4}$ s^{-2} in all the runs throughout the airstreams' evolution. In fact, negative values occur in the jet55 run between -3 and 3 hours from identification time. However, during this time period the SJ is far from saturated so conditional instability cannot be released. In the next four sections the results of the different sets of experiments are treated separately, with Table 6.6 providing a summary of the main values later on and synthesis plots concluding the sensitivity analysis.

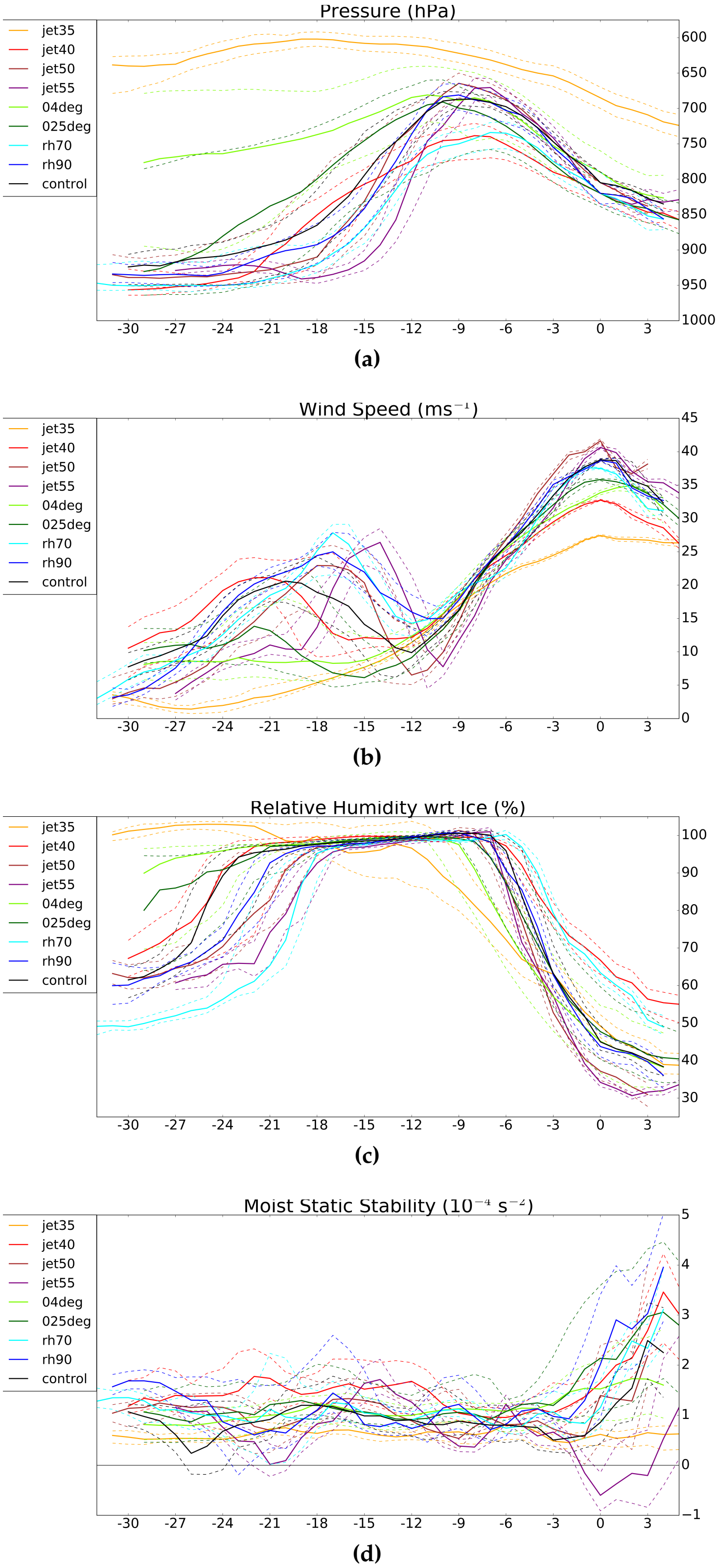

Figure 6.9: Timeseries (hours from the identification time of each airstream) of (a) pressure, (b) wind speed, (c) relative humidity wrt ice and (d) moist static stability along SJ trajectories for all the sensitivity experiments. Colours indicate the different simulation as specified in the label. For each run the solid line indicates the median trajectory and the lower (upper) dashed line indicates the 25th (75th) percentile trajectory.

6.4.4 Sensitivity to model resolution

The panels in Figure 6.10 summarise the main features of the SJ that are affected by changes in horizontal and vertical model resolution. Figure 6.10a shows that there are differences in the initial ascent such that it gets weaker as the resolution gets coarser. The 025deg and 04deg runs display a very different initial behaviour between 25th- and 75th-quartile trajectories. The subsequent descent instead is very similar to first order in terms of timing and magnitude, with all the SJs descending from around 700 hPa to below the 800 hPa level in the 10 hours before their identification times. The control run shows an increase in pressure equal to 95 hPa in 5 hours during the intense stage of descent. With values of, respectively, 84 hPa/5 hours and 76.5 hPa/5 hours, the 025deg and 04deg runs display a descent that is similar in its main features but less intense than in the control simulation. An analogous situation of similar pattern but different intensity is present also in the wind speed evolution (Figure 6.10b). After an initial oscillation that is much weaker for the coarser runs, the three SJs share the same pattern of acceleration in the 12 hours before the identification times. This acceleration is more intense for the control run, where the SJ reaches a maximum wind speed close to 39 m s^{-1} whereas in the 025deg and 04deg runs the SJ is, respectively, 3 m s^{-1} and 4 m s^{-1} weaker.

The last panels suggest what could be, at least partially, at the origin of this differences in intensity. Figure 6.10c shows the evolution of PV in the three SJs. While the two coarse runs do not show any sign of PV reduction during the SJ evolution, the 25th percentile trajectory becomes negative in the control run, at a time that is just before the start of the SJ descent. The maximum number of trajectories which are symmetrically unstable (i.e. with negative PV) is 33 for the control run whereas none of the trajectories can be labelled as symmetrically unstable in both the coarse runs. The 025deg and 04deg runs thus fail to generate any symmetric instability associated with the SJ dynamics, as also happened when performing the same sensitivity experiment for windstorm Tini (Section 5.3). A similar signal comes from Figure 6.10d, in which the evolution of moist saturated PV (MPV*) is displayed. The control run shows smaller values than the coarse runs, with the 25th percentile trajectory around zero around 12 hours before identification time, indicating a favourable environment for CSI (negative values present at later times in the plot are not associated with the release of CSI as the airstream is no longer saturated).

6.4.5 Sensitivity to initial moisture content

The panels in Figure 6.11 summarise the main features of the SJ that are affected by changes in the moisture content. Figure 6.11a shows that the three different runs share the same pattern of an initial ascent from below the 900 hPa pressure level up to 700 hPa (750 hPa for the rh70 run) followed by a descent back to around 850 hPa. The SJ in the moister simulation (rh90) stays within a 20 hPa vertical distance from the control run throughout all the evolution, showing an impressive similarity. The drier simulation (rh70) instead contains a SJ that ascends less than the other two and also undertakes a weaker descent. The maximum pressure increase in 5 hour during the SJs descent is just above 75 hPa for rh70, less than the 95 hPa for the control run. The SJ in the rh90 run undergoes a descent that is particularly intense in its second half, reaching a pressure increase value around 110 hPa in 5 hours. The general similarity in the pressure evolution is reflected in the wind speed pattern, this time also for the initial oscillation due to the airstream rotation around the zonally moving cyclone centre. The main feature to signal is the slightly weaker acceleration of the SJ in the drier simulation, with a maximum speed close to 38 m s^{-1}, whereas rh90 and the control run have an almost identical value, close to 39 m s^{-1}.

Figure 6.11c and Figure 6.11d show that a substantial difference between the rh70 run and the similar rh90 and control runs lies in the evolution of instabilities along the SJ. While both the control and rh90 runs display more than 25 trajectories (respectively up to 33 and to 38) in their SJ airstream having negative PV at the start of the descent, only up to 10 SJ trajectories become symmetrically unstable in the rh70 run. Also when looking at CSI the drier run is more stable than the other two runs, which also in this field display a remarkable similarity. To summarise, increasing the central initial value of relative humidity from 80% to 90% produces a very similar airstream both in terms of kinematics (apart from a more intense second part of descent) and of dynamics (i.e. in terms of evolution of instability on the SJ). Decreasing the RH to 70% produces instead a SJ that undergoes weaker vertical motions and shows substantially less involvement of instability release in the dynamics. Nevertheless, its maximum wind speed is just 1 m s^{-1} lower than in the other two runs.

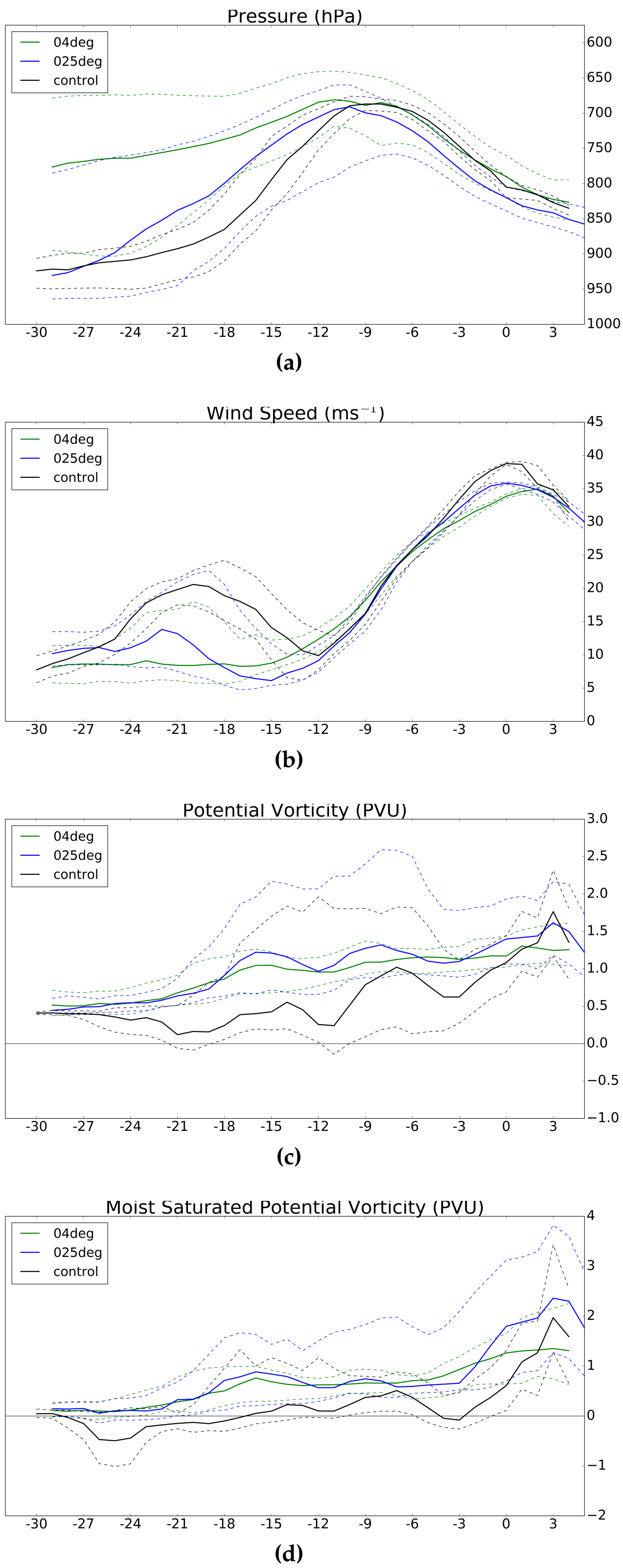

Figure 6.10: Timeseries (hours from the identification time of each airstream) of (a) pressure, (b) wind speed, (c) PV and (d) MPV* along SJ trajectories for the sensitivity experiments on model resolution. Colours indicate the different simulations as specified in the label. For each run the solid line indicates the median trajectory and the lower (upper) dashed line indicates the 25th (75th) percentile trajectory.

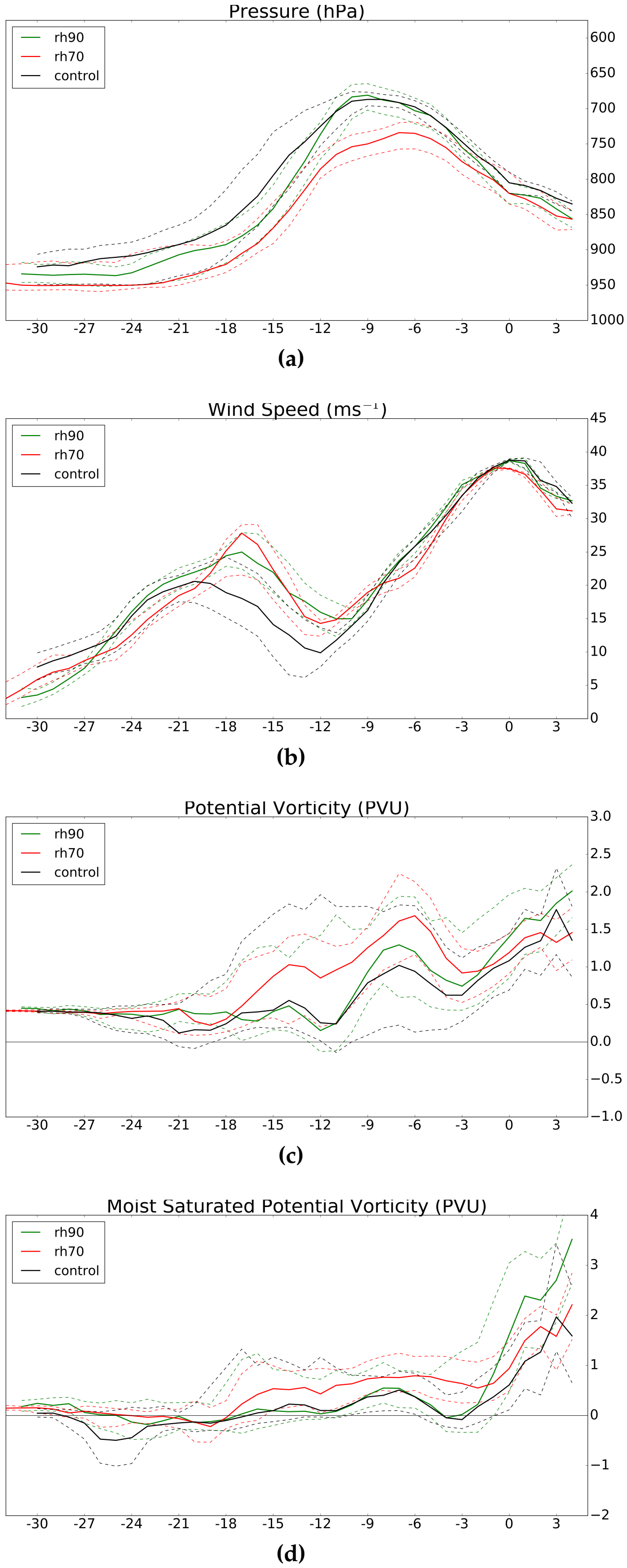

Figure 6.11: Timeseries (hours from the identification time of each airstream) of (a) pressure, (b) wind speed, (c) PV and (d) MPV* along SJ trajectories for the sensitivity experiments on moisture content. Colours indicate the different simulations as specified in the label. For each run the solid line indicates the median trajectory and the lower (upper) dashed line indicates the 25th (75th) percentile trajectory.

6.4.6 Sensitivity to upper-level jet strength

The panels in Figure 6.12 summarise the main features of the SJ that are affected by changes in the initial strength of the upper-level jet.

Figure 6.12a confirms that the airstream identified in the jet35 run, although being the only airstream exiting from the cloud-head tip, descending (weakly) and accelerating into the frontal-fracture region and being located close to an area of buckling θ_w-lines, cannot be defined as a SJ according to the definition by Clark and Gray (2018) presented at the end of Chapter 2 and recalled in Sections 6.3 and 6.4.2 . In fact, the airstream is always located between 600 hPa and 750 hPa and does not show a substantial descent towards low levels. The SJs identified in the other runs instead show the ascent-descent pattern already described in the other sets of experiments, with different magnitudes (although the initial ascent is not necessary to fit in the definition). Vertical motions are stronger in runs with larger initial upper-level-jet wind speed. The maximum descent in 5 hours exceeds 110 hPa and 100 hPa for the jet55 and jet50 runs, respectively, while it is 95 hPa for the control run. In the jet40 run it does not even reach 60 hPa. Figure 6.12b shows that also the maximum SJ wind speed is larger for runs with stronger jet stream. The increase is linear between the jet35, jet40 and control runs with values increasing by 5 m s^{-1} for each run. The jet50 and jet55 runs instead have maximum SJ windspeeds just above 40 m s^{-1}, with the jet50 run showing the most intense SJ, suggesting a saturation in maximum wind speed for high values of the jet-stream speed. All the airstreams share the same evolution with an oscillation followed by strong acceleration.

An analogous situation to what was just shown for the wind speed is depicted in Figure 6.12c where the two runs with stronger jet stream show more SI than in the control run whereas in the jet40 run the airstream is much more stable. PV is instead approximately constant throughout the evolution of the SJ in the jet35 run suggesting that the airstream is simply advected by the synoptic-scale dynamics. The maximum number of SI-unstable trajectories is 6, 4, 33, 42 and 50 in the jet35, jet40, control, jet50 and jet55 runs, respectively, illustrating this difference in the extent of instability. Similar conclusions can be drawn by looking at Figure 6.12d, with the 25th percentile trajectories of the airstreams in the jet50 and jet55 runs staying on negative values throughout the period going from the start of the ascent to the whole descent (with CSI present as long as the airstreams stay close to saturated). A final remark on this set of experiments concerns the speed of evolution of the cyclone. In all the other runs the cyclones evolve at similar speed, as the fact that all the trajectory identification times are between 93 and 96 hours from run start would suggest. In this set of experiments instead there is a large variation in terms of speed of the storm evolution, almost linearly varying with the initial strength of the jet stream. Identification times of SJ trajectories (assumed to be related to the same evolution stage of the storm) are 115, 104, 94, 85 and 76 hours from the run start for the jet35, jet40, control, jet50 and jet55 runs, respectively.

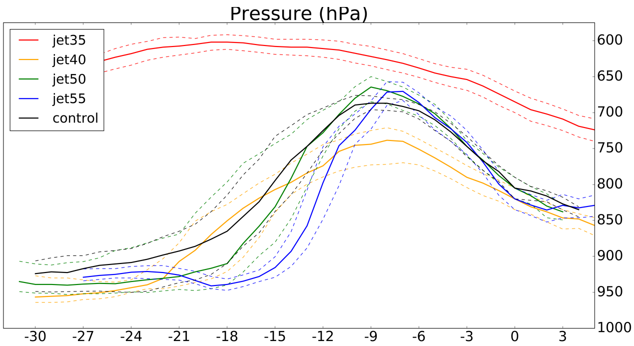

(a)

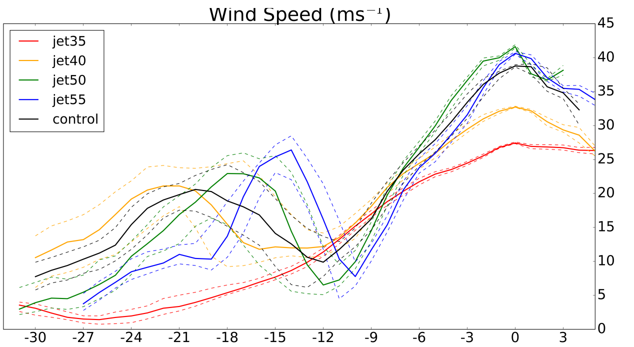

(b)

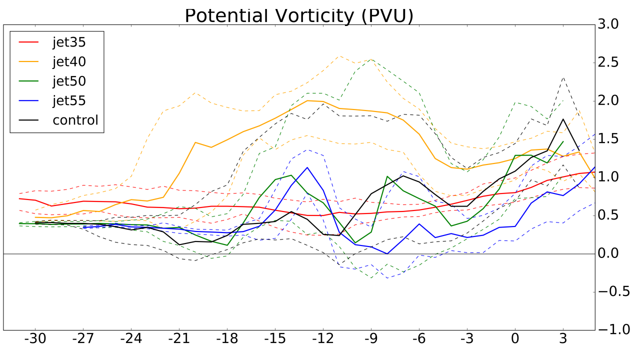

(c)

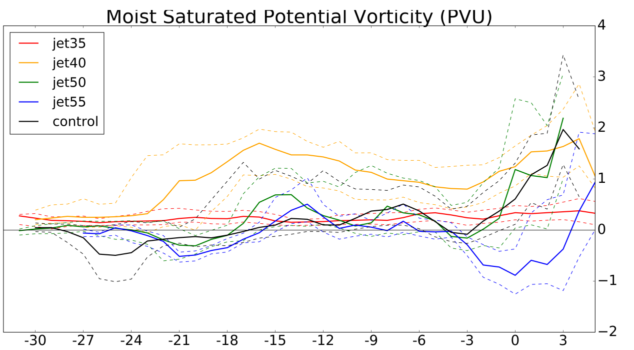

(d)

Figure 6.12: Timeseries (hours from the identification time of each airstream) of (a) pressure, (b) wind speed, (c) PV and (d) MPV* along SJ trajectories for the sensitivity experiments on jet strength. Colours indicate the different simulations as specified in the label. For each run the solid line indicates the median trajectory and the lower (upper) dashed line indicates the 25th (75th) percentile trajectory.

6.4.7 Sensitivity to latent heat

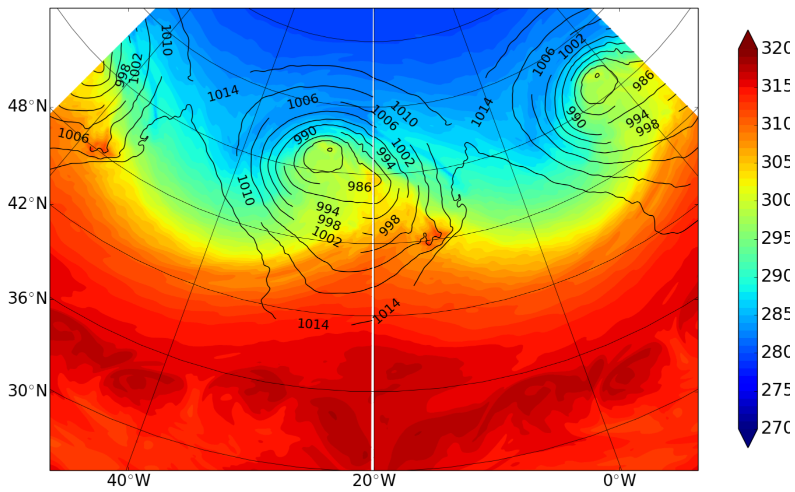

(a)

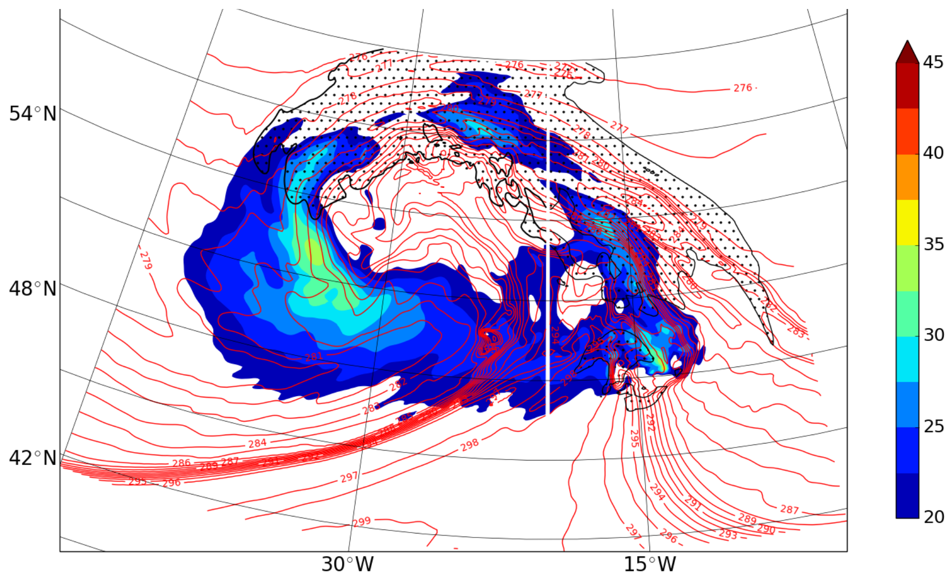

(b)

Figure 6.13: Surface pressure (black contours, hPa) and potential temperature at 850 hPa (colours, K) after 96 hours from the start of the lh125 simulation. (b) Wind speed at 850 hPa (contours, m s^{-1}), wet-bulb potential temperature at 850 hPa (K, red lines) and cloudy regions at 700 hPa (RH_{ice} >80%, black lines and dotted regions) after 95 hours from the start of the lh125 simulation. Note that the model domain (whose original zonal extension goes from 20°W to 25°E with periodic E-W boundary conditions) is repeated zonally to facilitate visualisation but only data between 45°W and 5°W are shown in panel (b).

The panels in Figures 6.13 and 6.14 display the cyclone structure and summarise the main features of the SJ that are affected by changes in the values of latent heat constants of condensation/evaporation and freezing/melting. Scaling the latent heat constants has the effect of changing the amount of energy that a parcel gets or realises when the water species it contains changes its physical state. For example, when a parcel ascends up to the point of becoming saturated, it then starts to follow a moist adiabat rather than a dry one. This increases the chances of the parcel of keeping itself warmer (and so more buoyant) than the environment. Hence, the latent heat released by water-vapour condensation favours a stronger ascent, i.e. a deeper and more vigorous convection, of the parcel (of course analogous considerations apply to a descending parcel). For this reason a change in the latent heat constant causes also a variation in the moist static stability of the environment, with large values of the constants favouring instability. Another consequence, if there are widespread vertical motions (caused for instance by frontal dynamics) that can cause latent heat release, is the change in PV (MPV*), which contains dry (moist) static stability in its definition. It is then expected that the runs with higher (lower) values of latent heat constants will be less (more) stable to upright convection. Hence, although it generates an evolution that cannot happen in the real world, scaling the values of latent heat constants is a way to enhance or decrease static stability and the importance of moist processes in parcels' ascent-descent without impacting on the vertical temperature gradient.

As expected, the lh125 run is the most unstable to upright convection and on the other side the lh75 run is the least unstable. The enhanced instability in the lh125 run prevents the simulation from forming a fully-developed Shapiro-Keyser cyclone. Figure 6.13a shows the widespread convection occurring in the subtropics and the reduced depth of the cyclone, which does not show a well-formed warm seclusion (compare with Figure 6.1c for the control simulation). Figure 6.13b (that can be compared with Figure 6.2a for the control run and with Figure 6.8a for the rh90 run) shows that, although there is a gap between the primary cold front and the warm front, a frontal-fracture region with weak θ_w cannot be identified. The wind maximum exiting the tip of the cloud head is what has been identified as 'SJ-like airstream' for this run. Given the fundamental differences in the cyclone's evolution it is not surprising to see that this airstream (which is not a SJ, according to the definition) does not share all the features of the SJs identified in the other runs, whose cyclones' evolution resembles closely the control run.

Figure 6.14a shows the evolution of pressure on the identified airstreams, confirming that the airstream in the lh125 run does not start from low levels, whereas all the other runs share the same ascent-descent pattern of the SJ airstreams. The descent of the airstream is weaker than in the control run for the lh75, in particular, and lh87 runs with only around 60 hPa and 70 hPa 5h-descent values, respectively. The extent of the 5-hours SJ descent in the lh112 run is instead similar to the 95 hPa of the control run. The descent is stronger in the lh125 run, even close to 110 hPa. Figure 6.14b shows that despite having weaker descents the airstreams in the lh75 and lh87 runs reach slightly larger speeds than in the control run, above 39 m s^{-1}, with the airstream in the lh112 run also on similar values and the one in the lh125 run on a substantially lower maximum below 34 m s^{-1} (and also missing the initial speed oscillation).

Figure 6.14c shows that the airstreams in the lh87 and lh112 runs have a behaviour similar to the control run in terms of PV, with the 25th percentile trajectories being negative just before the start of their descents. The SJ in the lh75 run instead is much more stable, with the one in the lh125 run staying on values closer to the control run but without reaching instability. The maximum number of SI-unstable trajectories is 2, 34, 33, 40 and 10 in the lh75, lh87, control, lh112 and lh125 runs, respectively. The same considerations apply to MPV* as Figure 6.14d shows and, with the exception of lh125 being the least stable SJ, to moist static stability (not shown).

To summarise, the cyclone structure and SJ occurrence is fairly robust to small changes in latent heat constants as the lh112 and lh87 runs contain a SJ with a very similar evolution to that in the control run. In the lh75 run instead the effectively increased static stability produces a SJ that reaches even slightly faster wind speed than in the control run without a strong descent or an active role of SI. On the contrary in the lh125 run the cyclone evolution is affected by the enhanced convection and a SJ fails to form.

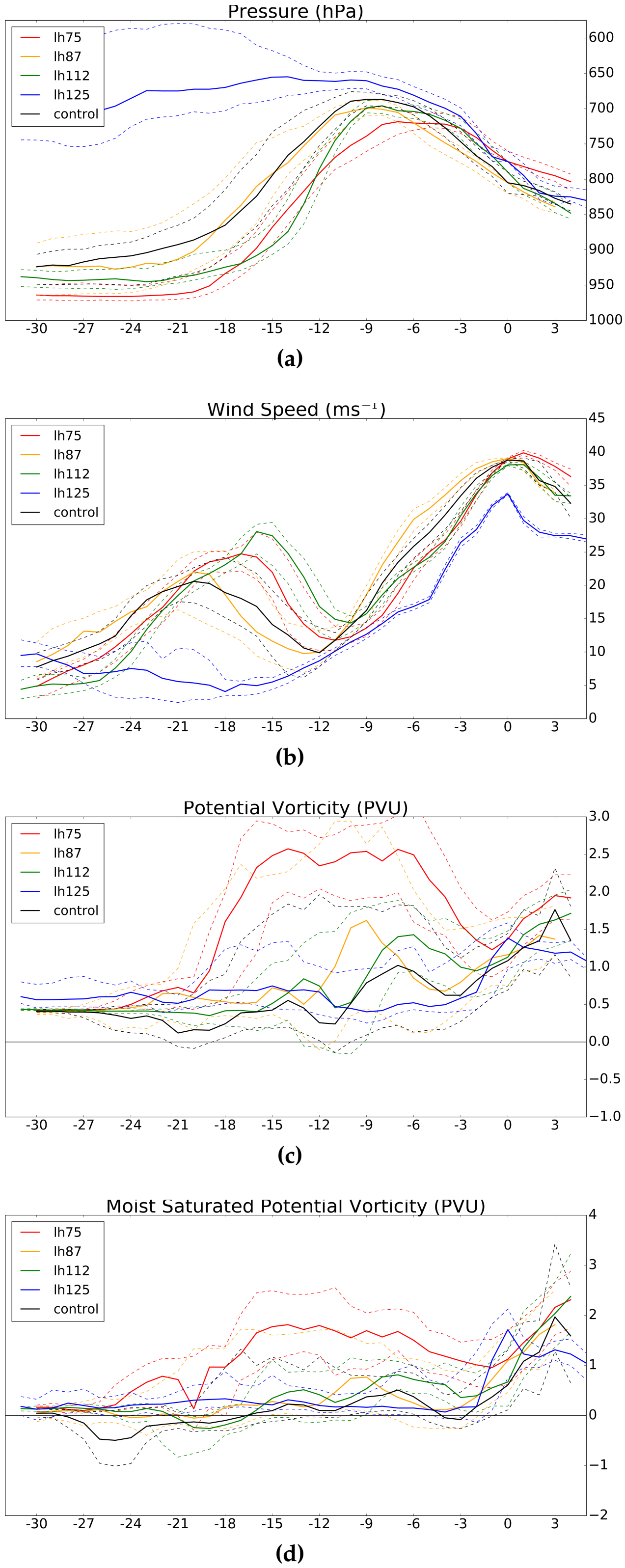

Figure 6.14: Timeseries (hours from the identification time of each airstream) of (a) pressure, (b) wind speed, (c) PV and (d) MPV* along SJ trajectories for the sensitivity experiments on latent heat. Colours indicate the different simulations as specified in the label. For each run the solid line indicates the median trajectory and the lower (upper) dashed line indicates the 25th (75th) percentile trajectory.

6.4.8 General discussion of the results of the sensitivity experiments

Exp.	$\lvert\mathbf{U}\rvert$ (m s^{-1})	$\lvert\mathbf{U}\rvert_{sys}$ (m s^{-1})	$p_{\lvert\mathbf{U}\rvert}$ (hPa)	Δp_{5h} (hPa)	trajs$_{PV<0}$	SI points (%)
control	38.77	28.33	805	95	33	9.8
025deg	35.83	24.55	820	84	0	0.0
04deg	34.94	23.68	816	76.5	0	0.0
rh90	38.70	30.82	820	110.5	38	9.3
rh70	37.60	29.29	801	77.5	10	5.3
jet35	27.44	19.48	685	48	6	2.1
jet40	32.72	24.11	820	58	4	3.3
jet50	41.63	30.34	805	103.5	42	14.1
jet55	40.64	28.18	820	113.5	50	19.2
lh75	39.86	28.89	782	61	2	3.5
lh87	39.02	27.54	805	71	34	12.2
lh112	38.09	29.65	813	96.5	40	11.5
lh125	33.71	29.74	775	108.5	10	10.6

Table 6.6: Table showing the main results for the SJ (or SJ-like) airstreams selected in the different sensitivity experiments. $\lvert\mathbf{U}\rvert$ indicates the maximum speed of the median trajectory and $\lvert\mathbf{U}\rvert_{sys}$ indicates the system-relative speed of the median trajectory at the time when $\lvert\mathbf{U}\rvert$ is reached. $p_{\lvert\mathbf{U}\rvert}$ indicates the pressure of the median trajectory at the time when $\lvert\mathbf{U}\rvert$ is reached and Δp_{5h} indicates the maximum pressure increase in 5 hours for the median trajectory. trajs$_{PV<0}$ indicates the maximum number of trajectories with negative PV in any of the instants within 15 hours from the time at which the trajectories are selected (i.e. identification time). SI points indicates the maximum percentage of points with negative PV, evaluated in the same time window as trajs$_{PV<0}$, in a volume centred on the location of the median trajectory and extending for 20 grid points in latitude, 40 grid points in longitude and 3 pressure levels (evenly spaced by 15 hPa) in the vertical.

Table 6.6 contains the main results coming from the SJ (or SJ-like) airstreams identified in the different experiments, some of which have already been mentioned when analysing separately the different sets of experiments. The first two columns, displaying $\lvert\mathbf{U}\rvert$ and $\lvert\mathbf{U}\rvert_{sys}$, show the spread in the maximum speed reached by the identified airstreams, in the earth-relative and system-relative frame of reference, respectively. System-relative speed has been computed by subtracting a centred 16-hour running mean speed of the surface pressure minimum from the earth-relative wind speed of the trajectories. It provides similar information to its earth-relative counterpart as all the experiment with $\lvert\mathbf{U}\rvert$ between 37.5 m s^{-1} and 42 m s^{-1} have $\lvert\mathbf{U}\rvert_{sys}$ within 27.5 m s^{-1}

and 31 m s^{-1}. As expected, the airstreams in the jet50 and jet55 runs experience a slightly larger reduction in wind speed when moving to a system-relative reference frame as their cyclone speed, dependent on the upper-level jet strength, is slightly larger than in the other runs. Both fields highlight that the experiments with coarser resolution (025deg and 04deg runs), weaker jet stream (jet35 and jet40 runs) or a non-fully-developed Shapiro-Keyser structure (lh125 run) produce a weaker SJ (or even fail to produce one in the jet35 and lh125 runs) whereas the other 8 runs have comparable maximum wind speed.

The two central columns provide information on the vertical position of the airstreams. The values of $p_{|\mathbf{U}|}$ show that all the airstreams are located around the 800 hPa pressure level (apart from the airstream in the jet35 run, as already discussed) at the time of SJ maximum intensity. The diagnosed Δp_{5h} shows the different pressure-depth of descent in the different experiments; this will be examined more in depth with a few plots later on in this section. The last two columns are focused on the role of instability in the evolution of the SJs, during their ascent and following descent (hence the choice to consider only the 15 hours up to the identification time of trajectories). Looking at the values of trajs$_{PV<0}$ it is possible to assess the maximum number of trajectories in the airstream that become unstable whereas SI points looks at the portion of grid points in the region surrounding the trajectories. These two diagnostics are almost linearly related, consistent with the idea of SI developing in localised regions along the airstreams (as shown for the control simulation in Section 6.3.6). This relationship does not apply for the lh125 run, where the diffuse mesoscale instability is not primarily associated with the SJ-like airstream.

Summary plots

In this section some plots are presented that illustrate the link between the characteristics and environmental conditions of the SJ (SJ-like airstream in the jet35 run) in the different experiments with the maximum wind speed and descent of the SJ itself. The experiments in which the latent heat constants have been changed are not considered, as they do not represent a realistic evolution of the system. Figures 6.15, 6.16 and 6.17 look, respectively, at the effects of horizontal resolution, initial relative humidity and initial strength of the jet stream on the SJ maximum speed and descent rate.

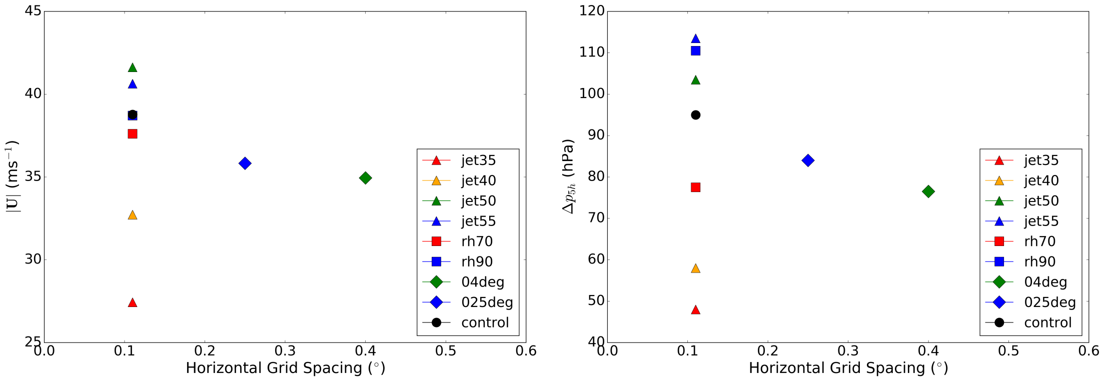

(a) **(b)**

Figure 6.15: Scatterplots showing for the different experiments the horizontal grid spacing on the x-axis and: (a) the maximum median-trajectory SJ speed $|\mathbf{U}|$ (m s^{-1}), (b) the maximum median-trajectory SJ 5h-descent Δp_{5h} (hPa) on the y-axis (See Table 6.6).

The plots in Figure 6.15 show that the runs with coarser resolution (i.e. larger grid spacing) yield lower values of descent and maximum wind speed than in the majority of the other runs. However, there are experiments with higher resolution (i.e. smaller grid spacing) displaying even weaker descent and wind speed. This suggests that high resolution is necessary to resolve the full descent and acceleration of the SJ, but there are also other main parameters controlling these features of the jet. Furthermore, the values of both fields in the two coarse-resolution runs are very similar to each other, indicating that the "cut-off value" for horizontal spacing necessary to resolve adequately the SJ dynamics is in between 0.11° and 0.25° and not beyond the latter value.

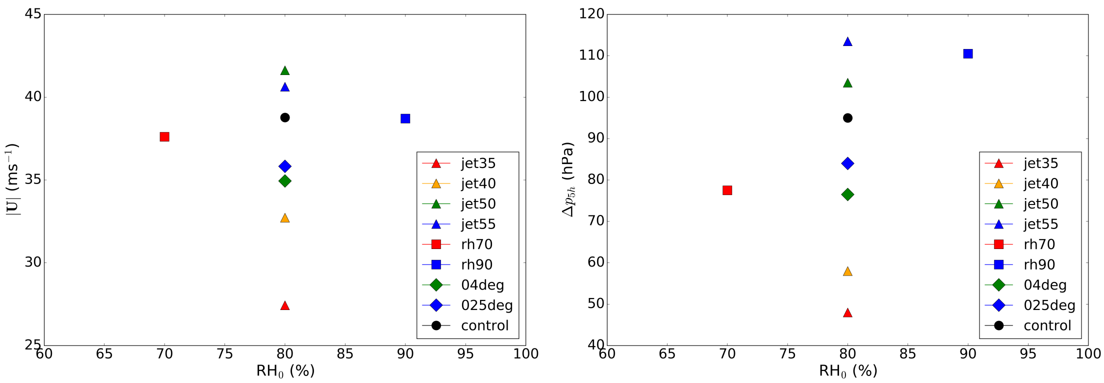

(a) **(b)**

Figure 6.16: Scatterplots showing for the different experiments the initial central value of relative humidity on the x-axis and: (a) the maximum median-trajectory SJ speed $|\mathbf{U}|$ (m s^{-1}), (b) the maximum median-trajectory SJ 5h-descent Δp_{5h} (hPa) on the y-axis (See Table 6.6).

The plots in Figure 6.16 show that the initial relative humidity RH$_0$ has an influence on the pressure-depth of the SJ strong descent, with the SJ in the moister run having a value of Δp_{5h} more than 30 hPa larger than the one in the drier run. The two values are located approximately at the top and at the bottom of the range of values occurred in the other simulations (excluding the jet35 and jet40 runs, which have weaker airstreams for different reasons). On the contrary, RH_0 does not have a noticeable effect in the maximum speed reached by the jet, as the values in moister and drier runs are very close to each other and to the value in the control run.

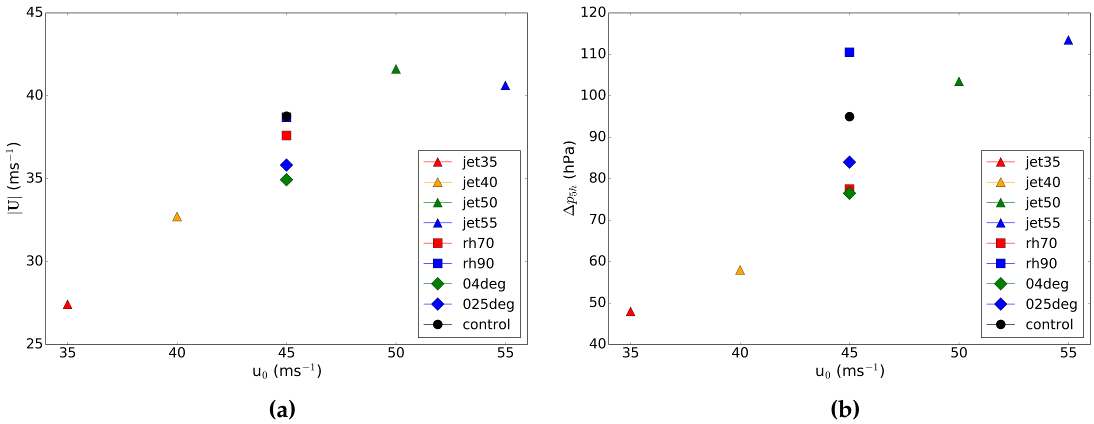

Figure 6.17: Scatterplots showing for the different experiments the initial central value of the jet stream u_0 (m s^{-1}) on the x-axis and: (a) the maximum median-trajectory SJ speed $|\mathbf{U}|$ (m s^{-1}), (b) the maximum median-trajectory SJ 5h-descent Δp_{5h} (hPa) on the y-axis (See Table 6.6).

The plots in Figure 6.17 summarise the effect of the initial strength of the upper-level jet stream on the evolution of the SJ in the storms generated in the different experiments. Figure 6.17a shows that without a strong jet stream it is unlikely that a strong SJ will form, as per the low values of $|\mathbf{U}|$ in the jet35 and jet40 runs (with the identified airstream not even being a SJ in the former). On the other hand the two runs with the strongest jet streams (jet50 and jet55) display also the strongest SJs (even though this is true only in an earth-relative reference frame). However, the absence of a further increase in wind speed from the SJ in the jet50 run to the one in the jet55 run suggests the possibility of a "saturation" of the dependency between SJ and jet stream strengths when the latter reaches certain values. All the other runs have $u_0 = 45$ m s^{-1}. If we exclude the coarser-resolution runs, 025deg and 04deg, where mesoscale processes are not fully resolved as explained earlier in this section, in all those runs the maximum speed reached by the SJ is in the range 37.5 m s^{-1} to 40 m s^{-1}. This gives a fairly robust indication of the wind speed expected in a SJ generated in an idealised cyclone with an initial jet stream equal to 45 m s^{-1}, regardless from the values of the other parameters.

Figure 6.17b confirms that a similar dependence on the strength of the jet stream also holds for the pressure-depth of intense descent that the SJs undergo. A value of maximum 5-hourly descent lower than 60 hPa is detected in the jet40 run (and in the SJ-like airstream in the jet35 run) whereas the values are above 100 hPa in the jet50 and jet55 runs. In this case the depth of descent continues to increase when moving from the jet50 to the jet55 run so it is not possible to talk about "saturation". However, it is clear from the plot (see values in Table 6.6) that there is a step in Δp_{5h} between the jet40 and the control run (with an upper-level jet speed of 45 m s^{-1}), whereas the values of the control, jet50 and jet55 runs are around 10 hPa away from each other. The other information highlighted by this plot is the large variability in Δp_{5h}, unlike in $|\mathbf{U}|$ among all the runs with $u_0 = 45$ m s^{-1}. Values ranging from around 75 hPa up to around 110 hPa indicate that different environmental conditions can substantially influence the pressure-depth of SJ descent in idealised cyclones having the same initial strength of the jet stream.

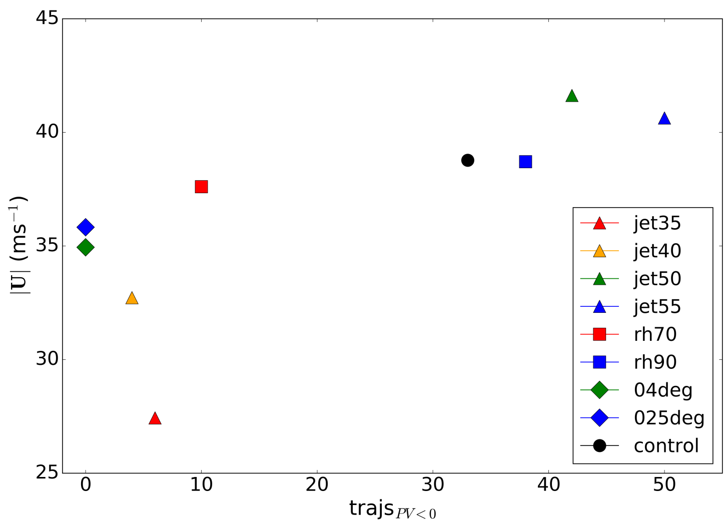

Figure 6.18: Same as panels in Figure 6.17 but with trajs$_{PV<0}$ on the x-axis and $|\mathbf{U}|$ (hPa) on the y-axis (See Table 6.6).

Figure 6.18 and 6.19 constitute an attempt to divide the SJs in clusters depending on their behaviour and to link a possible dynamical cause, the occurrence of symmetric instability along the airstreams, with kinematic consequences such as the pressure-depth of descent in the SJs or their maximum wind speed. Both figures clearly show the existence of two groups of SJ: the "SI-stable SJs" that do not exceed 10 as maximum number of

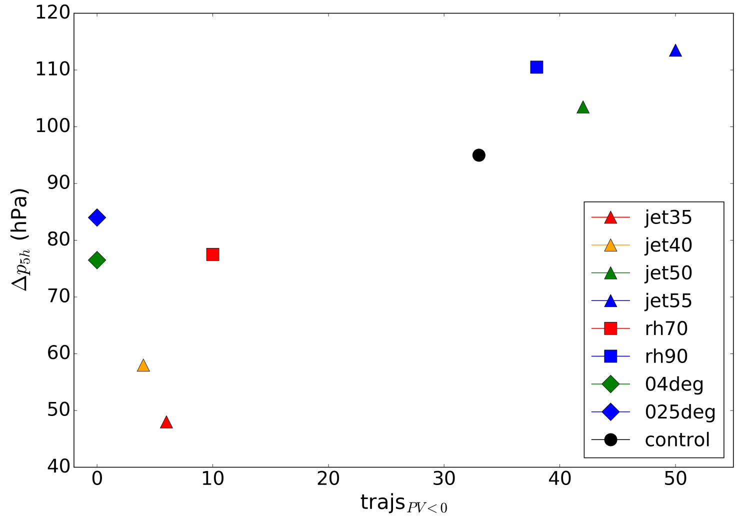

Figure 6.19: Same as panels in Figure 6.17 but with trajs$_{PV<0}$ on the x-axis and Δp_{5h} (hPa) on the y-axis (See Table 6.6).

SI-unstable trajectories (plus the SJ-like airstream in the jet35 run, included for completeness) and the "SI-unstable SJs", comprised of airstreams having more than 30 SI-unstable trajectories at the peak of the instability along the airstreams. Although the small number of experiments prevents a robust conclusion, none of the runs shows an "intermediate" behaviour, with $10 <$ trajs$_{PV<0} < 30$.

Figure 6.18 shows that the "SI-unstable SJs" have larger maximum wind speed than the "SI-stable SJs". It is difficult to quantify the increase in wind speed due to the occurrence of SI as other factors do play a role in modulating the wind speed (e.g. the initial speed of the jet stream). However, a signal of increase in $|\mathbf{U}|$ when moving from "SI-stable SJs"to "SI-unstable SJs" is visible in the figure.

In Figure 6.19 there is a signal of a link between the amount of SI occurring on the SJ, trajs$_{PV<0}$, and the pressure-depth of SJ descent, Δp_{5h}. This signal is more evident than the one in $|\mathbf{U}|$. Airstreams in the "SI-stable SJs" group display a weaker descent than the ones in the "SI-unstable SJs" group, with the more stable runs showing a descent around 80 hPa or even weaker for the SJ in the jet40 run (and for the SJ-like airstream in the jet35 run), although in this case the weaker baroclinic forcing caused by a weaker jet stream might be playing an important role. The "SI-unstable SJs" have instead values of Δp_{5h} all close to or above 100 hPa.

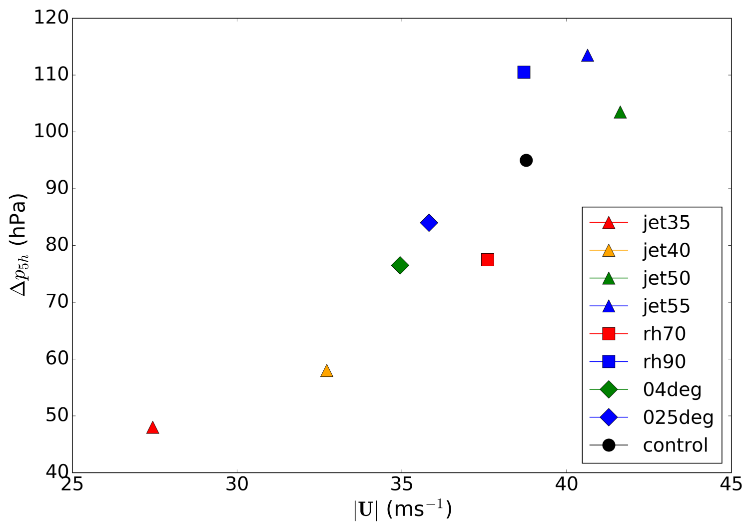

Figure 6.20: Same as panels in Figure 6.17 but with $|\mathbf{U}|$ on the x-axis and Δp_{5h} (hPa) on the y-axis (See Table 6.6).

Figure 6.20 concludes the list of plots of the chapter showing that a linear relationship can be suggested between the maximum wind speed of the SJs and the pressure-depth of their descents. Airstreams with larger peak wind speed have also larger descent. This result integrates the findings of the sensitivity study that are summarised, along with the other results of the chapter, in the next section.

6.5 Comparison of the results with previous idealised studies

As stated in the introduction of this chapter, this study builds on the initial findings of the two studies investigating the occurrence of SJs in moist idealised cyclones present in the literature (Baker et al., 2014; Coronel et al., 2016). In particular, the idealised simulations presented in this thesis can be seen as the natural continuation of Baker et al. (2014). A summary of the main results from those studies is repeated here:

- a SJ can occur in an idealised cyclone that follows the Shapiro-Keyser conceptual model of evolution;
- moisture is a key ingredient in the evolution of the SJ-containing Shapiro-Keyser cyclone;

- the SJ can be associated with an environment neutral or even unstable with respect to mesoscale instabilities such as CSI and (only in Baker et al. (2014)) II;
- domain resolution — horizontal and vertical — affects the occurrence of these instabilities and the dynamics of the associated SJ;
- the occurrence of SJ is robust to changes in environmental static stability whereas its connection to mesoscale instabilities is dependent on these changes.

The results presented in this chapter confirm the points listed above and go further in the understanding of SJ dynamics in idealised simulations and in assessing its robustness to environmental conditions. The occurrence of the SJ as an airstream descending from the cloud-head tip into the frontal-fracture region while increasing its wind speed has been confirmed. The control simulation of this study shows that the SJ descends for almost 100 hPa in 5 hours and has a peak wind speed close to 40 m s^{-1}. These values are close to the results in Coronel et al. (2016) and the maximum wind speed is around 10 m s^{-1} larger than in Baker et al. (2014). The control simulation in Baker et al. (2014) displays the occurrence of CSI along the SJ, while in the cloud head, and Coronel et al. (2016) show that the SJ descends from the cloud-head in an environment close to neutral with respect to CSI. The presence of CSI along the SJ during its evolution is confirmed by the present study. However, while Coronel et al. (2016) claim that the SJ descent is not driven by instability, the results from the control simulation presented in this chapter show how mesoscale instabilities play a role in enhancing the SJ strength. The occurrence of SI along the SJ, associated with regions of negative PV created in the cloud head along a narrow frontal zone, is illustrated and related to the mechanism of vorticity tilting outlined in the analysis of windstorm Tini. Baker et al. (2014) see evidence of dry mesoscale instabilities in a simulation with reduced static stability, speculating that there is potential for the release of dry mesoscale instabilities as additional mechanisms acting on SJ evolution. The results of the control simulation and the sensitivity experiments presented in this chapter are consistent with this initial hypothesis, showing how the occurrence of SI is part of the SJ evolution in a number of different environmental conditions. These experiments also confirm, using a wider set of environmental conditions, the robustness of the SJ as a feature of moist idealised simulations of Shapiro-Keyser extratropical cyclones. The extent of SJ descent and speed, along with the importance of instabilities on its dynamics, depend on the environment, as shown in detail when analysing sensitivity experiments in Section 6.4. Consistent with Coronel et al. (2016), these results show that the cyclone dynamics is the main forcing of the SJ evolution, with local instabilities that can act on top of it, with the mechanism outlined earlier. In any case, the comparison of SI-unstable and SI-stable SJs suggests that larger amount of instability on the airstream is usually associated with a larger peak wind speed and deeper descent.

In summary, this study confirms the initial results outlined in Baker et al. (2014) and Coronel et al. (2016), describing the SJ as a robust feature of Shapiro-Keyser cyclones, and adds further insight on its dynamics while also illustrating its typical strength and its relationship with different environmental conditions.

6.6 Summary and conclusion of the idealised study

Idealised simulations of Shapiro-Keyser cyclones developing a SJ are presented in this chapter. The setup and initial state of the simulations follow from Baker et al. (2014) which is in turn based on the LC1 baroclinic lifecycle in Thorncroft et al. (1993) (with the addition of moisture). Thanks to an improved and accurate implementation of thermal wind balance in the initial state, it has been possible to use a realistic temperature profile without static stability issues. The model is capable of generating a cyclone that fits the Shapiro-Keyser conceptual model and develops a SJ whose dynamics are associated with the evolution of symmetric instability along the airstream. It is important to remark that this is the first study in which an idealised SJ is associated with a SI-unstable environment in its control simulation, which is designed to most closely represent the real environment. The evolution of the SJ is assessed by using Lagrangian trajectories.

The SJ develops from air that ascends up to 700 hPa into the cloud head, similar to previous literature (see Section 2.4) and to windstorm Tini. The airstream then descends, gaining 95 hPa in 5 hours, while leaving the cloud-head banded tip towards the frontal-fracture region. The frontal-fracture region is shown as an area of buckling of the already-sloped θ_w lines. While travelling in this region, the SJ displays a large acceleration that produces a peak wind speed close to 40 m s^{-1}. The SJ also speeds up in a system-relative framework, although to a lesser extent than in windstorm Tini. This suggests a link with mesoscale processes on top of the synoptic evolution. The occurrence of condensation during the ascent of the airstream is evident while evaporative/sublimational cooling at the start of the descent is much less so.

The analysis of the evolution of mesoscale instabilities along the airstream shows that both CSI and SI are present in more than 30% of the trajectories just before the start of its descent, when their number gradually decreases towards zero. The number of trajectories unstable to dry mesoscale instabilities is significantly smaller (less than half) than in windstorm Tini. However, the evolution depicted suggests that the release of dry mesoscale instabilities, such as SI and II, has a role in the dynamics of SJ acceleration and descent. The analysis of the control run is completed by PV-maps confirming the generation of negative PV in localised regions of the cloud head, just on the outer side of the bent-back front and that the SJ moves towards the tip of the cloud head along with one of those regions.

The other main part of this chapter is comprised of sensitivity experiments, with the aim to analyse the evolution of an idealised SJ (if present) in a wider range of environmental conditions with respect to previous literature and to assess the robustness of its occurrence, strength and the link with mesoscale instabilities. The four sets of experiments performed include variations in model resolution, initial moisture content, initial strength of the jet stream and latent heat constants. This last set of experiments produces non-real conditions and is associated with small inconsistencies in the model and so is treated separately. However, it represents an attempt to assess changes in static stability in vertical motions and consequently in PV distribution without changing the initial vertical temperature profile.

The majority of the simulations produce cyclones resembling the control run, with SJs that have several common features as the saturated ascent in the cloud head (which is not part of the SJ definition) followed by a descent into the frontal-fracture region in which the airstream accelerates up to around 37.5-40 m s^{-1} in the absence of conditional instability. The only runs failing to produce a SJ, according to the definition in Section 2.4, recalled in Sections 6.3 and 6.4.2, are jet35 and lh125, with the enhancement of upright convection in the latter run even preventing the storm to develop according to the Shapiro-Keyser model of evolution.

Coarser resolution runs show SJs around 3-4 m s^{-1} weaker than in the control run, with a descent around 15 hPa smaller and without the development of any mesoscale instabilities (confirming the results of the analysis of windstorm Tini on the resolution constraints needed for the unstable dynamics to develop). The run with increased RH$_0$ produces a SJ with maximum wind speed and SI contribution almost identical to the one in the control run and a descent of around 15 hPa more. On the contrary, the run with decreased RH$_0$ shows a SJ with substantially less instability and a weaker descent but with a peak wind speed only 1 m s^{-1} lower than in the control run. Sensitivity to the initial strength of the jet stream shows substantially weaker SJs for the runs with decreased u_0. The SJs in the two runs with increased u_0 both peak at just above 40 m s^{-1}, suggesting a "saturation" of SJ wind speed when moving towards high values of initial jet stream strength. Also the pressure-depth of SJ descent and the contribution of instability grow with the initial strength of the jet stream, with the jet55 run reaching a descent of 113.5 hPa in 5 hours after up to half of the trajectories had become unstable to SI.

Sensitivity to latent heat assesses the robustness of the SJ evolution to these effective changes in conditional stability for vertical motions. The runs in which latent heat constants are increased and decreased by 12.5% contain airstreams with similar properties to the control-run SJ. The lh125 run instead shows an airstream that does not fulfil the SJ definition and the lh75 run displays instead a SJ that is difficult to interpret, slightly stronger than in the control run but without SI and with a substantially weaker descent. This suggests that the SJ structure is robust to changes to the latent heat constants up to 12.5 % but not up to 25 %. In any case, these results need to be looked at keeping in mind that the conditions are non-real and small inconsistencies occur in the model.

As a whole, these experiments give a fairly robust indication that the wind speed expected in a SJ generated in an idealised cyclone with an initial jet stream equal to 45 m s^{-1} (in a high-resolution simulation) stays within 37.5 m s^{-1} and 40 m s^{-1}, regardless of the values of the other parameters . The maximum wind speed peaks slightly above 40 m s^{-1} in case of a stronger jet stream and is substantially reduced in case of a weaker jet stream. The amount of descent is instead quite variable, with the maximum 5-hourly descent ranging between approximately 60 hPa and 110 hPa for the runs with u_0 =45 m s^{-1} with again a small increase for stronger jet streams and an evident decrease for weaker jet streams. The different runs can be divided into two clusters, the "SI-stable SJs" that do not go beyond 10 SI-unstable trajectories and the “SI-unstable SJ”, that have more than 30 SI-unstable trajectories at their instability peak. There is an indication that a larger amount of instability on the airstream is usually associated with a larger peak wind speed and bigger descent, although it is difficult to quantify the impact. Further analysis is required to properly explain the link between the amount of instability on the airstream as a dynamical cause and the SJ descent and wind speed as kinematic consequences. In any case, airstreams with larger peak wind speed are also more likely to have a larger descent.

To summarise, these simulations of idealised Shapiro-Keyser cyclones show the SJ as a robust feature which can be, depending on the environment, more or less associated with the localised release of symmetric instability on the airstream. The control simulation clearly shows the evolution of a SJ associated with mesoscale instability that is generated along the airstream while it ascends, saturated, into the cloud head before descending and accelerating towards the frontal-fracture region. The sensitivity experiments show the robustness of the SJ occurrence, highlight constraints in model resolution and in the storm environment. Further work is needed to explain how the amount of instability on the SJ is linked to its intensity (both in terms of speed and descent) and which other factors could be modulating it.

Chapter 7

Conclusion

7.1 Introduction

The term "Sting Jet" (SJ) has quickly become of common use in current meteorological literature and in the media (although mainly in Europe). It was first used by Browning (2004) to describe an observed mesoscale region of extremely strong surface winds distinct from the winds associated with the warm conveyor belt (WCB) and cold conveyor belt (CCB) in the Great Storm of 16 October 1987, an extra-tropical cyclone that devastated southeast England. Climatological studies (see Section 2.4) have revealed that SJs are likely to occur frequently in extra-tropical cyclones, although they may be the direct cause of the strongest surface winds and gusts over land more rarely.

In this thesis we adopt the definition of a SJ proposed in the recent review by Clark and Gray (2018), consistent with the description given by Schultz and Browning (2017):

> The SJ is defined as a coherent air flow that descends from mid-levels inside the cloud head into the frontal-fracture region of a Shapiro-Keyser cyclone over a period of a few hours leading to a distinct region of near-surface stronger winds. It therefore lies above the CCB during some stage in its life, but, at least in some cases, descends to reach the top of the boundary layer ahead of the CCB. It is not attributed to a specific mechanism in this definition.

In fact, despite increasing usage of this term (Schultz and Browning, 2017), the mechanisms leading to the generation and descent of the SJ are still matter of debate. Key issues in this debate revolve around the contributions of "large-scale" dynamics, mesoscale instability release, frontal dynamics and evaporative cooling.

In the next section these key topics are outlined (see Chapter 2 for further details on the underlying theory), leading to the formulation of the research questions addressed in this thesis. The answers to these questions will then be listed in Section 7.4, after having reviewed the main results of this study in Section 7.3. An outline of future plans and areas still to be investigated (Section 7.5) completes the chapter, concluding the thesis.

7.2 Overview of the current key issues in SJ research and of the related questions addressed in the thesis

Large-scale dynamics (mentioned in the previous section as possible leading mechanism driving the SJ evolution) refers here to the balanced dynamics taking place within the cloud head and frontal-fracture region of cyclones. As recognised by Browning (2004), gradient wind balance is sufficient to account for a large part of the strength of the winds in the frontal-fracture region. Subsequent studies (Schultz and Sienkiewicz, 2013; Slater et al., 2017; Coronel et al., 2016) have demonstrated association between SJ-type airstreams and frontolysis, divergent **Q** vectors, and/or quasi-geostrophic omega. This body of work has established that downwards advection of strong winds by the frontolytical secondary circulation (implicitly found in the frontal-fracture region of a cyclone) followed by acceleration by the low-level pressure gradient can give rise to strong winds. Indeed in simulations by models that are unable to resolve mesoscale features, these large-scale dynamical mechanisms are the only ones that can yield SJ-like features in cyclones.

Browning (2004) speculated, due to the banded nature of the cloud head, that the release of the mesoscale instability known as conditional symmetric instability (CSI) may have strengthened the SJ in the October 1987 storm. Subsequent studies (Clark et al., 2005; Gray et al., 2011; Martínez-Alvarado et al., 2014a; Baker et al., 2014) have provided evidence that mesoscale instability release (in particular of CSI, but also of conditional instability (CI), symmetric instability (SI) and inertial instability (II)) is associated with the presence and descent of SJ in SJ storms. In contrast, other studies (e.g. the case study of windstorm Ulli from 2012 by Smart and Browning (2014)) have found no evidence of a strong contribution from CSI release.

Several studies have also attempted to diagnose the contribution from the cooling necessarily associated with the evaporation of cloud as the SJ leaves the cloud head. While Clark et al. (2005) demonstrated a plausible contribution of evaporative cooling to the descent of the SJ in the October 1987 storm (with the SJ-airstream trajectories that descended the most exhibiting potential cooling of 3–8 K), other studies, in particular idealised modelling studies in which the effect of evaporative cooling has been diagnosed by turning it off (Baker et al., 2014; Coronel et al., 2016), have found little impact on the SJ strength or descent rate. These results lead to the formulation of the first group of research questions addressed in this thesis, aiming to tackle the debate on the mechanisms driving SJ evolution:

- **Do 'frontolysis' and 'mesoscale instabilities' mechanisms both play a role in driving SJ evolution?**

  - If yes, how do they co-exist and co-operate? What is the relative importance of each of these mechanisms?

  - Are other processes (e.g. evaporative/sublimational cooling) involved in SJ evolution?

- **If mesoscale instability does take part in SJ evolution, how is it generated?**

  - Is it possible to outline a mechanism of generation of instability along the SJ?

The discussion about the contributions of these different mechanisms in the evolution of SJs and their possible co-existence is initially addressed in this thesis through the analysis of a case study, as in most of the relevant works in the current literature. Having developed some hypotheses from the case study, idealised simulations are then performed. At the moment idealised modelling of SJ cyclones remains a rather unexplored method of analysis. However, idealised simulations provide several advantages compared with case studies, such as a framework in which external parameters can be systematically changed. This makes possible to investigate different processes, isolate their effects within the overall cyclone evolution and look at the dependence of the SJ dynamics on to different environmental and larger-scale conditions. The only two studies investigating the occurrence of SJs in moist idealised cyclones to date in the literature (Baker et al., 2014; Coronel et al., 2016), have proved that a SJ can occur in an idealised Shapiro-Keyser cyclone. They showed that its presence is robust to changes in environmental static stability whereas its connection to mesoscale instabilities is dependent on these changes. Domain resolution — horizontal and vertical — also affects the occurrence of these instabilities and the dynamics of the associated SJ and moisture is a key ingredient in the evolution. These initial findings are consistent with the results coming from the works analysing case studies. However, much of the potential of idealised simulations of SJ cyclones still has to be realised. Idealised simulations are used in this study (in addition to confirm the results of the analysis on the SJ driving mechanisms) to answer to this second group of questions, to which they are particularly suited by virtue of their more general framework:

- **Which environmental and large-scale conditions favour the development and strengthening of a SJ?**
- **Is the SJ a robust feature of intense extratropical cyclones evolving according to the Shapiro-Keyser model?**

Finally, whether the modelling is idealised or of real case studies, model resolution is a key aspect when investigating the dynamics of mesoscale phenomena (such as SJs) that form part of evolving synoptic-scale weather systems such as extra-tropical cyclones. Baroclinic systems are generally dominated by shallow slantwise motions of order 1:100 (roughly $f : N$, where f is the Coriolis parameter and N the Brunt-Väisälä frequency). Systems with strong frontal dynamics and/or the release of conditional symmetric instability (CSI) are often somewhat steeper (e.g. 1:50). Previous research has demonstrated that it is important to resolve the vertical spacing and aspect ratio of CSI-related circulations (Persson and Warner, 1993; Lean and Clark, 2003), which requires a grid spacing of 200–250 m in the lower mid-troposphere or better. With 1:50 slope this implies a horizontal spacing of around 10–12 km. In practice, the solution developed by the model tends to be dominated by the poorer of the horizontal and the vertical resolution divided by the aspect ratio of the flow (so a 20 km horizontal grid simulating a flow with 1:50 aspect ratio tends to produce a solution similar to a model with 400 m vertical grid spacing even if the actual vertical spacing is smaller). Incidentally, if ice sublimation is important in the frontal dynamics of a system (as it often is), a similar resolution is required to capture the depth-scale of sublimation (Forbes and Clark, 2003). Previous simulations of SJs have shown that they descend out of the cloud head with roughly this (1:50) aspect ratio and have shallow vertical depth requiring a grid spacing of 200–250 m (Clark et al., 2005; Gray et al., 2011). Hence, to reinforce and clarify these findings a research question arises

- **What are the model constraints, in terms of horizontal and vertical resolution, to correctly simulate SJ evolution and allow the relevant processes to act?**

These key SJ issues have been addressed in the thesis using a two-stages approach. At first, the case study analysis of windstorm Tini, chosen as a potential SJ case, has been performed to learn about the role of different mechanisms and to demonstrate the ability of the model in simulating SJs. These results are in process of being published in Volonté et al. (2018). Secondly, the findings have been extended through idealised simulations to look at the sensitivity to large-scale drivers. The main results of, respectively, the case study of windstorm Tini and idealised simulations of SJ cyclones, consisting in both cases of numerical simulations run with the MetUM, are reviewed in the next section. See the concluding sections of, respectively, Chapters 5 and 6 for more details. The answers to the research questions presented here follow in Section 7.4.

7.3 Summary of the main results of the thesis

7.3.1 Case Study of a SJ cyclone: windstorm Tini

A high-resolution simulation of windstorm Tini was shown to agree very well with available observations, both in overall development and in mesoscale structure. The validation of the model with respect to the observations is particularly important in this area of research, where it is very difficult to perform a detailed examination of mechanisms without using a model, relying only on observations.

The SJ contained in the high-resolution simulation of windstorm Tini has been identified as a coherent airstream exiting from the cloud head, descending strongly (150 hPa in 3 h) while accelerating into the frontal-fracture region and producing a strong and focused wind maximum close to 60 $\mathrm{m\,s^{-1}}$. This airstream descends in an environment that is already broadly descending, with slanted θ_w lines showing evidence of folding. Through most of its lifetime, the SJ has a horizontal extent around 50 km and a vertical extent of no more than 1 km. The θ_w range characteristic of the SJ is intermediate between those of the WCB and the CCB. The evolution of the SJ is clearly different to the one that the CCB undergoes. Its descent can be divided in two stages:

1. Strong descent accompanied by decrease in θ_w (cooling via sublimation) without system-relative acceleration;
2. Even stronger descent conserving θ_w and with large system-relative acceleration.

During the descent, the horizontal system-relative wind speed increases by around 15 $\mathrm{m\,s^{-1}}$ suggesting mesoscale contributions to the acceleration of the airstream.

Lagrangian back-trajectories show that mesoscale instabilities are associated with the evolution of the SJ, which becomes at first largely unstable to CSI and then to SI/II. The number of unstable trajectories associated with the SJ reaches a maximum as the SJ starts descending; hence the descent of the SJ corresponds with the reduction of these instabilities, and by the time it reaches the top of the boundary layer most of the instability has been released. The early stages of descent are most likely associated with the release of diagnosed CSI, but, as the descending airstream loses access to condensed water to evaporate or sublimate, the airstream is no longer diagnosed as unstable to this process. However, by this time, the airstream is also unstable to SI/II. While it is very difficult to prove that the release of an instability causes the flow, this process of destabilisation and subsequent release (or removal) of mesoscale instability in the airstream can be strongly hypothesised to be affecting SJ dynamics.

The production of negative MPV* (associated with CSI) and, ultimately, PV (associated with SI) arises through diabatic heating and cooling in the cloud head. However, this manifests itself through the tilting of horizontal vorticity to produce negative values of the vertical component of absolute vorticity (ζ_z, associated with II), which is then amplified before the final stage of descent by stretching. Figure 5.19 highlights this mechanism, which is strongly forced by diabatic processes, primarily condensation and evaporation.

The SJ typically lies (as indicated by its later descent in the frontal-fracture region) in the intermediate θ_w region of the frontal zone, between strong ascent and descent. The horizontal buoyancy gradient here generates horizontal vorticity (associated with the ascent and descent) along the SJ flow that is subsequently tilted downwards when the SJ starts to descend (initially probably due to frontolysis). This therefore generates negative vertical vorticity.

As a consequence, a slantwise-banded structure is present in ζ_z in the region. The SJ travels towards the tip of the cloud head along with a band of negative ζ_z that grows in amplitude while retaining its shape and extent and, at the same time, descending and acquiring a substantial slope. This strongly suggests that the growth of mesoscale instability is a process taking place along the SJ, in a Lagrangian sense. This mesoscale banding substantially modifies the frontogenesis field. Whereas the broad structure of frontogenesis resembles that already found in previous studies, with widespread frontolysis corresponding to the frontal-fracture region, smaller-scale patterns are present at the tip of the cloud head related to the SJ motion, and the small SJ region is actually associated with a local region of frontogenesis. On reaching the top of the boundary layer, ζ_z rapidly becomes positive, most likely reflecting boundary-layer mixing.

A lower-resolution simulation (with resolution coarser than that required to release mesoscale instabilities) also shows a region of relatively strong winds descending out of the cloud head. On its own, this would satisfy the definition of a SJ: the peak wind speed achieved in the jet is notably strong, around 48 $\mathrm{m\,s^{-1}}$. However, the life history of the SJ in this lower-resolution simulation is in marked contrast to the flow observed in the higher-resolution simulation. The amount of descent is significantly less, so the peak wind speed barely reaches 800 hPa and there is no clear wind maximum at low levels. The SJ peak wind speed, while strong, is substantially weaker than the 60 $\mathrm{m\,s^{-1}}$ achieved in the SJ in the higher-resolution simulation, although the other main conveyor belts in the system are well represented and only marginally weakened by the lower resolution. The descent occurs in a region associated with frontolysis in the frontal-fracture region, and there is almost no indication of the generation and release of mesoscale instabilities.

The SJ in the lower-resolution simulation is entirely consistent with the hypothesis of strong winds caused by the frontal dynamics in the region: descent due to frontolysis into a region with high pressure gradient with flow aligned with the system motion. There is much less fine-scale structure in the frontogenesis field and the broad picture is in close agreement with what is shown in Schultz and Sienkiewicz (2013). The results from the lower-resolution simulation are similar to those found by Slater et al. (2017), who simulated storm Tini, and it is reasonable to suppose that this frontolysis-associated SJ, resulting from essentially balanced dynamics, is a relatively robust feature. Given that the authors ran a different model with different initial conditions, it is unknown whether a SJ of the nature found in our higher-resolution simulation would have formed if they had run the model with adequate resolution to enable it to do so.

7.3.2 Idealised simulations of SJ cyclones

Idealised simulations of Shapiro-Keyser cyclones developing a SJ have been performed, with a setup and initial state of the simulations following from Baker et al. (2014) which is in turn based on the LC1 baroclinic lifecycle in Thorncroft et al. (1993) (with the addition of moisture). The model is capable of generating a cyclone that, with a realistic temperature profile, fits the Shapiro-Keyser conceptual model and develops a SJ whose dynamics are associated with the evolution of symmetric instability along the airstream. This is the first study in which an idealised SJ is associated with a SI-unstable environment in its control simulation, a simulation specifically designed to closely represent the real environment.

The SJ develops from air that ascends up to 700 hPa into the cloud head, similar to previous literature (see Section 2.4) and to windstorm Tini. The airstream then descends by almost 100 hPa in 5 hours, while leaving the cloud-head banded tip towards the frontal-fracture region. The frontal-fracture region is shown as an area of buckling of the already-sloped θ_w lines. While travelling in this region, the SJ undertakes a large acceleration that produces a peak wind speed close to 40 m s^{-1}, substantially less than Tini. The occurrence of condensation during the ascent of the airstream is evident while evaporative/sublimational cooling at the start of the descent is much less so. The analysis of the evolution of mesoscale instabilities along the airstream shows that both CSI and SI are present in more than 30% of the trajectories just before the start of its descent, when their number gradually decreases towards zero. The number of trajectories unstable to dry mesoscale instabilities is significantly smaller (less than half) than in windstorm Tini. However, the evolution depicted suggests that the release of dry mesoscale instabilities, such as SI and II, has a role in the dynamics of SJ acceleration and descent. Negative PV is generated in localised regions of the cloud head, just on the outer side of the bent-back front, with the SJ moving towards the tip of the cloud head along with one of those regions.

The four sets of experiments performed include variations in model resolution, initial moisture content, initial strength of the jet stream and latent heat constants (although this last set of experiments produces non-real conditions and is treated separately, see Chapter 6 for the results). The majority of the simulations produce cyclones resembling the control run, with SJs that show a saturated ascent in the cloud head (which is not necessary to fulfil the SJ definition) followed by a descent into the frontal-fracture region in which the airstream accelerates in the absence of CI. These experiments indicate that the maximum wind speed of a SJ generated by a high-resolution simulation of an idealised cyclone is expected to be close to 40 m s^{-1}. Slightly stronger wind speed is expected in case of a stronger jet whereas wind speed is substantially reduced in case of a weaker jet stream. The amount of descent undertook by SJs in these simulations is instead quite variable, with the maximum 5-hourly descent ranging between 60 hPa and 110 hPa, and again a small increase for stronger jet streams and an evident decrease for weaker jet streams. The run with the weakest jet stream even fails to produce a SJ. Coarser resolution runs show SJs around 3-4 m s^{-1} weaker than in the control run, with a descent around 15 hPa smaller and without the development of any mesoscale instabilities. This confirms the results of the analysis of windstorm Tini on the resolution constraints needed for the unstable dynamics to develop.

The different runs can be divided into two clusters, the “SI-stable SJs” that do not go beyond 10 SI-unstable trajectories and the “SI-unstable SJ”, that have more than 30 SI-unstable trajectories at their instability peak. The SI-unstable runs are the ones with the strongest jet stream. A larger amount of instability on the airstream is associated with a larger peak wind speed and bigger descent, although it is difficult to quantify the impact and to identify the factors modulating it. Airstreams with larger peak wind speed are also more likely to have a larger descent.

This study confirms the initial results outlined in Baker et al. (2014) and Coronel et al. (2016), describing the SJ as a robust feature of Shapiro-Keyser cyclones, and adds further insight on its dynamics while also illustrating its typical strength and its relationship with different environmental conditions. In fact, these simulations of idealised Shapiro-Keyser cyclones show the SJ as a robust feature which can be, in a good number of environmental conditions, associated with the localised release of symmetric instability on the airstream. The control simulation shows the evolution of a SJ with descent and peak wind speed of similar magnitude to that in Coronel et al. (2016). The maximum wind speed is around 10 m s^{-1} larger than in Baker et al. (2014). This SJ is clearly associated with mesoscale instability that is generated along the airstream while it ascends, saturated, into the cloud head before descending and accelerating towards the frontal-fracture region. On one hand, this result confirms the possible occurrence of CSI release along the SJ hypothesised in those two studies. On the other hand, while Coronel et al. (2016) claim that the SJ descent is not driven by instability, the results from the control simulation presented in this chapter show that mesoscale instabilities play a main role in enhancing the SJ strength. Furthermore, as already mentioned, this is the first idealised study showing the occurrence of SI in its control simulation; Baker et al. (2014) see evidence of dry mesoscale instabilities only in a simulation with reduced static stability. As a whole, the control simulation and sensitivity experiments presented in this thesis highlight that the occurrence of SI is part of the SJ evolution in a number of different environmental conditions and has an effect in strengthening it. These experiments also confirm, using a wider set of environmental conditions, the robustness of the SJ as a feature of moist idealised simulations of Shapiro-Keyser extratropical cyclones.

7.4 Key results of this thesis

This section begins by addressing the questions posed in Chapter 1 and in Section 7.2, based on the results obtained in this thesis. This is followed by a summary of the novel contributions to research coming from this work.

Do 'frontolysis' and 'mesoscale instabilities' mechanisms both play a role in driving SJ evolution?

The analysis of model experiments simulating windstorm Tini and of idealised simulations demonstrates, for the first time, that both frontolysis and mesoscale instabilities can operate, in the same storm, to produce strong SJs, with the release of mesoscale instabilities substantially enhancing the SJ strength.

○ *If yes, how do they co-exist and co-operate? What is the relative importance of each of these mechanisms?*

Frontolysis is generally operating in Shapiro-Keyser cyclones and can, in extreme cases, produce relatively strong SJs. However, in this case, strong, diabatically-produced MPV*/PV reduction occurs, leading to a continuum of behaviour, with the frontolysis often occurring in an environment close to neutral or unstable with respect to CSI or even SI. It is likely that the frontolysis itself contributes to this by providing some, at least, initial descent to tilt horizontal vorticity that has been diabatically-generated in the cloud head. The CSI/SI generated can then lead to a substantial enhancement of the SJ, both in strength and in depth of descent.

○ *Are other processes (e.g. evaporative/sublimational cooling) involved in SJ evolution?*

The analysis of windstorm Tini suggests that evaporative and sublimational cooling, associated with a decrease in θ_w, can have a role in the first stages of SJ descent. However, both the case study and the idealised simulations do not indicate this process as contributing to the large acceleration experienced by the SJ during its strong descent.

If mesoscale instability does take part in SJ evolution, how is it generated?

In this thesis the mechanism of generation of dry symmetric instabilities along the SJ is outlined, for the first time to the author's knowledge, in the analysis of windstorm Tini (see Figure 5.19). Results from the control run in the idealised simulation are consistent with the mechanism hypothesised.

○ *Is it possible to outline a mechanism of generation of instability along the SJ?*

The production of negative MPV* and sometimes PV (respectively, associated with CSI and SI) is caused by diabatic heating (by condensation and freezing) and cooling (by evaporation and sublimation) associated with frontal motions in the cloud head. In detail, as the SJ travels in the intermediate θ_w region of the bent-back frontal zone, between strong ascent and descent, downward tilting of the thereby generated negative horizontal vorticity produces negative ζ_z (associated with II), which is then amplified before the final stage of SJ descent by stretching. This process of tilting, initially probably due to frontolysis, takes place along the SJ flow, in a Lagrangian sense and negative PV is associated with the negative ζ_z generated.

Which environmental and large-scale conditions favour the development and strengthening of a SJ?

Idealised simulations suggest that 'SI-unstable' SJs are likely to show stronger maximum wind speed and larger descent, in agreement with the analyisis of windstorm Tini. These results also indicate the strength of the jet stream as an important driver of SJ intensity with other factors, such as small variations in the amount of moisture in the cyclone, having a secondary effect.

Is the SJ a robust feature of intense extratropical cyclones evolving according to the Shapiro-Keyser model?

This study describes the SJ as a robust feature of intense Shapiro-Keyser cyclones (where the word 'intense' refers also to the strength of the upper-level jet). The additional intensification provided by the generation of mesoscale instability on top of the synoptic evolution can occur in a number of different conditions. The idealised study shows that a SJ occurs in all cases except where the jet stream was too weak to produce a SJ storm.

What are the model constraints, in terms of horizontal and vertical resolution, to correctly simulate SJ evolution and allow the relevant processes to act?

Other studies have shown that it is essential that models are run with sufficiently high resolution to allow mesoscale instabilities to be released (i.e. horizontal spacing not larger than 10–12 km and vertical spacing not larger than 200–250 m in the lower mid-troposphere). This is confirmed by this study, which also highlights that substantially weaker SJs can form in models whose resolution prevents release (and even formation) of mesoscale instabilities. Presumably, therefore, SJs may form in real cyclones that would not develop such instabilities.

7.4.1 Summary list of novel contributions from this work to the SJ research

- **Demonstrating the co-existence of 'frontolysis' and 'mesoscale instabilities' in SJ evolution**
  The results presented in this thesis address the debate between the 'frontolysis' and 'mesoscale instabilities' mechanisms clearly proving, for the first time to the author's knowledge, that they can co-exist and establishing their roles. These results have enabled us to draw the conclusion that mesoscale instabilities form in a background of (and probably enhanced by) synoptic and frontal dynamics that, in themselves, can lead to SJs, but that the release of these mesoscale instabilities can substantially enhance the final wind speed.

- **Showing a succession of mesoscale instabilities evolving along the SJ**
  The formation and eventual release of a succession of mesoscale instabilities, from CSI through to SI and II, has been demonstrated; this succession had only been suggested, but not highlighted, in other studies.

- **Outlining a precise mechanism for the generation of SI/II on the SJ**
  This study has outlined for the first time the mechanism of generation of dry symmetric instabilities along the SJ. The mechanism explains the generation of negative ζ_z (and hence negative PV) in localised regions in the cloud head, associated with the occurrence of II (and SI) on the SJ.

- **Showing the occurrence of SI on the SJ in idealised simulations**
  This is the first study in which an idealised SJ is associated with a SI-unstable environment in its control simulation and in around half of the runs among the sensitivity experiments. This result shows that the additional intensification provided by the generation of mesoscale instability on top of the synoptic evolution can occur in a number of different environmental conditions.

- **Providing evidence that the SJ is a robust feature of intense Shapiro-Keyser extratropical cyclones**
  The SJ, which can be additionally strengthened by the possible occurrence of mesoscale instabilities, is in itself a common feature of intense Shapiro-Keyser extratropical cyclones.

- **Further clarifying the model resolution constraints that apply to the simulation of SJ dynamics**
  Finally, the suppression of the release, and even formation, of these mesoscale instabilities in coarser-resolution models has been clearly demonstrated.

7.5 Possible future work and open questions

The main results of this study are documented throughout this chapter, and the previous section in particular. These findings represent a substantial step in improving the knowledge and the description of SJ dynamics. Nevertheless, several questions are still open and new ones have arisen from this study. Here some main areas of possible future investigation are briefly described.

- **Extension of sensitivity experiments**
  The sensitivity experiments performed in this study are already exploring a wider set of conditions than in previous literature. However, extending the number of experiments would be beneficial in understanding the dependence of the SJ evolution on different environmental conditions. This can be done by increasing the population in the set of experiments already under investigation (e.g. looking at other values of model resolution, initial relative humidity and jet stream strength)

or by looking at new sets of experiments.

- **Assessment of the contribution of moist processes to SJ dynamics**
  Diabatic processes associated with frontal motions are at the heart of the generation of instability along the SJ and of its overall dynamics. Idealised simulations can be performed switching on/off moist processes such as evaporation, condensation and sublimation during part or all of the SJ evolution to isolate the effects of the processes on the dynamics of the airstream (in a more effective way than the PV-tracers analysis already performed). This would also help in clarifying which environmental conditions are more favourable to the occurrence of 'SI-unstable' SJ, providing thus a link between larger-scale conditions and localised moist processes.

- **Quantitative link of the energy release due to instability with the acceleration of the SJ**
  While outlining the mechanism of generation of instability along the SJ, this study did not assess the amount of energy that the release of instability can transfer to the airstream, increasing its wind speed. To reach this target, the use of diagnostics like SCAPE (see Section 2.3 for more details) can thus be implemented onto the different available simulations.

- **Investigation of the occurrence of multiple 'SJ-pulses' in the same cyclone**
  Both the analysis of windstorm Tini and of the idealised control run show the presence of other localised regions with negative PV (and/or ζ_z) located in the cloud head, on the outer side of the bent-back front. This is consistent with the mechanism outlined, as frontal motions and the tilting of horizontal vorticity are not confined to the small region in which the SJ lies. These areas, travelling ahead or behind the SI-unstable region associated with the SJ could also be associated with the generation of strong winds, although they might fail to reach the frontal-fracture region during its widening stage and thus to fully accelerate and descend towards the ground. Detailed Lagrangian analysis could shed light on their evolution.

- **Resolution-dependent investigation of SJ structure and evolution**
  This study highlighted the model resolution constraints that apply when simulating a SJ. High-resolution modelling ($O(10\,km)$ of horizontal spacing and 1:50 aspect ratio) is necessary to correctly depict the evolution of the SJ, with the possible gen-

eration of instability along it. The accurate assessment of this resolution threshold is worth performing as it looks critical for a sharp change in behaviour in the model simulations. In addition to this, going to even higher resolution ($O(1\ km)$ in the horizontal while keeping the same aspect ratio) would allow a more detailed view of the SJ structure.

- **Assessment of the potential impact of the SJ on the ground**
  For impact purposes the width/area of the SJ is probably as important as its strength in terms of maximum wind speed. This could be diagnosed from the idealised simulations considering the area with winds exceeding some percentile of the maximum wind speed in that run. Another relevant metric that could be considered is the duration of strong SJ-related winds at the surface. An accurate discussion of the boundary-layer representation in the model simulations will be necessary when performing this investigation.

- **Investigating the link between the intensity of the SJ and of the other airstreams**
  Although a SJ is associated by definition with very strong winds in the low levels, other airstreams can produce even stronger winds in some cyclones. The different idealised simulations can be used to assess the relationship between the strength of the SJ and the intensity of other airstreams, i.e. CCB, WCB and DI (dry-air intrusion) present in Shapiro-Keyser extratropical cyclones. The PV framework can be used to look at the link of these different airstreams with the overall evolution of the storm. Metrics describing the intensity of the cyclone, such as the Eady growth rate (instead than just look at the initial strength of the jet stream), can be used to assess the dependence of the SJ strength on the storm intensity.

Bibliography

Arakawa, A. and V. R. Lamb, 1977: Computational design of the basic dynamical processes of the UCLA general circulation model. *Methods Comput. Phys.*, **17**, 173–265.

Bader, M. J., G. S. Forbes, J. R. Grant, R. B. E. Lilley, and A. J. Waters, 1995: *Images in weather forecasting. A practical guide for interpreting satellite and radar imagery*. Cambridge University Press.

Baker, L. H., 2009: Sting jets in severe Northern European wind storms. *Weather*, **64**, 143–148.

— 2011: *Sting jets in extratropical cyclones*. Ph.D. thesis, University of Reading.

Baker, L. H., S. L. Gray, and P. A. Clark, 2014: Idealised simulations of sting-jet cyclones. *Q. J. R. Meteorol. Soc.*, **140**, 96–110, doi:10.1002/qj.2131.

Bennetts, D. A. and B. J. Hoskins, 1979: Conditional symmetric instability - a possible explanation for frontal rainbands. *Q. J. R. Meteorol. Soc.*, **105**, 945–962.

Bjerknes, A., 1919: On the structure of moving cyclones. *Geofys. Publ.*, **1**, 1–8.

Bjerknes, A. and H. Solberg, 1922: Life cycle of cyclones and the polar front theory of atmospheric circulation. *Geofys. Publ.*, **3**, 3–18.

Böttger, H., M. Eckardt, and U. Katergiannakis, 1975: Forecasting extratropical storms with hurricane intensity using satellite information. *J. Appl. Meteorol.*, **14**, 1259–1265.

Boutle, I., S. Belcher, and R. Plant, 2011: Moisture transport in midlatitude cyclones. *Q. J. R. Meteorol. Soc.*, **137**, 360–373.

Browning, K. A., 1990: Organization of clouds and precipitation in extratropical cyclones. *Extratropical Cyclones: The Erik Palmén Memorial Volume*, 129–153.

— 2004: The sting at the end of the tail: Damaging winds associated with extratropical cyclones. *Q. J. R. Meteorol. Soc.*, **130**, 375–399.

— 2005: Observational synthesis of mesoscal structures within an explosively developing cyclone. *Q. J. R. Meteorol. Soc.*, **131**, 603–623.

Browning, K. A. and M. Field, 2004: Evidence from Meteosat imagery of the interaction of sting jets with the boundary layer. *Meteorol. Appl.*, **135**, 663–680.

Browning, K. A. and N. M. Roberts, 1994: Structure of a frontal cyclone. *Q. J. R. Meteorol. Soc.*, **120**, 1535–1557.

Browning, K. A., D. J. Smart, M. R. Clark, and A. J. Illingworth, 2015: The role of evaporating showers in the transfer of sting-jet momentum surface. *Q. J. R. Meteorol. Soc.*, **141**, 2956–2971, doi: 10.1002/qj.2581.

Büeler, D. and S. Pfahl, 2017: Potential Vorticity Diagnostics to Quantify Effects of Latent Heating in Extratropical Cyclones. Part I: Methodology. *J. Atmos. Sci.*, **74**, 3567–3590, doi:10.1175/JAS-D-17-0041.1.

Carlson, T. N., 1980: Airflow through midlatitude cyclones and the comma cloud pattern. *Mon. Weather Rev.*, **108**, 1498–1509.

Catto, J. L., 2016: Extratropical cyclone classification and its use in climate studies. *Reviews of Geophysics*, **54**, 486–520, doi:10.1002/2016RG000519.

Chagnon, J. M. and S. L. Gray, 2009: Horizontal potential vorticity dipoles on the convective storm scale. *Q. J. R. Meteorol. Soc.*, **135**, 1392–1408, doi:10.1002/qj.468.

Chagnon, J. M., S. L. Gray, and J. Methven, 2013: Diabatic processes modifying potential vorticity in a North Atlantic cyclone. *Q. J. R. Meteorol. Soc.*, **139**, 1270–1282, doi:10.1002/qj.2037.

Charney, J., 1947: The dynamics of long waves in a baroclinic westerly current. *J. Meteor.*, **4**, 136–162.

Charney, J. G. and N. A. Phillips, 1953: Numerical integration of the quasi-geostrophic equations for barotropic and simple baroclinic flows. *J. Meteor.*, **10**, 7199.

Clark, P. A., K. A. Browning, and C. Wang, 2005: The sting at the end of the tail: Model diagnostics of fine-scale three-dimensional structure of the cloud head. *Q. J. R. Meteorol. Soc.*, **131**, 2263–2292.

Clark, P. A. and S. L. Gray, 2018: Sting Jets in extratropical cyclones: a review. *Q. J. R. Meteorol. Soc.*, doi:10.1002/qj.3267.

Clough, S. and R. Franks, 1991: The evaporation of frontal and other stratiform precipitation. *Q. J. R. Meteorol. Soc.*, **117**, 1057–1080.

Coronel, B., D. Ricard, G. Rivière, and P. Arbogast, 2015: Role of moist processes in the tracks of idealized midlatitude surface cyclones. *J. Atmos. Sci.*, **72**, 2979–2996.

— 2016: Cold-conveyor-belt jet, sting jet and slantwise circulations in idealized simulations of extratropical cyclones. *Q. J. R. Meteorol. Soc.*, **142**, 1781–1796.

Davies, H., C. Schär, and H. Wernli, 1991: The palette of fronts and cyclones within a baroclinic wave development. *J. Atmos. Sci.*, **48**, 1666–1689.

Davies, T., M. J. P. Cullen, A. J. Malcolm, M. H. Mawson, A. Staniforth, A. A. White, and N. Wood, 2005: A new dynamical core for the Met Office's global and regional modelling of the atmosphere. *Q. J. R. Meteorol. Soc.*, **131**, 1759–1782, doi:10.1256/qj.04.101.

Dee, D., S. Uppala, A. Simmons, P. Berrisford, P. Poli, S. Kobayashi, U. Andrae, M. Balmaseda, G. Balsamo, P. Bauer, et al., 2011: The Era-Interim reanalysis: Configuration and performance of the data assimilation system. *Q. J. R. Meteorol. Soc.*, **137**, 553–597.

Durran, D. R. and J. B. Klemp, 1982: On the Effects of Moisture on the Brunt-Väisälä Frequency. *J. Atmos. Sci.*, **39**, 2152–2158.

Eady, E. T., 1949: Long Waves and Cyclone Waves. *Tellus*, **1**, 33–52, doi:10.1111/j.2153-3490.1949.tb01265.x.

Edwards, J. and A. Slingo, 1996: Studies with a flexible new radiation code. Part I: Choosing a configuration for a large-scale model. *Q. J. R. Meteorol. Soc.*, **122**, 689719, doi:10.1002/qj.49712253107.

Eliassen, A., 1962: On the vertical circulation in frontal zones. *Geofys. Publ*, **24**, 147–160.

Emanuel, K. A., 1994: *Atmospheric convection*. Oxford University Press.

Forbes, R. M. and P. A. Clark, 2003: Sensitivity of extratropical cyclone mesoscale structure to the parametrization of ice microphysical processes. *Q. J. R. Meteorol. Soc.*, **129**, 1123–1148, doi:10.1256/qj.01.171.

Gilet, J. B., M. Plu, and G. Rivière, 2009: Nonlinear Baroclinic Dynamics of Surface Cyclones Crossing a Zonal Jet. *J. Atmos. Sci.*, **66**, 3021–3041.

Grant, A. L. M., 2001: Cloud-base fluxes in the cumulus-capped boundary layer. *Q. J. R. Meteorol. Soc.*, **127**, 407–421, doi:10.1002/qj.49712757209.

Gray, S. L., O. Martínez-Alvarado, L. H. Baker, and P. A. Clark, 2011: Conditional symmetric instability in sting-jet storms. *Q. J. R. Meteorol. Soc.*, **137**, 1482–1500.

Gray, S. L. and A. Thorpe, 2001: Parcel theory in three dimensions and the calculation of SCAPE. *Mon. Weather Rev.*, **129**, 1656–1672.

Gregory, D., P. Inness, A. Maidens, R. Wong, and R. Stratton, 2009: Unified Model Documentation Paper No. 27. Accessed from http://cms.ncas.ac.uk/wiki/Docs/MetOfficeDocs.

Gregory, D. and P. R. Rowntree, 1990: A mass flux convection scheme with representation of cloud ensemble characteristics and stability-dependent closure. *Mon. Weather Rev.*, **118**, 1483–1506.

Grønås, S., 1995: The seclusion intensification of the New Year's Day storm 1992. *Tellus*, **47A**, 733–746.

Harrold, T. W., 1973: Mechanisms influencing the distribution of precipitation within baroclinic disturbances. *Q. J. R. Meteorol. Soc.*, **99**, 232–251, doi:10.1002/qj.49709942003.

Hart, N. C. G., S. L. Gray, and P. A. Clark, 2017: Sting-Jet Windstorms over the North Atlantic: Climatology and Contribution to Extreme Wind Risk. *J. Climate*, **30**, 5455–5471, doi:10.1175/JCLI-D-16-0791.1.

Hewson, T. D. and U. Neu, 2015: Cyclones, windstorms and the IMILAST project. *Tellus A: Dynamic Meteorology and Oceanography*, **67**, 27128, doi:10.3402/tellusa.v67.27128.

Holton, J. R., 2004: *An Introduction to Dynamic Meteorology*. Academic Press, 4th edition.

Hoskins, B., 1974: The role of potential vorticity in symmetric stability and instability. *Q. J. R. Meteorol. Soc.*, **100**, 480–482.

Hoskins, B. and P. Berrisford, 1988: A potential vorticity perspective of the storm of 15-16 October 1987. *Weather*, **43**, 122–129, doi:10.1002/j.1477-8696.1988.tb03890.x.

Hoskins, B. J. and I. N. James, 2014: *Fluid Dynamics of the Mid-Latitude Atmosphere*. John Wiley & Sons.

Hoskins, B. J., M. E. McIntyre, and A. W. Robertson, 1985: On the use and significance of isentropic potential vorticity maps. *Q. J. R. Meteorol. Soc.*, **111**, 877–946.

Joos, H. and H. Wernli, 2012: Influence of microphysical processes on the potential vorticity development in a warm conveyor belt: a case-study with the limited area model cosmo. *Q. J. R. Meteorol. Soc.*, **138**, 407–418, doi:10.1002/qj.934.

Keyser, D., M. J. Reeder, and R. J. Reed, 2000: A generalization of Petterssen's frontogenesis function and its relation to the forcing of vertical motion. *Mon. Weather Rev.*, **116**, 762–780.

Lean, H. W. and P. A. Clark, 2003: The effects of changing resolution on mesocale modelling of line convection and slantwise circulations in FASTEX IOP16. *Q. J. R. Meteorol. Soc.*, **129**, 2255–2278, doi:10.1256/qj.02.57.

Lean, H. W., P. A. Clark, M. Dixon, N. M. Roberts, A. Fitch, R. Forbes, and C. Halliwell, 2008: Characteristics of High-Resolution Versions of the Met Office Unified Model for Forecasting Convection over the United Kingdom. *Mon. Weather Rev.*, **136**, 3408–3424, doi:10.1175/2008MWR2332.1.

Lock, A. P., 2001: The Numerical Representation of Entrainment in Parameterizations of Boundary Layer Turbulent Mixing. *Mon. Weather Rev.*, **129**, 1148–1163.

Lock, A. P., A. R. Brown, M. R. Bush, G. M. Martin, and R. N. B. Smith, 2000: A new boundary layer mixing scheme. Part I: Scheme description and single-column model tests. *Mon. Weather Rev.*, **128**, 3187–3199.

Markowski, P. and Y. Richardson, 2010: *Mesoscale meteorology in Midlatitudes*. Wiley.

Martínez-Alvarado, O., L. H. Baker, S. L. Gray, J. Methven, and R. S. Plant, 2014a: Distinguishing the cold conveyor belt and sting jet air streams in an intense extratropical cyclone. *Mon. Weather Rev.*, **142**, 2571–2595, doi:10.1175/MWR-D-13-00348.1.

Martínez-Alvarado, O., S. L. Gray, J. L. Catto, and P. A. Clark, 2012: Sting Jets in intense winter North-Atlantic windstorms. *Env. Res. Lett.*, **7**, doi: 10.1088/1748-9326/7/2/024014.

— 2014b: Corrigendum: Sting jets in intense winter North-Atlantic windstorms. *Env. Res. Lett.*, **9**.

Martínez-Alvarado, O., S. L. Gray, P. A. Clark, and L. H. Baker, 2013: Objective detection of sting jets in low-resolution datasets. *Meteorol. Appl.*, **20**, 41–55, doi: 10.1002/met.297.

Martínez-Alvarado, O., F. Weidle, and S. L. Gray, 2010: Sting Jets in Simulations of a Real Cyclone by Two Mesoscale Models. *Mon. Weather Rev.*, **138**, 4054–4075.

Matthews, T., C. Murphy, R. L. Wilby, and S. Harrigan, 2014: Stormiest winter on record for Ireland and UK. *Nature Climate Change*, **4**, 738–740, doi:10.1038/nclimate2336.

Morris, R. M. and A. J. Gadd, 1988: Forecasting the storm of 15-16 October 1987. *Weather*, **43**, 70–90, doi:10.1002/j.1477-8696.1988.tb03884.x.

Natural Environment Research Council, Aberystwyth Radar Facility [Hooper, D.], 2017: The NERC Mesosphere-Stratosphere-Troposphere (MST) Radar Facility at Aberystwyth. British Atmospheric Data Centre, 2006-,2017-01-30,.

Panagi, P., 2011: NDdiag: A Fortran90 program to compute diagnostics on pressure levels from Unified Model data on model levels. Accessed from https://puma.nerc.ac.uk/trac/UM_TOOLS/wiki/NDdiag.

Parton, G., A. Dore, and G. Vaughan, 2010: A climatology of mid-tropospheric mesoscale strong wind events as observed by the MST radar, Aberystwyth. *Meteorol. Appl.*, **17**, 340–354.

Parton, G. A., G. Vaughan, E. G. Norton, K. A. Browning, and P. A. Clark, 2009: Wind profiler observations of a sting jet. *Q. J. R. Meteorol. Soc.*, **135**, 663–680.

Persson, P. O. G. and T. T. Warner, 1993: Nonlinear Hydrostatic Conditional Symmetric Instability: Implications for Numerical Weather Prediction. *Mon. Weather Rev.*, **121**, 1821–1833.

Petterssen, S., 1936: Contribution to the theory of frontogenesis. *Geofys. Publ.*, **11**, 1–27.

Pinto, J. G., S. Zacharias, A. H. Fink, G. C. Leckebusch, and U. Ulbrich, 2009: Factors contributing to the development of extreme North Atlantic cyclones and their relationship with the NAO. *Climate Dynamics*, **32**, 711–737.

Polvani, L. M. and J. G. Esler, 2007: Transport and mixing of chemical air masses in idealized baroclinic lifecycles. *J. Geophys. Res.*, **112**, doi:10.1029/2007JD008555.

Raveh-Rubin, S., 2017: Dry Intrusions: Lagrangian Climatology and Dynamical Impact on the Planetary Boundary Layer. *J. Climate*, **30**, 6661–6682, doi:10.1175/JCLI-D-16-0782.1.

Research Excellence Framework, 2014: REF Impact Case Studies: Storm prediction improved by sting jet discovery. Accessed from http://impact.ref.ac.uk/CaseStudies/CaseStudy.aspx?Id=37296.

Risk Management Solutions, 2014: RMS - White Paper: 2013–2014 Winter Storms in Europe. An Insurance and Catastrophe Modeling Perspective. Accessed from http://www.rms.com/publications/natural-catastrophes.

Rivière, G., P. Arbogast, K. Maynard, and A. Joly, 2015: Eddy kinetic energy redistribution within windstorms Klaus and Friedhelm. *Q. J. R. Meteorol. Soc.*, **141**, 925–938, doi:10.1002/qj.2412.

Saffin, L., J. Methven, and S. L. Gray, 2016: The non-conservation of potential vorticity by a dynamical core compared with the effects of parametrized physical processes. *Q. J. R. Meteorol. Soc.*, **142**, 1265–1275, doi:10.1002/qj.2729.

Sanders, F. and J. R. Gyakum, 1980: Synoptic-dynamic climatology of the 'bomb'. *Mon. Weather Rev.*, **108**, 1589–1606.

Sawyer, J., 1956: The vertical circulation at meteorological fronts and its relation to frontogenesis. *Proceedings of the Royal Society of London A: Mathematical, Physical and Engineering Sciences*, The Royal Society, volume 234, 346–362.

Schemm, S. and H. Wernli, 2014: The Linkage between the Warm and Cold Conveyor Belts in an Idealized Extratropical Cyclone. *J. Atmos. Sci.*, **71**, 1443–1459.

Schultz, D. M., 2001: Reexamining the cold conveyor belt. *Mon. Weather Rev.*, **129**, 2205–2225.

Schultz, D. M. and K. A. Browning, 2017: What is a sting jet? *Weather*, **72**, 63–66, doi:10.1002/wea.2795.

Schultz, D. M., D. Keyser, and L. F. Bosart, 1998: The effect of large-scale flow on low-level frontal structure and evolution in midlatitude cyclones. *Mon. Weather Rev.*, **126**, 1767–1791.

Schultz, D. M. and P. N. Schumacher, 1999: The use and Misuse of Conditional Symmetric Instability. *Mon. Weather Rev.*, **127**, 2709–2732.

Schultz, D. M., P. N. Schumacher, and C. A. Doswell III, 2000: The intricacies of instabilities. *Mon. Weather Rev.*, **128**, 4143–4148.

Schultz, D. M. and J. M. Sienkiewicz, 2013: Using frontogenesis to identify sting jets in extratropical cyclones. *Weather and Forecasting*, **28**, 603–613.

Schultz, D. M. and G. Vaughan, 2011: Occluded Fronts and the Occlusion Process: A Fresh Look at Conventional Wisdom. *Bull. Amer. Meteor. Soc.*, **92**, 443–466.

Schultz, D. M. and F. Zhang, 2007: Baroclinic development within zonally-varying flows. *Q. J. R. Meteorol. Soc.*, **133**, 1101–1112.

Shapiro, M., H. Wernli, J.-W. Bao, J. Methven, X. Zou, J. Doyle, T. Holt, E. Donall-Grell, and P. Neiman, 1999: A planetary-scale to mesoscale perspective of the life cycles of extratropical cyclones: The bridge between theory and observations. *The life cycles of extratropical cyclones*, 139–185.

Shapiro, M. A. and D. Keyser, 1990: Fronts, jet streams and the tropopause. *Extratropical cyclones: the Erik Palmén memorial volume*, C. Newton and E. E O Holopainen, eds., American Meteorological Society, 167–191.

Shutts, G., 1990a: SCAPE charts from numerical weather prediction model fields. *Mon. Weather Rev.*, **118**, 2745–2751.

Shutts, G. J., 1990b: Dynamical aspects of the october storm, 1987: A study of a successful fine-mesh simulation. *Q. J. R. Meteorol. Soc.*, **116**, 1315–1347, doi:10.1002/qj.49711649604.

Simmons, A. J. and B. J. Hoskins, 1980: Barotropic influences on the growth and decay of nonlinear baroclinic waves. *J. Atmos. Sci.*, **37**, 1679–1684.

Slater, T. P., D. M. Schultz, and G. Vaughan, 2015: Acceleration of near-surface strong winds in a dry, idealised extratropical cyclone. *Q. J. R. Meteorol. Soc.*, **141**, 1004–1016, doi:10.1002/qj.2417.

— 2017: Near-surface strong winds in a marine extratropical cyclone: acceleration of the winds and the importance of surface fluxes. *Q. J. R. Meteorol. Soc.*, **143**, 321–332, doi:10.1002/qj.2924.

Smart, D. J. and K. A. Browning, 2014: Attribution of strong winds to a cold conveyor belt and sting jet. *Q. J. R. Meteorol. Soc.*, **140**, 595–610, doi:10.1002/qj.2162.

Smith, R. N. B., 1990: A scheme for predicting layer clouds and their water content in a general circulation model. *Q. J. R. Meteorol. Soc.*, **116**, 435–460, doi:10.1002/qj.49711649210.

Sprenger, M. and H. Wernli, 2015: The LAGRANTO Lagrangian analysis tool version 2.0. *Geosci. Model Dev.*, **8**, 2569–2586, doi:10.5194/gmd-8-2569-2015.

Staniforth, A., T. Melvin, and N. Wood, 2013: GungHo! A new dynamical core for the Unified Model. ECMWF Seminar on Numerical Methods for Atmosphere and Ocean Modelling, 2-5 September 2013.

Staniforth, A., A. White, N. Wood, J. Thuburn, M. Zerroukat, E. Cordero, T. Davies, and M. Tiamantakis, 2006: Unified Model Documentation Paper No. 15. Joy of U.M. 6.3 - Model Formulation. Accessed from http://cms.ncas.ac.uk/wiki/Docs/MetOfficeDocs.

Thorncroft, C. D., B. J. Hoskins, and M. E. McIntyre, 1993: Two paradigms of baroclinic-wave life-cycle behaviour. *Q. J. R. Meteorol. Soc.*, **119**, 17–56.

Uccellini, L. W., 1990: Processes contributing to the rapid development of extratropical cyclones. *Extratropical Cyclones: The Erik Palmén Memorial Volume*, 81–105.

UK Met Office, 2012a: The 1987 Great Storm - What is a Sting Jet? Accessed from http://www.metoffice.gov.uk/news/in-depth/1987-great-storm/sting-jet.

— 2012b: Unified Model Basic User Guide. Document Version: 8.2.0. Accessed from http://cms.ncas.ac.uk/wiki/Docs/MetOfficeDocs.

— 2015: Winter storms, January to February 2014. Accessed from http://www.metoffice.gov.uk/climate/uk/interesting/2014-janwind.

Vaughan, G., J. Methven, D. Anderson, B. Antonescu, L. Baker, T. Baker, S. Ballard, K. Bower, P. Brown, J. Chagnon, et al., 2015: Cloud banding and winds in intense European cyclones: Results from the DIAMET project. *Bull. Amer. Meteor. Soc.*, **96**, 249–265.

Volonté, A., P. A. Clark, and S. L. Gray, 2018: The Role of Mesoscale Instabilities in the Sting-Jet dynamics of Windstorm Tini. *Q. J. R. Meteorol. Soc.*, doi:10.1002/qj.3264.

Walters, D., N. Wood, S. Vosper, and S. Milton, 2014: ENDGame: A new dynamical core for seamless atmospheric prediction. Accessed from https://www.metoffice.gov.uk/binaries/content/assets/mohippo/pdf/s/h.

Wernli, H. and H. C. Davies, 1997: A Lagrangian-based analysis of extratropical cyclones. I: The method and some applications. *Q. J. R. Meteorol. Soc.*, **123**, 467–489.

Wernli, H., R. Fehlmann, and D. Lüthi, 1998: The effect of barotropic shear on upper-level induced cyclogenesis: Semigeostrophic and primitive equation numerical simulations. *J. Atmos. Sci.*, **55**, 2080–2094.

Wilson, D. R. and S. P. Ballard, 1999: A microphysically based precipitation scheme for the UK Meteorological Office Unified Model. *Q. J. R. Meteorol. Soc.*, **125**, 16071636.

Wood, N., A. Staniforth, A. White, T. Allen, M. Diamantakis, M. Gross, T. Melvin, C. Smith, S. Vosper, M. Zerroukat, and J. Thuburn, 2014: An inherently mass-conserving semi-implicit semi-Lagrangian discretization of the deep-atmosphere global non-hydrostatic equations. *Q. J. R. Meteorol. Soc.*, **140**, 1505–1520.

Xui, Q. and J. H. E. Clark, 1985: The Nature of Symmetric Instability and Its Similarity to Convective and Inertial Instability. *J. Atmos. Sci.*, **42**, 2880–2883.

Appendices

Appendix A

Initial Profiles for an Idealised Cyclone

by Prof. Peter Clark, 2017

A.1 New Dynamics/Endgame equations of motion

The equations of motion are taken from the UMDP 15 eqs. 2.71 to 2.79:

$$\frac{\mathrm{D}u}{\mathrm{D}t} = \frac{uv\tan\phi}{r} - \frac{uw}{r} + f_3 v - f_2 w - \frac{c_{pd}\theta_v}{r\cos\phi}\left(\frac{\partial\Pi}{\partial\lambda} - \frac{\partial\Pi}{\partial r}\frac{\partial r}{\partial\lambda}\right) + S^u \tag{A.1}$$

$$\frac{\mathrm{D}v}{\mathrm{D}t} = \frac{u^2\tan\phi}{r} - \frac{vw}{r} + f_1 w - f_3 u - \frac{c_{pd}\theta_v}{r}\left(\frac{\partial\Pi}{\partial\phi} - \frac{\partial\Pi}{\partial r}\frac{\partial r}{\partial\phi}\right) + S^v \tag{A.2}$$

$$\frac{\mathrm{D}w}{\mathrm{D}t} = \frac{u^2+v^2}{r} + f_2 u - f_1 v - g - c_{pd}\theta_v\frac{\partial\Pi}{\partial r} + S^w \tag{A.3}$$

where:

$$\frac{\mathrm{D}}{\mathrm{D}t} \equiv \frac{\partial}{\partial t} + \frac{u}{r\cos\phi}\frac{\partial}{\partial\lambda} + \frac{v}{r}\frac{\partial}{\partial\phi} + \dot{\eta}\frac{\partial}{\partial\eta} \tag{A.4}$$

$$\Pi = \left(\frac{p}{p_0}\right)^{\frac{R_d}{c_{pd}}}; \quad p_0 = 10^5 \text{ Pa} \tag{A.5}$$

$$\theta_v = \frac{T}{\Pi}\left(\frac{1+\frac{1}{\epsilon}m_v}{1+m_v+m_{cl}+m_{cf}}\right); \quad \epsilon = \frac{R_d}{R_v} = 0.622 \tag{A.6}$$

$$f_1 = 2\Omega\sin\lambda\cos\phi_0 \tag{A.7}$$

$$f_2 = 2\Omega\left(\cos\phi\sin\phi_0 + \sin\phi\cos\lambda\cos\phi_0\right) \tag{A.8}$$

$$f_3 = 2\Omega\left(\sin\phi\sin\phi_0 - \cos\phi\cos\lambda\cos\phi_0\right) \tag{A.9}$$

All derivatives with respect to λ and ϕ (i.e. 'horizontal' derivatives) are along constant η surfaces.

Note that ENDGAME does not use θ or θ_v as prognostic - all variables are related to *dry* density, ρ_d (i.e. the density of the air not including water vapour), so

$$\rho = \rho_d \left(1 + \sum m_X\right) = \rho_d \left(1 + m_v\right) \tag{A.10}$$

where $\sum m_X$ is the sum of all water species and this reduces to m_v in our case. Similarly,

$$\theta_{vd} = \theta \left(1 + \frac{1}{\epsilon} m_v\right) \tag{A.11}$$

and

$$\theta_v = \frac{\theta_{vd}}{\left(1 + \sum m_X\right)} \tag{A.12}$$

The equation of state is thus

$$\rho_d = \left(\frac{p_0}{R_d}\right) \frac{\Pi^{\frac{1-\kappa_d}{\kappa_d}}}{\theta_{vd}} \tag{A.13}$$

This can be rewritten

$$\rho_d = \left(\frac{p_0}{R_d}\right) \left(\frac{p}{p_0}\right) \frac{1}{\Pi \theta_{vd}} \Rightarrow p = R_d \rho_d T_{vd} \tag{A.14}$$

From the above, clearly we can also write

$$p = R_d \rho T_v \tag{A.15}$$

A.2 Thermal wind balance for uniform zonal flow

A.2.1 Balanced zonal flow

In the above we assume $v = w = 0$, $u \equiv u\left(\phi, \eta\right)$, and no surface orography, so $r \equiv r\left(\eta\right)$. Then eqs. (A.1) to (A.3) become:

$$0 = -\frac{c_{pd} \theta_v}{r \cos\phi} \frac{\partial \Pi}{\partial \lambda} \tag{A.16}$$

$$0 = \frac{u^2 \tan\phi}{r} - f_3 u - \frac{c_{pd}\theta_v}{r}\frac{\partial \Pi}{\partial \phi} \tag{A.17}$$

$$0 = \frac{u^2}{r} + f_2 u - g - c_{pd}\theta_v \frac{\partial \Pi}{\partial r} \tag{A.18}$$

The next step is to eliminate the Exner pressure by differentiating eq. (A.17) with respect to r and eq. (A.18) with respect to ϕ. For simplicity, we multiply eq. (A.17) by r first then differentiate:

$$0 = (2u\tan\phi - f_3 r)\frac{\partial u}{\partial r} - f_3 u - c_{pd}\frac{\partial \theta_v}{\partial r}\frac{\partial \Pi}{\partial \phi} - c_{pd}\theta_v \frac{\partial^2 \Pi}{\partial \phi \partial r} \tag{A.19}$$

Differentiating (A.18) with respect to ϕ:

$$0 = \left(\frac{2u}{r} + f_2\right)\frac{\partial u}{\partial \phi} - c_{pd}\frac{\partial \theta_v}{\partial \phi}\frac{\partial \Pi}{\partial r} - c_{pd}\theta_v \frac{\partial^2 \Pi}{\partial \phi \partial r} \tag{A.20}$$

A.2.2 Ian Boutle's approximation

Ian Boutle's idealised setup is based on shallow atmosphere thermal wind balance. It ignores the first two terms on the right hand side in eq. (A.18), to give the usual hydrostatic approximation:

$$0 = -g - c_{pd}\theta_v \frac{\partial \Pi}{\partial r} \tag{A.21}$$

so eq. (A.20) becomes:

$$\begin{aligned} 0 &= - c_{pd}\frac{\partial \theta_v}{\partial \phi}\frac{\partial \Pi}{\partial r} - c_{pd}\theta_v \frac{\partial^2 \Pi}{\partial \phi \partial r} \\ \Rightarrow -c_{pd}\theta_v \frac{\partial^2 \Pi}{\partial \phi \partial r} &= c_{pd}\frac{\partial \theta_v}{\partial \phi}\frac{\partial \Pi}{\partial r} \\ &= -\frac{g}{\theta_v}\frac{\partial \theta_v}{\partial \phi} \end{aligned} \tag{A.22}$$

where the final step uses eq. (A.21). Boutle also ignores the second and third terms in eq. (A.19), leading to:

$$0 = (2u\tan\phi - f_3 r)\frac{\partial u}{\partial r} - c_{pd}\theta_v \frac{\partial^2 \Pi}{\partial \phi \partial r} \tag{A.23}$$

Thus, using eq. (A.22), we obtain:

$$0 = (2u \tan\phi - f_3 r)\frac{\partial u}{\partial r} - \frac{g}{\theta_v}\frac{\partial \theta_v}{\partial \phi} \tag{A.24}$$

Finally, Boutle replaces r in the f_3 term in parentheses with a, the constant radius of the earth (consistent with ignoring the $f_3 u$ term), and sets $\theta_v = \theta_v(0)$ in the denominator of the last term, leading to:

$$\frac{\partial \theta_v}{\partial \phi} = \frac{\theta_v(0)}{g}(2u \tan\phi - f_3 a)\frac{\partial u}{\partial r} \tag{A.25}$$

We start with a reference profile, $\theta_v^{ref}(r)$. Then

$$\theta_v(r,\phi) = \theta_v^{ref}(r) + \int_{\phi_s}^{\phi} \frac{\theta_v(0)}{g}\left(2u\left(r,\phi'\right)\tan\phi' - f_3 a\right)\frac{\partial u}{\partial r}\mathrm{d}\phi \tag{A.26}$$

Polvani and Esler (2007) point out that the LC1 setup has zero wind at the surface, so it is sufficient to set the surface pressure to $p_s = 1000hPa$. They use pressure coordinates and so integrate the hydrostatic balance equation to obtain the height of pressure levels. The equivalent in height coordinates is to integrate eq. (A.21), thus:

$$\Pi(r) = \Pi_s - \int_0^r \frac{g}{c_{pd}\theta_v}\mathrm{d}r \tag{A.27}$$

where $\Pi_s = \left(\frac{p_s}{p_0}\right)^{\frac{R_d}{c_{pd}}}$, most conveniently set to 1 for the LC1 setup. This gives us a slight problem, in that Π is stored on model ρ levels. If we assume an adiabatic layer at the surface, then we can compute Π at the first ρ level and continue from there upwards.

More generally, there is a non-zero zonal wind at the surface. Polvani and Esler (2007) address this through an iterative procedure, as they are working in pressure coordinates which do not coincide with the surface. However, Boutle does make two further changes.

The first of these makes a correction to the temperature. In fact, he describes an algorithm which shall be detailed below, but the algorithm actually implemented (which we shall call 'profile correction option 1') is as follows: the vertical θ_v profile is adjusted everywhere using a constant value to make that at the surface at the jet centre equal to the reference. If we call the result of eq. (A.26) θ_v^1 then

$$\theta_v(r,\phi) = \theta_v^1(r,\phi) - \theta_v^1(r_0,\phi_0) + \theta_v^{ref}(r_0) \tag{A.28}$$

where ϕ_0 is the jet centre and r_0 is the value of r at the surface.

A first estimate of Exner pressure, Π^1 is then computed by integrating down from the model top:

$$\Pi^1(r,\phi) = \Pi_t - \int_{r_t}^{r} \frac{g}{c_{pd}\theta_v(r,\phi)} \mathrm{d}r \tag{A.29}$$

where r_t is the model top and Π_t the Exner pressure there. This is then adjusted to make the surface pressure at the jet centre equal to the required surface pressure:

$$\Pi^1(r,\phi) = \Pi^1(r,\phi) + \Pi_s - \Pi^1(0,\phi_0) \tag{A.30}$$

Π_t is thus irrelevant and is set to zero in the code.

This procedure ensures that the reference surface pressure and surface θ_v result at the jet centre, while the θ_v and Π fields satisfy hydrostatic and thermal wind balance.

Note that, if we approximate further, and take $u = 0$ in eq. (A.24) we obtain:

$$\frac{\partial u}{\partial r} = -\frac{g}{f_3 r \theta_v}\frac{\partial \theta_v}{\partial \phi} = -\frac{g}{f_3\theta_v}\frac{\partial \theta_v}{\partial y} \tag{A.31}$$

or

$$\frac{\partial u}{\partial \Pi} = \frac{c_{p_d}}{f_3}\frac{\partial \theta_v}{\partial y} \tag{A.32}$$

Note

$$\frac{\partial \Pi}{\partial p} = \frac{R}{c_{p_d}}\frac{\Pi}{p} \tag{A.33}$$

so

$$\frac{\partial u}{\partial \ln p} = \frac{R}{f_3}\frac{\partial T_v}{\partial y} \tag{A.34}$$

where the gradient on the right is along pressure surfaces. This corresponds to the 'text book' thermal wind equation.

A.2.3 An accurate algorithm

Rewrite (A.17) thus:

$$c_{pd}\frac{\partial \Pi}{\partial \phi} = \frac{A}{\theta_v}; \quad A = u^2 \tan\phi - f_3 ur \tag{A.35}$$

Rewrite (A.18) to obtain quasi-hydrostatic balance thus:

$$c_{pd}\frac{\partial \Pi}{\partial r} = \frac{B}{\theta_v}; \quad B = \frac{u^2}{r} + f_2 u - g \tag{A.36}$$

Differentiating the first with respect to r and the second with respect to ϕ we obtain the thermal wind relationship:

$$\frac{1}{\theta_v}\frac{\partial A}{\partial r} - \frac{A}{\theta_v^2}\frac{\partial \theta_v}{\partial r} = \frac{1}{\theta_v}\frac{\partial B}{\partial \phi} - \frac{B}{\theta_v^2}\frac{\partial \theta_v}{\partial \phi} \tag{A.37}$$

Thus:

$$B\frac{\partial \ln\theta_v}{\partial \phi} = \frac{\partial B}{\partial \phi} + A\frac{\partial \ln\theta_v}{\partial r} - \frac{\partial A}{\partial r} \tag{A.38}$$

Starting from a reference profile, $\theta_v^{ref}(r)$, we can formally integrate thus:

$$\ln\left[\theta_v(r,\phi)/\theta_v^{ref}\right] = \ln B(r,\phi) - \ln B(r,\phi_s) - \int_{\phi_s}^{\phi}\frac{1}{B}\left[\frac{\partial A}{\partial r} - A\frac{\partial \ln\theta_v}{\partial r}\right]\mathrm{d}\phi' \tag{A.39}$$

i.e.

$$\theta_v(r,\phi) = \theta_v^{ref}(r)\frac{B(r,\phi)}{B(r,\phi_s)}\exp\left(-\int_{\phi_s}^{\phi}\frac{1}{B}\left[\frac{\partial A}{\partial r} - A\frac{\partial \ln\theta_v}{\partial r}\right]\mathrm{d}\phi'\right) \tag{A.40}$$

In Boutle's approximation $B \approx -g$, $\exp(-I) \approx 1 - I$, where I is the integral expression, and the second term in the integral is ignored.

The main issue with the above is the second term in the integral; we anticipate that the thermal wind will only have a small impact on the stability so using θ_v^{ref} in this term is probably a good approximation. This suggests an iterative approach, using this as a starting estimate (or even Boutle's approximation), then refining the estimate using the previous iteration in this term.

Once θ_v is obtained, we can compute the Exner pressure from eq. (A.36):

$$\Pi\left(r\right) = \Pi_s + \int_0^r \frac{B}{c_{pd}\theta_v} \mathrm{d}r \tag{A.41}$$

The same adjustments can be made as in Boutle's algorithm; we repeat here for completeness. The algorithm we shall call 'profile correction option 1' is as follows: the vertical θ_v profile is adjusted everywhere using a constant value to make that at the surface at the jet centre equal to the reference. If we call the result of eq. (A.26) θ_v^1 then

$$\theta_v\left(r,\phi\right) = \theta_v^1\left(r,\phi\right) - \theta_v^1\left(a,\phi_0\right) + \theta_v^{ref}\left(a\right) \tag{A.42}$$

where ϕ_0 is the jet centre and a is the value of r at the surface.

The algorithm we shall call 'profile correction option 2' seeks to adjust the entire vertical θ_v profile everywhere to make that at the jet centre equal to the reference. With the result of eq. (A.40) denoted θ_v^1, the vertical θ_v profile is adjusted everywhere thus:

$$\theta_v\left(r,\phi\right) = \theta_v^1\left(r,\phi\right) - \theta_v^1\left(r,\phi_0\right) + \theta_v^{ref}\left(r\right) \tag{A.43}$$

where ϕ_0 is the jet centre. Note, however, that, apart from the $\frac{\partial \ln \theta_v}{\partial r}$, the factor multiplying θ_v^{ref} in eq. (A.40) is just a function of u, and hence r and ϕ, say $F\left(r,\phi\right)$. It would be better to write:

$$\theta_v\left(r,\phi\right) = \left(\theta_v^{ref}\left(r\right) + \theta_{corr}\left(r\right)\right) F\left(r,\phi\right) \tag{A.44}$$

Defining θ_v^1 as the solution with $\theta_{corr} = 0$, eq. (A.44) becomes, with our requirement that the reference profile appears at ϕ_0:

$$\begin{aligned}
\theta_v\left(r,\phi_0\right) = \left(\theta_v^{ref}\left(r\right) + \theta_{corr}\left(r\right)\right) F\left(r,\phi_0\right) &= \theta_v^{ref}\left(r\right) \\
\Rightarrow \left(\theta_v^{ref}\left(r\right) + \theta_{corr}\left(r\right)\right) \frac{\theta_v^1\left(r,\phi_0\right)}{\theta_v^{ref}\left(r\right)} &= \theta_v^{ref}\left(r\right) \\
\Rightarrow \theta_v^{ref}\left(r\right) + \theta_{corr}\left(r\right) &= \frac{\left(\theta_v^{ref}\left(r\right)\right)^2}{\theta_v^1\left(r,\phi_0\right)} \\
\Rightarrow \theta_{corr}\left(r\right) &= \frac{\left(\theta_v^{ref}\left(r\right)\right)^2}{\theta_v^1\left(r,\phi_0\right)} - \theta_v^{ref}\left(r\right)
\end{aligned} \tag{A.45}$$

If $\theta_{corr} \ll \theta_v^{ref}$ then this approximates as eq. (A.43).

A first estimate of Exner pressure, Π^1 is then computed by integrating down from the model top:

$$\Pi^1(r,\phi) = \Pi_t + \int_{r_t}^{r} \frac{B}{c_{pd}\theta_v(r,\phi)} \mathrm{d}r \tag{A.46}$$

where r_t is the model top and Π_t the Exner pressure there. This is then adjusted to make the surface pressure at the jet centre equal to the required surface pressure:

$$\Pi^1(r,\phi) = \Pi^1(r,\phi) + \Pi_s - \Pi^1(0,\phi_0) \tag{A.47}$$

Π_t is thus irrelevant and is set to zero in the code.

This procedure ensures that the reference surface pressure and θ_v profile result at the jet centre, while the θ_v and Π fields satisfy quasi-hydrostatic and thermal wind balance.

A.3 Reference θ_v Profile

Polvani and Esler (2007) use a reference profile given by

$$T_r(z) = T_0 + \frac{\Gamma_0}{\left(z_T^{-\alpha} + z^{-\alpha}\right)^{1/\alpha}} \tag{A.48}$$

with $T_0 = 300$ K, $\Gamma_0 = -6.5$ K/km, $z_T = 13$ km and $\alpha = 10$. This gives a constant dry lapse rate in the troposphere, transitioning smoothly to an isothermal layer in the stratosphere. Since Exner pressure is on a different level an iterative method is used to find a consistent integration of the hydrostatic relationship eq. (A.21) (with zero wind).

Baker et al. (2014) use a more straightforward piecewise constant profile:

$$\begin{aligned} \theta(z) =& \theta_0 + \Gamma_T z; && z \le z_T \\ =& \theta_0 + \Gamma_T z_T + \Gamma_S (z - z_T); && z > z_T \end{aligned} \tag{A.49}$$

with $\Gamma_T = 0.004$ K m^{-1}, $\Gamma_S = 0.016$ K m^{-1} and $z_T = 10^4$ m.

A.4 Jet Specification

The Polvani and Esler (2007) has been extended somewhat according to Baker et al. (2014). We assume the jet is confined between ϕ_s and ϕ_e. Define

$$\begin{aligned}\phi^* =& 0 && ;\phi_e < \phi \\ =& \frac{\pi}{2}\frac{\phi-\phi_s}{\phi_e-\phi_s} && ;\phi_s \le \phi \le \phi_e \\ =& 0 && ;\phi < \phi_s\end{aligned} \tag{A.50}$$

Then

$$u\left(r,\phi\right) = u_0 F_\phi\left(\phi\right) F_r\left(r\right) + u_s G_\phi\left(\phi\right) G_r\left(r\right) \tag{A.51}$$

where

$$F_\phi\left(\phi\right) = \sin^3\left(\pi \sin^2 \phi^*\right) \tag{A.52}$$

$$F_r\left(r\right) = \left(\frac{z}{z_T}\right)^\gamma \exp\left\{\delta\left[1-\left(\frac{z}{z_T}\right)^{\frac{\gamma}{\delta}}\right]\right\} \tag{A.53}$$

$$G_\phi\left(\phi\right) = \sin^2\left(2\phi\right)\left(\frac{\phi-\phi_{sh}}{\Delta\phi}\right)\exp\left[-\left(\frac{\phi-\phi_{sh}}{\Delta\phi}\right)^2\right] \tag{A.54}$$

$$G_r\left(r\right) = \frac{z}{z_s} \tag{A.55}$$

$z = r - r_0$, r_0 is r at the surface, z_T is the height of the tropopause above the surface, ϕ_{sh} is the latitude of the centre of the shear, $\Delta\phi$ the latitudinal width of the shear and z_s is the scale height of the shear.

Baker et al. (2014) use $\phi_s = 15°\mathrm{N}$, $\phi_e = 85°\mathrm{N}$ (so the jet centre is at $\phi_c = 50°\mathrm{N}$), $z_T = 10^4$ m, $u_0 = 45$ m s^{-1}, $u_s = 0$ m s^{-1}, $\delta = 0.2$ and $\gamma = 1$.

Polvani and Esler (2007) use $\phi_s = 0°\mathrm{N}$, $\phi_e = 90°\mathrm{N}$ (so the jet centre is at $\phi_c = 45°\mathrm{N}$), $z_T = 1.3 \times 10^4$ m, $u_0 = 45$ m s^{-1}, $u_s = 0$ m s^{-1}, $\delta = 0.5$ and $\gamma = 1$.

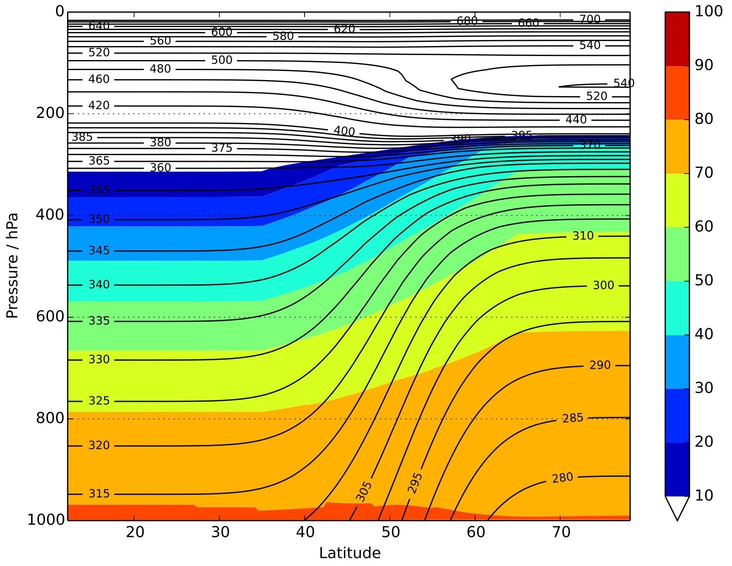

Figure A.1: Initial potential temperature and RH using setup according to Baker et al. (2014) but with $m_v = 10^{-8}$ in the stratosphere. Note θ contour interval changes from 5 K to 20 K at 400 K.

A.5 Moisture

The moisture profile is specified in terms of a specified relative humidity field $RH\,(r, \phi)$. A complicating factor is that the calculation above has been performed in terms of θ_v,

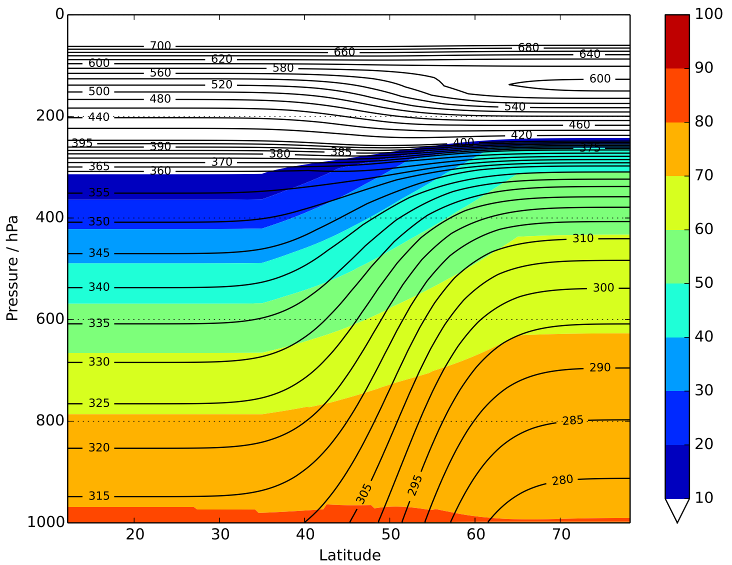

Figure A.2: Initial potential temperature and RH using setup according to Baker et al. (2014) but with $m_v = 10^{-8}$ in the stratosphere and $\Gamma_S = 0.025$, profile correction option 1. Note θ contour interval changes from 5 K to 20 K at 400 K.

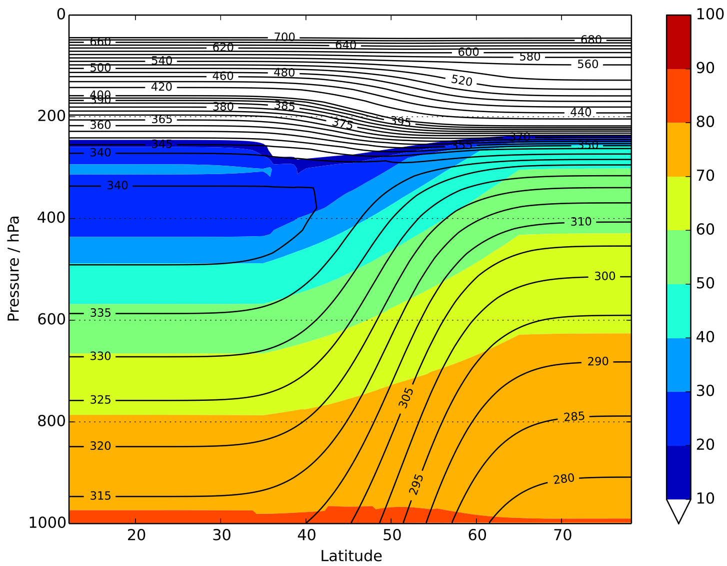

Figure A.3: Initial potential temperature and RH using setup according to Baker et al. (2014) but with $m_v = 10^{-8}$ in the stratosphere and $\Gamma_S = 0.025$, profile correction option 2. Note θ contour interval changes from 5 K to 20 K at 400 K.

without knowing m_v. We adopt the following procedure:

1. Assume $\theta \approx \theta_v$.

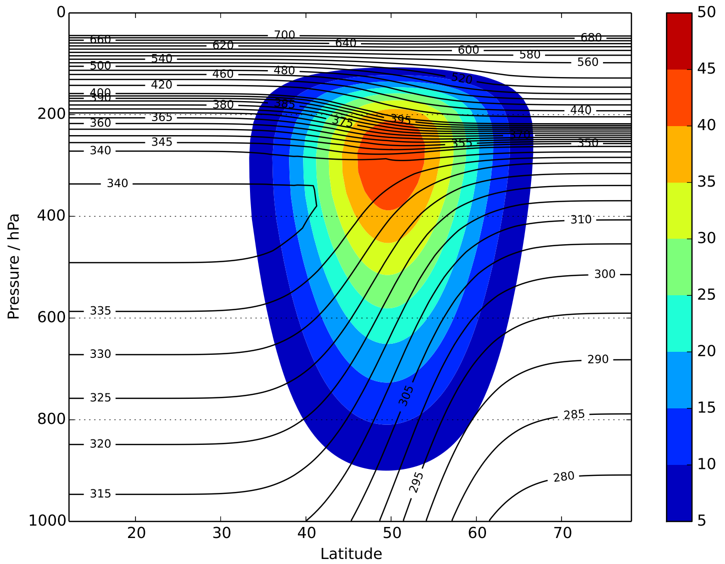

Figure A.4: Initial potential temperature and U wind using setup according to Baker et al. (2014) but with $m_v = 10^{-8}$ in the stratosphere and $\Gamma_S = 0.025$, profile correction option 2. Note θ contour interval changes from 5 K to 20 K at 400 K.

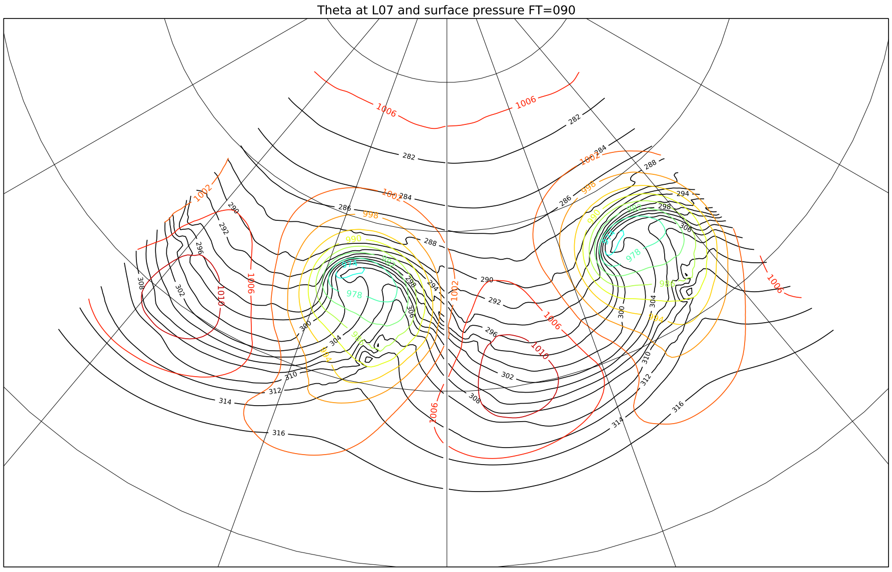

Figure A.5: Potential temperature on level 6 (1000 m, black, K) and surface pressure (coloured, hPa) after 3 days, 18 h, using setup according to Baker et al. (2014) but with $m_v = 10^{-8}$ in the stratosphere and $\Gamma_S = 0.025$, profile correction option 1.

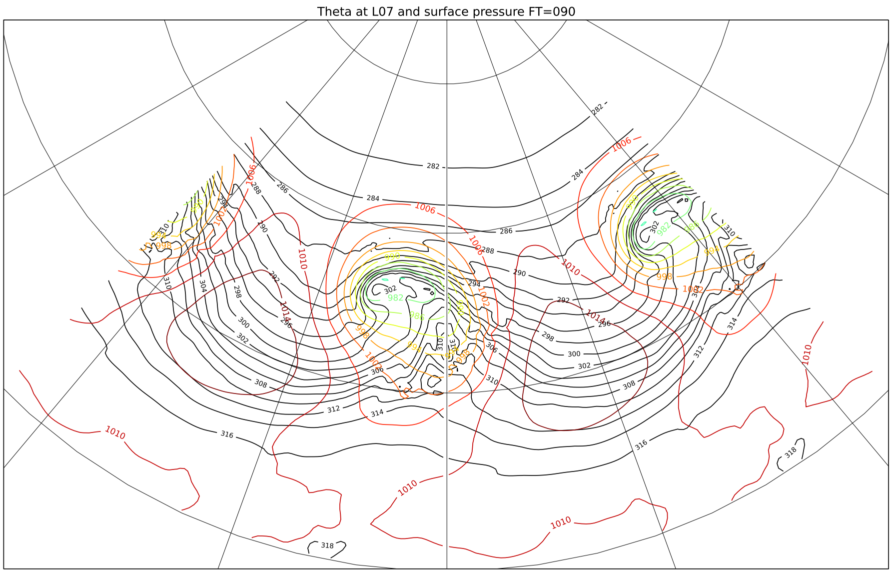

Figure A.6: Potential temperature on level 6 (1000 m, black, K) and surface pressure (coloured, hPa) after 3 days, 18 h, using setup according to Baker et al. (2014) but with $m_v = 10^{-8}$ in the stratosphere and $\Gamma_S = 0.025$, profile correction option 2.

2. Calculate the temperature and pressure using $T \approx \theta\Pi$ and $p = p_0\Pi^{\frac{1}{\kappa}}$.

3. Calculate m_v from

$$m_v(r,\phi) = RH(r,\phi)\, m_{vsat}(T,p) \tag{A.56}$$

4. Calculate θ from

$$\theta = \theta_v \left(\frac{1 + m_v}{1 + \frac{1}{\epsilon} m_v} \right) \tag{A.57}$$

5. Optionally iterate from 2 to 4 until convergence.

The RH profile is specified thus:

$$\begin{aligned} RH\left(r,\phi\right) =& RH_0 \left[1 - 0.9 R\left(\phi\right) \left(\frac{r - r_0}{z_T} \right)^{\alpha} \right] & ; r - r_0 \leq z_T \\ =& 0.0625 RH_0 & ; z_T \leq r - r_0 \end{aligned} \tag{A.58}$$

with

$$\begin{aligned} R\left(\phi\right) =& 1.0 & ; \phi < \phi_s \\ =& 1 - 0.5 \times \frac{\phi - \phi_s}{\phi_e - \phi_s} & ; \phi_s \leq \phi \leq \phi_e \\ =& 0.5 & ; \phi_e < \phi \end{aligned} \tag{A.59}$$

However, with the parameters chosen by Baker et al. (2014) produce a problem in the stratosphere; even though the RH is small, the temperature in the stratosphere is high enough that the calculated water vapour pressure is high enough to contribute substantially to the total pressure. The mixing ratio is thus very large (up to 0.4) resulting in low θ and, ultimately, a statically unstable profile. The model fails after about a day. This did not happen in Laura Baker's runs, presumably because the thermal wind was used to set *theta*, which was not changed when m_v was estimated using the approximate Exner pressure derived from hydrostatic balance not including moisture. No iteration was performed. The initial state was stable but unbalanced.

Setting the initial m_v to 10^{-8} above z_T helps but we still have a statically unstable layer (Fig. A.1). This presumably is a result of the more accurate computation of balanced pressure. Since we are not very concerned with the stratospheric stability, we have rerun with $\Gamma_S = 0.025$ K m^{-1}. Using profile correction option 1 we obtain the initial state shown in Fig. A.2. This has a very weakly unstable layer in the stratosphere but runs stably for 10 days (though with some suggestion of convective instability on the warm front).

Using profile correction option 2 we obtain the initial state shown in Fig. A.3. This transfers the unstable layer to the tropical troposphere, but also runs stably for 10 days (though with some suggestion of convective instability on the warm front). For reference, the jet is shown in Fig. A.4.

Note that both setups are notacably warmer than Baker's, which suggests that she did not use either profile correction option.

The forecast after 3 days, 18 h (corresponding to Fig. 5.6(d) of Laura Baker's thesis) is shown (on a polar-stereographic projection) in Figs. A.5 (profile correction option 1) and A.6 (profile correction option 2). Note that these only show data north of 30°N and we have plotted the domain twice, once displaced by 45° in longitude to make it easier to see the cyclone structure.

A.6 Initial Perturbation

The initial perturbation is purely of θ and is independent of height. It has the following form:

$$\Delta\theta = \Delta\theta_0 \cos\left(\frac{2\pi\lambda}{L_\lambda}\right)\left[\frac{1}{\cosh\left(n\left(\phi-\phi_c\right)\right)}\right]^2 \tag{A.60}$$

Here $\Delta\theta_0$ is the perturbation amplitude, L_λ is the total logitudinal extent of the domain, ϕ_c the centre of the jet, n the wavenumber of the system (i.e. the number of waves we anticipate along around the globe; we have used 8 compared with 6 used by Polvani and Esler (2007).

This formulation guarantees one full wave E-W perturbation in the modelled domain. It dies away in the S-N direction roughly as $4\exp\left(-2n(\phi-\phi_c)\right)$ so falls to $\frac{1}{2}$ in roughly $1/n$ radians from the jet core. With $n = 8$ this is about 7 degrees of latitude either side of the jet centre (so, taking twice this ether side leads to a total width of about 30 degrees.

Suppose we wish to run in a domain with periodicity different from n (say $n/2$). Then we might re-write this as:

$$
\begin{aligned}
\Delta\theta =& 0 && ; \ \lambda - \lambda_0 \leq 0 \\
=& \Delta\theta_0 \cos\left(n\left(\lambda - \lambda_0\right)\right)\left[\frac{1}{\cosh\left(n\left(\phi - \phi_c\right)\right)}\right]^2 && ; \ 0 < \lambda - \lambda_0 \leq 2\pi/n \\
=& 0 && ; \ \lambda - \lambda_0 > 2\pi/n
\end{aligned}
\tag{A.61}
$$

where λ_0 is the westmost extent of the perturbation (typically the western edge of the computational domain).